Terahertz Near-Field Imaging of Plasmonic Mode Resonances in Metamaterials

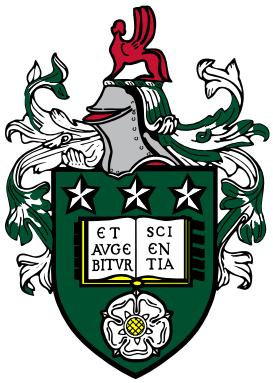

Nikollao Sulollari

Pollard Institute

School of Electronic and Electrical Engineering

The University of Leeds

Submitted in accordance with the requirements for the degree of

Doctor of Philosophy

June 2022

The PGR confirms that the work submitted is their own, except where work which has formed part of jointly authored publications has been included. The contribution of the PGR and the other authors to this work has been explicitly indicated below. The PGR confirms that appropriate credit has been given within the thesis where reference has been made to the work of others.

The results discussed in Chapter 3 formed the basis of a journal publication in the APL Photonics journal:

N. Sulollari, J. Keeley, S. Park, P. Rubino, A.D. Burnett, L. Li, M.C. Rosamond, E.H. Linfield, A.G. Davies, J.E. Cunningham, and P. Dean, "Coherent terahertz microscopy of modal field distributions in micro-resonators," APL Photonics, 6(6), p.066104, 2021

Paul Dean, Nikollao Sulollari, and James Keeley conceived the idea, developed the experimental setup, and performed the measurements. Resonator structures were designed by Nikollao Sulollari and SaeJune Park and fabricated by Nikollao Sulollari under the supervision of Mark C. Rosamond. Data were analyzed by Nikollao Sulollari and James Keeley with support from Paul Dean, John E. Cunningham, SaeJune Park, and Andrew D. Burnett. The QCL structure was grown by Lianhe Li under the supervision of Edumnd H. Linfield. Devices were processed by Pierluigi Rubino under the supervision of Edmund H. Linfield and A. Giles Davies. The manuscript was written by Nikollao Sulollari, Paul Dean, SaeJune Park, Andrew D. Burnett, and John E. Cunningham with contributions from all the authors.

This thesis is dedicated to my parents Elda and Jim who have always been supportive and believed in me. I am grateful, and hope to make you proud for everything you have done for me.

Acknowledgements

Firstly, I would like to thank my supervisors Dr Paul Dean and Professor John Cunningham for providing me the opportunity to work on this project. Their enthusiasm, expertise, and cooperation motivated me to achieve the goals of this project. I would also like to thank Professor Edmund Linfield and Professor Giles Davies for their guidance and valuable advice at the meetings.

Secondly, I would like to thank Dr James Keeley, Dr Saejune Park for their help in the THz lab, the cleanroom, and with the HFSS simulations. Thanks must go to Pierluigi Rubino, and Dr Iman Kundu for sharing their experience during conversations that gave me some direction for the project.

I would also like to thank Dr. Andrew Burnett for showing me how to use the THz-TDS system and the software to analyse the acquired data.

Special thanks must go to Dr Mark Rosamond for his extraordinary help and advice in the cleanroom and also for assisting with the fabrication of samples using electron-beam lithography.

I would also like to thank Dr Mohammed Salih, Dr Yingjun Han, and Dr Li Chen for the cleanroom training and sharing their knowledge.

Finally, I would like to thank Dr Lianhe Li for providing the QCL wafers which were grown using the in-house molecular beam epitaxy.

Abstract

Surface Plasmon Polaritons (SPPs) are electromagnetic waves that propagate at the interface of a metal and a dielectric material. The incoming light couples with the free electron gas on the metal surface and gives rise to these hybrid waves. Such waves occur at visible wavelengths owing to the optical properties of metals. However, metal surfaces do not support tightly-confined SPPs at terahertz (THz) frequencies. This physical limitation has led to the investigation of new ways to transfer the SPP ability to tightly confine light in deep subwavelength dimensions at lower frequencies. Such ability promises to open-up new opportunities for applications such as ultra-sensitive THz sensors, miniaturised THz integrated circuits and devices, and THz active elements including SPP switches, amplifiers, and frequency mixers. Metamaterials are artificial periodic structures whose features are smaller than the wavelength of the incident light. By altering the dimensions and the geometry of the structures, metamaterials can be engineered to support surface modes called Spoof Surface Plasmon Polaritons (SSPPs) at THz frequencies.

In this work, new techniques based on THz scattering-type near-field optical microscopy (s-SNOM) are developed. A novel THz-s-SNOM system is used to spatially map the out-of-plane electric field associated with localised SSPPs on two exemplar structures, the dipole antenna (DA) and the split-ring resonator (SRR). The acquired THz-s-SNOM images show good agreement with finite-element method (FEM) simulations. Furthermore, all-electronic coherent THz-s-SNOM is employed to spatially map the amplitude and phase of the out-of-plane field associated with localized SSPPs on the DA structure. It is shown that the THz-s-SNOM system can achieve a spatial imaging resolution of 35 nm, corresponding to $\lambda_0/2,500$, where $\lambda_0 \approx 87$ µm.

Novel structures that support propagating THz SSPPs are also designed and their operation is confirmed by FEM simulations. These include asymmetric and symmetric planar surface plasmon (PSP) waveguides, and directional couplers (DC). THz-s-SNOM is also used to confirm the operation of these structures, showing good agreement with FEM simulations. This new characterization technique opens the way for the future design and optimisation of novel THz optoelectronic devices based on sub-wavelength resonators and associated metamaterials, as well as the nanoscale mapping of THz SSPPs in 2D materials. Such structures can be used to create novel circuitry operating at THz frequencies, where the compact size of electronic circuits can be combined with the operational bandwidth of plasmonic circuits.

Contents

List of Figures

List of Tables

Chapter 1

Introduction

1.1 Terahertz radiation

The Terahertz (THz) range of frequencies (defined as the frequencies from 300 GHz to 10 THz) occupies the spectral band between infrared (IR) and microwave radiation [1, 2], and hence represents the "meeting point" between optical and electronic technologies. Until recently, it has been a region rarely utilised due to its position in the electromagnetic (EM) spectrum. In particular, the lack of a high-power and compact THz source, and of THz detectors which can operate at room temperature has hindered the development of systems operating in the region.

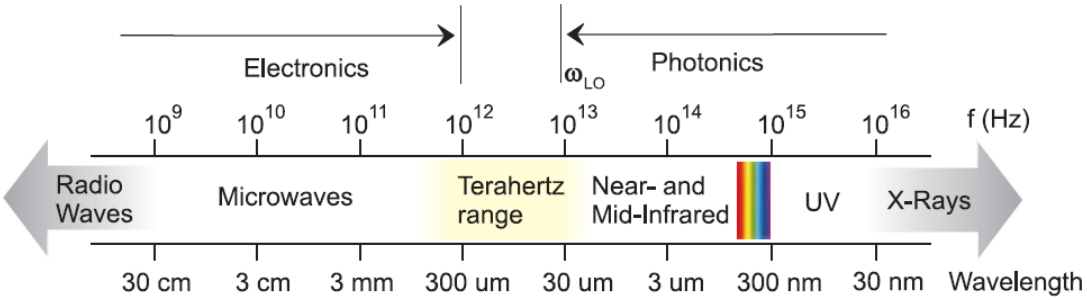

Figure 1.1: The EM spectrum indicating the THz region. Reproduced from [3]

THz radiation has gained particular interest from scientific and industrial communities due to the unique properties that it possesses. THz has the ability to penetrate through dry, solid, non-conducting materials such as carbon, plastic,

wood and clothing [4], which makes it an attractive prospect for security screening in airports [5] and non-invasive mail inspection for the detection of drugs and explosives [6]. Unlike X-rays, THz is non-ionising [7], and another promising application is in the field of medical imaging [8] where a THz system can be used to detect cancerous tissue [4, 9]. Furthermore, THz offers several unique opportunities for sensing applications, for example, the ability to probe electronic transitions in semiconductor or superconductor materials, to study long-range vibrations in crystalline materials such as proteins and pharmaceutical products, or to target the fundamental rotational modes of numerous important gas species [10].

1.2 Terahertz systems and applications

Early scientific interest in the THz region was shown in 1925 [11] and the first THz images in the field of astronomy were acquired in the 1960s [12]. In 1975, a THz imaging system was setup by D.H. Baker et al. [13], based on an HCN laser operating at a wavelength of 337 μm and an LED-based THz detector. The authors managed to obtain images of concealed objects using the raster-scanning method. In addition, they determined the transmittance of different materials, including clothing and biological samples at a frequency range of 0.3 to 0.9 THz [12]. These were the first findings which demonstrated the potential of THz imaging in various applications such as military, law enforcement, and medical imaging.

Despite the early interest in terahertz region, the industrial impact remained minimal for decades, mainly due to the lack of high-power sources, the large size of the THz experimental systems, and the high costs of the equipment. This has been described for a long time as the THz gap [1, 2]. Electronic devices such as Gunn oscillators and Schottky diode multipliers have demonstrated low powers at frequencies beyond 100 GHz. This phenomenon occurs due to the physical limitations of the electronic devices. At terahertz frequencies, the transit time becomes comparable to the electron oscillation period, leading to significantly reduced efficiency and frequency roll-off [14, 15]. In addition, photonic approaches for direct generation of radiation are limited to the material bandgap, which is at energies significantly higher than those associated with the THz region for most convenient direct-bandgap materials such as GaAs.

It wasn't until the mid-1990s when near-infrared (NIR) ultra-fast lasers were developed that a breakthrough occurred leading to the development of modern

day THz-time domain spectroscopy (THz-TDS) systems [16]. The most common source and detector of these systems is the photo-conductive antenna (PCA) [17], which produces broadband THz radiation from frequencies of 0.3 up to $\sim$ 5 THz. Subpicosecond pulses are generated by an ultra-fast laser and focused on the PCA. The pulses create electron-hole pairs with a short lifetime which produce transient currents in the device and lead to a broadband radiation emission in the THz range.

The first practical images acquired using THz-TDS were reported in [18] which rekindled academic and industrial interest in terahertz technology. THz-TDS proved to be a powerful tool for spectroscopic measurements of the properties of materials such as dielectrics, semiconductors, superconductors, liquids, and gasses. In addition, the detection is coherent as both the amplitude and phase of the THz waveform are measured, allowing the extraction of the complex dielectric constant of the material under investigation [18]. One of the notable technological advancements that promoted THz-TDS was the reduction of the acquisition time for each THz waveform from a few minutes down to $\sim$ 5 ms with a signal-to-noise (SNR) ration still higher than 100 : 1. Other advancements include the down-conversion of THz waveforms into the kilohertz range, and the real-time acquisition, processing and analysis of the data using a digital signal processor (DSP) [18].

Although the use of PCAs in THz-TDS systems paved the way for the exploitation of terahertz radiation in practical applications, they suffer from some considerable limitations. The most significant limitation of the PCAs is their low output power, typically $\sim \mu W$ for the optically pumped devices commonly employed [19]. Furthermore, their usable dynamic range is limited to $\sim$ 3 THz as the emission power drops significantly beyond that value. The PCAs also require expensive and bulky ultra-fast lasers to generate and detect THz radiation. The spectral resolution does not exceed 5 GHz and the acquisition rate is slow due to the requirement for mechanical scanning of the optical delay at each pixel. This is a consequence of the TDS system rather than the THz source. Another disadvantage of the device is that it can only emit broadband radiation. One example of an application that requires narrowband THz radiation is gas spectroscopy since gas absorption lines are very narrow [20]. Another example is the use of a THz source as a local oscillator in a heterodyne receiver [21]. Other applications which do not require broadband emission would also benefit from a narrowband, high power THz source.

These limitations have motivated researchers to invent alternative THz sources. A compact, high-power and coherent THz source would be appealing for the advancement of terahertz technology. In the NIR, devices such as the heterostructure laser diodes have exhibited high-power, coherent radiation and compact size. Developing a THz source which would mimic such properties and be based on the semiconductor laser model is a great challenge. Since materials with sufficiently small bandgap for the generation of THz radiation by intra-band electron transitions do not exist, other ways have been explored to overcome this limitation. Firstly proposed in 1971 by Kazarinov and Suris [22], artificial materials can be engineered to obtain the desired transitions by means of quantised subbands in 2D quantum wells. The design of multiple quantum wells separated by a thin barrier formed the first Quantum Cascade Laser (QCL) in 1994 which was demonstrated in Bell Labs [23]. The device emitted mid-IR radiation at a frequency of 75 THz. This was improved upon leading to the demonstration of the first THz-QCL in October of 2001 by Kohler et al. [24]. The maximum output power of the laser was 2 mW at the frequency of 4.4 THz and the maximum operating temperature was 50 K. The gain media of the QCL consists of hundreds of thin layers alternating between different semiconductor materials with different energy bandgaps, typically GaAs ($E_g \simeq 1.4\ eV$) and AlGaAs ($E_g \simeq 2\ eV$), grown using molecular-beam epitaxy (MBE). The emitted photon energy is not determined by the material bandgap but may be chosen by engineering the width of the quantum wells. Advances since then have led to THz-QCLs operating at a frequency range of $1.2 - 5.2$ THz, exhibiting peak powers of $\sim 2.4\ W$ [25], and maximum operating temperature of $\sim 250\ K$ [26], although these values were not obtained from the same device. More information on QCLs will be presented in Chapter 2. QCLs also offer the potential for frequency tunability [27], coherent imaging based on the self-mixing phenomenon in THz-QCLs, imaging with high-spatial resolution, long-range imaging, and material analysis.

1.3 Terahertz imaging using QCLs

As discussed in section 1.1, terahertz radiation is particularly suited for imaging in a variety of disciplines such as biomedicine, security control, non-destructive analysis and spectroscopic mapping of illicit materials [4, 28]. This is because terahertz demonstrates unique properties when compared to the neighbouring infrared and

microwave spectral regions. THz has the ability to penetrate through dry, solid, non-conducting materials such as carbon, plastic, wood and clothing which are typically opaque at visible/infrared frequencies. Furthermore, terahertz radiation offers sub-millimetre diffraction-limited imaging resolution. This combination of properties has sparked interest in the field of terahertz imaging within the security sector, non-destructive inspection, and quality control [29, 30]. The first reported image obtained using THz-TDS was of a semiconductor integrated circuit (IC) package. The THz transmission was colour coded according to the total intensity of the transmitted THz signal integrated over a 1 to 3 THz frequency range. The different materials of the IC showed different absorption strengths. The signal intensity dropped slightly through the plastic packaging, and moderately through the doped semiconductors. However, there was no signal observed through the metal [18]. The second acquired image showed the water content of a fresh cut leaf compared to the same leaf after 48 hours. It was observed that the fresh leaf caused significant absorption due to the water content whereas the leaf after 48 hours caused less absorption due to the evaporation of the water. Another example of terahertz imaging applications is the characterisation of thickness and uniformity of the coating on pharmaceutical tablets [29, 31]. Another important property of terahertz radiation is its ability to excite vibrational modes of materials which show no excitation from microwave and infrared radiation. This characterstic allows materials to be identified based on their chemical composition and their crystalline structure [6, 31]. This makes terahertz radiation an ideal candidate for imaging of concealed samples and the identification of chemicals such as illicit drugs and explosives [32–34]. Terahertz waves are also non-ionising and are highly absorbed by water. The degree of terahertz absorption can be used to distinguish between healthy and cancerous tissue, and between muscle and fat [35, 36].

The advantages of THz-QCLs over broadband sources such as PCAs are detailed in section 1.2. THz-QCLs can be used for incoherent imaging which is based solely on the amplitude of the detected THz beam. They can also be used for coherent imaging where both amplitude and phase information of the THz beam are obtained. Although incoherent imaging with THz-QCLs typically require a less complex experimental setup, coherent imaging systems have the advantage of providing phase information. One example where phase information is essential is to extract the complex permittivity of a sample under investigation.

1.3.1 Incoherent imaging with THz-QCLs

The early demonstrations of imaging using THz-QCLs [9, 37, 38] were based on incoherent imaging techniques for the purpose of system simplicity. Such systems typically employ cryogenically cooled bolometric detection [10, 37] or pyroelectric sensors [39] and demonstrated high sensitivity and high dynamic range up to 64 dB [10]. THz-QCLs imaging systems have also demonstrated higher spatial resolution compared to THz-TDS systems due to the reduced diffraction-limited beam resolution, which is a consequence of higher operating frequencies. An imaging resolution of $\sim$ 250 µm has been demonstrated [9, 40], which is still far above the wavelength dependant limit ($\sim$ 64 µm at 3 THz [41]). This fact is attributed to the irregular beam profiles exhibited by THz-QCLs. For this reason, QCL-based imaging systems have exclusively used semi-insulating surface plasmon (SISP) waveguides due to the superior beam quality and reduced beam divergence when compared with metal-metal waveguides [42, 43]. However, far-field beam profiles of such devices suffer from dual emission lobes originiating from beam diffraction from the substrate and the waveguide ridge [21, 44, 45]. Further efforts have been made to improve the beam quality by employing hollow dielectric waveguides that efficiently couple the QCL beam to the free-space [41, 46]. Another approach is to use spatial filtering of the beam which has been demonstrated in [47]. The QCL emmited light at 2.9 THz and the beam was spatially filtered using a 200 µm aperture that is larger than the emission wavelength, showing an improved imaging resolution of $\sim$ 70 µm.

Most THz-QCL imaging systems use the raster-scanning technique to obtain images where the sample is scanned through the beam and each pixel is recorded. However, this approach is very slow and less applicable to real-world applications. The image acquisition rate depends on multiple parameters such as the pixel size, integration time per pixel and detector response time. The commonly employed incoherent detectors such as cryogenically cooled bolometers and pyroelectric sensors have response times $\sim 1 - 100$ ms. However, a fast acquisition system was demonstrated in [48] which was capable of acquiring a two-dimensional (2D) image comprising 4550 pixels over an area of 36 mm $\times$ 40 mm within just 1.1 s ($\sim$ 4140 pixels per second (pps)). The collimated beam of a THz-QCL emitting at 2.5 THz was deflected onto a high density polyethylene (HDPE) lens using a flat scanning mirror, the angle of which could be controlled with a resolution of 2 µm. The varying deflection angle translated to a transverse displacement across the sample

controllable within 1 µm. The transmitted beam through the sample was focused on the fast Ge:Ga photoconductive detector [48]. The experimental system setup is shown in Fig. 1.2 (a). This system was also used to produce fast three-dimensional (3D) imaging by computer tomography (CT), achieved by successive 2D images acquired for different angles of the sample which was mount on a rotational stage. For 60 projection angles, an imaging time of 87 s was required which corresponded to $\sim$ 3100 pps. Figures 1.2 (b) and 1.2 (c) show a photograph and the CT image of a polyethylene bag filled with TPX pellets respectively. For comparison, CT systems [49, 50] employing raster-scanning reported imaging rates of only $\sim$ 6 pps.

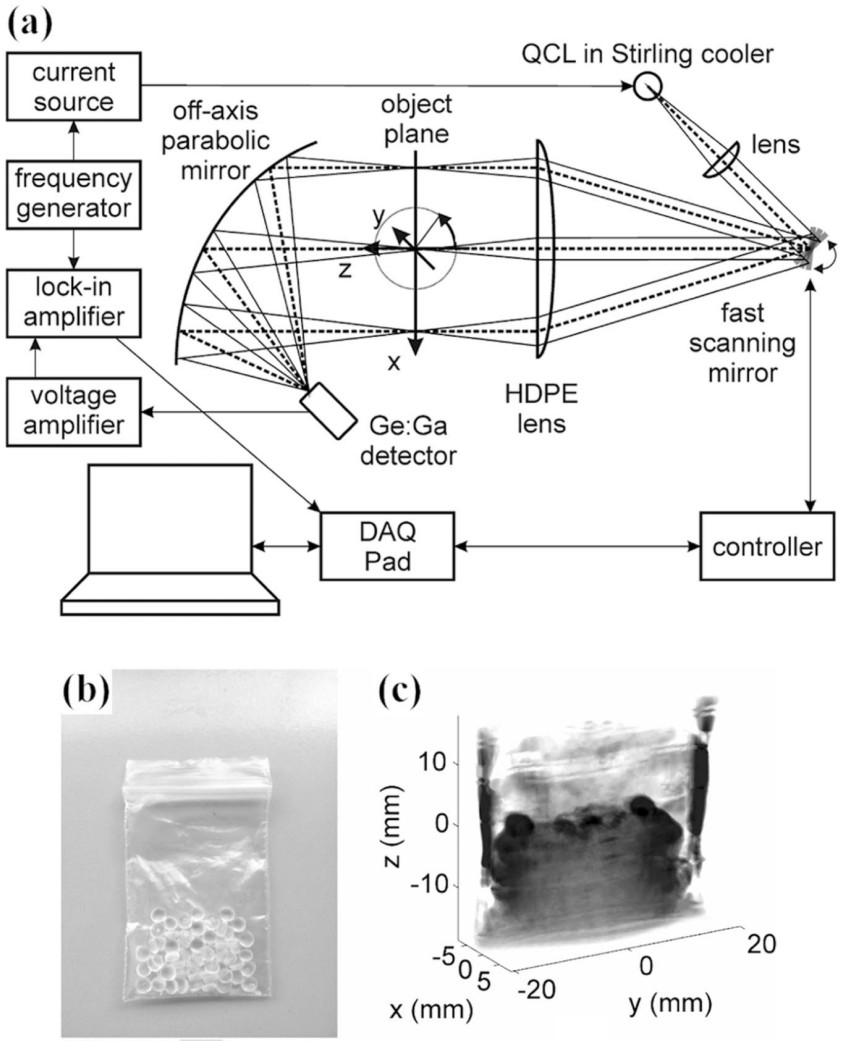

Figure 1.2: (a) Experimental system used for fast THz imaging and tomography. (b) Photograph and (c) CT image of a polyethylene bag filled with TPX pellets. Adapted from [48].

1.3.2 Coherent Imaging with THz-QCLs

Coherent imaging presents significant advantages over incoherent imaging as it allows for the amplitude and the phase of the terahertz field to be extracted. The amplitude and phase information are related to the complex permittivity of a sample under investigation, and can also be used for depth-resolved (3D) imaging. One method of implementing a THz-QCL coherent system is by mixing the terahertz field with a reference signal from a local oscillator to generate an intermediate frequency (IF) which can be measured using electronic detection. However, this approach requires a very frequency-stable terahertz source. THz-QCLs suffer from $\sim 1/f^2$ electrical and thermal noise components which lead to line broadening and frequency drift on the order of several MHz over periods of seconds [51, 52]. This creates the need for a feedback loop for dynamic control for the laser driving current and device temperature.

Another approach to coherent imaging employed frequency stabilisation to a free-running CO_2 laser-pumped molecular laser emitting at 2.41 THz [46]. An IF signal with frequency 1.05 GHz was generated by mixing the two laser sources on a Schottky mixer. With the QCL stabilised, coherent detection was possible through the use of the molecular laser as a local oscillator for the reflected terahertz field, collected at a second Schottky mixer. The experimental system of this coherent imaging system is shown in Fig. 1.3 (a). Figures 1.3 (b) and 1.3 (c) show a photograph of the sample and the azimuth/elevation terahertz image. A Fourier transform analysis of the data allowed amplitude and phase to be recorded with a resolution of 0.4 in azimuth and 0.6 mm in elevation directions of the sample.

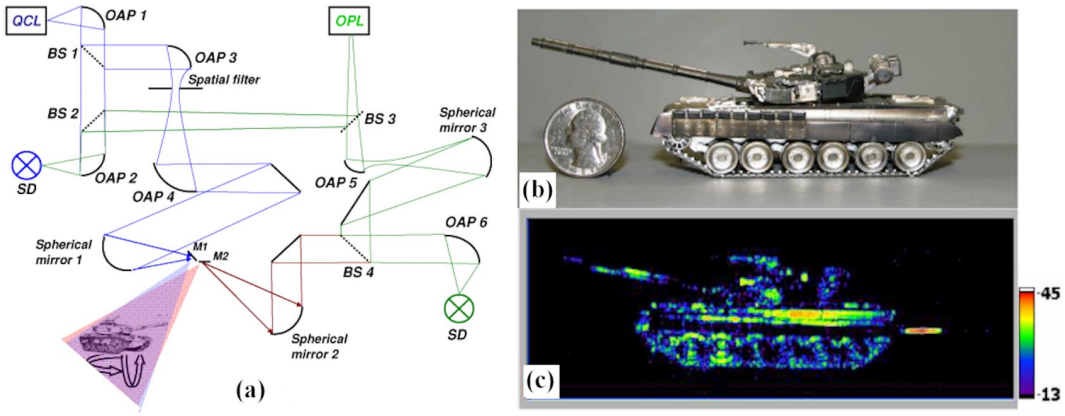

Figure 1.3: (a) Schematic of the ISAR imaging system. (b) photograph, (c) THz ISAR image of a aluminium-covered plastic tank. Adapted from Danylov [46].

While coherent systems described in this section provide the benefit of amplitude and phase extraction, they require complicated experimental set-ups with multiple laser sources and detectors for QCL stabilisation and detection. A much simpler and compact coherent imaging system is based on the self-mixing effect, which is an intrinsic phenomenon observed in a broad range of lasers. In a SM-THz-QCL imaging system, the QCL acts as the source and the detector. The self-mixing effect is detailed in the next section.

1.4 Self-Mixing

Terahertz detection technology suffers from the lack of coherent, fast and sensitive detectors that have hindered the development of a compact THz system for imaging applications. Coherent imaging, i.e. the ability to detect amplitude and phase contrast presents significant advantages as it can obtain information of the real and imaginary parts of the dielectric constant as well as depth information of the sample.

The Self-Mixing (SM) effect or Laser Feedback Interferometry (LFI) presents an elegant and powerful approach to THz imaging due to its sensitivity to both sample reflection and surface morphology as changes of amplitude and phase respectively. The SM effect occurs when a fraction of radiation emitted by a laser is reinjected into the cavity from an external reflector [53]. The reflected radiation interferes with the field in the laser cavity, causing changes in the electrical and optical properties of the laser [54, 55]. Such changes are the threshold gain, optical power, the lasing frequency, and in the case of semiconductor lasers, the laser terminal voltage (SM voltage or LFI signal). These perturbations depend on both the amplitude and the frequency of the reinjected field. In this way, a compact system is built with the laser being used as an interferometric sensor, comprising the source, local oscillator, mixer, and a sensitive detector.

The first demonstrations of the SM effect are documented in 1962 as a mode suppression technique of the Helium-Neon (He-Ne) or the variation of the output power as the external cavity length changed [56, 57]. In 1968, it was demonstrated that the threshold carrier density of the lasers could be changed under optical feedback (OF), and would depend on the phase of the reinjected field [58, 59]. Furthermore, the first theoretical model which describes the SM effect using mathematical equations was developed in 1980 by Lang and Kobayashi [60]. This

model describes the changes to the threshold carrier density and the emission frequency due to the changes to the laser's refractive index caused by the optical feedback. The steady state solutions for the threshold carrier density N and laser frequency ν are:

$$\phi_L = 2\pi\tau_{ext}(v_0 - v) + C\sin\left(2\pi\nu\tau_{ext} + \arctan\left(\alpha\right)\right) \tag{1.1}$$

$$N - N_0 = -\beta\cos\left(2\pi\nu\tau_{ext}\right), \tag{1.2}$$

where the subscript 0 denotes initial laser parameters, α is the linewidth enhancement factor (LEF), and β represents the coupling rate of feedback relative to the rate of carrier density gain. These perturbations to the carrier density and laser frequency are linked to the parameters of the external cavity length L_{ext} which determines the round-trip delay $\tau_{ext} = 2L_{ext}/c$, and the reflectance of the external cavity mirror or the sample under investigation R_{ext}. The parameter R_{ext} is used to calculate the value of the dimensionless feedback parameter C which defines the strength of the optical feedback and it is defined as

$$C = \varepsilon\frac{\tau_{ext}}{\tau_L}\sqrt{1+\alpha^2}\sqrt{\frac{R_{ext}}{R_L}}(1 - R_L)\,, \tag{1.3}$$

where ε is a coupling constant that accounts for partial re-injection into the laser cavity and other optical losses, τ_L is the laser cavity round-trip time, and R_L is the reflectance of the laser facet.

The equation 1.1 is known as the excess phase equation which determines the lasing frequency under OF. This equation exhibits a unique solution when $C < 1$, which is the weak feedback regime. Under this regime, the lasing frequency is almost equal to the frequency without OF ($\nu \approx \nu_0$).

The light reinjected into the laser cavity causes perturbations to the electrical and optical properties of the laser. One parameter which experiences perturbations under OF is the threshold gain. This is important from an experimental point of view, since the self-mixing signal is measured by monitoring the change in the laser voltage, which is proportional to the change in gain. The expression of the threshold gain has been derived in [61, 62] which yields

$$\Delta g = -\frac{\varepsilon}{L}\sqrt{\frac{R_{ext}}{R_L}}(1 - R_L)\cos\left(2\pi\nu\tau_{ext}\right), \tag{1.4}$$

where L_{ext} is the laser cavity length, ν is the laser frequency, and τ_{ext} is the round-trip delay. The cosine term contains the round-trip phase shift of the external cavity, hence the change in gain threshold is periodic with L_{ext}. Also, $|\Delta g = 0|$ when $\phi_{ext} = (1 + 2m)\pi/2$ where m is an integer. An expression for the change in voltage can be derived based on Eq. 1.4:

$$\Delta V_{SM} \propto \varepsilon\sqrt{R_{ext}}cos(\frac{4\pi L_{ext}\nu}{c}). \tag{1.5}$$

The dependence of the voltage change on the external cavity length allows for extraction of amplitude and phase information of a sample under investigation, hence the self-mixing effect can be used for terahertz coherent imaging. The description above is described in terms of a reflective target with reflectance R_{ext}, however this can be equivalently be a scattering source such as an atomic force microscope tip. This is the case in a self-mixing based THz scattering-type scanning near-field microscopy system (see section 1.5) and is fundamental to the work presented in this thesis (Chapters 3-6). For the complete derivation of the SM voltage and further theory of the SM effect, the reader is referred to [61, 62].

1.4.1 The Self-Mixing Effect in THz-QCLs

Over the past decades, the SM effect has been investigated in visible and near-infrared lasers for sensing applications [63]. However, it was not until recently that the phenomenon of OF in THz-QCLs has been studied and its potential for imaging applications has been discovered [64, 65]. Firstly, the SM effect in the THz region offers a great alternative to the use of THz detectors which are slow, bulky and often require cryogenic cooling. The THz-QCL is used as the source and detector which simplifies the experimental setup and facilitates the development of compact THz imaging systems. Furthermore, the large voltage perturbation observed in THz-QCLs under OF can be two orders of magnitude greater than that observed in traditional laser diodes [64]. The voltage sensing approach in THz-QCLs also offers the possibility of extremely fast detection bandwidths since the speed of response to OF is fundamentally determined by elastic and inelastic scattering mechanisms. In THz-QCLs, these occur on picosecond time scales [66, 67], suggesting response bandwidths on the order of $\sim$ 10–100 GHz should be achievable. One further remarkable consideration of the SM effect in THz-QCLs is the extremely high detection sensitivity that it provides. The self-coherent

nature of SM inherently ensures the suppression of background radiation entering the laser cavity. When combined with the large voltage perturbations induced by coherent reinjection to the laser, detection sensitivities at the $\sim$pW/$\sqrt{Hz}$ level can be achieved, which is comparable to that obtained in commercially available cryogenically cooled THz detectors [68].

An example of THz imaging using the SM effect on a THz-QCL is the two-dimensional (2D) imaging of two exemplar samples reported in [69]. The imaging system shown in Fig. 1.4(a) was composed of a QCL with a 10 μm thick BTC active region, and a SI-SP waveguide with dimensions 3 $mm \times 140\ \mu m$, emitting light at $\sim$ 2.6 THz in CW mode. The laser was embedded into a cryostat and was cooled at a constant temperature of 25 K. The radiation emitted by the laser was focused onto the sample, creating an external cavity between the target and the laser facet. A mechanical chopper was used to modulate the THz field and a lock-in amplification was used to measure the small ($\sim$mV) SM perturbation to the laser terminal voltage. The sample was raster-scanned at the focus of the beam with a pixel size of 250 µm for Fig. 1.4(b) and 100 µm for Fig. 1.4(c). The SM voltage is detected at each pixel and it is proportional to the sample surface reflectivity, and also depends on the external cavity length. Changes in the cavity length due to surface morphology and sample tilt also affect the SM voltage through a phase perturbation to the returning field. This phase change shows as fringes on the surface of the scalpel blade in Fig. 1.4(b).

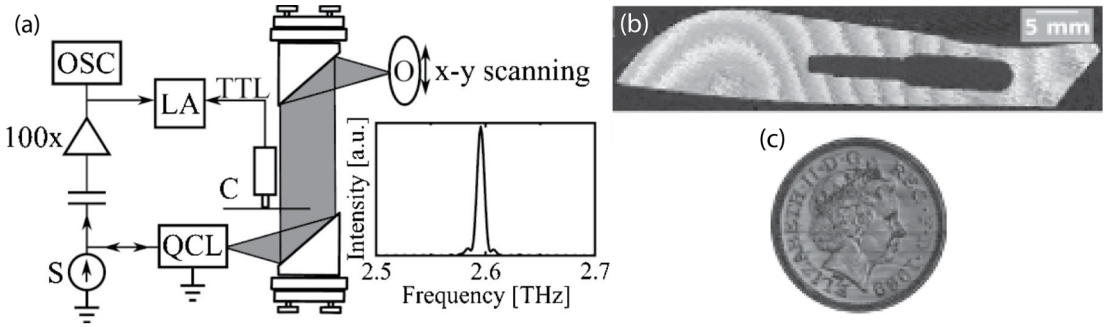

Figure 1.4: (a) Schematic of the imaging system based on a THz-QCL and SM. *S*, current source; *OSC*, oscilloscope; LA, lock-in amplifier; *C*, mechanical chopper. Inset: emission spectrum of the THz-QCL, measured using a Fourier-Transform spectrometer. (b) THz image of a scalpel blade concealed behind a high-density polyethylene FedEx envelope with a resolution of 250 µm. (c) THz image of a British two-pence coin with a resolutio of 100 µm. Adapted from Dean [69].

Further SM work has been reported for 3D imaging [70], material analysis [71], biomedical imaging [72], fast THz imaging [73], and real-time THz imaging [74].

1.5 Near-Field Microscopy

The spatial resolution of a far-field terahertz imaging system is limited by the Rayleigh criterion which states that for a free-space EM wave, the highest spatial resolution is given by the equation:

$$R = 0.61\frac{\lambda}{NA'}, \tag{1.6}$$

where λ is the wavelength of the incident wave and NA is the numerical aperture of the system. This leads to a resolution of $\sim \lambda/2$ for Far-Field THz imaging systems.

The highest spatial resolution that could be achieved in a far-field terahertz imaging system which uses a THz-QCL with a frequency of $\sim$ 2.6 THz does not exceed 70 µm. In order to exploit terahertz radiation for imaging applications that require sub-wavelength resolution such as in biomedical imaging, semiconductor device inspection of surface defects, mapping the charge carrier concentration, and mapping the out-of-plane electric field distribution of plasmons and resonator modes supported by metamaterials micro- and nano-scale resonators, near-field microscopy techniques are required [75–81]. The Near-Field (NF) signal can be measured when the distance between the detector and the sample is smaller than the incident wavelength $d \ll \lambda$. One way of conducting near-field imaging is to bring the detector in close proximity to the sample. However, this approach requires an inconvenient setup. An alternative method is to employ an aperture (pinhole) with diameter $d \ll \lambda$ [82]. The incoming field is squeezed inside the aperture and only what passes through it is detected. The main drawback of this method is that the resolution is not completely independent of the wavelength as the aperture behaves as a high-pass filter with a cut-off frequency of:

$$f_c = \frac{1.841c}{\pi d}, \tag{1.7}$$

where c is the speed of light in vacuum and d is the diameter of the aperture. For example, for a diameter of 100 μm, the cut-off frequency would be 1.76 THz.

1.5.1 Introducing s-SNOM

One powerful technique that is truly wavelength-independent is scattering-type near-field scanning optical imaging (s-SNOM). The s-SNOM technique is based on the Atomic Force Microscope (AFM) technology [83, 84] which uses a probe to measure the surface topography of a sample. An AFM comprises of a probing tip which is held in close proximity to the surface of a sample. The sample is mounted to a piezo-electric scanner which allows its vertical position to be controlled with nanometre scale precision. The probe is mounted on a cantilever which oscillates vertically at its resonant frequency. In this tapping mode, the sample is brought into contact with the oscillating probe, which allows the height of the surface to be determined. By raster scanning the sample orthogonal to the probe axis, the topography of the surface can be measured with an in-plane resolution equal to the radius of the probe [85].

In the s-SNOM scheme the AFM probe also acts as a nanoscale light source when an external beam is focused at its apex. The incoming beam induces a dipole in the probe apex which then induces an image dipole in the dielectric sample. The coupled dipole scatters radiation to the far-field and the scattering efficiency is enhanced relative to the scattering of the bare tip due to the permittivity of the sample in the near-field of the tip [86–88]. The spatial resolution principally depends on the tip-apex size and the tip-sample distance, both of which are considerably smaller than the wavelength of the incoming wave.

The spatial contrast is achieved by the dipole moment that is induced by the incident radiation in the tip and the region below the surface of the sample. The most commonly used model to describe the interaction between the illuminated probe and dielectric sample is the point-dipole model [89–92]. The model treats the probe tip as a sphere with radius R, permittivity function ε_t and polarizability α that is polarised by an incident field E_0, whose polarisation is in parallel with the direction of the probe tip (p-polarised). This model simplifies the tip-sample interaction by making two major assumptions; only the tip of s-SNOM probe causes the near-field interaction with the sample, and the dipole on the tip induced by the incoming wave is infinitely small, located at the centre of the sphere as shown in Fig. 1.5.

The tip dipole induces an image dipole in the sample, with strength βp where

$$\beta = \frac{\varepsilon_s - 1}{\varepsilon_s + 1} \tag{1.8}$$

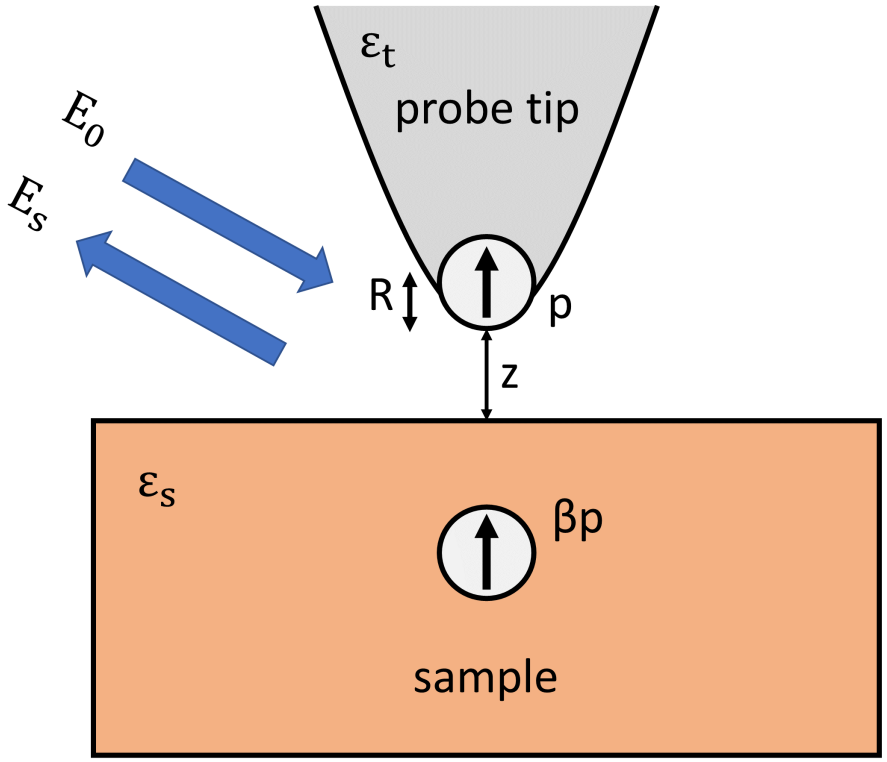

Figure 1.5: Schematic diagram of the point-dipole model. The s-SNOM probe is placed at a distance z above the surface of the sample and an infinitely small dipole is induced by the incident wave E_0. This causes an image dipole moment βp within the sample which enhances the scattering efficiency of the tip in the far-field. The scattered light is collected by an external detector.

is the surface response function, ε_s being the permittivity function of the sample. The image dipole interacts with the tip dipole and creates a field enhancement which increases the scattering efficiency of the tip to the far-field [85]. The effect of the image dipole on the scattered light can be shown by first relating the tip's dipole moment with the polarisability of the tip α and the incident wave without the presence of the sample:

$$p = \alpha E_0 \,, \tag{1.9}$$

where E_0 is the incident field and the polarisability is given by:

$$\alpha = 4\pi R^3 \frac{\varepsilon_t - 1}{\varepsilon_t + 2} \,. \tag{1.10}$$

Under the presence of a sample, the polarisability is replaced with an effective polarisabilty to describe the near-field interaction between both dipoles:

$$\alpha_{eff} = \frac{\alpha}{1 - \frac{\alpha\beta}{16\pi(R+z)^3}}. \tag{1.11}$$

The scattered field is directly proportional to its polarisability, $E_s \propto \alpha_{eff} E_0$. When the s-SNOM probe is at large distance from the sample ($z \to \infty$), Eq. 1.11 shows that the effective polarisability is approximated by the polarisability of the tip dipole, $\alpha_{eff} \approx \alpha$. The point-dipole model considers the tip dipole to be infinitely small, hence the scattered field would be infinitely small $E_s \to 0$. As the distance between the s-SNOM tip and the sample decreases ($z \to 0$), according to the Eq. 1.11 the effective polarisability becomes significantly larger than the tip dipole polarisability. This leads to a strong near-field interaction between the tip and the sample which yields a strong scattered field E_s. Equation 1.11 shows that the effective polarisability is strongly dependent also on the radius of the tip. The optimum radius of the tip is the one which leads the term $\alpha\beta/(16\pi(R+z)^3)$ closest to unity. Furthermore, due to the strong nonlinear dependence of the near-field interaction with the distance between the tip and the sample, the near-field component can be discriminated against the unwanted background signal (e.g. scattering directly from the probe shaft) through demodulation at higher harmonics of the tip modulation frequency [85, 87, 91].

However, experimental results reported by Chen et al. [93] showed that the scattering efficiency for an incident wave with a centre frequency $f_c = 2$ THz is small, with 0.4% of the incoming THz wave scattered from a tungsten tip with a radius of 1 µm. These results show that for a THz-s-SNOM system, a sensitive detector is required. The employment of the self-mixing effect on such a system is appealing due to its high sensitivity.

Although this model can qualitatively describe the near-field interaction between the tip and the sample, the assumptions of the model lead to inaccurate quantitative analysis. One demonstration from Chen et al [93] showed that when they reduced the size of the tip from 1 μm to 100 nm, they did not observe a signal reduction of 10^{-3} as expected from the point-dipole model. These results question the accuracy of the model, as it does not consider the upper part of the needle, which acts as an antenna and leads to a highly-confined field below the tip [93]. Hence a more accurate model was developed where the probe is modelled as an external spheroid, the monopole model [94].

Probing the local permittivity of samples is one of the applications of s-SNOM. In this case, the polarisation of the incident field, E_0 is set to be in parallel with the direction of the probe tip (p-polarised) in order to reach a maximum value of the polarisability, α_{eff}, hence the scattered field due to the tip-sample interaction, $E_s \propto \alpha_{eff} E_0$ is large. This is illustrated in Fig. 1.6 (a). In addition to probing the local permittivity of samples, s-SNOM can also be used to measure surface fields supported by structures. This technique has been used in a number of situations, such as imaging resonant modes in resonators at visible frequencies [95, 96], and imaging surface plasmon polaritons in graphene at mid-infrared [97–104] and terahertz [105, 106] frequencies. This approach will be used for imaging the fields supported by resonators and metamaterials in Chapters 3-6. An incident field, E_0 illuminates the probe tip and a sample which supports surface fields, and gives rise to an out-of-plane field, $E_\perp$. This field is scattered by the probe tip and it is p-polarised. If the polarisation of the incident field, E_0 is p-polarised, the scattered field, $E_{s,tot}$ will be a superposition of the field excited due to the tip-sample interaction, E_s and the out-of-plane field, $E_\perp$. The field due to the dipole moment, E_s can be suppressed by illuminating the probe tip with s-polarised light (i.e. the polarisation of the incident field, E_0 is perpendicular to the probe tip axis). This is illustrated in Fig. 1.6 (b).

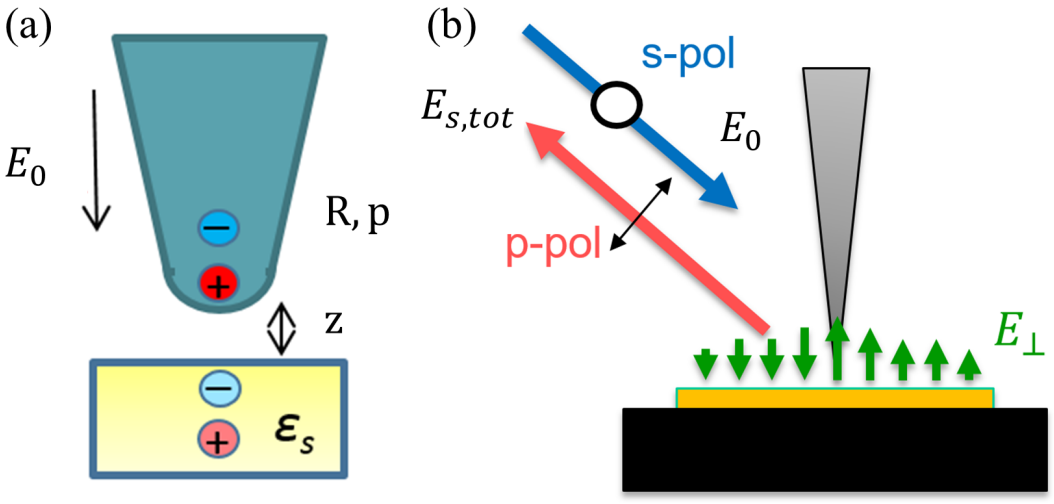

Figure 1.6: (a) A p-polarised light creates a dipole moment between the tip and the sample. (b) A sample which supports plasmonic resonances is illuminated by s-polarised light. The dipole moment between the tip and the sample is now much weaker. Only the out-of-plane field, $E_\perp$ is scattered from the tip.

1.5.2 THz-s-SNOM

The first demonstration of THz-s-SNOM using a THz QCL [107] and the self-mixing effect was reported by Dean et al in 2016 [108]. The THz QCL presented an attractive alternative to the broadband THz sources, due to its compact size, broad spectral coverage, and high output power. The self-mixing detection scheme removes the need for an external terahertz detector, and offers a compact and simple semiconductor-based platform for near-field terahertz imaging. The scheme is also coherent in nature, which allows both the amplitude and phase of the scattered field to be resolved without the need for an external interferometer [109], or synchronisation of the source to an ultrafast laser [110, 111]. Furthermore, the self-mixing scheme offers very fast detection, since it is only limited by electron transport in the QCL [73]. The THz QCL illuminated the the tip and the sample with a frequency of 2.53 THz, and the achieved imaging resolutions were $\sim$ 1 µm ($\sim \lambda/100$) and $\sim$ 7 µm along orthogonal directions of the sample surface.

In 2017, Degl'Innocenti et al [112] demonstrated a THz-s-SNOM system which employed a THz QCL operating at $\sim$ 2.85 THz, and the self-mixing detection scheme. The system was used to investigate the plasmonic resonances supported by a bidimensional photonic crystal triangular hole array, and the electric field enhancmenent supported in the gap of a graphene/plasmonic antenna THz detector [112]. Furthermore, the authors reported an in-plane resolution of $\sim$ 78 nm, which corresponded to $> \lambda/1,000$.

Another demonstration of a THz-s-SNOM system which used a THz QCL as the source and the detector was reported by Giordano et al [113]. The authors exploited the coherent nature of the self-mixing detection and acquired both amplitude and phase contrast with deep sub-wavelength in-plane spatial resolutions (60-70 nm). These findings make it possible to map the complex permittivity of a target using QCLs, with a spatial resolution of tens of nanometers.

1.6 Plasmonics

1.6.1 Surface Plasmons

Surface Plasmons (SPs) arise from the coupling of incoming light and free electrons on the surface between a conductor and a dielectric material (e.g. gold and air) [114]. The term *plasmon* refers to collective oscillations of electrons on a free electron gas (e.g. a metal). Such waves are hybrid in nature due to the coupling of photons and electrons, which gives rise to their unique properties. The most attractive aspects of SPs is the subwavelength confinement of light and the strong field enhancement in the vicinity of metal-dielectric interfaces. SPs offer a bridge between electronic and photonic technologies, offering a potential route to creating new miniaturised and fast plasmonic circuits. They are also exploited in applications such as magneto-optic storage, microscopy, solar cells, and biosensing [114–116].There are two kinds of SPs which depend on the geometry of the interface [117]. Flat metal surfaces support the propagation of surface plasmon polaritons (SPPs), electromagnetic (EM) modes with a subwavelength confinement that propagate along a surface. On the other hand, metal particles with dimensions smaller than the incoming wavelength can also sustain SPs, but the EM modes are then localised and behave as standing waves along the small particles. These EM modes are called localised Surface Plasmons (LSPs) [118].

The existence of SPs is a characteristic feature of the optical response of metals, which can be characterised by the dielectric permittivity $\varepsilon(\omega)$, where ω is the frequency of light [118]. For metals, the permittivity function depends strongly on the frequency of light, which is expressed by the Drude model as

$$\varepsilon(\omega) = \varepsilon_\infty(1 - \frac{\omega_p^2}{\omega^2 + i\gamma\omega}), \tag{1.12}$$

where ω_p is the plasma frequency, γ is the damping constant of electrons, and ε_∞ is a high frequency offset. The bulk plasma frequency is a characteristic of each metal given as

$$\omega_p = \sqrt{\frac{n\,e^2}{m_e\,\varepsilon_0}}, \tag{1.13}$$

with n being the electron density, e is the electron charge, m_e is the effective mass, and ε_0 is the permittivity in vaccuum. For noble metals such as gold and silver, the plasma frequency lies in the ultraviolet (UV) regime, $\omega_p \sim 10^{16} Hz$

[118]. The Drude model accurately shows that the real part of $\varepsilon(\omega)$ is negative for incident frequencies below the plasma frequency, $\omega < \omega_p$. At incident frequencies beyond the plasma frequency, $\omega > \omega_p$, the imaginary part of $\varepsilon(\omega)$ increases due to interband transitions caused by photons that promote electrons to the conduction band. The Drude model fails to give an accurate description of this fact, hence a more accurate modeling of $\varepsilon(\omega)$ for higher frequencies is given by the Drude-Lorentz model. The electron-photon interaction on the surface of a conductor leads to the wave-vector of the SP mode being greater than the free-space momentum $k_{SP} > k_0$. Solving Maxwell's equations for the SP modes under the appropriate boundary conditions yields the SP dispersion relation:

$$k_{SP} = k_0 \sqrt{\frac{\varepsilon_d \varepsilon_m}{\varepsilon_d + \varepsilon_m}}, \tag{1.14}$$

where ε_d and ε_m are the permittivities of the dielectric and the metal respectively. In order to create an SP mode, two conditions need to be satisfied; $\varepsilon_m \cdot \varepsilon_d < 0$ and $\varepsilon_m + \varepsilon_d < 0$. The real part of the permittivity function of the metal needs to have a negative sign for the conditions to be satisfied. Figure 1.7 shows the dispersion relation of the SPs. At low incident frequenices ω, SPs are weakly bound on the metal surface, and the wave-vector of the SP k_{SP} equals the incident wave-vector k_0. As the incident frequency increases, the real part of the permittivity function of the metal becomes less negative. For values of ε_m where $\varepsilon_d + \varepsilon_m \to 0$, the SP wave-vector becomes greater than the incident wave-vector, leading to deep sub-wavelength confinement on the surface of the metal.

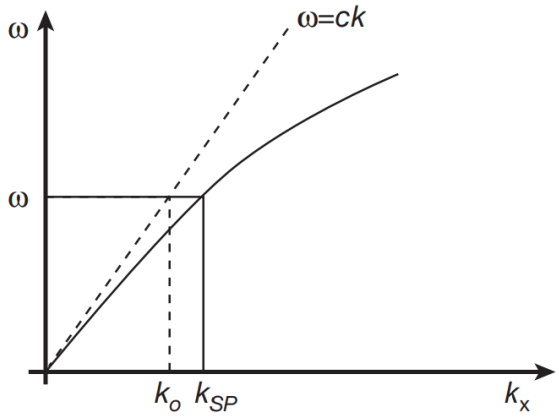

Figure 1.7: The dispersion relation for a SP mode shows the momentum mismatch problem that has to be overcome. Adapted from Barnes [114].

Figure 1.8 shows a diagram of SPs propagating at the interface between a metal and a dielectric. The electric field of the SPs is transverse magnetic (perpendicular to the metal surface), and it decays exponentially with distance from the surface. The field is called evanescent and is a consequence of the bound or non-radiative nature of SPs.

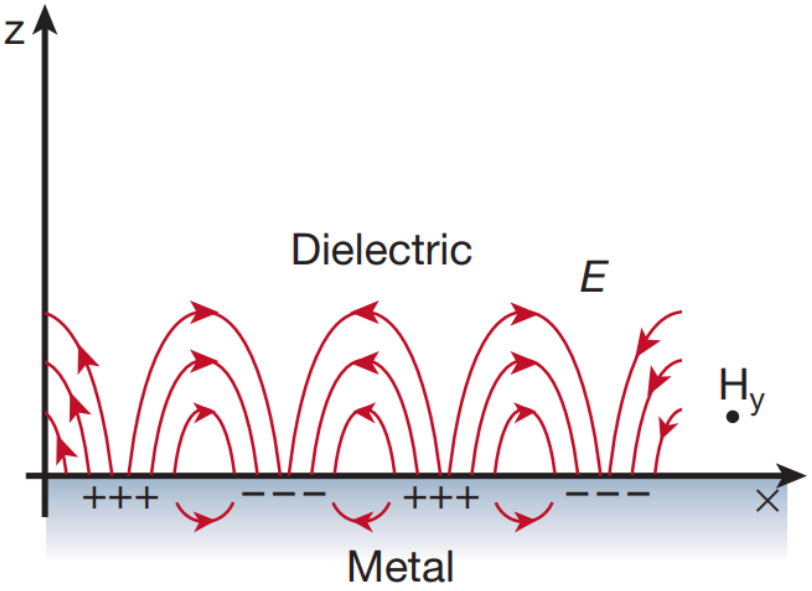

Figure 1.8: SPs at the interface of a metal and a dielectric material arise due to coupling of an EM wave and the electrons on the surface of the metal. They are transverse magnetic in character (H is in the y direction). The SP field is perpendicular to the surface. Adapted from Barnes [114].

Fig. 1.9 shows the relationship between the strength of the electric field and the distance from the surface. SPs are evanescent waves and are highly confined on the metal surface. The electric field decays exponentially away from the surface. In the dielectric medium, the decay length of the electric field δ_d is in the order of half the wavelength of the incident light, whereas the decay length into the metal δ_m is determined by the skin depth. The SP will gradually attenuate due to the absorption from the metal. This attenuation depends on the permittivity function of the metal at the oscillation frequency of the SP. The value of k_{SP} is complex, $k_{SP} = \Re e\{k_{SP}\} + \Im m\{k_{SP}\}$. The imaginary part of k_{SP} determines the

propagation length δ_{SP}:

$$\delta_{SP} = \frac{1}{2\mathcal{I}m\{k_{SP}\}} = \frac{c}{\omega}\left(\frac{\mathcal{R}e\{\varepsilon_m\}+\varepsilon_d}{\mathcal{R}e\{\varepsilon_m\}\varepsilon_d}\right)^{\frac{3}{2}}\frac{\mathcal{R}e\{\varepsilon_m\}^2}{\mathcal{I}m\{\varepsilon_m\}}, \tag{1.15}$$

where $\varepsilon_m = \mathcal{R}e\{\varepsilon_m\} + \mathcal{I}m\{\varepsilon_m\}$ is the dielectric function of the metal, ε_d is the dielectric constant of the dielectric material, ω is the frequency of the incident light, and c is the speed of light. As ω increases, k_{SP} becomes greater leading to deeper subwavelength confinement but the propagation length decreases, as shown in Eq. 1.15. Thus, there is a trade-off between confinement and propagation [119].

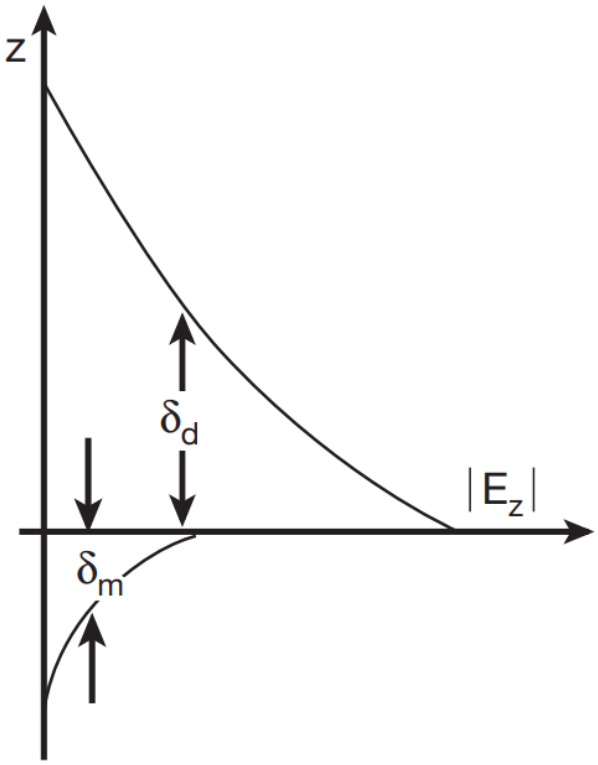

Figure 1.9: The SP field is perpendicular to the surface of the metal and it is said to be evanescent due to its non-radiative nature. The decay length into the metal is determined by the skin depth. Adapted from Barnes [114].

The momentum mismatch between the free-space momentum and SP momentum must be bridged in order to generate SPs. Techniques that are employed for such cause are prism coupling, scattering from a topological defect on the surface,

and periodic corrugations on the surface [120]. The momentum mismatch can also be provided using s-SNOM. In this case, the scattering of the incident field from the probe can itself provide the momentum mismatch to generate SPs. This is a convenient technique as the same system can be used to generate and detect SPs.

1.6.2 Spoof Surface Plasmons

The properties of SPs are closely related to the behaviour of the permittivity function of the metal, which strongly depends on the incident frequency. Equation 1.12 shows the relationship between the metal permittivity and the incident frequency. Furthermore, metal permittivity is also related to the bulk plasma frequency which is expressed by Eq. 1.13. For most metals, the bulk plasma frequency lies in the UV regime. For this reason, plasmonic effects are in principle limited to the high frequency range of the spectrum (UV, optical frequencies, and near infrared). For lower frequency ranges of the EM spectrum, the real and imaginary parts of the permittivity function of the metal become larger. In this regime, the permittivity is dominated by the conductivity $\varepsilon(\omega) \sim i\sigma/\omega$, and free electrons respond immediately to any EM perturbation, thereby shielding the metal from the EM field [118]. For frequencies between radio and terahertz, metals resemble perfect electric conductors (PEC) and do not support tightly bound modes. Only poorly confined modes exist at this frequency range which extend mainly in the dielectric. These are called Zenneck and Sommerfeld waves [118].

The penetration depth of the metal (skin depth), δ, can be used to characterise the PEC limit. It is defined as the inverse of the imaginary part of the wave-vector inside the metal, $\delta = 1/Im\{k\}$. Since $k = k_0\sqrt{\varepsilon(\omega)}$, the ratio between the skin depth and the incident wavelength is

$$\frac{\delta}{\lambda} = \frac{1}{2\pi}\frac{1}{Im\sqrt{\varepsilon(\omega)}}. \tag{1.16}$$

This ratio is related to the impedance of a metal surface, $Z_s(\omega) = 1/\sqrt{\varepsilon(\omega)}$. Therefore, PEC approximation is very accurate for low frequencies ($Z_s = 0$), and it becomes less accurate for higher frequencies.

In order to overcome the natural limitations of metals and create highly confined surface modes at lower frequencies (radio to terahertz), a novel engineering approach is required. The addition of subwavelength corrugations to a metal surface produces an enhanced surface impedance. This method allows light to be

coupled on the surface of such structures, even in the limit of perfect conductivity [121, 122]. In 2004, Pendry et al [123] presented a structure with a corrugated periodic array of holes on the surface of a conductor, as is shown in Fig. 1.10. The dimensions of the holes and the periodicity of the structure are smaller than the incoming wavelength of the radiation $\alpha < d \ll \lambda_0$. Such structures are called metamaterials, which are artificial materials whose EM properties depend on the geometry of the structure rather than their atomic composition. Metamaterials can be described by an effective dielectric permittivity [118, 123], provided that the dimensions of the features are much smaller than the wavelength of the incoming radiation. These structures can support EM modes which are bound on the surface, mimicking the properties of SPs. These waves are known as spoof surface plasmons (SSPs) and their dispersion relation follows closely the one of SPs, which occur at higher frequencies (near-IR, visible, UV). The plasma frequency depends mainly on the geometry of the structure and in the case of a corrugate array of holes is given by the cut-off frequency of the hole waveguide. Metamaterials are also called negative-index materials because at the resonant frequency, the permittivity and the permeability can have negative values [124–128].

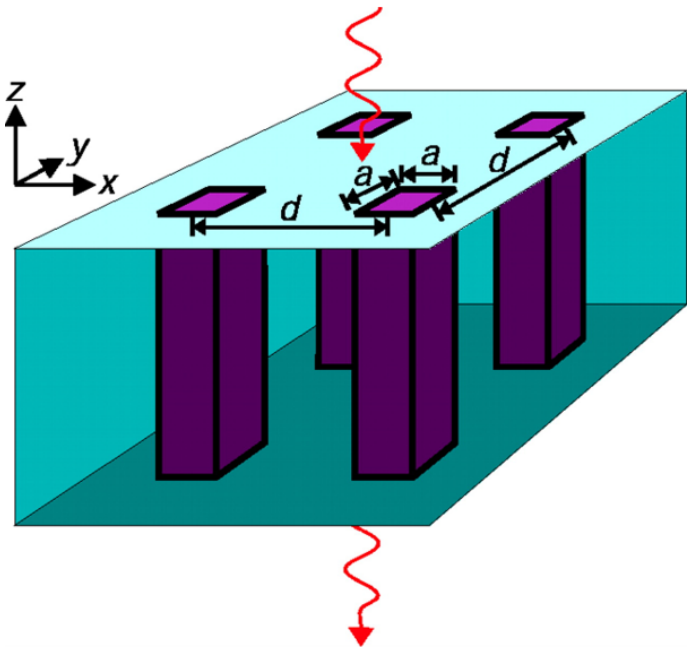

Figure 1.10: A metamaterial structure with a corrugated array of holes with dimensions $a \times a$ arranged on a $d \times d$ lattice. The structure supports spoof localised surface plasmons within the holes. Adapted from Pendry [123].

Experimental observations of SSPs in 2D structured flat surfaces have been demonstrated in the microwave [129, 130] and terahertz regimes [131, 132]. Other metamaterials are metallic nano-wires [95, 133] and split-ring resonators (SRRs) [134, 135]. Such structures support spoof LSPs. In addition, 2D and 3D waveguides has been designed based on metamaterial building blocks [136, 137]. Such structures can support propagating modes from the microwave to the infrared spectral regions, and display strong field confinement and low propagation losses. The design, realisation and experimental investigation of novel structures designed to support SSPs at THz frequencies will be presented in Chapters 4, 5 and 6.

1.7 Thesis Outline

Chapter 2 discusses the laser design concepts to create solid-state lasers at infrared frequencies. Various active region designs, and waveguide designs of the QCL are discussed. The fabrication steps to create functional QCLs, and their characterisation which includes Light-current-voltage (LIV) and spectral characteristics in both pulsed mode and continuous wave operation are also presented. The realisation of a QCL device that operates in continuous wave with emission on a single longitudinal mode is critical to the development of the THz microscopy techniques used throughout this thesis.

In Chapter 3 the use of s-SNOM employing a THz-frequency QCL is demonstrated for coherently probing the localized field supported by individual microresonator structures. A dipole antenna (DA) and a split-ring resonator (SRR) structure are designed in ANSYS HFSS to absorb light with an incident frequency of 3.45 THz. A THz-s-SNOM system was used to map the field distribution on the surface of these structures associated with the resonator modes with deep subwavelength resolution. It is shown that the THz-s-SNOM system can achieve a spatial resolution of 35 nm, corresponding to $\lambda_0/2,500$. By exploiting electronic tuning of the QCL in conjunction with the coherent self-mixing effect in these lasers, both the magnitude and the phase of the out-of-plane field are resolved. Furthermore it is shown that the elliptically polarized state of the QCL field can be exploited for the simultaneous excitation and measurement of plasmonic resonances in these structures while suppressing the otherwise dominant signal arising from the local material permittivity. This new characterization technique opens the way for the future design and optimisation of novel THz optoelectronic devices

based on subwavelength resonators and associated metamaterials, as well as the nanoscale mapping of THz plasmons in 2D materials.

In Chapter 4, a novel metamaterial asymmetric waveguide is designed and investigated experimentally that supports terahertz-frequency spoof surface plasmon polaritons (SSPPs). These waveguides are realised using nearly zero-thickness metal strips printed on rigid substrates. Initially, the dispersion relation of the waveguide was obtained using an eigen-mode solver. Next, a waveguide was simulated using excitation ports at the two ends of the structure to launch and detect the SSPPs propagating on the waveguide. Furthermore, the waveguide was simulated using a free-space beam, and the effects of varying the beam direction, the polarisation and the angle of incidence were investigated. A grating structure was designed and investigated to increase the coupling strength of light to SSPPs propagating on the waveguide. A QCL was used to illuminate the fabricated structures with an incident frequency of 3.45 THz and the s-SNOM system was used to measure the out-of-plane electric field, E_z associated with the SSPPs propagating on the surface of the waveguide. The experiments confirm that this structure support THz SSPPs and show good agreement with FEM simulations.

In Chapter 5, a metamaterial symmetric waveguide is presented which also supports terahertz-frequency SSPPs. Well-confined SSPPs can be supported on either side of the symmetric waveguide. The SSPPs supported by the two sides will interact with each other, and split into two supermodes: even mode (symmetric) and odd mode (anti-symmetric). Theoretical studies of symmetric PSP waveguides and their experimental verification is reported in the terahertz range (3.45 THz). The dispersion relations of the two modes were obtained using an eigen-mode solver. A waveguide was simulated using excitation ports to launch and detect the SSPPs propagating on the waveguide. Furthermore, the waveguide was also simulated using a free-space beam obliquely incident on the structure which was polarised in the perpendicular direction of the waveguide axis. A QCL was used to illuminate the fabricated structures with an incident frequency of 3.45 THz, and the s-SNOM system was used to measure the out-of-plane electric field, E_z associated with the even and odd modes propagating on the surface of the waveguide. The experiments show good agreement with FEM simulations, confirming that this structure supports even and odd modes.

In Chapter 6, the potential to realise different functional plasmonic components at terahertz frequencies is investigated, such as directional couplers (DC) based on the asymmetric metamaterial waveguides. Such structures are essential in the realisation of plasmonic demultiplexing components which offer a compact size of electronic circuits combined with the operational bandwidth of photonic circuits. DC structures allow the control of the spatial distribution of SSPPs between two spatially separated waveguides, depending on the gap size, g in the interaction region (IR), and the coupling length of the IR, L_c. The dispersion relations were calculated using an eigen-mode solver. Next, DC structures were simulated using excitation ports to analyse the electric field distribution on the structures using a phenomenological analysis, and the supermode analysis. This analysis confirmed the desired behaviour whereby the energy associated with SSPPs is transferred between waveguides within the IR and depending on the gap size, g. Furthermore, DCs were simulated using a free-space beam obliquely incident on the structure with its polarisation perpendicular to the DC structure axis. These simulations presented significant differences when compared to the simulations with excitation ports, as unwanted coupling of SSPPs was observed at the start of WG2, and at the end of the S-bend region. These effects complicated the analysis of the free-space beam simulations. Therefore, a phenomenological equation was used to interpret the simulation data and the experimental data obtained using THz-s-SNOM. The wave-vector values of the even and odd modes propagating on the IR obtained from the free-space beam simulations and the experimental data concurred with the wave-vector values from the dispersion relations. The analysis of the experimental data of the S-bend region confirmed the expected behaviour of DC structures.

Chapter 7 summarises the results of this work and suggests tasks for future work.

Chapter 2

Quantum Cascade Lasers

2.1 Semiconductor Laser concepts

A semiconductor has a direct bandgap when the lowest energy (E_c) at the conduction band (CB), and the highest energy (E_v) in the valence band (VB) occur at the same wave-vector value. For a direct-bandgap semiconductor, light can be emitted from a p-n junction under forward bias due to electron-hole pair (EHP) recombination. The energy of the photon is equal to or greater than the material bandgap (E_g), $E_{ph} \geq E_g = E_c - E_v$. An example of such devices is the light emitting diode (LED). The emission in LEDs is spontaneous and it occurs at random times, and in a random direction. Spontaneous emission occurs when an electron drops from the upper energy state to the lower energy state by its own volition, as shown in Fig. 2.1 (a). In the case of the LED the upper state lies in the CB and the lower state in the VB. An electron in the valence band can also absorb an incoming photon if its energy is greater than the energy of the bandgap, $E_{ph} > E_g$ and rise to the conduction band. This effect is shown in Fig. 2.1 (b). If an electron populates the CB, an incoming photon with energy greater than the bandgap can trigger the electron to drop to the VB, realising a photon with energy also greater than the bandgap. This effect is illustrated in Fig. 2.1 (c), and it is called stimulated emission. In this case both photons exiting the semiconductor have the same frequency, phase, and direction. This leads to coherent (monochromatic) radiation and it's the basis of light amplification, also called optical gain (1 photon in $\rightarrow$ 2 photons out). The term **'LASER'** is an acronym which stands for *"light amplification by stimulated emission of radiation"*. The generated photons are concentrated in the laser cavity where a strong photon field is created due to

reflection from the end-mirrors.

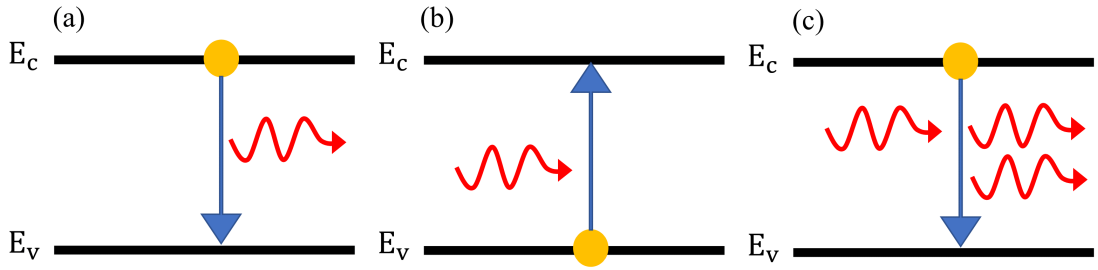

Figure 2.1: (a) Spontaneous emission, (b) photon absorption, and (c) stimulated emission in a direct bandgap semiconductor device.

In order to obtain net amplification (net gain), the rate of stimulated emission must exceed the rate of absorption. This is achieved when more electrons occupy higher energy states than lower energy states. This is known as population inversion and for semiconductor lasers it is usually prepared by electrical pumping.

The optical gain is proportional to the population inversion:

$$g \sim N_2 - N_1, \tag{2.1}$$

where g is the gain of the laser, N_2 is the number of electrons in the upper energy state (E_c), and N_1 is the number of electrons in the lower energy state (E_v).

For interband lasers, lasing occurs when electrons drop from the CB to the VB, hence the upper and lower energy states are E_c and E_v respectively. An example of an interband laser is the p-n junction diode laser, which follows a similar design to the LED, however the positively doped (p$-$) and negatively doped (n$-$type) semicondcutors are very heavily doped with the fermi energies E_{Fn} and E_{Fp} lying in the VB and CB respectively [138, 139]. A schematic diagram of the p-n junction laser diode is shown in Fig 2.2. As a consequence, the space-charge layer is very narrow and no longer depleted of carriers. Under forward bias, free electrons in the conduction band flow into the space-charge layer from the n^+-type semiconductor, and free holes in the valence band also flow in the space-charge layer from the p^+-type semiconductor. In the space-charge layer, there are more electrons in the conduction band than there are in the valence band, hence population inversion is achieved. The population inversion region is a layer along the junction and is called the active region (AR). In such a system, more photons will experience gain than absorption, hence optical gain is achieved.

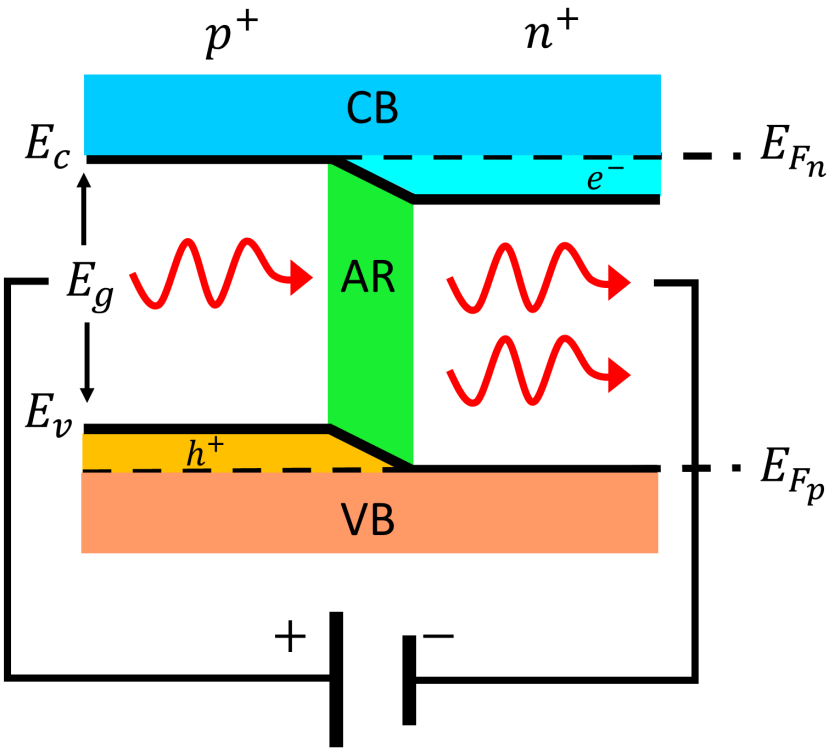

Figure 2.2: Schematic diagram of the p-n junction laser diode.

If the laser diode is built by only one material, it is known as a homojunction diode laser. The junction is between the p− and n− type semiconductor and the material used to create such structures is usually GaAs or AlGaAs [139]. Homojunction diode lasers suffer from several limitations such as very high threshold currents are required to achieve population inversion and they can only operate at cryogenic temperatures. Heterostructure diode lasers are designed using different semiconductors with different bandgap energies, usually GaAs and AlGaAs. A block diagram of the double heterojunction diode laser is shown in Fig. 2.3. Such structures allow the threshold current to be reduced by orders of magnitude by improving the electron and hole confinement, and the photon confinement. An example of a double heterojunction laser diode contains a thin region of p^+−type GaAs ($\sim$ 0.1 µm) which has a bandgap energy of $E_g \sim 1.42$ eV at room temperature inserted between a n−type AlGaAs and a p^+−type AlGaAs which has a bandgap energy of $E_g \sim 2.0$ eV at room temperature. The GaAs potential well confines the injected electrons and holes to a narrow region, which results

in a reduced threshold current that leads to a large build-up of electrons and achieves population inversion. Furthermore, the wider bandgap AlGaAs material has a lower refractive index, hence an optical waveguide is formed which confines photons in the GaAs semiconductor. This fact leads to reduced photon losses, increased photon concentration, increased optical gain and also reduced threshold current [139].

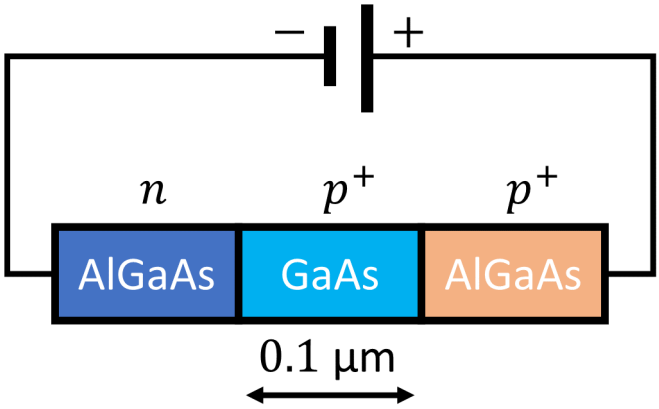

Figure 2.3: Block diagram of the double heterojunction laser diode.

In homodyne and heterodyne diode lasers the photon energy is determined by the material bandgap. This limitation can be partly overcome using a different laser design which is based on quantum wells (QWs) to produce multiple energy levels known as subbands [140] within the conduction and the valence bands. A schematic diagram of the QW laser design is shown in Fig. 2.4 (a). The strong quantum confinement leads to lasing frequencies which are not imposed by the energy bandgap but the width of the QWs which control the energy levels [141]. The first QW laser was invented by Van der Ziel et al [142] which consisted of a GaAs-$Al_{0.2}Ga_{0.8}As$ multilayer grown on a GaAs substrate where lasing at a wavelength $\lambda \sim 820$ nm was achieved by optical pumping. However, one limitation of the QW lasers is that the emission energy is always greater than the energy bandgap, and materials with sufficiently small bandgap for THz generation by inter-band electron transitions do not exist. Quantised subbands in 2D QWs can also be engineered to allow intra-band electron transitions between different states within the conduction band or the valence band. The photon energy is also dictated by the energy difference between the upper and lower energy levels, but it is now independent of the material energy bandgap. This laser design concept allows for generation of photons at terahertz frequencies, corresponding to photon energies

in the meV range. A schematic diagram of the intra-band laser design is shown in Fig. 2.4 (b).

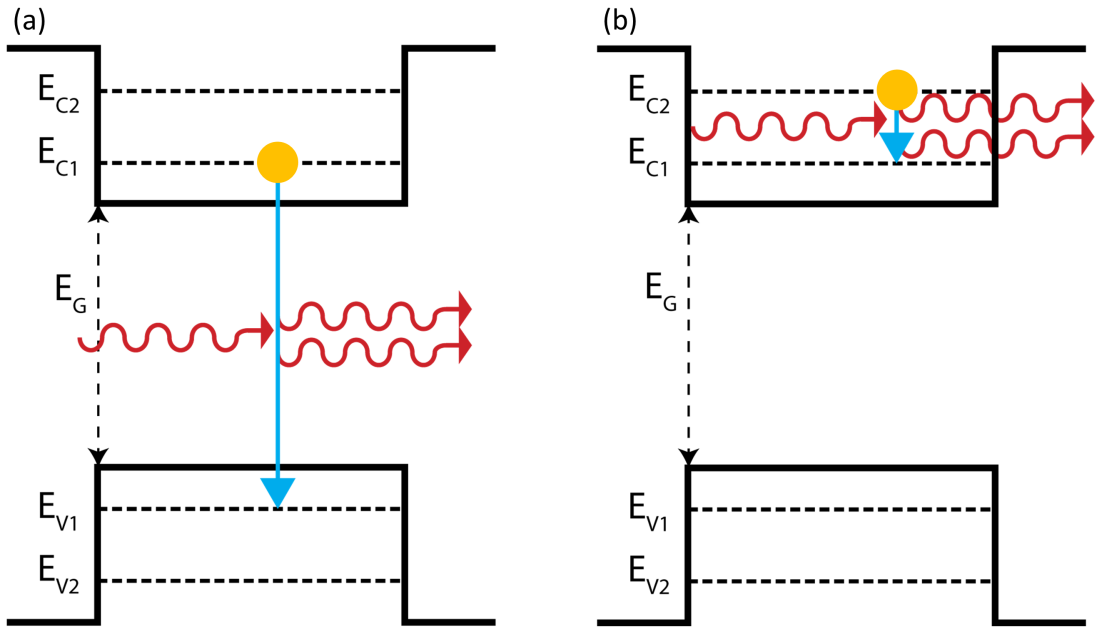

Figure 2.4: Schematic diagram of laser designs (a) In a QW laser, the conduction and valence band subbands control the transition of the electrons between energy levels, and therefore the energy of the emitted photons which is greater than the bandgap energy. (b) Intra-band lasers involve the transition of electrons between subbands within the conduction band or the valence band. The photon energy of the emitted photons is independent of the bandgap energy. Reproduced from [61].

2.2 Quantum Cascade Lasers

A typical Quantum Cascade Laser (QCL) is traditionally formed by stacking together quantum wells and potential barriers to create a superlattice, where energy states from multiple quantum wells are designed to overlap and form minibands. These minibands form injector and extractor stages in order to transport electrons between quantum wells. QCLs are unipolar devices because the laser active region is designed only in the conduction or the valence band. They are also heterostructure devices, since the quantum wells and the potential barriers have different materials, usually GaAs and AlGaAs. The lasing process is initiated when an external bias is applied hence QCLs are electrically pumped. For a sufficiently

high bias, the energy levels of the quantum wells are aligned and the injector stage allows electrons to efficiently tunnel into the upper lasing state. The electron then transitions between two energy levels where their energy difference dictates the emission frequency. Due to the sufficient bias applied across the device, the lower energy state and the extractor miniband are coupled, allowing the electron to quickly tunnel out of the well and through the potential barrier. The extractor miniband forms the injector miniband of the next QW, leading to a single electron cascading through multiple QWs and emitting multiple photons which lead to a higher optical gain. Figure 2.5 (a) shows the injector and extractor stages, and Fig. 2.5 (b) shows a schematic diagram of the electron cascading process.

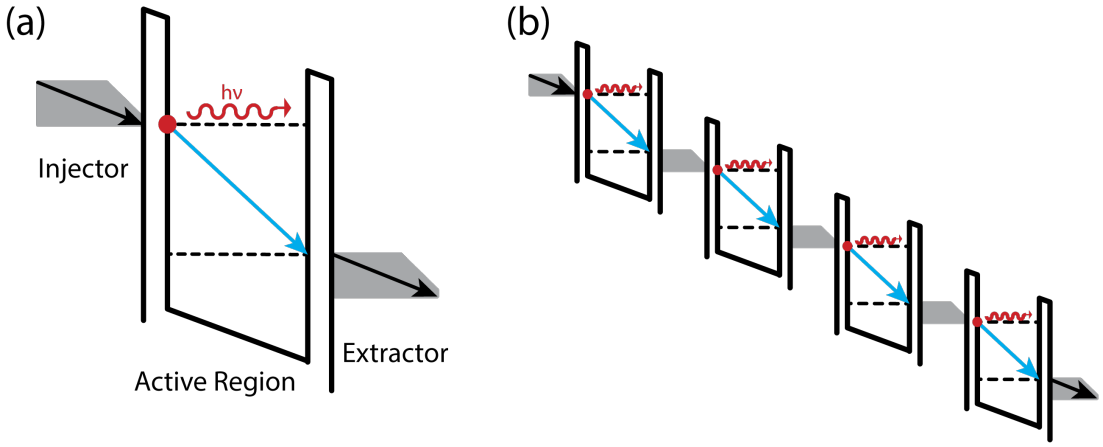

Figure 2.5: Diagram of a QCL AR. (a) Electrons from the injector stage tunnel into the upper energy level, transitions to the lower energy level emitting a photon, an quickly tunnels out of the potential barrier at the extractor stage. (b) Electrons cascade through multiple QWs, emitting multiple photos. Adapted from [143].

The first QCL was demonstrated 1994 in Bell Labs by Faist et al [23], where they created a superlattice of $Al_{0.48}In_{0.52}As/Ga_{0.47}In_{0.53}As$ grown on a InP substrate. The method of which electrons were transported from the lower energy level to the upper energy level of the next QW was Longitudinal optical (LO) phonon scattering. The device operated at cryogenic temperatures and emitted radiation with a wavelength of $\lambda \sim 4.2$ µm which corresponds toa frequency $\nu \sim 71$ THz. Continuous wave emission was demonstrated in 1995 [144], and room temperature operation was achieved in 1996 [145]. The first THz-QCL was demonstrated in 2002 [24]. The peak output power of the laser was 2 mW, the emission frequency was 4.4 THz, and the maximum operating temperature was 50 K. THz-QCLs have

reached a remarkable growth since then, operating at a frequency range of 1.2 - 5.2 THz [19], exhibiting peak powers of $\sim$ 2.4 W [25], and operating at a maximum temperature of $\sim$ 250 K [26], although these values were not obtained from the same device.

2.2.1 Active region designs

For an epitaxially grown GaAs/$Al_xGa_{1-x}As$ THz-QCL, a population inversion must be achieved between the upper and lower energy levels to obtain optical gain. To compare some of the various active region designs, the peak optical gain of an intersubband transition is given by the equation; $g(\nu_0) \propto \Delta N f_{21}/\Delta\nu$, where ΔN is the three-dimensional intersubband population inversion, and $\Delta\nu$ is the transition linewidth [146]. The osccilator strength f_{21} is the ratio of the quantum optical strength of the transition to that of a classical electron oscillator [147]. It is proportional to the stimulated-emission cross section, and depends on the overlap and symmetry of the wave-functions responsible for photon emission. Examples of various active region designs are: chirped superlattice (CSL), bound-to-continuum (BTC), resonant-phonon (RP), and hybrid which is also known as interlaced. Each design offers specific benefits and drawbacks.

2.2.2 Chirped Superlattice (CSL)

The CSL is designed to couple the wave-functions of several quantum wells together in a superlattice to create minibands. Photon generation occurs when electrons transit from the lowest state of the upper miniband (2) to the highest state of the lower miniband (1) as shown in Fig 2.6 (a). A population inversion is created because electron-electron intra-miniband scattering is favoured over inter-miniband transition. Electrons tend to relax to the bottom of the minibands, leaving state 1 empty. One of the advantages that the CSL AR design offers is the low threshold current density which is reached by applying an external bias across the device and initiates the lasing process. However, the design suffers from thermal backfilling which limits the maximum operating temperature of the QCL. Backfilling of electrons from the heavily populated injector to the lower radiative state occurs either by thermal excitation according to the Boltzmann distribution, or by reabsorption of non-equilibrium LO-phonons [147].

2.2.3 Bound-to-continuum (BTC)

The BTC design (Fig. 2.6 (b)) improves upon the CSL. In this case, the depopulation mechanism operates in the same way as the CSL, but a thin well is placed next to the injection barrier which forms a bound defect state in the minigap. This causes a diagonal transition of the electron in space as it loses energy. In this design, the oscillator strength drops slightly from $f_{21} \approx 2.5-3$ to $f_{21} \approx 1.5-2$, when compared with the CSL design as the overlap with the miniband states drops, but the upper-state lifetime increases as non-radiative scattering is reduced [147]. Furthermore, the design demonstrates improvements such as increase in the injection efficiency, lower thermal backfilling of the lower lasing level, and most importantly higher operating temperature and increase in optical power [66, 148].

2.2.4 Resonant Phonon (RP)

Another major AR design is the RP design. The extractor and the injector (see Fig. 2.6 (c)) are designed to have an energy difference of 36 meV, which is the LO phonon energy for GaAs. As such electrons scatter very quickly from the extractor to the injector emitting an LO-phonon, thereby quickly depopulating the lower energy level. This design approach presented some challenges at first due to the small subband energy spacing meaning it was difficult to depopulate the lower radiative states without also depopulating the upper state. In addition, the miniband region used in the BTC deisgn has been removed, which reduces the oscillation strength ($f_{21} = 0.5 - 1$). On the other hand, the length of an RP module (along the growth direction) is shorter than the length of a BTC module. This partially compensates for the reduced oscillation strength since the produced gain is inversely related to the length of the device $g \propto L_{mod}^{-1}$, where g is the gain and L_{mod} is the length of a module [147]. The absence of a lower miniband also reduces the complexity of fabrication. Furthermore, the high energy required (36 meV) to transport electrons to the next QW system reduces the effect of thermal backfilling substantially, and improves the temperature performance [149]. However, the electric field needs to be increased in order to achieve band alignment, and therefore the threshold current is typically large in this type of design.

2.2.5 Hybrid/Interlaced

The hybrid, or interlaced AR design (Fig. 2.6 (d)) combines the phonon-assisted depopulation of the RP design with the diagonal transition of the BTC design [150, 151]. The QCL which is utilised to conduct the measurements in Chapters 3-6 is based on the interaced AR design. The main advantage that this device presents is the continuous wave emission with high operating temperatures. Other advantages of this AR design include low threshold current, high output power, and long wavelength operation.

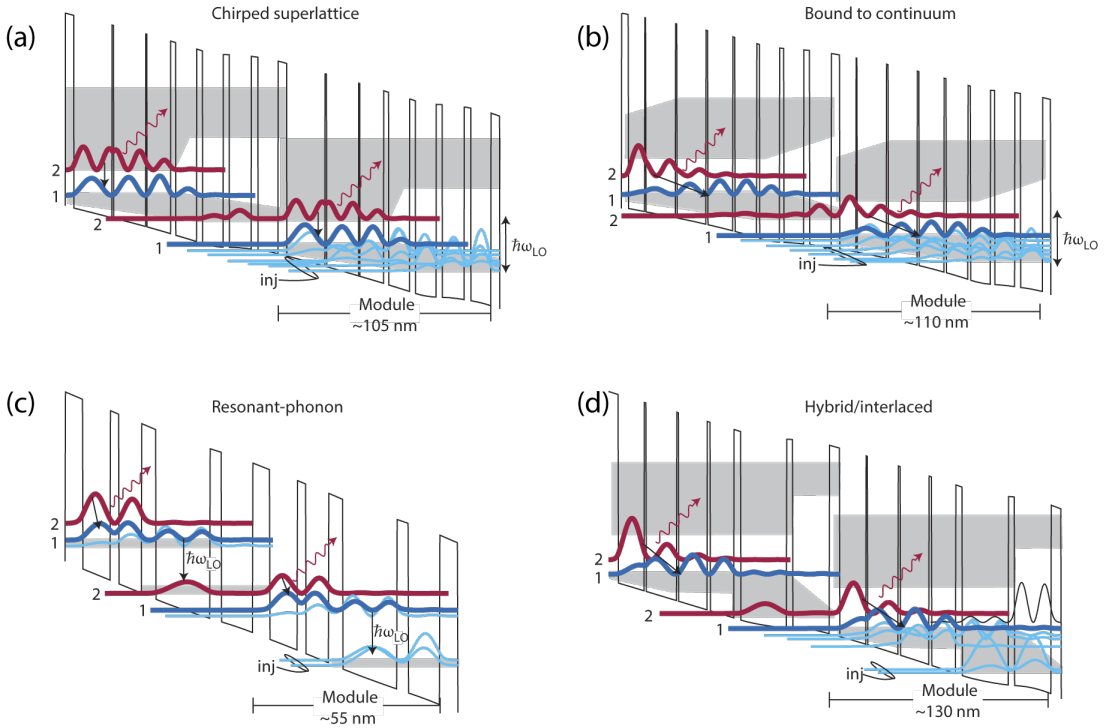

Figure 2.6: THz-QCL active region designs: (a) Chirped Superlattice, (b) Bount-To-Continuum, (c), Resonant-Phonon, and (d) Hybrid/Interlaced. Two identical QW systems are shown here, although typically 100-200 cascaded QW systems are grown to form active regions. **Red** wave-function indicates the upper enrgy level. **Blue** wave-function indicates the lower energy level. **Grey** band indicates the miniband. Adapted from [147].

2.2.6 Waveguide designs

The development of unique waveguides was necessary for the confinement of terahertz radiation in the active region. The two types of waveguides used at present for THz-QCLs are: the semi-insulating surface plasmon (SI-SP), and the metal-metal (MM) waveguide. The performance of a waveguide can be evaluated by the parameters: α_w which is the loss coefficient and accounts for scattering and absorption within the waveguide, α_m which is the mirror loss coefficient and accounts for losses due to optical coupling, typically caused due to finite refelctivities of the facets, and the confinement factor Γ which represents the overlap of the waveguide mode with the active region. These parameters are used to obtain the required gain lasing threshold, which occurs when the confinement factor (Γ) exceeds the losses ($\alpha_w + \alpha_m$), and is given by the equation, $g_{th} = (\alpha_w + \alpha_m)/\Gamma$.

The first waveguide reported was the SI-SP [24, 152, 153]. This design involved the growth of a thin ($0.2 - 0.8$ µm), highly doped (n+) layer of GaAs beneath the AR, and also on top of the semi-insulating GaAs substrate. A thin metal film ($150 - 500$ nm), typically of Au material, is deposited on the top of the active region. Due to the lack of a material with a high confinement on the bottom of the active region, the confinement factor (Γ) in this waveguide is quite low ($\Gamma \approx 0.1 - 0.5$), and the modes tend to extend substantially into the substrate. As a result, the SI-SP waveguide provides a good beam pattern, and high output powers. However, due to the low mode confinement within the active region, the device suffers from low temperature performance. A diagram of a QCL fabricated with a SI-SP waveguide along with its waveguide mode is shown in Fig. 2.7 (a).

The (MM) waveguide was designed to improve the thermal performance of the QCL. These designs are fabricated using wafer bonding, where a metal layer is placed on the bottom as well as on top of the active region [154]. This leads to almost perfect confinement of the photons in the active region ($\Gamma \sim 1$), which reduces the required gain to reach the lasing threshold of the device. MM waveguides exhibit lower threshold current densities required to initiate lasing, and can operate at higher temperatures [155, 156]. On the other hand, THz-QCLs emit radiation with a range of wavelengths from ~ 200 to 60 µm, whereas the width of the active region is typically ~ 10 µm. As a result, photons are squeezed within the waveguide, and the far-field profile MM THz-QCLs is highly divergent, often with interference fringes [157, 158]. The MM waveguides also suffer from low output powers due to the fact that the mirror losses ($\alpha_m = 1 - 2$ cm^{-1}) are much

smaller than the waveguide losses ($\alpha_w = 10 - 20$ cm^{-1}), which lead to only a small fraction ($5 - 20\%$) of the generated photons escaping the cavity without being reabsorbed [159]. A diagram of a QCL fabricated with a MM waveguide along with its waveguide mode is shown in Fig. 2.7 (b). It is significantly easier to couple radiation back into the SISP waveguide, since the overlap is smaller and the waveguide mode extends over a greater distance, as shown in Fig. 2.7. This makes the SISP waveguide much more suitable for self-mixing detection. Hence, the QCL used to conduct the measurements presented in Chapter 3, 4, 5 and 6 was fabricated using a SI-SP waveguide.

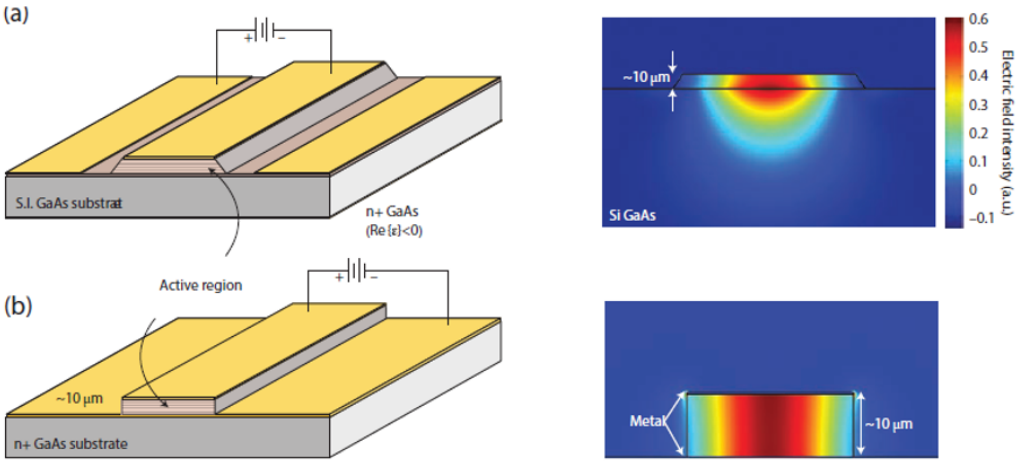

Figure 2.7: THz-QCL waveguide designs and waveguide modes, (a) Semi Insulating-Surface Surface Plasmon, and (b) Metal-Metal waveguides. Adapted from [147].

2.3 Fabrication of SI-SP THz-QCLs

In this section and the next section the techniques undertaken for fabricating and characterising THz-QCLs are presented for use in other parts of this thesis. However, due to the COVID-19 pandemic, it became necessary to use QCLs fabricated by others for all the experimental work in Chapters 3, 4, 5, and 6.

THz-QCLs which are fabricated with SI-SP waveguides are grown on a semi-insulating GaAs substrate using MBE. The MBE-grown QCL wafers are then diced and processed individually into functional lasers, following a series of well-

established micro and nano-fabrication techniques. The grown wafer which was processed in this project was L1536. The following are the major processing stages:

1. Sample cleaning and edge bead removal.
2. Mesa etching using wet chemicals to form laser ridge.
3. Deposition of ohmic side contacts.
4. Annealing of ohmic side contacts.
5. Deposition of ohmic top contacts.
6. Deposition of over-layer.
7. Substrate etching and metallisation.
8. Sintering of top ohmic contact.
9. Cleaving, soldering and packaging of laser ridges.

2.3.1 Sample cleaning and edge bead removal

Firstly, the sample was cleaned using acetone and isopropyl alcohol (IPA) to remove contaminants and organic residues. The sample was placed in three acetone beakers, and then in two IPA beakers, for one minute in each beaker. The sample was then baked on a hotplate at 180 °C for two minutes, and placed on a heatsink for one minute to cool down. Follwing the wet cleaning, the sample was placed in an oxygen plasma asher for five minutes at a power of 50 W to remove stray organic residue. This cleaning procedure was repeated before each optical lithography process. The clean sample was spin coated with Microposit S1813 positive photoresist, at rate of 5,000 rpm for 30 seconds. This resulted in a resist thickness of ∼1.2 µm. The resist-coated sample was pre-baked using a hotplate at temperature of 115 °C for 1 minute, and cooled down for 20 seconds. This step was performed to dry the resist and improve adhesion. A thicker build up of resist was formed in the corners and along the edge of the sample. Hence, the first photo-lithography process would remove the build up of resist using an edge removal mask set. An optical mask aligner was used to expose the samples with 310 nm UV radiation. The exposure dose was 10 mW/cm^2 for ten seconds. For the rest of the lithography processes, three seconds of exposure will be used. Following the UV exposure, the resist was developed in the Microposit MF-319 developer for two minutes. The sample was then rinsed with de-ionised (DI) water and dried with a nitrogen jet. The removal of the thick resist along the perimeter allowed

better contact between the chrome mask and the sample, and results in better pattern exposure in subsequent lithography steps [160].

2.3.2 Mesa etching using wet chemicals to form laser ridge

This process aims to etch ridges on the sample surface exposing the buried contact layer. The etching depth is critical to form an efficient electrical contact to the device, and it depends on the active-region design. The edge depth of a typical QCL active region varies between 10 to 14 µm. If the sample is over-etched, this could lead to the removal of the buried contact, which is essential to form a good electrical contact to the device. Firstly, an optical lithography process was performed to define the ridges with width of ∼ 150 µm, forming the laser cavity (Fig. 2.8 (a)). The sample was developed using the Microposit MF-319 for two minutes, and rinsed in DI water for thirty seconds. A wet chemical etching solution was used with a combination of H_2SO_4, H_2O_2 and H_2O, and ratio 1:8:40 (×5) ml respectively. The etched ridge is shown in Fig. 2.8 (b).

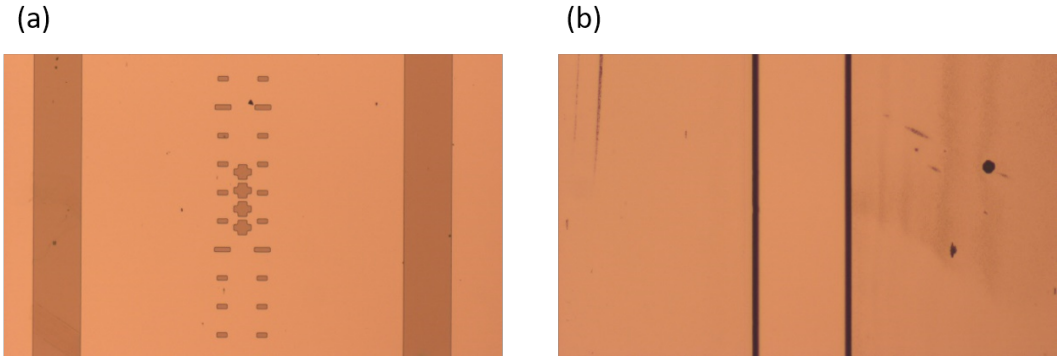

Figure 2.8: Optical microscope images of the ridges of the L1536 QCL (a) photolithography of the ridges (b) the ridges formed after the etching process.

Due to the active-region design of the L1536 QCL, the etching depth should be 10 µm. Initially, the resist thickness was measured using a stylus based Alpha step surface profiler, which determined a thickness ∼ 1.2 µm. Hence, the sample would be etched with depth of ∼ 11.2 µm, as the resist layer would be removed at the end of the process. The etching rate was ∼ 0.8 µm/min which is determined by the ratio of the used wet chemical etching solution.

2.3.3 Deposition of ohmic side contacts

Ohmic contacts were deposited on both sides of the laser ridge. An alloy of Au/Ge/Ni was used to form a low resistance ohmic contact to the buried contact layer. This alloy is an established contact material for GaAs/AlGaAs heterostructures and n-GaAs [161, 162]. The ohmic contacts were defined on the sample using optical lithography. The samples were then soaked in chlorobenzene for two minutes to ease the lift-off process [163]. An oxygen plasma asher was used at 25 W to remove stray organic residues form the surface. Furthermore, a Leybold UNIVEX 300 thermal evaporator was used to evaporate the Au/Ge/Ni alloy. The alloy was evaporated at a rate of $1-2$ Å/sec with a chamber pressure lower than 2×10^{-6} mBar. The evaporated metal resulted in a thickness of $250-300$ nm. Following the metal deposition, the sample was placed in acetone over-night to ease the lift-off process. The unwanted metal part was finally removed using a thin brush. An optical microscopy image of the sample after lift-off is shown in Fig. 2.9.

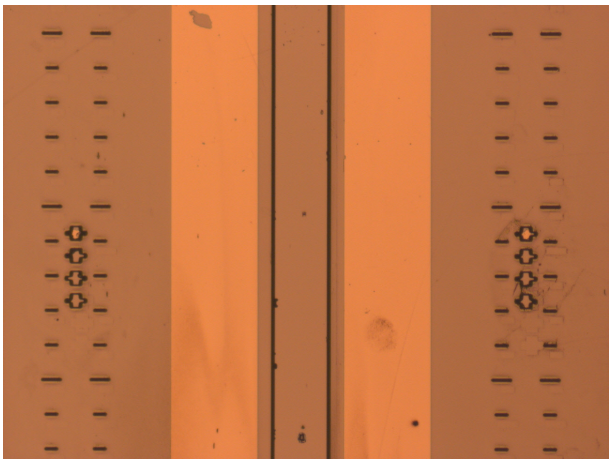

Figure 2.9: Optical microscopy image of the side contact deposition

2.3.4 Annealing of ohmic side contacts

After the metal deposition, the ohmic side contacts were annealed at 430 °C for one minute using an AnnealSys rapid thermal annealer. At such temperatures, Ge atoms diffuse into the GaAs and subsitute Ga atoms in the crystal. This results in a high n^+-doped region in the semiconductor [164]. The diffusion of Ge atoms

is enhanced by the Ni atoms, which also diffuse into the GaAs crystal [162]. The resistivity of the Au/Ge/Ni contacts is low, on the order of $\sim 10^{-6}$ Ω/cm^2. Due to the diffusion of Ge and Ni into the substrate, the morphology of the Au/Ge/Ni layer changes. An optical microscopy image of the sample after annealing is shown in Fig. 2.10.

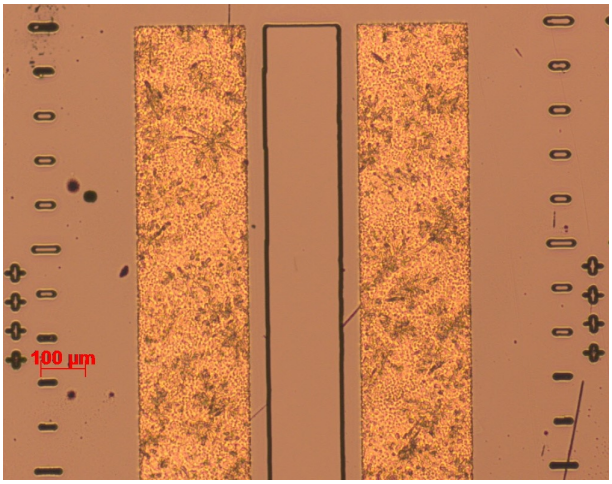

Figure 2.10: Optical microscopy image of the side contact deposition

2.3.5 Deposition of ohmic top contacts

Two 10-µm wide ohmic strips were deposited on the top of the QCL ridges to form a low resistance top contact. The top ohmic contacts reduce the free carrier loss in the waveguide [165]. The strips were initially formed using optical lithography and the sample was then soaked in chlorobenzene and developed with MF-319. An oxygen plasma asher was used at 25 W for 70 seconds. Finally, a Leybold UNIVEX 300 thermal evaporator was used to deposit a Au/Ge/Ni layer with thickness of $\sim$ 100 nm. After the evaporation, the sample was placed in acetone over-night to assist lift-off. The unwanted part of the metal was then removed using a thin brush. The QCL was not annealed at this stage of fabrication to prevent damage in the active region due to the diffusion of the Au/Ge/Ni layer. An optical microscopy image of the same after depositing the ohmic top contacts is shown in Fig. 2.11.

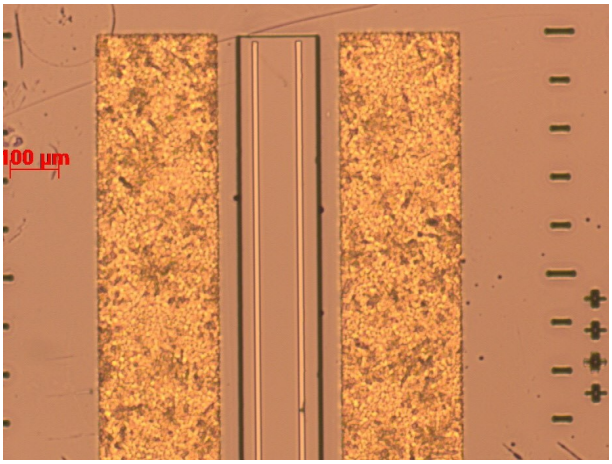

Figure 2.11: Optical microscopy of the top ohmic contacts

2.3.6 Deposition of over-layer

A separate layer of Ti/Au was evaporated on the entire surface of the laser ridge to confine the radiation inside the laser cavity. A thin layer of $\sim$ 20 nm Ti was firstly evaporated to promote adhesion of the $\sim$ 150 nm Au layer on the ridge surface. After evaporation, the samples were placed in acetone to lift-off the unwanted metal part. An optical microscopy image of the same after depositing the over-layer is shown in Fig. 2.12.

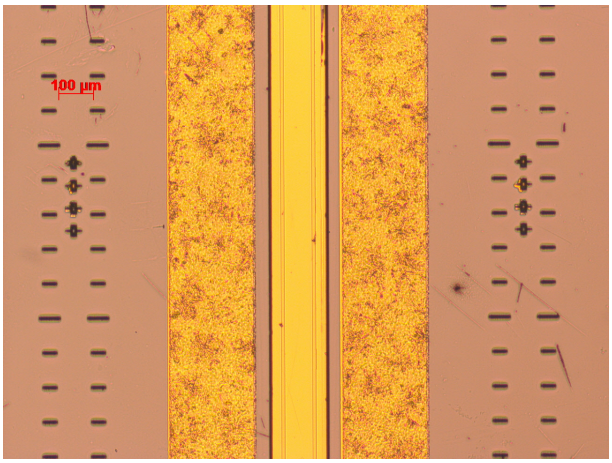

Figure 2.12: Optical microscopy of the sample with over-layer

2.3.7 Substrate etching and metallisation

The GaAs substrate was thinned to ~ 200 µm to improve the thermal dissipation from the QCL ridges. The sample was mounted with wax to a glass slide. A Tesatronic micrometre was then used to measure the height of the wax-mounted sample. The glass height was taken as the reference where the height would be zero. The etching solution used was H_2SO_4:H_2O_2:H_2O with a volume ratio of 1: 8: 1 ($\times 5$) ml respectively, which provided an etching rate of ~ 15 µm/min. The etching depth was measured every $5 - 10$ minutes to obtain this etching rate and ensure that the substrate was not over-etched. The sample was then rinsed in DI water for 30 seconds to stop the etching process. Trichloroethylene was used to separate the sample from the glass and remove the wax. Acetone, IPA, and an oxygen plasma asher were used then to clean the sample. Finaly, the back of the substrate was evaporated with a Ti/Au layer of thickness 20 nm and 150 nm respectively using an electron-beam evaporator. This layer was required to form a bond with an indium layer during the packaging process.

2.3.8 Sintering of top ohmic contact

The top ohmic contact was annealed at 270 °C for four minutes using the rapid thermal annealer. A lower annealing temperature was used to anneal the top contact compared to the bottom contacts which were annealed at 430 °C. The reason for this was to prevent the diffusion of alloy metals from the ohmic strips at the top of the ridge in the active region. The annealing process enhanced the adhesion of the top contact and the over-layer to the surface of the QCL.

2.3.9 Cleaving, soldering and packaging of laser ridges

The next step was to cleave the sample into individual QCLs. The sample contained three ridges, each ridge was 6 mm long. The ridges were first separated using an SFP s-100 automated scriber with a diamond cutter. Each ridge was then cleaved to form ridges of the desired length, in this case one device with length of 2.5 mm. This process also ensured mirror-like facets were formed at the ends of the ridge to form Fabry-Pérot cavities with a minimum mirror loss.

After cleaving, the device was mount on a copper block and were wire-bonded. Three ceramic pads were attached to the copper block with GE-vanish which was

placed on a hotplate for five minutes at $\sim$ 120 °C. The copper block was then placed on the hotplate at temperature of 165 °C, which is higher than the melting temperature of indium (156.6 °C). A thin layer of indium was then deposited on the copper block. Once a uniform indium layer was formed on the copper block, the hotplate was set to 150 °C. where the indium was solidified. A QCL was placed on the indium surface and the hotplate was set to 190 °C for five minutes to form a bond between the Au on the bottom of the laser ridge and the indium. Then the temperature was set back to 150 °C. Finally, a ball-bonder was used to connect the top and bottom contacts with the ceramic pads. A schematic of a fabricated THz-QCL is shown in Fig. 2.13.

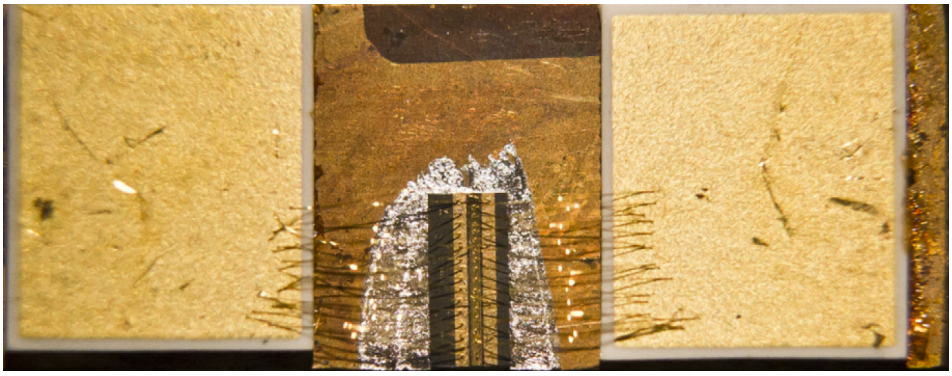

Figure 2.13: Image of a fabricated THz-QCL.

2.4 Characterisation of THz-QCLs

The electrical and optical characterisation of QCLs involves experimentally obtaining the light-current-voltage (LIV) and spectral characteristics. The LIV characteristics assess the voltage and output light behaviour as a function of current and temperature. Important parameters that can be obtain from LIV characteristics are threshold current density (J_{th}), maximum operating temperature (T_{max}), slope efficiency (η_s), and peak output power (P_{max}). Furthermore, the spectral characteristics determine the emission frequencies of the QCL using a Fourier-Transform Infrared spectrometer (FTIR). The spectral characteristics are measured for different driving currents to study and calibrate the changes in emission frequency. The results from the spectral characterisation are of particular importance when using the QCL for swept-frequency self-mixing measurements in Chapter 3.

2.4.1 Experimental setup

A diagram of the LIV measurement setup is shown in Fig. 2.14. The QCL was mounted on a continuous-flow cryostat (Janis ST-100) which was fixed on the optical bench in a position which provides alignment with the experimental setup. A turbo vacuum pump was first used to evacuate the cryostat to a pressure of 2×10^{-6} mBar, and the device then cooled to 4 K using liquid helium. A temperature controller was connected to the cryostat to detect and set the operating temperature of the device. An agilent pulse generator was used to drive the QCL at a pulse repetition rate of 10 kHz with a 2% duty cycle (pulsed-mode). The duty cycle was kept low to reduce Joule heating of the QCL. The emission from the QCL was first collimated by an off-axis parabolic mirror and then focused on the detector using a second parabolic mirror. A cryogenically cooled bolometer with a Ge thermistor was used for detection. This bolometer was used to analyse the LIV characteristics whereas a pressure transducer based power meter was later used to obtain the absolute power of the device. The voltage signal from each detector was recovered using a DSP lock-in amplifier (LIA). Both detectors required a different modulation frequency to match their optimum responsivity.

An ISO-TECH signal generator was used to match the optimum responsivity of the detector generating a square wave at a frequency of $f_{mod} = 165$ Hz for the bolometer and $f_{mod} = 30$ Hz for the power meter. This square wave was used to gate the 10 kHz pulses from the pulse generator. The output of the pulse generator was connected to the cryostat input through an inductive loop current probe. The current loop was terminated with a 50 Ω load and was connected to an Agilent digital oscilloscope (OSC). The current through the QCL was measured as a proportional voltage in the current loop. The voltage across the QCL was measured through a 50 Ω '*sense*' circuit, and was also connected to the same OSC. The OSC and the LIA were connected to a computer and the LIV measurements were recorded using a LabView program.

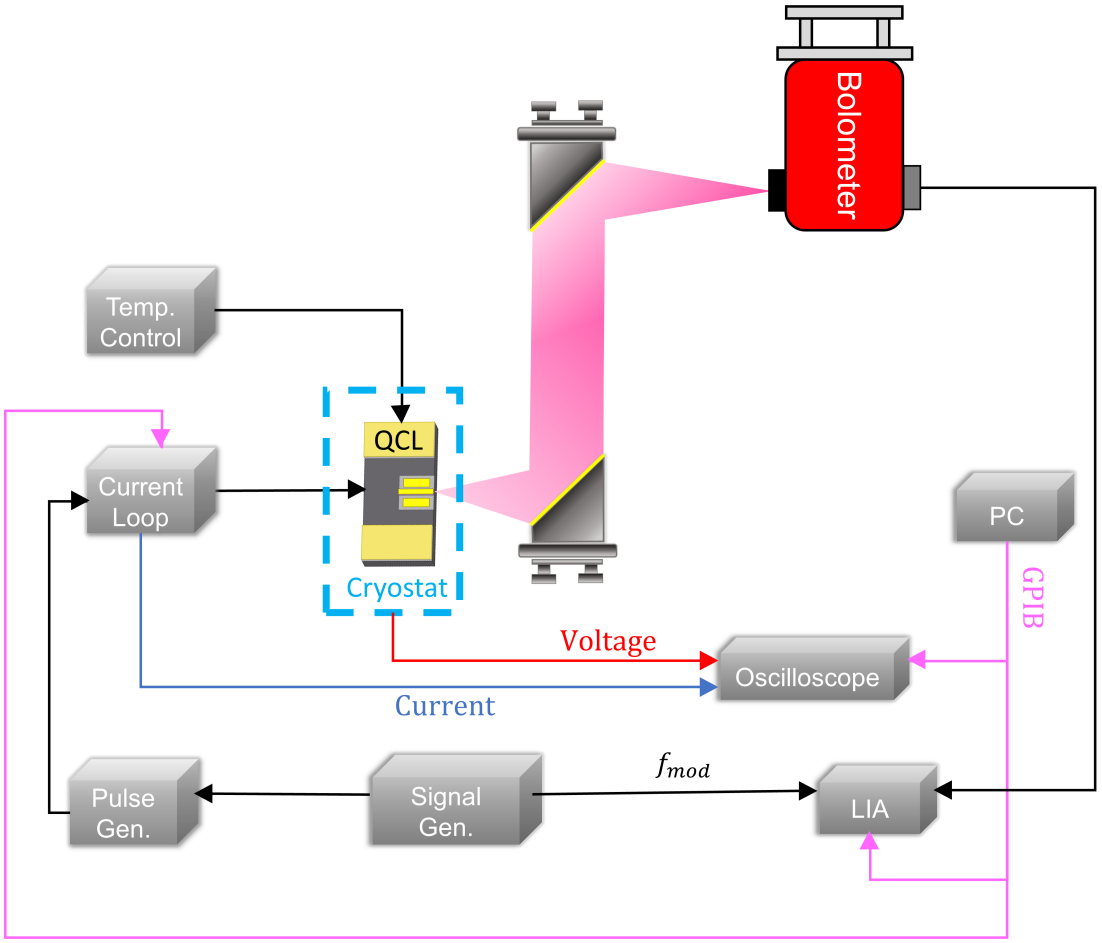

Figure 2.14: Experimental setup for the LIV characteristics of the THz-QCL.

A diagram of the spectral measurement setup is shown in Fig. 2.15. The experimental setup for obtaining spectral measurements was composed of three off-axis parabolic mirrors. The first mirror collimates the beam, the second mirror focuses the beam, and the third mirror collimates and demagnifies the beam to a smaller diameter. The FTIR spectrometer is based on a Michelson Interferometer with a resolution of 7.5 GHz. A modulation signal of 165 Hz was also used for the spectra measurements. Both the LIV and spectral measurement setups were enclosed in a nitrogen-purged box to reduce THz absorption by water molecules in the atmosphere.

An FTIR spectrometer measures the spectrum of the light through the built-in detector which captures two waves of the same frequency but at different phase and produces an interferogram. Then the Fourier transform of the data is implemented to find the emission frequency. The transmitted beam is directed into a

flexible split mirror which splits the radiation into two different paths. The phase between the beams depends on the position of the mirror which is adjustable. The two signals are combined into the next parabolic mirror, producing an interference pattern. The difference between the lengths of the paths determines if the interference is constructive $|L_1 - L_2| = \lambda/2$ or destructive $|L_1 - L_2| = \lambda/4$.

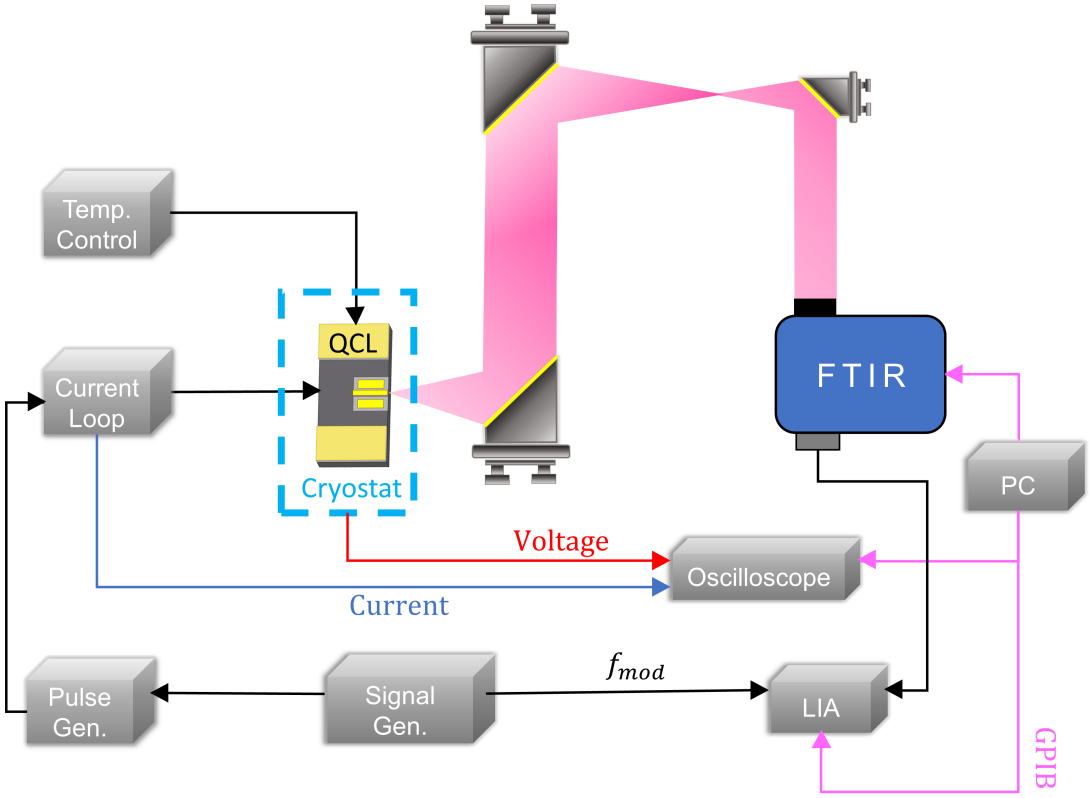

Figure 2.15: Experimental setup for the spectral characteristics of the THz-QCL.

2.4.2 Pulsed characterisation of a hybrid QCL with SI-SP waveguide

In this section, the characterisation results of a QCL with a SI-SP waveguide processed from wafer L1536 are presented. The device is based on a hybrid active region design [150], which is a combination of the BTC and RP designs. The QCL with dimensions of 2.5 mm × 150 µm was mounted on a copper block. Measurements were acquired for temperatures between 15 and 123 K and the LIV characteristics are shown in Fig. 2.16. At 15 K, a peak power of ∼ 70 mW was

obtained using the THz power meter and a current threshold density of $\sim$ 400 Acm^{-2} was recorded.

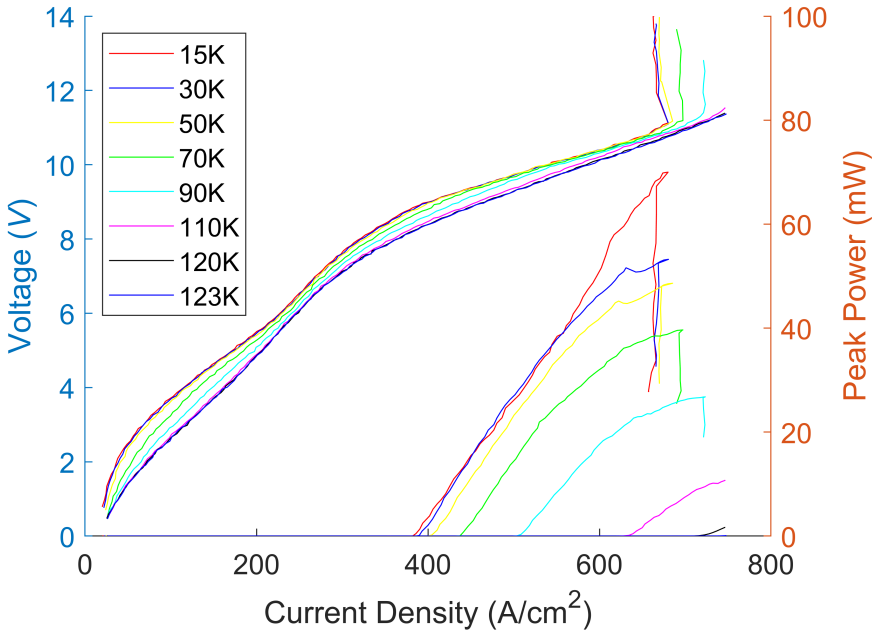

Figure 2.16: LIV characteristics of the L1536 SI-SP THz-QCL.

The voltage across the device determines the alignment of the lasing states in the QWs. For low voltage values, the lasing states are not aligned and this inhibits the electron transport through the structure. As the voltage across the QCL increases, the upper and lower lasing states start to align in energy. Electrons start tunneling through the QWs emitting photons which are confined in the medium cavity where they are bounded between the two end-mirrors creating a photon field. When the optical gain exceeds the waveguide losses lasing occurs. The current measured through the device when optical power is visible dictates the threshold current. The optical power increases as more electrons tunnel to the upper lasing state. The peak optical power occurs when the alignment of the QWs is optimal. If the bias across the device is further increased, the QWs start to misalign, resulting in an increase in the differential resistance, and an abrupt decay in lasing power. This effect can be seen from the IV curve in Fig. 2.16 at $V \approx 11$ V. Figure 2.17 demonstrates the relationship between the peak power and the operating temperature of the QCL. The peak performance of the QCL occurs at the lowest operating temperature. As the temperature increases, the

output power decays. This is due to the small energy separation between the quantum states in the active region of the device, and thermal backfilling occurs. A Boltzmann's fit was used to fit the data which followed theoretical predictions [166]:

$$P = P_0 - P_1 \exp \frac{T}{T_0}\,, \tag{2.2}$$

where the fit parameter values are $P_0 = 75$ mW, $P_1 = 6$ mW, $T_0 = 50$ K, and T is the operating temperature of the QCL. The optical power drops to zero at $T \sim 123$ K in this device.

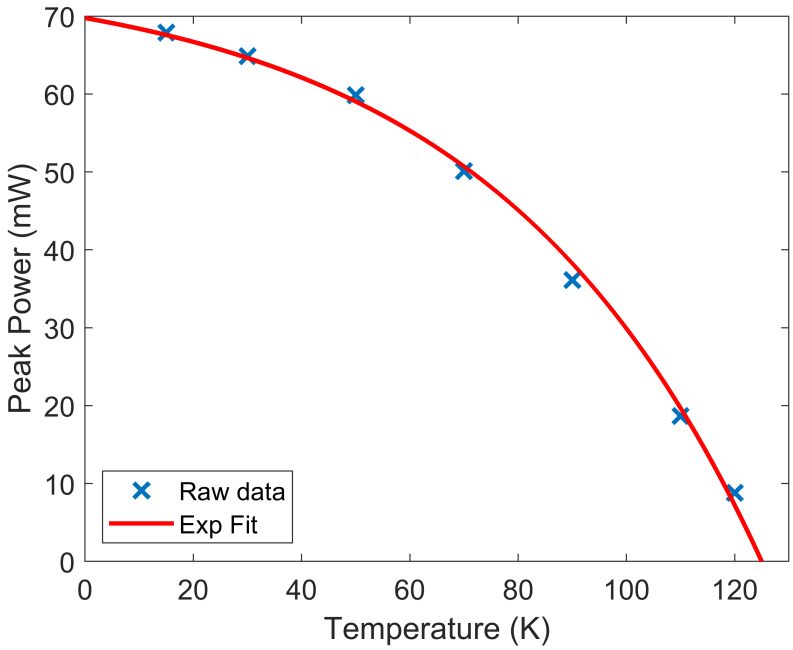

Figure 2.17: Output peak power as a function of temperature.

Figure 2.18 shows the relationship between the threshold current density and the operating temperature of the QCL. At higher operating temperatures, the alignment voltage will remain constant, but due to thermal backfilling a lower population inversion is achieved, and a larger current is required in order for the optical gain to exceed the losses. Hence, the threshold current increases. The relationship between the operating temperature of the device and the threshold current density can be represented using a Boltzmann's fit which also follows theoretical predictions [166]:

$$J_{TH} = J_0 + J_1 \exp \frac{T}{T_0}\,, \tag{2.3}$$

where the parameter values are $J_0 = 390$ Acm^{-2}, $J_1 = 3$ Acm^{-2}, $T_0 = 25$ K, and T is the operating temperature of the QCL.

Finally, it should be noted that the results from the LIV curves for the L1536 QCL are obtained in pulsed mode operation, whereas for a measurement system using SM for detection, the QCL needs to operate in continuous wave (CW) mode. Nonetheless, the results presented in this section demonstrate the successful fabrication of a THz-QCL with a high peak power (70 mW), a maximum operating temperature of 123 K, and a low current density threshold value (390 Acm^{-2}).

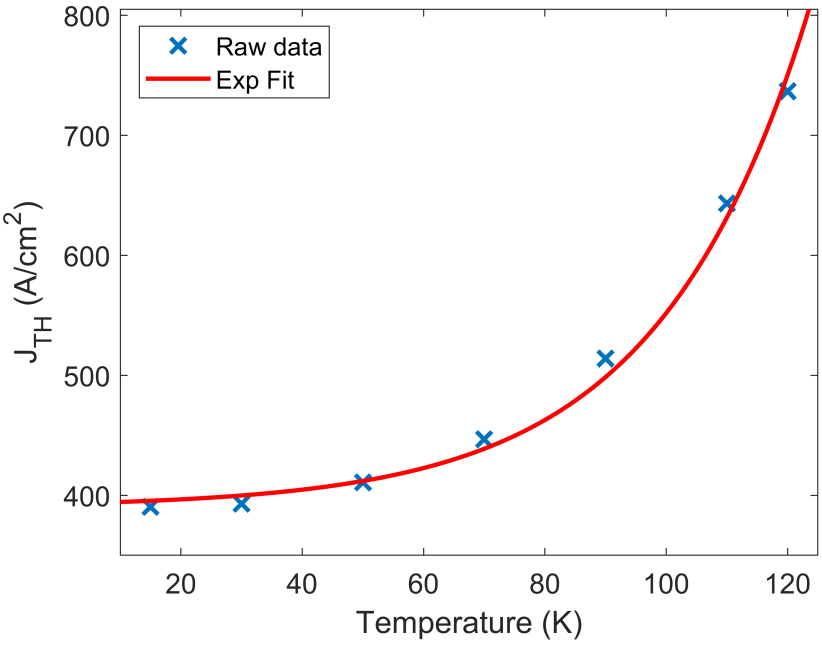

Figure 2.18: Threshold current density as a function of temperature.

Spectral properties of the THz-QCL

The spectral measurements shown in Fig. 2.19 were conducted at a QCL temperature of 15 K using the measurement setup described in section 2.4.1. Spectra were acquired at different currents through the device and show multi-mode frequency lasing. For current values between 1.5 A and 1.9 A, multi-mode emission centred at $\sim$ 3.38 THz is observed. The intensity of the multiple modes varies as the current through the device changes, and their frequency separation is dictated by

the Fabry-Pérot mode spacing, which is given by the equation:

$$\Delta\nu = \frac{c}{2\eta L}, \tag{2.4}$$

where $\Delta\nu$ is the frequency difference between the modes, c is the speed of light, η is the refractive index of the gain medium, and L is the cavity length of the ridge. These values are: $L \approx 2.5$ mm for this device, and $\eta \approx 3.5$ for GaAs yielding a mode spacing of $\Delta\nu \sim 17$ GHz, which concurs with the experimental mode spacing also yielding a value of $\Delta\nu \sim 17$ GHz. For current values between 1.9 A and 2 A, the lasing frequency of the mode with the highest intensity changes from ~ 3.38 THz to ~ 3.46 THz. This occurs due to the change in the energy separation between the lasing states, as a larger bias leads to a slightly greater energy separation, which will cause the gain curve to shift to slightly higher frequencies.

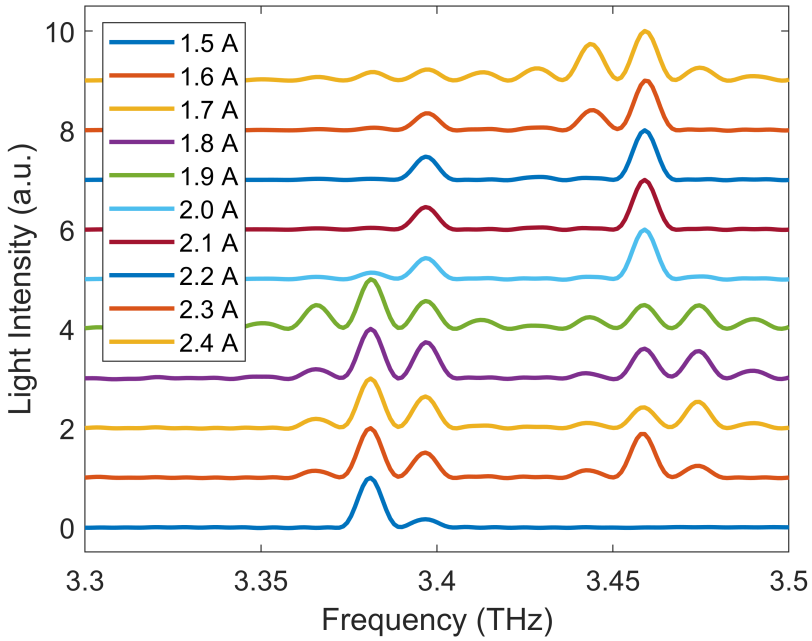

Figure 2.19: Spectra obtained at various drive currents at a QCL temperature of 15 K. Multi-mode emission is observed with peak emissions centred at ~ 3.38 THz for drive currents between 1.5 A and 1.9 A. For drive currents greater than 2 A, the peak emission shifts to ~ 3.46 THz.

Finally, the results from the spectral measurements show that the L1536 QCL is multi-mode, whereas to obtain coherent measurements using the self-mixing technique a single-mode QCL is required.

2.4.3 CW characterisation of a single-mode hybrid QCL

Due to the COVID-19 pandemic, it became necessary to use QCLs fabricated by others. A QCL (wafer L1180) [151] was used in the work presented in Chapters 3 – 6, which was fabricated and characterised by Dr P. Rubino [62].

The device was based on a nine-well hybrid QCL design with AR thickness of 14 µm. The AR layer sequence in each case (starting from the injection barrier), with $Al_{0.18}5Ga_{0.82}As$ barriers indicated in bold, was **38**/108/**5**/126/**10**/129/**19**/113/**29**/91/**29**/82/**29**/68/**29**/<u>163</u>/**29**/142 A°. The uniformly doped layer where $N_d = 3 \times 10^{16}$ cm^{-3} is underlined. The AR was sandwiched between upper 50-nm-thick ($N_d = 5 \times 10^{18}$ cm^{-3}) and lower 700-nm-thick ($N_d = 2 \times 10^{18}$ cm^{-3}) GaAs contact layers. The device was processed with an SI-SP waveguide with ridge width of 150 µm, and length of 1.8 mm.

The LIV characteristics of the QCL were measured in CW mode for operating temperatures between 30 K and 60 K with a step of 5 K, as shown in Fig. 2.20 (a). A peak power of $\sim$ 13 mW and a threshold current desnity of $\sim$ 150 Acm^{-2} were obtained at a temperature of 30 K. A maximum operating temperature of 60 K was observed. Furthermore, the spectral characteristics of the device were obtained for an operating temperature of 30 K for a range of drive currents between 400 mA and 1200 mA with a step of 100 mA, as shown in Fig. 2.20 (b). The spectral results show a blue shift in the dominant lasing mode ranging from $\sim$ 3.35 THz to $\sim$ 3.41 THz as the current increases. The Fabry-Perot modes spacing can be calculated using Eq. 2.4 where the cavity length of this QCL is $L = 1.8$ mm. The calculated mode spacing is $\Delta\nu \sim 21$ GHz which agrees with the spectral results.

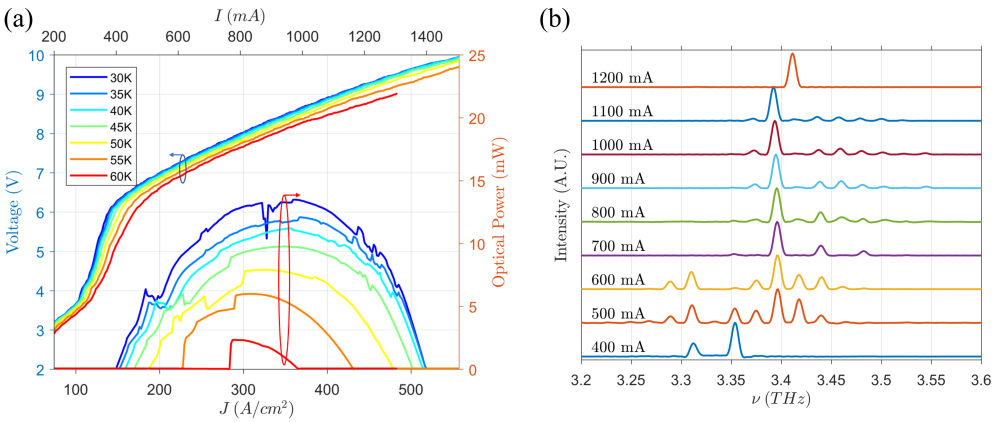

Figure 2.20: (a) LIV, and (b) spectral characteristics of the L1180 QCL in CW mode. Figure reproduced from [62].

Single mode emission

Single mode emission is important for measurement systems which use self-mixing detection with a THz-QCL for far-field imaging [69], for spectroscopy [20], or for near-field imaging [108, 167]. This is particularly important when a swept-frequency scheme is used for the measurement of both the amplitude and phase of the reinjected THz field [71]. The work presented in Chapters 3, 4, 5 and 6 is based on a measurement system which utilises the L1180 THz-QCL and the self-mixing technique to acquire near-field images using s-SNOM. As such, it is important to understand the spectral characteristics of this QCL device. As shown by Kundu et al [168], frequency tunability and spectral control can be achieved by exploiting a phase-adjusted finite-defect site Photonic Lattice (PL), created by focus ion beam (FIB) milling on the top metal layer and penetrating into the active region of the QCL which was fabricated with a SI-SP waveguide. This creates a photonic stopband with a narrow pass band at the Bragg frequency of the PL because of the strong refractive index contrast between the metallised and etched parts of the waveguide. In order to achieve single-mode emission with the L1180 QCL, a PL 166 µm long, using a 13.2 µm grating period with a 70% duty cycle and a central 8 µm wide phase defect was created using FIB milling by Dr I. Kundu on the surface of the top metal layer [62]. A scanning electron microscope (SEM) image of the QCL top metal layer is shown in Fig. 2.21 (a) and the resulting emission spectra obtained from the device after FIB milling is shown in Fig. 2.21 (b).

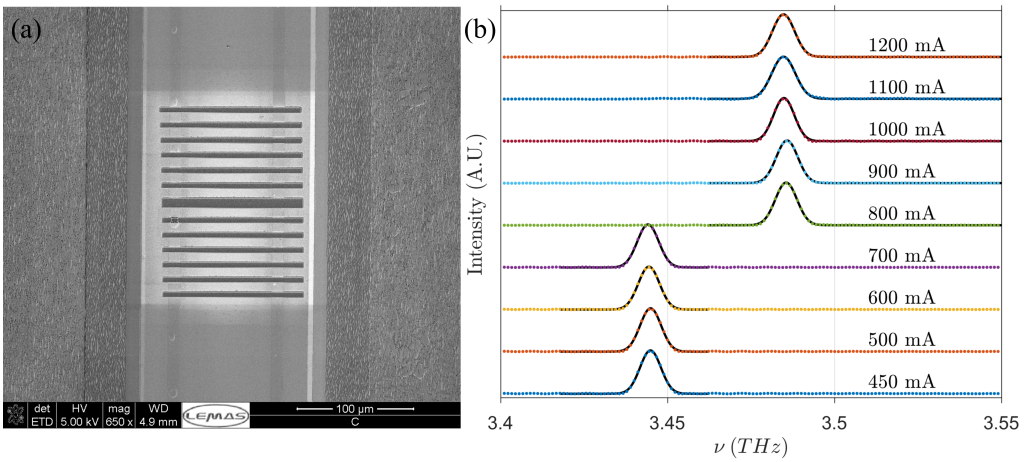

Figure 2.21: (a) SEM image of a PL 166 µm long etched on the top metal layer of the L1180 QCL. (b) Spectra obtained in CW mode at 30 K after FIB milling. Figure reproduced from [62].

Single mode emission of $\nu \sim 3.445$ THz is observed at drive currents between $I = 450$ mA and $I = 700$ mA. As the current increases to $I = 800$ mA, a shift in the frequency of the dominant mode is observed where the new lasing frequency is $\nu \sim 3.485$ THz. A frequency shift of $\Delta\nu \sim 40$ GHz is obtained which is in good agreement with [168]. Furthermore, a continuous frequency tuning of ~ 1 GHz per current step of $I = 50$ mA is obtained for the single mode emission of the two discrete frequencies as shown in Fig. 2.22. This single mode emission, combined with a degree of continuous frequency tuning as the driving current is varied, makes this device well suited to self-mixing detection, and in particular to the use of swept-frequency approaches for coherent imaging.

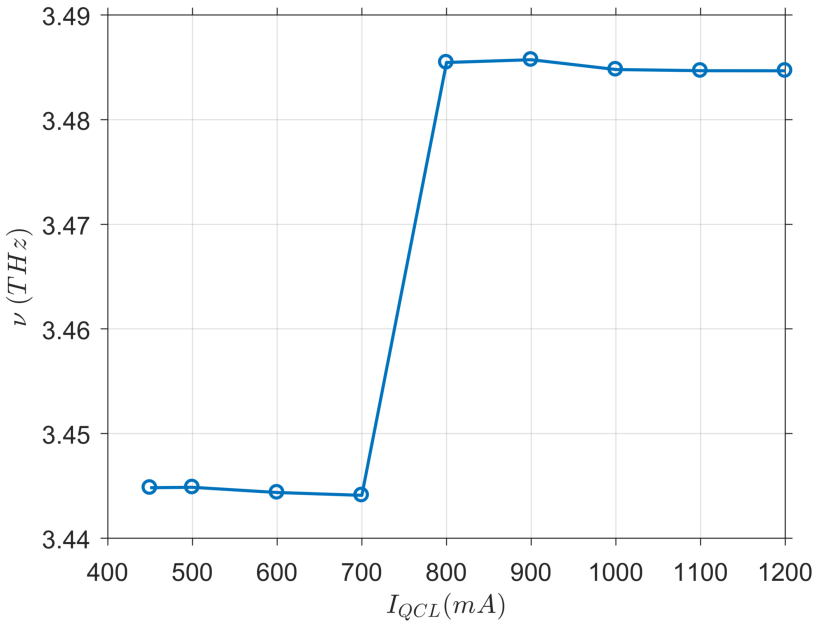

Figure 2.22: Frequency tuning of ~ 1 GHz is shown per change in current of $I = 50$ mA for the single mode emission of the two discrete frequencies. Figure reproduced from [62].

2.5 Conclusion

In this chapter several laser concepts which are used in the design of semiconductor lasers such as the homojunction diode laser, the heterostructure diode laser, the quantum well laser, and the quantum cascade laser were presented. Furthermore, the design and function of the quantum cascade laser were discussed and a range of active region and waveguide designs for the THz-QCL were presented. The L1536 QCL wafer was processed into a functional device with a SI-SP waveguide through a series of fabrication steps. The fabricated QCL which was based on a hybrid BTC+RP active region was characterised and the LIV and spectral characteristics were presented in pulsed mode operation. Due to the COVID-19 pandemic, it became necessary to use existing QCLs which could operate in CW mode with single-mode emission. The L1180 QCL based on a hybrid BTC+RP active region with a SI-SP waveguide was fabricated and characterised by Dr P. Rubino and a $\pi-$phase adjusted finite defect photonic lattice was created by Dr I. Kundu using FIB milling. This QCL has been utilised for the experiments presented in Chapters 3, 4, 5 and 6.

Chapter 3

Coherent terahertz microscopy of modal field distributions in micro-resonators

3.1 Introduction

Micro- and nano-scale resonators are an essential component enabling a variety of technologies and devices operating in the THz frequency range, including THz detectors [169, 170], sensors [171] and optoelectronic modulators [172–174]. Individual resonators play a vital role in the strong subwavelength confinement of THz fields in such devices, thereby enhancing the interaction between light and matter, which may otherwise be weak owing to the relatively long wavelength of THz radiation. Subwavelength resonators are also an important building block in the design of THz metamaterials and metasurfaces [175, 176] underpinning a range of efficient and compact THz optoelectronic devices[177–182] as well as enabling the development of novel optical elements including magnetic mirrors [183], focusing elements [184] and negative refractive index materials [185]. Among the wide variety of possible applications, metamaterials and structures based on subwavelength resonators have enabled THz sensing [186] and spectroscopy, where highly localized THz fields have made possible the detection of single microorganisms [187], spectroscopic measurements of low-dimensional structures including quantum dots [171], and the investigation of strong light-matter coupling in quantum heterostructures [188, 189].

Owing to the small cross-section of subwavelength resonators and single meta-

material elements, their interaction with diffraction-limited THz beams is typically weak. As such the development and characterization of devices based on these structures most commonly relies on measurement of the optical response of periodic or aperiodic arrays of nominally identical resonators in the far-field [169, 171–174, 180–183, 185, 187, 189]. However, such approaches are sensitive only to the ensemble-averaged optical properties of the array and can reveal only limited insights into the underlying light-matter interactions on the microscopic scale. In fact, these complex interactions can be strongly affected by radiative [190], capacitive [191] or plasmonic [192] coupling between array elements, which can directly influence the field confinement and spectral response of individual resonators, so impeding the experimental investigation of their inherent electromagnetic properties. In addition to the well-known spectral broadening effects that afflict resonator arrays, significant spectral shifts have been observed when comparing the optical response of THz plasmonic nanoantennas and resonators measured in the near-field and far-field regimes [193, 194] – a phenomena attributed to the Fano interference of incident and scattered THz fields in the far-field [195]. In view of these considerations it is becoming increasingly clear that the far-field characterization of sub-wavelength resonator arrays and associated metamaterials is insufficient to understand fully the complex interaction of THz waves with these structures.

To this end, there has been considerable interest in the application of near-field microscopy techniques for visualizing the localized THz fields supported by resonators and microstructured surfaces with subwavelength resolution. These include the use of miniaturised photoconductive [196], electro-optic [197, 198], or micron-scale aperture-based probes [199, 200] positioned directly in the near-field of the sample under investigation. However, in addition to the experimental complexity of these approaches, they typically suffer from small signals and poor dynamic range, meaning that the achievable spatial resolution is limited to the range $\sim 1-30$ µm. Furthermore, their reliance on THz generation schemes based on near-infrared fs lasers limits the spectral range to frequencies below ~ 2 THz. An alternative approach offering sub-micron spatial resolution has been adapted from s-SNOM [201]. This technique has been applied with great success to the mapping of localised fields and plasmonic effects at near-infrared and mid-infrared frequencies [95–97, 102, 202], with a nanometer-scale spatial resolution that is independent of the radiation wavelength.

One example is the work reported in [95], which studies the near-field optical behaviour of Fabry-Pérot resonances in thin metal nanowires, also refereed to as

quasi one-dimensional plasmonic nanoantennas. The authors measure the wavelength and reflection phase of plasmons in thin metal wires of finite length by obtaining images of amplitude and phase of local electric field components. The experimental situation at the sample is illustrated in Fig. 3.1 (a). An s-polarised beam from a tunable continuous wave light source (Ti:Sa, Coherent 899) tuned to 942 nm wavelength excites the sample, and it is focused onto a commercial non-contact AFM tip (Nanosensors AdvancedTEC NC). The backscattered light is amplified with an interferometric detection scheme which provides access to both the optical amplitude and phase.

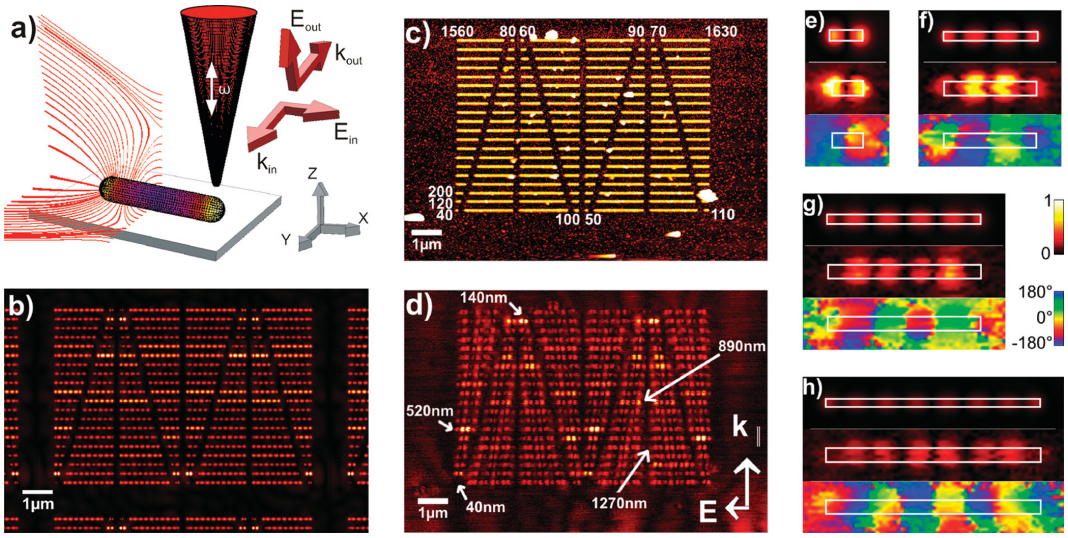

Figure 3.1: (a) Scheme of the setup. Weakly focused s-polarized radiation excites nanowires largely unperturbed by the probing tip. A typical response field is indicated by the electric field strength distribution on the wire surface and a snapshot of selected field lines. Backscattered light is modulated by the tip vibration (frequency ω) and polarization-analyzed along the tip axis. (b) Simulated magnitude of the z-component of the electric field 24 nm above the structure shown in (c). (c) Topography of the metallic nanowires. The wires of different length are arranged in a compact manner, though sufficiently separated to reasonably assume they are noninteracting. (d) Simultaneously obtained, baseline-corrected near-field optical amplitude image for an excitation wavelength of $\lambda = 942$ nm. (e-h) Compound images of simulated magnitude (top), measured magnitude (middle), and phase (bottom) for the 140, 520, 890, and 1270 nm long wires, respectively, which represent the odd order resonances. White rectangles indicate the contours of the wires as taken from the nominal and measured geometry. Figure reproduced from [95].

The authors investigate 40 nm wide wires with a length distribution from 40 nm to 1630 nm in steps of 10 nm. Figure 3.1 (b) shows the z-component of the electric field 24 nm above the structure, extracted from simulations. Wires are arranged in several interlaced columns as shown in Fig. 3.1 (c) with a spacing of 260 nm. Figure 3.1 (d) displays the near-field image of the sample shown in Fig. 3.1 (c) recorded with excitation polarization parallel to the wire axis. The signal strength varies strongly from wire to wire, and the first-order resonance observed for a wire length of $\approx$ 140 nm (Fig. 3.1 (e)) shows the strongest near-field signal. Longer wires show higher order resonances, where the third-order resonance is observed for a wire length of $\approx$ 520 nm (Fig. 3.1 (f)), the fifth for $\approx$ 890 nm (Fig. 3.1 (g)), and the seventh for $\approx$ 1270 nm (Fig. 3.1 (h)).

One notable recent innovation to the s-SNOM approach has been the use of a single QCL device as both THz source and coherent detector, through exploiting the SM effect in these lasers [108]. The SM scheme offers remarkably low noise-equivalent powers at the $\sim pW/\sqrt{Hz}$ level [203], and it is therefore ideally suited to the detection of weak fields scattered from nanometer probes in THz-s-SNOM. This approach has recently been applied to the mapping of THz plasmonic resonances supported by photonic crystals and planar antennas, with a spatial resolution of 78 nm [112]. However, this implementation permitted visualization only of the real component of the surface fields and could not resolve the field magnitude and phase separately. In fact, the mixing process between reinjected and intracavity fields in the laser SM scheme is inherently coherent, which has enabled the complex THz permittivity of samples to be probed in both near-field and far-field regimes [71, 204].

In this chapter all-electronic THz-s-SNOM is applied using a THz QCL to map both the magnitude and phase of the localized field spatially supported by individual micro-resonator structures, achieving a spatial resolution of $\sim$ 35nm. It is shown that the imperfect linear polarized state of the QCL field can nonetheless be exploited for the simultaneous excitation and measurement of plasmonic resonances in these structures whilst suppressing the otherwise dominant signal arising from the local material permittivity. This new characterization technique opens the way for the future design and optimisation of novel THz optoelectronic devices based on subwavelength resonators and associated metamaterials, as well as the nanoscale mapping of THz plasmons in emerging 2D materials and Van der Waals heterostructures [106, 205].

3.2 THz-s-SNOM system

3.2.1 System set-up

The THz-s-SNOM instrument used in the remainder of this thesis is based on a commercial s-SNOM/AFM platform (neaSNOM, neaspec GmbH) but incorporates an external THz QCL source emitting at $\nu \sim 3.45$ THz. The QCL used was the L1180 which was fabricated by Dr P. Rubino and the LIV and spectral characteristics were presented in section 2.4.3. The QCL consisted of a 14-µm-thick GaAs/AlGaAs nine-well hybrid active region lasing at ~ 3.45 THz, which was processed into a SI-SP ridge waveguide with dimensions of 1.8 mm $\times$ 150 µm. The QCL was cooled using a continuous-flow L–He cryostat and maintained at a heat sink temperature of 20 ± 0.01 K. A current source was used to drive the laser with a dc current of 420 mA, just above the lasing threshold current of $\sim$ 400 mA. At this driving current, the QCL voltage was 6.4 V and the emitted power was $\sim$ 1 mW. Emission from the QCL was focused to a vertically aligned Rocky Mountain platinum-iridium tip of the s-SNOM system with an apex of $\sim$ 20 nm, and tip length of $\sim$ 80 µm. The radiation from the QCL was obliquely incident on the tip with an angle of $\sim 54^{o}$ relative to the surface normal, and the length of the external cavity formed between the tip and the QCL facet was $L_{ext} = 60$ cm. A diagram of the s-SNOM system is shown in Fig. 3.2. The radiation scattered to the far-field by the probe is coupled back to the QCL along the same optical path as the incident beam and reinjected to the laser cavity. The resulting mixing process between the intra-cavity and reinjected fields generates a perturbation to the laser voltage, via the laser SM effect, that is proportional to the reinjected field (see section 1.4). This detection approach provides a high detection sensitivity while removing the need for both an external detector and an external interferometer to resolve the scattered field coherently [69]. To isolate the signal component arising from the near-field interaction between the probe and the sample, the microscope probe was operated in a tapping mode and the QCL terminal voltage, after amplification using an ac-coupled low-noise voltage amplifier with gain $A = 5 \times 10^3$, was demodulated at harmonics of the tip tapping frequency ($\Omega \sim 80$ kHz) using a lock-in amplifier. By raster-scanning the sample in two dimensions, images with deep sub-wavelength resolution could, thereby, be obtained up to the $n = 5$ signal harmonic.

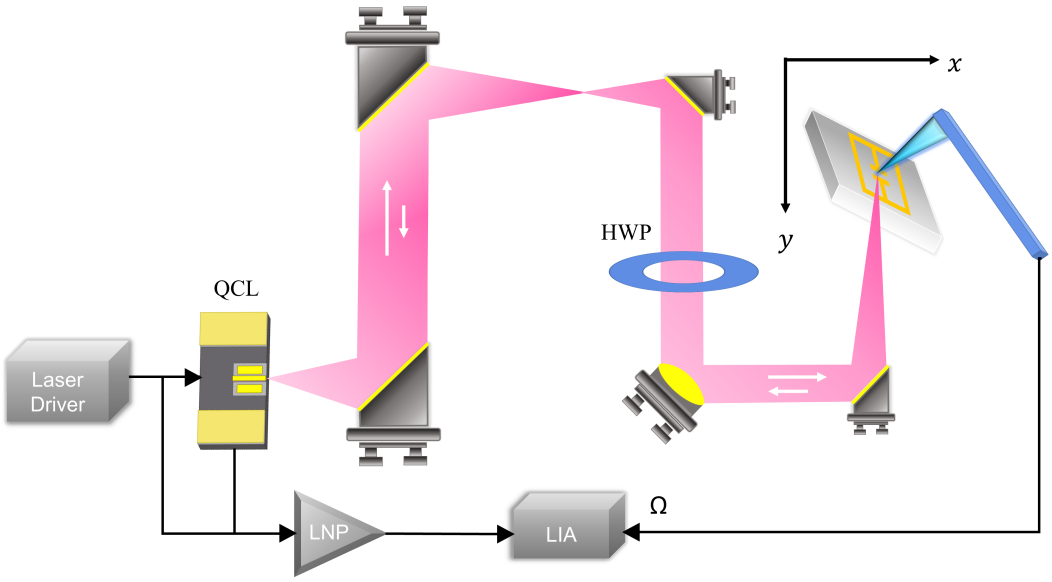

Figure 3.2: Experimental diagram of the THz-s-SNOM system in which radiation from a THz QCL is coupled to and from the tip of an AFM probe. LIA: Lock-in amplifier and LNP: Low-noise preamplifier.

3.2.2 Measurement of spatial resolution

To quantify the spatial resolution of the THz-s-SNOM instrument, two-dimensional images were acquired using a resolution target comprising 50 nm-thick gold stripes patterned on a silicon substrate using electron-beam lithography. The emitted radiation was collected and focused to the apex of the near-field microscope probe, which was positioned in the near-field of the sample surface. Under excitation from a p-polarized beam, radiation is strongly confined at the nanoscale tip apex. The interaction between the probe tip and the sample surface causes a near-field enhancement of the scattering cross section of the tip–sample system that depends on the local sample permittivity. This mechanism has been described previously using various numeric and analytic theoretical frameworks, including point dipole [87, 206], finite dipole [207], and electrodynamic lightning rod models [208].

Figures 3.3(a) and 3.3(b) show, respectively, the sample topography recorded by an AFM and the corresponding THz near-field image obtained from the $n = 3$ harmonic signal. By averaging the signal measured from ten adjacent rows of pixels, the edge response function (ERF) shown in Fig. 3.3(c) is obtained.

Applying the 20%—80% criterion to the ERF yields a spatial resolution of 35 nm, which is comparable to the tip diameter. This resolution corresponds to a sub-wavelength resolution of $\sim \lambda/2$, 500, and it is the highest resolution reported to date for a THz-s-SNOM system using a THz QCL. It should be noted that this resolution depends principally on the tip apex size and the tapping amplitude and could, in principle, be further reduced at the expense of signal size through the use of a sharper tip and smaller amplitude. It should also be noted that this measured value of resolution may be influenced by the topography of our resolution target, which is known to introduce topography-induced contrast, as well as by screening effects in the metallic layer [209–211].

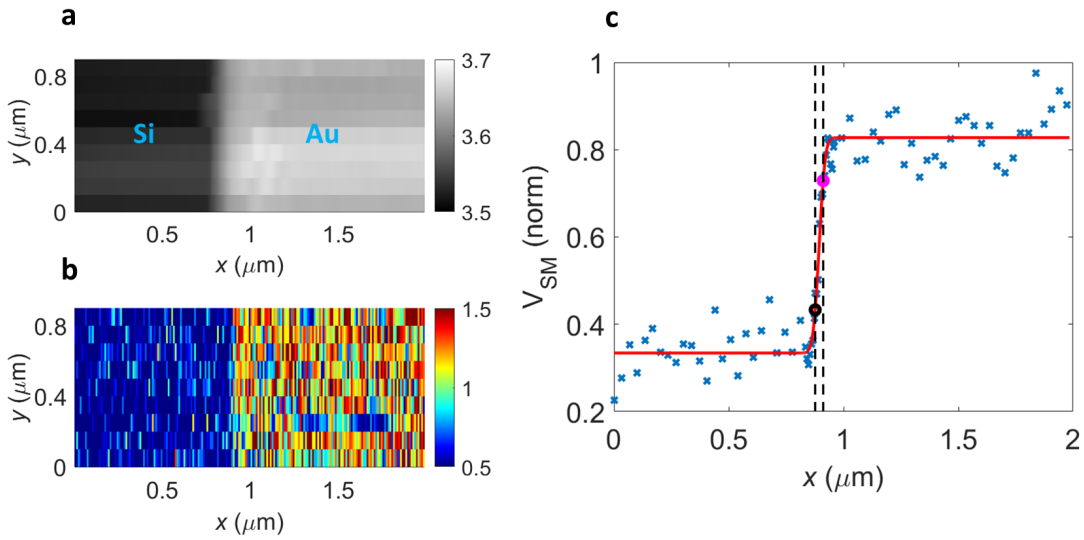

Figure 3.3: (a) AFM image and (b) THz-s-SNOM image of a gold-on-silicon resolution target. The scan area of each image is 2×1 µm^2 with a 10 nm step size in the x direction and 100 nm step size in the y direction. The tapping amplitude was 30 nm. (c) The ERF determined from the voltage signals extracted along the x direction of (b), yielding a spatial resolution of 35 nm. Blue dots: experimental data. Red line: fitted ERF.

3.3 Sample design, fabrication, and characterisation

Mapping of the localized field distribution supported by individual micro-scale resonators using terahertz microscopy will be presented in section 3.7. Two exemplar structures were designed to have a resonant frequency that matches the QCL emission frequency. The design, fabrication, and characterisation of these resonators are presented in this section.

3.3.1 Design and simulation

The first resonator consisted of a simple dipole antenna (DA) structure that was engineered to support a plasmonic resonance at the excitation frequency ν_{res} of $\sim$ 3.45 THz. The dipole antenna can be described as a quasi-one-dimensional Fabry–Pérot resonator of length L given by [95]

$$L = \frac{m\,\lambda_p}{2} = \frac{m\,c}{2n_{eff}\nu_{res}}, \tag{3.1}$$

where λ_p is the plasmon wavelength, c is the speed of light, and n_{eff} is the effective refractive index of the plasmonic mode.

Finite-element method (FEM) simulations of the structure was performed using Ansys HFSS software. Metallic regions were treated as a perfect electrical conductor with thickness 100 nm defined on a 50 µm silicon substrate with permittivity 11.65, determined experimentally from THz time-domain spectroscopy (THz-TDS) measurements. The structure was illuminated by a linearly polarized plane wave under either normal illumination (in the case of Figs. 3.4 and 3.5) or with an angle of incidence of 54° to reproduce the experimental conditions in the s-SNOM system (in the case of section 3.4.2). Periodic boundary conditions were defined at the edges of the simulation volume with a 13 µm spacing between the dipole resonators. Wave ports positioned 250 µm apart and lying in the x–y planes above and below the structure were used to obtain S21 parameters.

Figure 3.4 shows the simulated S_{21} parameter for a 100-nm-thick gold structure with dimensions 15 × 2 µm^2. A sharp first-order (m = 1) resonance is observed at ν_{res} = 3.45 THz, indicating a plasmon wavelength of λ_p = 30 µm and a value of n_{eff} = 2.9 obtained from Eq. 3.1. To visualize this plasmonic mode driven

by the incoming wave, the magnitude and phase of the out-of-plane electric field component E_z were calculated in the x–y plane at a distance of 20 nm above the sample surface. As shown in Figs. 3.5 (a) and 3.5 (b), the field is strongly enhanced at both ends of the structure, with a π radian phase difference between the two ends.

The second resonator structure designed was a THz metamaterial consisting of a periodic array of split ring resonators (SRRs). Each SRR supports an inductive–capacitive resonance, whereby surface current modes are strongly excited by interaction with the incident field. Figure 3.4 shows the simulated S_{21} parameter for a 9 × 9 µm^2 structure with a gap width of 2 µm and a periodicity of 12.5 µm ($\approx \lambda_{res}/7$). The magnitude and phase of E_z at the resonant frequency $\nu_{\mathrm{res}} \sim 3.45$ THz are shown in Figs. 3.5 (c) and 3.5 (d), respectively. In this case, the electric field is strongly enhanced at the edges of the capacitive gap and the field oscillates in these regions with a 0 or π radian phase difference with respect to the incident field.

Based on these simulated parameters shown in Fig. 3.4, both the dipole antenna and SRR structures exhibit a resonance at $\sim$ 3.45 THz, with Q factors of 69 and 39, respectively.

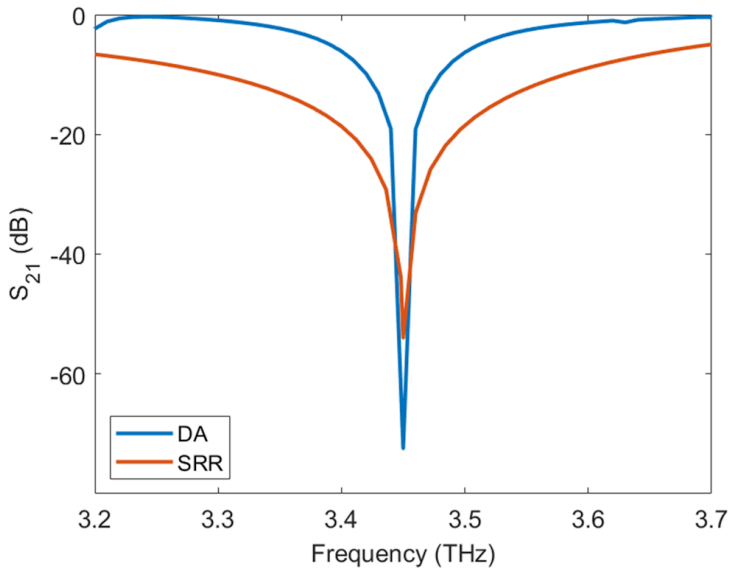

Figure 3.4: S_{21} parameters obtained from finite-difference time-domain simulations of the dipole antenna (DA, blue line) and split ring resonator (SRR, red line) structures, each showing a resonance close to the design frequency $\sim$ 3.45 THz.

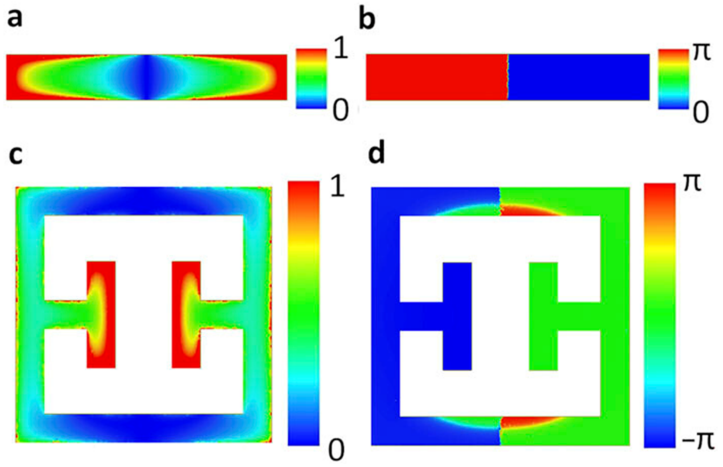

Figure 3.5: Simulated (a) magnitude and (b) phase of the out-of-plane field measured in the x–y plane 20 nm above a dipole antenna structure. The structures are illuminated at normal incidence with an x–polarized (horizontally-polarised) plane wave with frequency 3.45 THz. (c) Magnitude and (d) phase maps for a split ring resonator (SRR) structure for the same excitation conditions. The colour scales in (a) and (c) are normalized to the maximum field magnitude in each case.

3.3.2 Fabrication

Structures were fabricated using standard electron-beam lithography on a high resistivity (>10,000 Ω cm) undoped silicon substrate with a thickness of 525 ± 25 µm. The thickness of the Ti/Au resonators was ∼ 2 nm/ ∼ 100 nm. Structures were patterned across a 2 × 2 mm^2 region with a periodicity of 12.5 µm for the SRRs and a spacing of 13 µm between the dipole resonators. Figures 3.6 (a) and 3.6 (b) show AFM images of periodic arrays of each resonator.

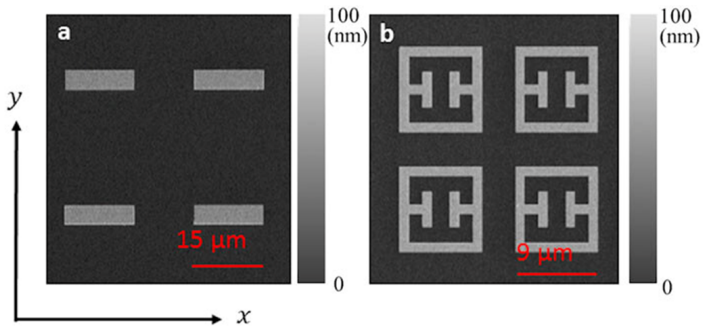

Figure 3.6: AFM images of fabricated (a) DA and (b) SRR structures.

3.3.3 Terahertz Time-domain spectroscopy

In order to confirm the resonant frequency of the fabricated structures, their absorption parameters were measured using THz-TDS. The THz-TDS system used has been described in detail elsewhere [212]. In brief, a 800 nm wavelength mode-locked Ti:sapphire laser (Vitara, Coherent) providing pulses with a width of 20 fs at an 80 MHz repetition rate was used to generate THz pulses from a photoconductive (PC) emitter comprising a 300-nm-thick piece of low temperature grown GaAs (LT-GaAs) bonded onto a 5-mm-thick quartz substrate [212]. Detection was achieved using a time-delayed probe beam derived from the fs laser to excite an identical second PC device. Measurements were conducted in a nitrogen environment to remove the effect of water absorption in atmosphere. The transmission parameters of the fabricated arrays measured by THz time-domain spectroscopy are shown in Fig. 3.7. In each case, a clear resonance is observed at the design frequency when the polarization of the incident beam is aligned in the horizontal (x) direction. It was confirmed that the resonance disappears when the polarisation of the incident beam is aligned in the vertical (y) direction. The weaker and broader resonances observed experimentally, when compared to the simulations, can be attributed to limitations in the spatial resolution ($1 - 2$ µm) of the lithographic technique and lift-off process used during fabrication, as well as losses in the metallic layers of experimental devices.

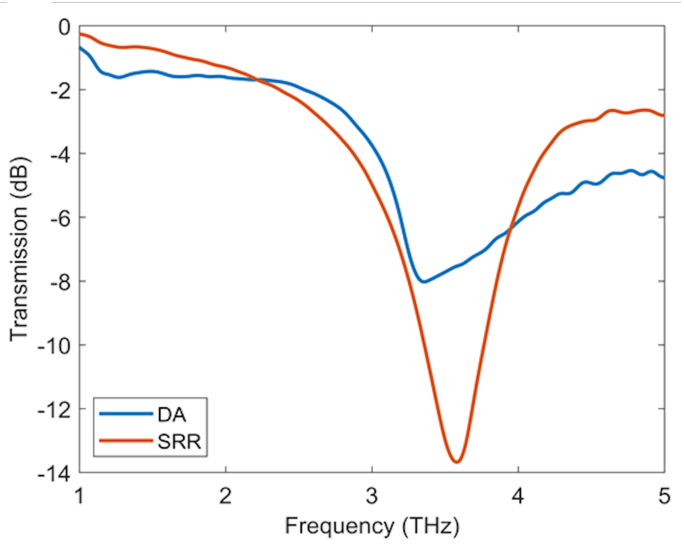

Figure 3.7: THz transmission properties of the fabricated arrays obtained using THz-TDS, each showing a resonance close to the design frequency of ~ 3.45 THz.

3.4 THz-s-SNOM of microscale resonators

3.4.1 Description of self-mixing voltage

In the case of samples as shown in Fig. 3.2, which do not support resonant modes at the radiation frequency, image contrast arises solely from the spatial variation of the local dielectric properties of the sample in the near-field of the tip (see section 1.5). To engage this imaging mode efficiently requires a p-polarized excitation beam, for which the interaction with the vertically aligned probe is significantly stronger than for s-polarized radiation [87]. In the case of resonant samples, however, in-plane modes may be excited directly using s-polarized radiation of the appropriate frequency. Any out-of-plane (z direction) fields supported by the excited resonant sample will then be scattered strongly to the far-field, whereas in-plane field components will scatter only weakly from the vertically aligned probe. In the more general case of a resonant sample illuminated by an incident beam of arbitrary polarization, the predominantly p-polarized field scattered to the far-field can therefore be expressed as

$$E_{scat} = \sigma_\varepsilon E_\perp + \sigma_z E_z \,. \tag{3.2}$$

Here, $E_\perp$ represents the out-of-plane component of the incident field and σ_ε is the complex scattering efficiency that encapsulates the near-field dipole interaction between the illuminated tip and the sample surface [213]. E_z represents the out-of-plane field component associated with resonant modes supported by the sample, which can be excited by appropriately oriented in-plane components of the incident field $E_\parallel$, and the complex parameter σ_z quantifies the efficiency with which E_z is scattered to the far-field.

In the experiment, radiation scattered by the probe to the far-field is typically weak, and the laser is therefore operated in the regime of weak optical feedback [54]. Under these conditions, the measured SM voltage signal V_{SM} is proportional to the scattered field that is reinjected to the laser cavity after accumulating a roundtrip phase $\phi_L = 4\pi L_{ext}\nu/c$ in the external cavity of length L_{ext} formed between the laser facet and the probe tip [214]. A variation in the roundtrip phase, accomplished through either mechanical extension of the external cavity [215] or electronic control of the laser frequency [70], can thereby induce a series of interferometric fringes in the demodulated SM voltage signal, the complex amplitude

of which relates directly to the scattered field E_{scat}. Following Eq. 3.2, and by analogy with Eq. 1.5 the SM signal can be expressed in terms of the amplitudes s_ε and s_z, and phases, ϕ_ε and ϕ_z, of the complex scattering efficiencies corresponding to the respective scattering terms (see Eq. 3.2) according to

$$V_{SM} = s_\varepsilon \cos\left(\frac{4\pi L_{ext}\,\nu}{c} - \phi_\varepsilon\right) + s_z \cos\left(\frac{4\pi L_{ext}\,\nu}{c} - \phi_z\right) \tag{3.3}$$

The demodulated SM voltage can thereby be written in complex notation as

$$V_{SM} = \left(s_\varepsilon\, e^{-i\phi_\varepsilon} + s_z\, e^{-i\phi_z}\right) e^{i\phi_L}. \tag{3.4}$$

Here, the magnitudes s_ε and s_z encapsulate several factors, including the respective excitation field strengths, the feedback parameter (itself accounting for the reinjection efficiency to the laser cavity), and the optoelectronic response of the laser active region. We can, furthermore, note that the phase $\phi_\varepsilon \approx 0$ for radiation frequencies far away from any phonon or bulk plasmonic material resonances [204]. This also permits the round-trip phase $\phi_L = 2\pi m$ to be set experimentally, through a fine adjustment of the external cavity length, by maximizing the signal measured from a region of the sample where no out-of-plane field exists (i.e., for which $s_z = 0$). The SM voltage signal then simplifies to

$$V_{SM} = s_\varepsilon + s_z\, e^{-i\phi_z}\,. \tag{3.5}$$

Hence, the s-SNOM signal may comprise two contributions: the first, s_ε, is principally excited by p-polarized components of the incident radiation and captures information on the local permittivity of the sample. The second is excited by in-plane components of the incident field and is insensitive to the bulk material properties but captures the spatial distribution of the out-of-plane field supported by the sample under resonant excitation. The relative contributions of these two terms can be controlled through either control of the polarization state of the incident field or through the variation of the sample orientation with respect to this field. The former of these approaches will be demonstrated in Section 3.6 and the latter approach will be demonstrated in the next sub-section.

3.4.2 THz-s-SNOM of microscale resonators using p-polarised excitation

In the system, the epitaxial growth direction of the QCL heterostructure stack is aligned parallel to the probe axis (z direction). Owing to the selection rules for intersubband transitions in QCLs, which dictate the emission of predominantly transverse magnetic (TM) polarized modes, the excitation field is therefore predominantly p-polarized with an in-plane component along the x direction. Figures 3.8(a) and 3.8(c) show, respectively, THz near-field images of the dipole antenna structure and SRR structure each with their principal axis orientated along this direction. For this image, the pixel size is 200 nm, and the sampling time is 200 ms. For comparison, THz images of both structures when orientated along the orthogonal (y) direction are shown in Figs. 3.8(b) and 3.8(d). The noise in these images can be attributed to several sources, including surface roughness of the metallic layers, mechanical vibration, thermal drift of the QCL operating temperature, and laser voltage noise. Figures 3.8(e)–3.8(h) show the corresponding spatial maps of E_z obtained from finite-element method (FEM) simulations of each structure assuming a p-polarized excitation beam. The simulations were performed with a beam at an angle of 54° to match the experimental conditions. Excellent agreement between experimental and simulated images is obtained, albeit with the experimentally measured signals being offset by a constant (spatially homogeneous) positive voltage across the structure (see below). In particular, the THz image reveals clear signal contrast between opposite ends of the dipole structure when the resonator axis is aligned along the x direction ["on resonance" orientation; Fig. 3.8(a)]. These features, which do not appear for the orthogonal sample orientation ["off resonance" Fig. 3.8(b)], are a clear indication of a dipolar plasmonic mode being excited in the structure and subsequently probed in the near-field using our approach. A strong in-plane resonant mode, characterized by opposing surface fields supported at the edges of the capacitive gap, is similarly revealed in the THz image of the SRR structure only when orientated appropriately with respect to the incident field ["on resonance" orientation; Fig. 3.8(c)]. In the "off resonance" orientation [Fig. 3.8(d)], this mode is not excited although a larger voltage signal is recorded along one edge of the structure. This feature, which is also predicted through simulation of the out-of-plane field distribution [Fig. 3.8(h)], can be attributed to a mode excited in the outer ring of the SRR with the asymmetry arising from the oblique illumination geometry.

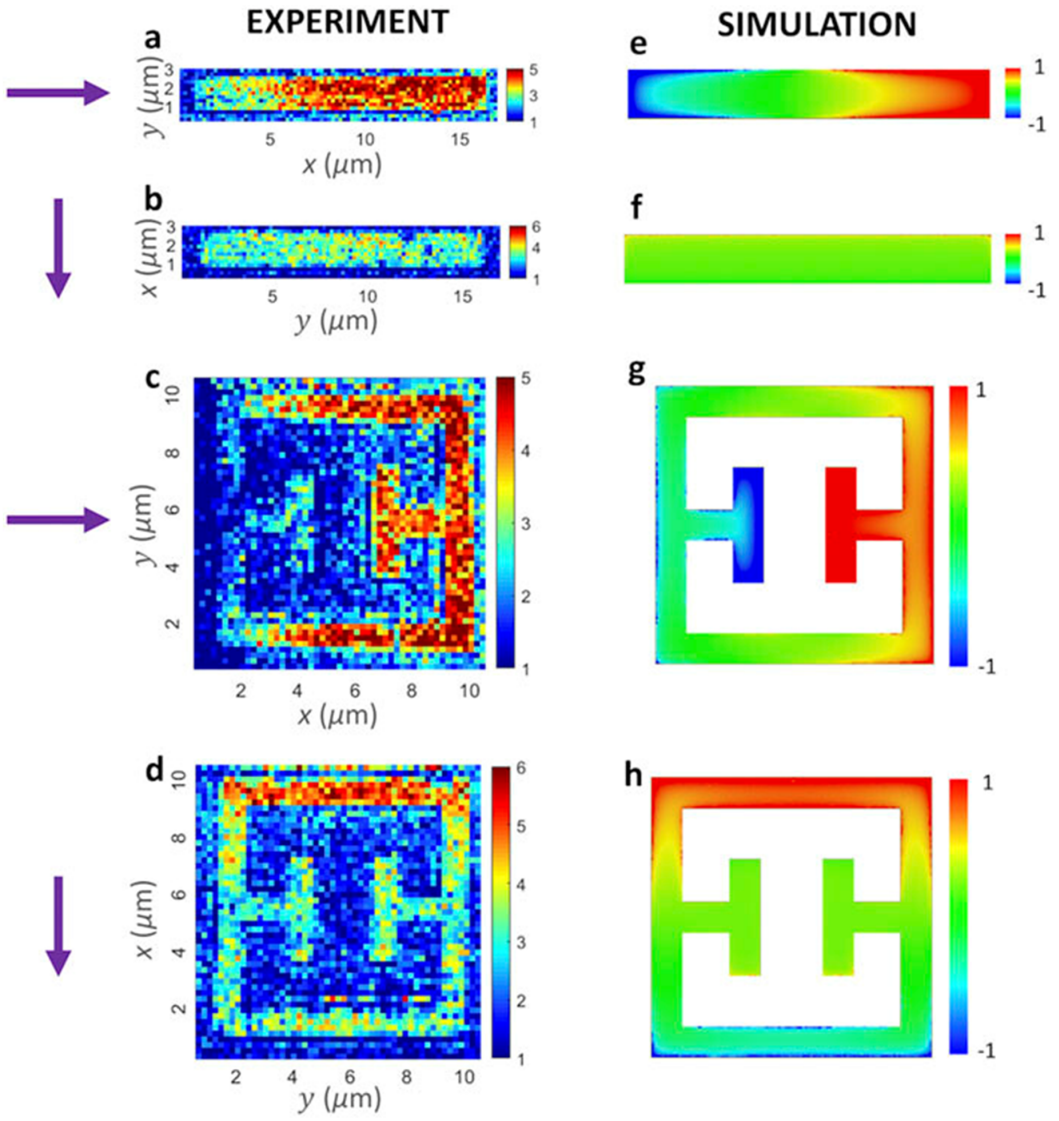

Figure 3.8: THz-s-SNOM images of the individual [(a) and (b)] dipole antenna and [(c) and (d)] SRR structures measured at the resonant frequency of $\sim$ 3.45 THz. The color scale represents the measured SM voltage signal, described by the real part of Eq. 3.5. The arrows indicate the in-plane polarization of the excitation field; in (a) and (c), the field is orientated to excite a resonance in each structure ("on resonance" orientation), whereas in (b) and (d), no resonance is excited ("off resonance" orientation). [(e)–(h)] Corresponding simulations of the out-of-plane field in the x–y plane 20 nm above the sample surface. The colour scales are normalized to the maximum field value of the real part of the out-of-plane field.

This oblique illumination, which causes the phase of the excitation field to vary linearly along the x direction, will also give rise to a spatial variation in the phase of the scattered field as the spatially structured sample is scanned within the beam. This phenomenon is expected to manifest in all the recorded images shown in Fig. 3.8, although its effect may be obscured by the field distribution of the sample's resonant mode or may be negligible when the sample is spatially small along the y dimension. Further differences between measured and simulated results in Fig. 3.8 may arise from shadowing effects or through coupling of the tip and resonator, altering the resonant properties of the resonators. This latter effect would be dependent on both the geometry and dielectric properties of the tip.

Although experimentally convenient, the images shown in Fig. 3.8 highlight two limitations of employing a p-polarized excitation beam for mapping resonant modes in such structures. First, the generation of field components necessary for the excitation of in-plane modes unavoidably results in a component of beam propagation along the principal axis of the resonator. The recorded images are thereby susceptible to phase retardation effects that can obscure the spatial distribution of the out-of-plane field supported by the sample, as discussed above. Second, a p-polarized beam is extremely efficient at exciting a near-field interaction between the illuminated tip and the sample surface, giving rise to a strong signal component, s_ε, that depends only on the local material properties of the sample. On the other hand, an s-polarized excitation beam may be employed to excite in-plane resonant modes selectively while mitigating against phase retardation effects along the resonator axis. This approach has been adopted in mid-infrared s-SNOM of antennas [216]. In order to investigate the use of s-polarisation in THz-s-SNOM it was necessary to fully characterise the polarisation properties of the QCL emission, which are presented in the following section.

3.5 Measurement of polarisation characteristics of THz QCL emission

The QCL polarisation was characterised using two complementary approaches: Jones vectors and Stokes parameters.

3.5.1 Description of Jones vector analysis

One representation of polarised light was invented by R. Clark Jones in 1941 [217]. The technique has the advantage of being extremely concise, although it is applicable only to polarised waves. The radiation is represented in terms of the electric vector, and the Jones vector is:

$$\mathbf{E} = \begin{bmatrix} E_x(t) \\ E_y(t) \end{bmatrix}, \tag{3.6}$$

where $E_x(t)$ and $E_y(t)$ are the instantaneous scalar components of $\mathbf{E}$ along the $x-$ and $y-$directions. Rewriting the vector in complex form yields:

$$\mathbf{E} = \begin{bmatrix} E_{0x}\, e^{i\,\phi_x} \\ E_{0y}\, e^{i\,\phi_y} \end{bmatrix}, \tag{3.7}$$

where ϕ_x and ϕ_y are the phases of the horizontal and vertical electric field components.

As a first example, consider a linearly polarised beam. The horizontal and vertical polarisation states are described by the Jones vector as:

$$\mathbf{E_h} = \begin{bmatrix} E_{0x}\, e^{i\,\phi_x} \\ 0 \end{bmatrix} \quad \text{and} \quad \mathbf{E_v} = \begin{bmatrix} 0 \\ E_{0y}\, e^{i\,\phi_y} \end{bmatrix}, \tag{3.8}$$

respectively, where $\mathbf{E} = \mathbf{E_h} + \mathbf{E_v}$. To simplify the analysis, the Jones vector can be normalised by dividing both elements in the vector by the same scalar quantity, such that the sum of the squares of the components is 1. This leads to:

$$\mathbf{E_h} = \begin{bmatrix} 1 \\ 0 \end{bmatrix} \quad \text{and} \quad \mathbf{E_v} = \begin{bmatrix} 0 \\ 1 \end{bmatrix}. \tag{3.9}$$

As a second example, the Jones vector can be used to describe circularly polarised light. Right-circular light has $E_{0x} = E_{0y}$, and the vertical ($y-$) component leads the horizontal ($x-$) component by 90°. The Jones vector then is:

$$\mathbf{E} = \begin{bmatrix} E_{0x}\, e^{i\,\phi_x} \\ E_{0x}\, e^{i\,(\phi_x - \pi/2)} \end{bmatrix}. \tag{3.10}$$

Dividing both components by $E_{0x}e^{i\phi_x}$ yields:

$$\mathbf{E} = \begin{bmatrix} 1 \\ e^{-i\pi/2} \end{bmatrix} = \begin{bmatrix} 1 \\ -i \end{bmatrix}. \tag{3.11}$$

Hence, the normalised Jones vectors for left- and right-circular polarised light are:

$$\mathbf{E_R} = \frac{1}{\sqrt{2}} \begin{bmatrix} 1 \\ -i \end{bmatrix} \quad \text{and} \quad \mathbf{E_L} = \frac{1}{\sqrt{2}} \begin{bmatrix} 1 \\ i \end{bmatrix}, \tag{3.12}$$

where $\mathbf{E_R}$ and $\mathbf{E_L}$ are the vector fields for right and left circularly polarised light respectively. The Jones vector for elliptical light can be obtained by the same procedure used to arrive at $\mathbf{E_R}$ and $\mathbf{E_L}$, where now E_{0x} may not be equal to E_{0y}, and the phase difference may not be 90°. The ellipticity of the beam is defined by the elliptic coefficient $R = E_{0x}/E_{0y}$. A value of $R = 0$ represents vertically linear polarisation, and $R = \infty$ represents horizontally linear polarisation. A value of $R = -1$ represents right circular polarisation and $R = +1$ represents left circular polarisation. For values of $R > 1$ the major axis of the polarisation ellipse is horizontal, whereas for values of $R < 1$ the major axis of the ellipse is vertical. The Jones vector of an elliptically polarised beam orientated along x or y can be written as:

$$\mathbf{E} = E_{0x} \begin{bmatrix} 1 \\ i\frac{1}{R} \end{bmatrix}. \tag{3.13}$$

The total light intensity is given by the norm of the Jones vector:

$$I_0 = E_{0x}^2 (1 + \frac{1}{R^2}). \tag{3.14}$$

Now suppose that the incident beam represented by its Jones vector $\mathbf{E_i}$ passes through an optical element such as a linear polariser, a new vector, $\mathbf{E_t}$ emerges

which has been transformed by the optical element. This process can be described mathematically using a 2×2 transformation matrix, $\mathbf{A}$. Then:

$$\mathbf{E_t} = \mathbf{A}\mathbf{E_i}, \tag{3.15}$$

where

$$\mathbf{A} = \begin{bmatrix} a_{11} & a_{12} \\ a_{21} & a_{22} \end{bmatrix}. \tag{3.16}$$

Expanding Eq. 3.15 yields:

$$E_{tx} = a_{11}E_{ix} + a_{12}E_{iy}, \tag{3.17}$$

and

$$E_{ty} = a_{21}E_{ix} + a_{22}E_{iy}. \tag{3.18}$$

An ideal polariser causes no attenuation of the output intensity at angle of 0° and it completely blocks the signal at an angle of 90°. In the general case, the transformation matrix is given by:

$$\mathbf{A}(\theta) = \begin{pmatrix} \cos^2\theta & -\cos\theta\sin\theta \\ -\cos\theta\sin\theta & \sin^2\theta \end{pmatrix}, \tag{3.19}$$

where θ is the angle of the linear polariser relative to the horizontal (x) direction. A non-ideal polariser can be modelled by introducing two factors: isotropic power attenuation μ^2 which shows the percentage of power transmitted through the polariser at an angle of 0°, and the leakage factor η^2 which shows the percentage of power leaking through the polariser at an angle of 90°. The transformation matrix for a non-ideal polariser is rewritten as:

$$\mathbf{A}(\theta) = \sqrt{\mu}\begin{pmatrix} \cos^2\theta + \eta\sin^2\theta & (\eta-1)\cos\theta\sin\theta \\ (\eta-1)\cos\theta\sin\theta & \sin^2\theta + \eta\cos^2\theta \end{pmatrix}, \tag{3.20}$$

where $0 \leq \eta \leq 1$ defines the fraction of the electric field that leaks through the polariser at the minimum transmission angle, and μ^2 accounts for the dissipated power due to the non-ideality of the polariser.

The Microtech G50 wire-grid polariser which was used in this experiment exhibits a non-ideal behaviour at THz frequencies. In the experimental procedure for determining the Jones vector of the QCL source, firstly only one polariser was placed in front of the QCL and the transmitted power was recorded as a function of the polariser angle for angles of 0° to 180° with a step of 10°. Then, the polariser was set at maximum transmission (0°) and a second polariser was placed into the system, after the first polariser. The transmitted power was then recorded for angles of 0° to 180° of the second polariser with a step of 10°.

The maximum power transmitted through the first polariser is obtained for an angle $\theta = 0^o$. Using Eq. 3.15 this yields:

$$\mathbf{E_t} = \mathbf{A}(\theta = 0^o)\mathbf{E_i}. \tag{3.21}$$

Using Eq. 3.14, the maximum power through the first polariser is:

$$I_1(0^o) = I_0\mu(\frac{R^2 + \eta^2}{R^2 + 1}). \tag{3.22}$$

The minimum transmitted power through the first polariser occurs for an angle $\theta = 90^o$. Using Eq. 3.15 this yields:

$$\mathbf{E_t} = \mathbf{A}(\theta = 90^o)\mathbf{E_i}. \tag{3.23}$$

Using Eq. 3.14, the minimum power through the first polariser is:

$$I_1(90^o) = I_0\mu(\frac{\eta^2 R^2 + 1}{R^2 + 1}). \tag{3.24}$$

The maximum power transmitted through the second polariser ($\theta = 0^o$) when the first polariser is also placed at angle $\theta = 0^o$ can be obtained using Eq. 3.15:

$$\mathbf{E_t} = \mathbf{A}(\theta = 0^o)\mathbf{A}(\theta = 0^o)\mathbf{E_i}. \tag{3.25}$$

Using Eq. 3.14, the maximum power through the second polariser is:

$$I_2(0^o, 0^o) = I_0\mu^2(\frac{R^2 + \eta^4}{R^2 + 1}). \tag{3.26}$$

The minimum power transmitted through the second polariser ($\theta = 90^o$) when the first polariser is placed at angle $\theta = 0^o$ can be obtained using Eq. 3.15:

$$\mathbf{E_t} = \mathbf{A}(\theta = 90^o)\mathbf{A}(\theta = 0^o)\mathbf{E_i}. \tag{3.27}$$

Using Eq. 3.14, the minimum power through the second polariser is:

$$I_2(0^o, 90^o) = I_0 \mu^2 \eta^2 \,. \tag{3.28}$$

Hence by performing a measurement of I_0, $I_1(0)$, $I_1(90)$, $I_2(0,0)$ and $I_2(0,90)$ and solving Equations 3.22, 3.24, 3.26, and 3.28, the parameters η, μ, and R can be determined.

A schematic of the system setup is shown in Fig. 3.9. The QCL was driven by a DC current source (Arroyo Laser driver) at a temperature of 20 K. A mechanical chopper was used to modulate the beam at 120 Hz and a lock-in amplifier was locked at the same frequency to recover the radiation detected by the bolometer.

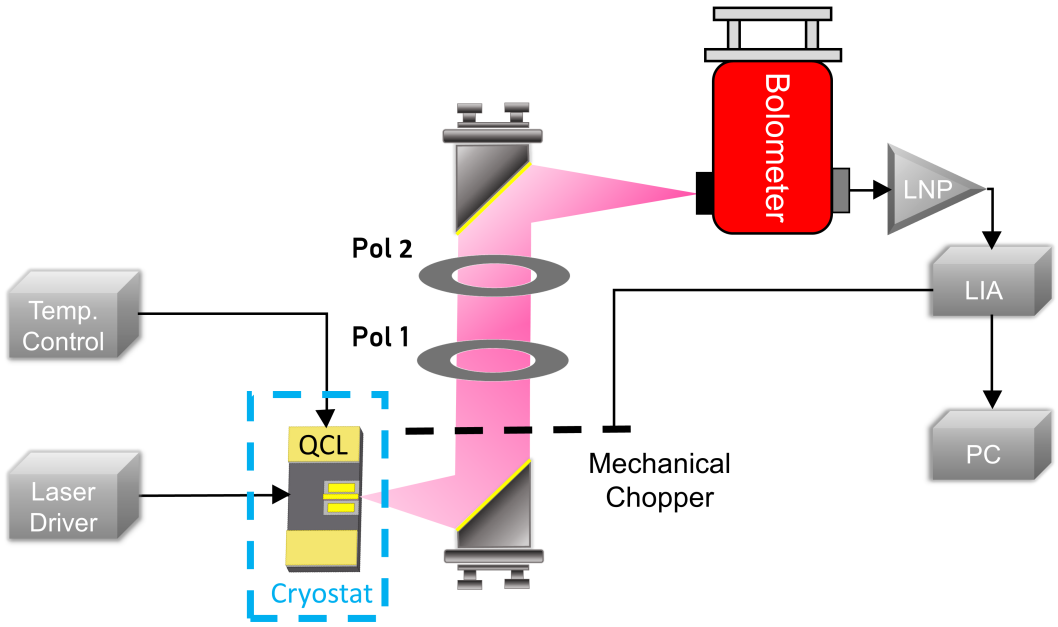

Figure 3.9: Schematic of the system setup of the Jones Vectors measurements to assess the polarisation state of the QCL.

The Jones vector was determined for a range of driving currents, 420, 600, 650, and 700 mA in order to determine the effect on the polarisation state of the QCL, and similar results were obtained for all cases. The results presented in this section were recorded for a driving current of 600 mA. The measurements of the power transmitted through the polarisers with different orientations are summarised in Fig. 3.10. The incident power recorded in the absence of the polarisers was $I_0 = 640$ mV. From this figure it can be seen that the transmitted

power recorded when the first polariser was placed in the system at an angle of maximum transmission was $I_1(0^o) = 520$ mV. The transmitted power recorded when the polariser angle was set to minimum transmission was $I_1(90^o) = 35$ mV. The power recorded when the second polariser was placed in the system and both angles were set to maximum transmittance was $I_2(0^0, 0^o) = 410$ mV, and the power recorded when the first polariser was set to 0° and the second polariser was set to 90° was $I_2(0^o, 90^o) = 20$ mV. Solving the simultaneous equations 3.22, 3.24, 3.26 and 3.28, the values $R \approx 0.18$, $\mu = 0.814$, and $\eta = 0.32$ were determined. The power leakage factor was $\eta^2 \approx 10\%$ and the isotropic attenuation factor $\mu^2 \approx 66\%$. The result $R = 0.18 < 1$ shows that the beam is elliptically polarised with its major axis oscillating vertically (parallel to the active region growth direction of the QCL). The ellipticity angle angle $\sin(\chi) = R$ yielded a value of $\chi \approx 10^o$.

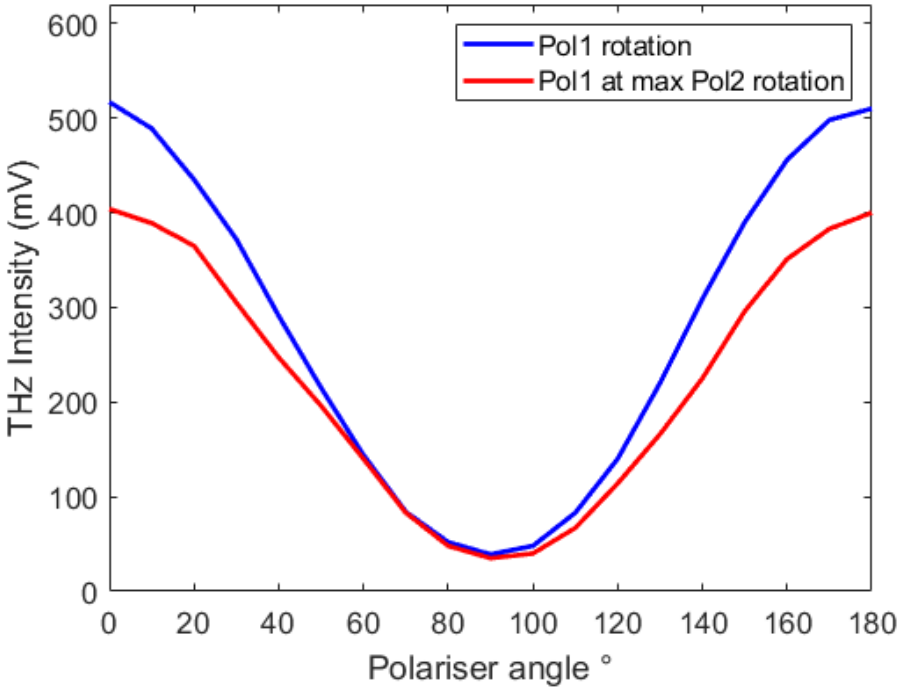

Figure 3.10: THz beam crossing the first polariser and rotated for angles of 0° to 180° (blue). The first polariser was set at maximum transmittance and the second polariser was rotated for the same angles (red).

3.5.2 Description of Stokes parameters

The polarisation state of an EM wave can also be described using a set of parameters known as the Stokes parameters [217, 218]. This method of analysing the polarisation state was developed by George Gabriel Stokes in 1852. The first parameter, S_0 is the power of the incident wave whereas the next three parameters,S_1, S_2, and S_3 describe the state of polarisation. The value of S_1 represents how linearly polarised the incoming wave is either horizontally ($S_1 > 0$) or vertically ($S_1 < 0$). The parameter S_2 represents the linearity of light at +45° ($S_2 > 0$) or -45° ($S_2 < 0$). The parameter S_3 represents the circularity of light, where ($S_3 > 0$) for right-handed circular light and ($S_3 < 0$) for left-handed circular light. When a parameter is equal to zero, the state of polarisation that is represented by the parameter is not apparent in the relevant EM beam.

The Stokes parameters can be calculated using the values of the electric field components in the $x-$ and $y-$ directions:

$$S_0 = E_{0x}^2 + E_{0y}^2 \tag{3.29}$$

$$S_1 = E_{0x}^2 - E_{0y}^2 \tag{3.30}$$

$$S_2 = 2\,E_{0x}\,E_{0y}\,\cos\phi \tag{3.31}$$

$$S_3 = 2\,E_{0x}\,E_{0y}\,\sin\phi \tag{3.32}$$

where $\phi = \phi_x - \phi_y$.

The Stokes parameters can characterise completely polarised, partially polarised, and unpolarised light. If the light is completely polarised, Eq. 3.33 equals to unity:

$$S_0^2 \geq S_1^2 + S_2^2 + S_3^2\,. \tag{3.33}$$

For partially or unpolarised light, Eq. 3.33 results to greater than one. Furthermore, the degree of polarisation (DoP) is defined as:

$$P = \frac{(S_1^2 + S_2^2 + S_3^2)^{1/2}}{S_0}\,. \tag{3.34}$$

The set of the Stokes parameters are commonly represented as a column vector:

$$\mathbf{S} = \begin{bmatrix} S_0 \\ S_1 \\ S_2 \\ S_3 \end{bmatrix} . \tag{3.35}$$

In the experimental procedure for determining the Stokes parameters of the QCL source, the THz beam is passed through a quarter wave-plate (QWP) followed by a linear polariser, and the transmitted power is measured for their different orientations. In this arrangement, the Stokes formula which relates the parameters with the transmitted power is [218]:

$$I(\phi, \theta) = \frac{1}{2}(S_0 + S_1 \cos\theta + S_2 \cos\phi \sin 2\theta + S_3 \sin\phi \sin 2\theta) . \tag{3.36}$$

The Stokes parameters can be obtained by measuring the intensity at four different combinations of ϕ (QWP angle) and θ (polariser angle) relative to the horizontal (x) axis. The first three parameters; S_0, S_1, S_2 are measured by placing the QWP at angle $\phi = 0$, and rotating the polariser angle θ to 0°, 45° and 90° respectively. The parameter S_3 is measured by placing the QWP angle $\phi = 90^o$ and the polariser angle $\theta = 45^o$. Using Eq. 3.36 the Stokes parameters can be related to the measured powers, according to equations 3.37, 3.38, 3.39, and 3.40.

$$I(0^o, 0^o) = \frac{1}{2}(S_0 + S_1) \tag{3.37}$$

$$I(0^o, 45^o) = \frac{1}{2}(S_0 + S_2) \tag{3.38}$$

$$I(0^o, 90^o) = \frac{1}{2}(S_0 - S_1) \tag{3.39}$$

$$I(90^o, 45^o) = \frac{1}{2}(S_0 + S_3) \tag{3.40}$$

The values of $I(0^o, 0^o)$, $I(0^o, 45^o)$, $I(0^o, 90^o)$, and $I(90^o, 45^o)$ are obtained experimentally. Hence, the Stokes parameters are obtained by rearranging the equations above:

$$S_0 = I(0^o, 0^o) + I(0^o, 90^o) \tag{3.41}$$

$$S_1 = I(0^o, 0^o) - I(0^o, 90^o) \tag{3.42}$$

$$S_2 = 2I(0^o, 45^o) - S_0 \tag{3.43}$$

$$S_3 = 2I(90^o, 45^o) - S_0 \tag{3.44}$$

The relationships presented in the equations 3.37, 3.38, 3.39, and 3.40 are applicable only when the polariser is ideal (i.e the leakage power factor $\eta^2 = 0$). To accurately calculate the Stokes Parameters of the THz-QCL, the leakage power factor calculated from the Jones vectors analysis ($\eta^2 \approx 10\%$) needs to be taken into account. Accounting for this leakage the measured powers (I_m) are then related to the ideal powers (I) according to these relations:

$$I_m(0^o, 0^o) = I(0^o, 0^o) \tag{3.45}$$

$$I_m(0^o, 90^o) = I(0^o, 90^o) + \eta^2 I(0^o, 0^o) \tag{3.46}$$

$$I_m(0^o, 45^o) = I(0^o, 45^o) + \frac{\eta^2}{2} I(0^o, 0^o) \tag{3.47}$$

$$I_m(90^o, 45^o) = I(90^o, 45^o) + \frac{\eta^2}{2} I(0^o, 0^o) \tag{3.48}$$

Using these relationships we can then rewrite the equations for the Stokes parameters in terms of the measured intensities:

$$S_0 = (1 - \eta^2) I_m(0^o, 0^o) + I_m(0^o, 90^o) \tag{3.49}$$

$$S_1 = (1 + \eta^2) I_m(0^o, 0^o) - I_m(0^o, 90^o) \tag{3.50}$$

$$S_2 = 2I_m(0^o, 45^o) - I_m(0^o, 0^o) - I_m(0^o, 90^o) \tag{3.51}$$

$$S_3 = I_m(0^o, 0^o) + I_m(0^o, 90^o) - 2I_m(90^o, 45^o) \tag{3.52}$$

3.5.3 Measurement of Stokes parameters of a THz-QCL

The QCL was embedded into a continuous-flow cryostat and was operated in CW mode, at a constant temperature of 20 K. The QCL was modulated using a mechanical chopper. The bolometer was used to detect the THz signal and the lock-in amplifier was used to lock the frequency at $\sim$ 100 Hz and remove the background noise. A quarter wave-plate (QWP) and a linear polariser were used to obtain the Stokes parameters. The light would first pass through the QWP and the linear polariser and it would be collected by the bolometer. A diagram of the system setup is shown in Fig. 3.11.

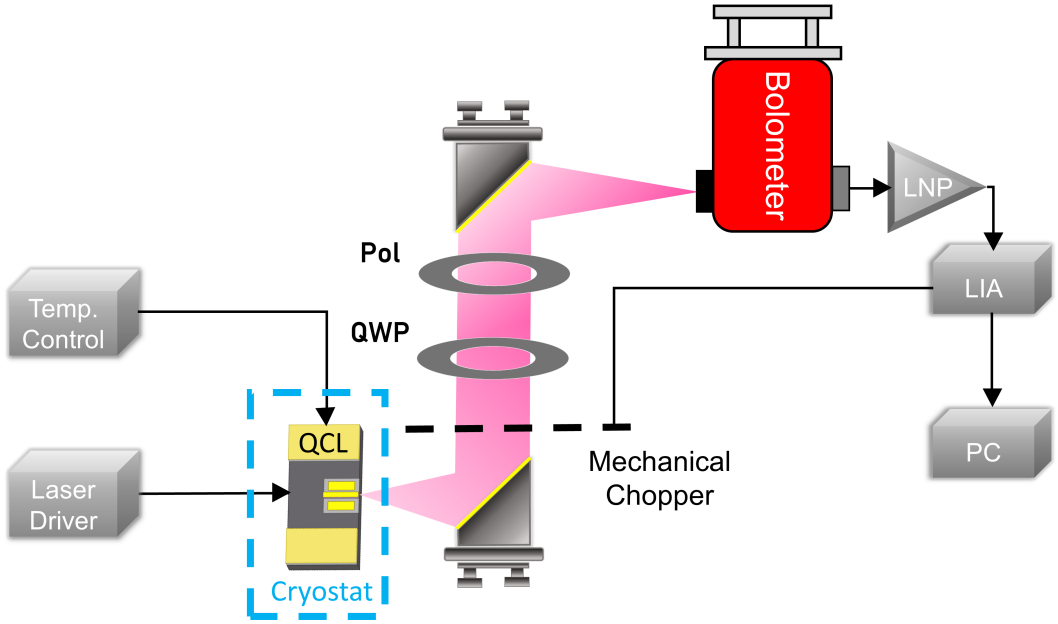

Figure 3.11: Schematic of the system setup of the Stokes measurements to assess the polarisation state of the QCL.

The results from the Stokes parameters measurements are summarised in table 3.1. Here the Stokes parameters have been normalised by dividing each parameter by the value of S_0.

Current, I (mA)	S_1	S_2	S_3	P
420	0.96	0	0.27	1
600	0.94	0	0.32	1
650	0.93	0	0.32	1
700	0.96	0	0.26	1

Table 3.1: Summary of the Stokes parameters of a THz-QCL for different driving currents.

At all driving currents the QCL is seen to maintain a high degree of polarisation ($P \approx 1$) and to contain a non-negligible degree of right circularly polarized light ($S_3 > 0$). The occurrence of a non-pure TM polarisation has similarly been observed in mid-infrared QCLs, where it has been attributed to residual birefringence

present in the QCL waveguide, resulting in a conversion of linear polarization into a circular polarization [219, 220]. The parameter $S_2 = 0$ indicates the polarization ellipse is orientated parallel to the QCL growth direction in all cases, yielding a polarisation ellipse with orientation angle $\tan(2\psi) = S_2/S_1$, thus $\psi = 0^o$. The ellipticity angle $\sin(2\chi) = S_3/S_0$ yielded a value of $\chi = 8^o$. This agrees well with the value obtained from the Jones analysis, where $\chi = 10^o$.

3.6 Microscopy of plasmonic modes using s-polarised excitation

In the previous measurements (section 3.4) the excitation beam was p-polarised. Alternatively, to reduce the signal compoment s_ε that depends only on the sample permittivity, and to directly excite plasmonic modes in structures, s-polarised excitation can be employed. To that end, a quartz zero-order half-wave plate (HWP), positioned in the beam path between the QCL and the near-field probe, was employed to control the incident polarization state in the system, as shown in Fig. 3.2. By aligning the fast axis at $\vartheta_{WP} = 45^o$ to the z direction, a predominantly s-polarized excitation beam can be generated from the predominantly p-polarised emission from the QCL. At the same time, this results in the p-polarized field scattered by the probe also being rotated such that the field reinjected to the QCL cavity becomes polarized perpendicular to the growth direction of the heterostructure. It is expected that such field components would not mix efficiently with the orthogonally polarized intracavity laser field and would therefore not generate a measurable SM voltage signal. Nevertheless, as shown in section 3.5, a full characterization of the polarization properties of the THz beam emitted by the QCL has revealed a small but non-negligible component of circularly polarized light. In this way, and as is demonstrated experimentally below, the linearly polarized reinjected field may mix with a non-negligible component of the QCL field, generating a small but measurable voltage perturbation via the SM effect.

To demonstrate the near-field mapping of in-plane resonant modes under s-polarized excitation, THz near-field images were recorded for different orientations of the HWP. Figure 3.12 shows a series of images acquired with a step size of 200 nm and sampling time of 200 ms for the dipole structure orientated with its axis along the y direction for wave plate angles in the range of $\vartheta_{WP} = 0^o$ - 45^o.

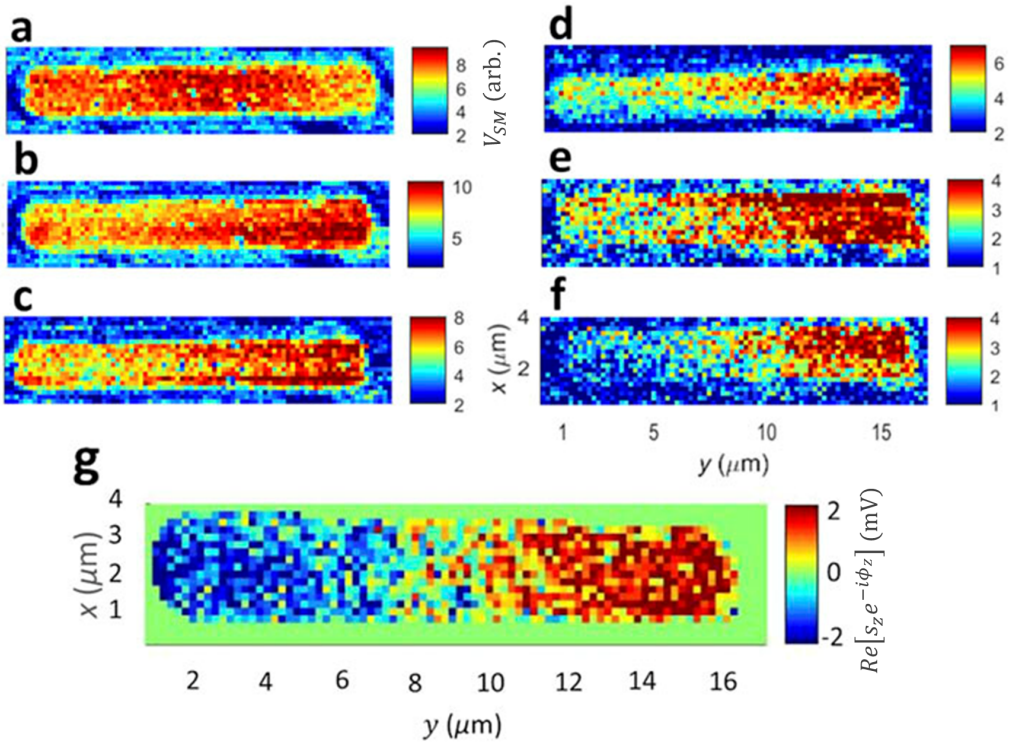

Figure 3.12: THz-s-SNOM images of an individual dipole antenna structure orientated with its axis along the y direction, acquired with the fast axis of the half-wave plate orientated at angles (a) $\vartheta_{\mathrm{WP}} = 0^{\mathrm{o}}$ (p-polarized), (b) 20°, (c) 30°, (d) 35°, (e) 40°, and (f) 45° (s-polarized) relative to the z direction. (g) Post-processed THz-s-SNOM image acquired with an s-polarized excitation beam, revealing only the out-of-plane field distribution supported by the sample under resonant excitation. The spatially homogeneous signal arising from the dipole interaction between the tip and the sample has been subtracted from the image. To improve visibility of the image features, the corresponding AFM image has been used as a mask to null the substrate signal outside the borders of the dipole antenna.

In each image, the measured signal is expected to follow Eq. 3.4 in which the relative size of the two terms is determined by the incident field components $E_\perp$ and $E_\parallel$, which, in turn, are controlled through ϑ_{WP}. With $\vartheta_{\mathrm{WP}} = 0^\mathrm{o}$, the incident field is p-polarized and $s_z = 0$. As such, this image captures only the local permittivity of the sample, which is spatially homogeneous within the metallic regions [see Fig. 3.12(a)]. Conversely, with $\vartheta_{\mathrm{WP}} = 45^\mathrm{o}$, the term s_ε is small and the image predominantly captures the out-of-plane field component associated with the plasmonic mode supported by the sample, E_z [see Fig. 3.12]. The use of s-polarised excitation is therefore seen to be effective in selectively exciting plasmonic modes in the sample while against retardation effects and, by virtue of the elliptically polarized QCL field, retains the capability of sensing the p-polarized radiation scattered to the far-field.

To further quantify the data presented in Figure 3.12, the parameter Γ is defined:

$$\Gamma = \frac{V_+ - V_-}{V_+ + V_-}. \tag{3.53}$$

Here V_+ and V_- represent the voltage signals measured at opposite ends of the dipole antenna, which are obtained by spatially averaging the respective signals across 10 pixel $\times$ 5 pixel regions of each image. According to this definition $\Gamma = 0$ for an image in which the contrast arises only from the sample permittivity. On the other hand, noting that the first-order plasmonic mode is characterised by field components E_z of equal magnitude but opposite sign at opposing ends of the structure (i.e. $V_+ = -V_-$; see Figure 3.8 (e)), $\Gamma = \infty$ for an image capturing only the resonant in-plane modal distribution. Figure 3.13 shows the results of this analysis for the series of images shown in Figure 3.12. As can be seen from the increasing value of Γ for increasing wave plate angles ϑ_{WP}, our experimental approach is effective at selectively exciting the plasmonic mode in the structure. However, the finite value of Γ obtained at $\vartheta_{\mathrm{WP}} = 45^\mathrm{o}$ indicates a signal component persists that arises from the dipole interaction between tip and sample and is sensitive to the local material permittivity.

The quantitative analysis of these images reveals a signal component s_ε persists even for an HWP angle $\vartheta_{\mathrm{WP}} = 45^\mathrm{o}$. This can be attributed to a combination of factors that cause the origin of the measured signals to deviate from the simplified description given above. First, the elliptically polarized QCL field has the effect of exciting the sample with non-vanishing p- and s-polarized field components

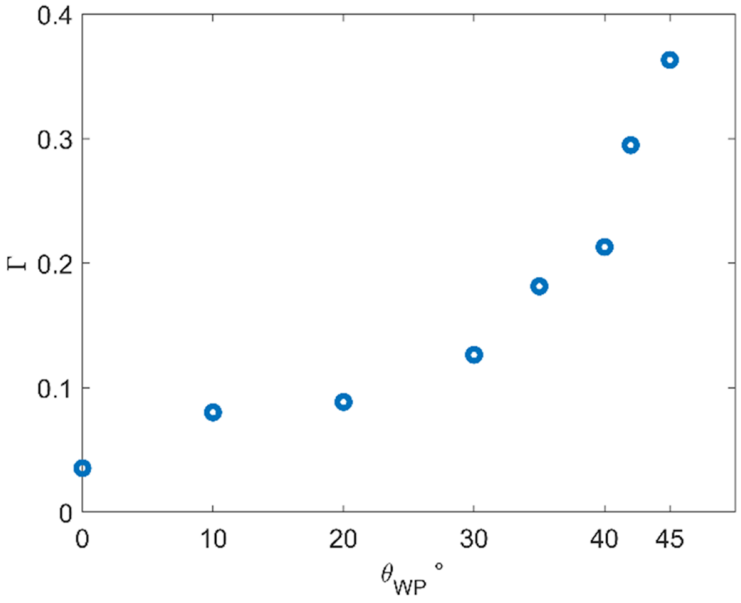

Figure 3.13: Values of the parameter Γ, calculated using Equation 3.53, for THz-s-SNOM images of an individual dipole antenna structure acquired with the fast axis of the HWP orientated at an angle $\boldsymbol{\vartheta_{WP}}$ relative to the z-direction.

irrespective of the wave plate orientation. This effect is further compounded by the imperfect nature of the HWP retardation, which acts to accentuate the polarization ellipticity in both the incident and reinjected fields. Nevertheless, it is noted that the field distribution associated with the in-plane plasmonic mode exhibits equal magnitude but opposite phase in opposite halves of the structure [i.e., $s_z e^{-i\phi_z}$ is spatially asymmetric; see, for example, Figs. 3.5(a), 3.5(b), and 3.8(e)] and will therefore spatially average to zero. As such, the signal component s_ε can be readily estimated from the spatial average of the signal recorded across all gold regions of the sample. Subtraction of this component from each pixel in the image then retains only a measurement of the out-of-plane field distribution supported by the sample under resonant excitation. The result of this post-processing is shown in Fig. 3.12(g) and shows excellent agreement with simulations.

It should be noted that the spatial resolution determined from Fig. 3.2(d) for imaging dielectric contrast in samples is not replicated when imaging out-of-plane field distributions, as shown in Fig. 3.12(g).This possibility arises first from the distinct physical mechanisms, giving rise to these two signal components, which may influence the spatial variation of the measured signal differently, particu-

larly at sample edges and near material boundaries [94, 210, 211]. Furthermore, typically weaker THz field enhancements are supported by resonator structures under s-polarized excitation compared to at the apex of the scattering tip under p-polarized excitation. This results in a smaller signal-to-noise ratio (SNR) when imaging the out-of-plane field distributions, which may, in turn, limit the practical spatial resolution of these measurements. Nevertheless, our measurements provide some insight into the relative size of this signal. From Fig. 3.12(a), we obtain a signal magnitude of $s_\varepsilon \sim 7.8$ mV arising from the local sample permittivity with p-polarized excitation. This is compared to a maximum signal magnitude of $s_z \sim 1.5$ mV obtained with s-polarized excitation from Fig. 3.12(g). Although slightly smaller, this value suggests that an adequate SNR is retained, sufficient for deep sub-wavelength mapping of the field distributions associated with in-plane resonator modes. This is also borne out by the quality of the images obtained in Figs. 3.8 and 3.12. However, further measurements would be required to obtain a quantitative estimate of this spatial resolution. For this purpose, resonator structures supporting modes that are both well-defined spatially and are confined on sub-micron scales would be desirable.

3.7 Coherent THz-s-SNOM of microscale resonators

The coherent mixing process between reinjected and laser cavity fields in the SM scheme offers the possibility of electronically capturing both the magnitude and the phase of the scattered field, E_{scat}. In this section this is demonstrated using a measurement approach adapted from coherent far-field THz imaging [71] and recently applied to the coherent microscopy of a phonon-polariton-resonant crystal [167]. Self-mixing interferometric fringes can be obtained by varying the drive current through the QCL which tunes the emission frequency, and recording the self-mixing voltage for each value of the drive current. An example of interferometric fringes obtained for gold and KBr regions of a Au/KBr sample is shown in Fig. 3.14. In addition to offering reduced experimental complexity compared to alternative approaches based on the mechanical extension of the optical beam path [204], electronic modulation schemes have been demonstrated to enable faster acquisition in far-field THz imaging and also to improve phase stability significantly owing to the associated reduction in the slow thermal drift of the QCL emission

frequency [70].

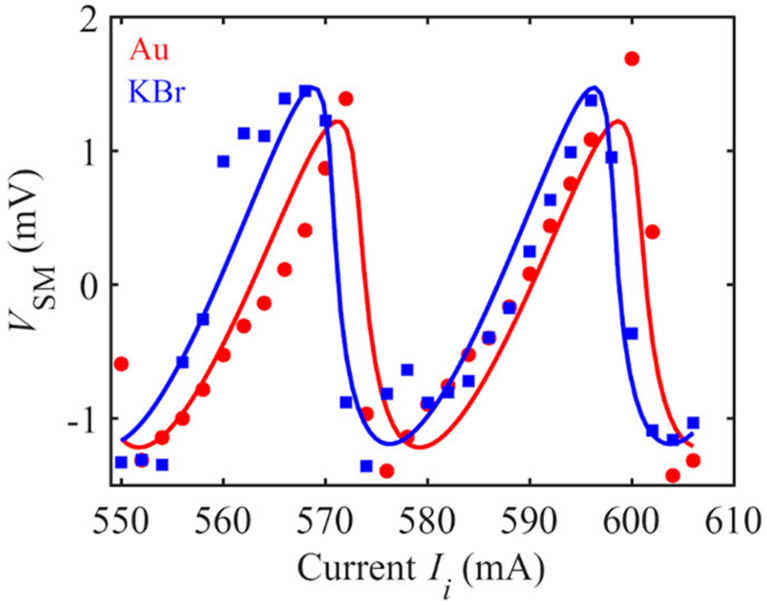

Figure 3.14: Interferometric fringes obtained for gold (red circles) and KBr (blue squares) regions of a Au/KBr sample, showing a phase contrast arising from the phonon mode of KBr in the THz frequency band. The solid lines show fits of the data to Eq. 3.3 (in this case $s_z = 0$). Figure reproduced from [167].

3.7.1 Theoretical description of the self-mixing voltage in coherent s-SNOM measurements

For coherent s-SNOM measurements the self-mixing voltage is described by Eq. 3.3, but in which the laser emission frequency is controlled through the laser driving current I according to the relationship

$$\nu = \nu_0 + \Delta\nu = \nu_0 + \gamma(I - I_0) \tag{3.54}$$

in which γ is the current tuning coefficient and ν_0 is the emission frequency of the solitary laser at a drive current I_0. By substituting Eq. 3.54 and expressing Eq. 3.3 as a Fourier series to first order in $\tau = 4\pi L_{ext}/c$, V_{SM} can be written as

$$\begin{aligned} V_{SM} &= a_1 \cos(\frac{4\pi L_{ext}\Delta\nu}{c}) + b_1 \sin(\frac{4\pi L_{ext}\Delta\nu}{c}) \\ &= c_1 \exp(\frac{i\,4\pi L_{ext}\Delta\nu}{c}) + c_{-1} \exp(\frac{-i\,4\pi L_{ext}\Delta\nu}{c}) \end{aligned} \tag{3.55}$$

where, after noting that the phase $\phi_\varepsilon = 0$ for radiation frequencies far away from any phonon or bulk plasmonic material resonances,

$$a_1 = s_\varepsilon + s_z \cos\phi_z \tag{3.56}$$

and

$$b_1 = s_z \sin\phi_z \tag{3.57}$$

and the complex amplitude coefficients,

$$c_{\pm 1} = \frac{a_1}{2} \pm i\frac{b_1}{2} = s_n e^{\pm i\phi n}. \tag{3.58}$$

The magnitude s_n and phase ϕ_n of the complex amplitude of the SM fringes can thus be obtained experimentally through complex Fourier analysis of the SM voltage signals measured as a function of driving current. Specifically, these are obtained from the relations

$$s_n = |\mathcal{F}(\tau)| \tag{3.59}$$

and

$$\phi_n = \arctan(\mathcal{I}[\mathcal{F}(\tau)]/\mathcal{R}[\mathcal{F}(\tau)]) \tag{3.60}$$

where $\mathcal{F}(\tau)$ is the complex Fourier transform of the voltage signal evaluated at the fundamental (positive) fringe periodicity τ. By exploiting the spatial asymmetry of the term $s_z e^{-i\phi_z}$, the spatially constant parameter s_ε can be obtained from the spatial average of the complex amplitude c_1. The amplitude s_z and phase ϕ_z can then be obtained at each pixel using the relations $s_z = \sqrt{(a_1 - s_\varepsilon)^2 + b_1^2}$ and $\phi_z = \arctan(b_1/(a_1 - s_\varepsilon))$.

3.7.2 Coherent THz-s-SNOM of microscale resonators

Coherent microscopy of both the amplitude and phase of the out-of-plane electric fields supported by THz-frequency micro-resonators was demonstrated experimentally using the DA structures. Successive images were acquired with the QCL driving current being stepped incrementally in the range of $598 - 704$ mA with a step of 1 mA. Over this operating range the QCL emits on a single longitudinal

cavity mode that tunes over a frequency range $\sim$ 900 MHz, corresponding to $\sim$ three interferometric fringes in the SM voltage signal. For these coherent measurements, images were acquired with a pixel sixe of 200 $\times$ 200 nm, a sampling time of 200 ms, and with the lasing frequency being tuned electronically by $\sim$ 9 MHz between successive raster scans of the sample. For each image pixel, a series of interferometric fringes in the $n = 3$ harmonic of the demodulated SM voltage signal was thereby obtained. The magnitude of the complex amplitude of the fringes can then be calculated on a pixel-by-pixel basis using Eq. 3.59 and the phase using Eq. 3.60 [70]. Figures 3.15(a) and 3.15(b) show the magnitude and phase determined in this way and spatially averaged across three adjacent rows of pixels spanning the long axis of the dipole structure.

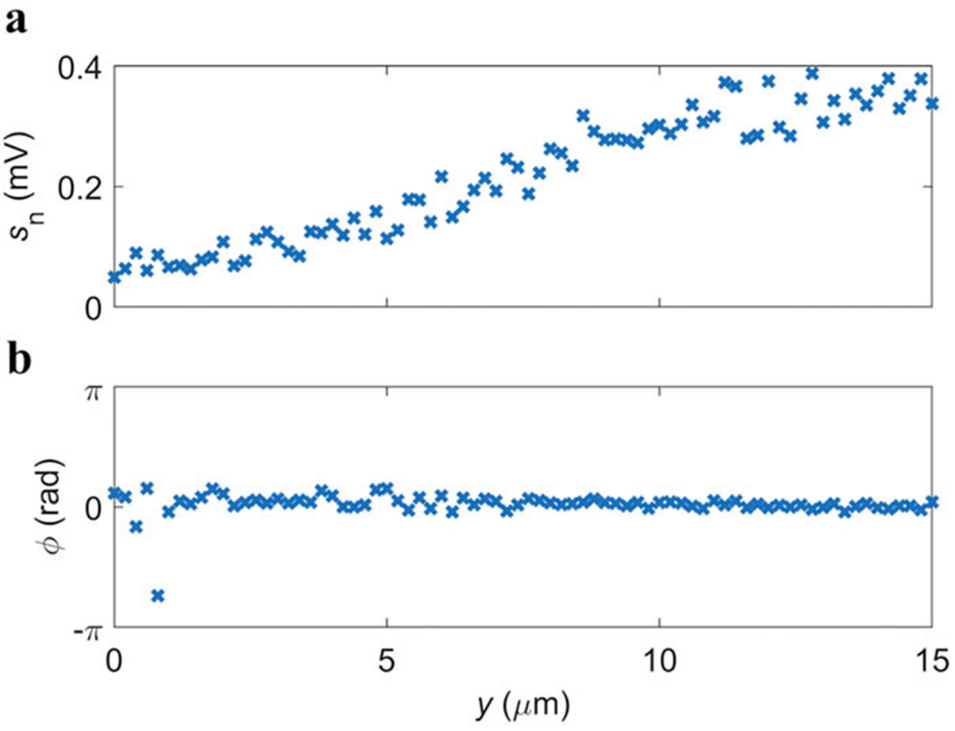

Figure 3.15: (a) Magnitude and (b) phase of the SM voltage interferograms obtained from coherent THz-s-SNOM measurements along the long axis (y direction) of an individual dipole antenna. The step size is 200 nm.

Similarly to the images shown in Fig. 3.12, a non-negligible signal component arising from the dipole interaction between the tip and the dielectric sample is evident, which can be quantified from the spatial average of the complex amplitude recorded across all gold regions of the sample, as described previously. Finally, the

magnitude s_z and phase ϕ_z of the signal component associated with the plasmonic mode can be isolated for each pixel in the image. The results of this analysis are shown in Fig. 3.16. For comparison, the magnitude and phase of the out-of-plane electric field component E_z associated with the plasmonic mode, calculated from FEM simulations, are also shown. Excellent agreement is obtained between measurement and simulation, with the principal characteristics of the first-order dipolar plasmonic mode being faithfully captured by our coherent near-field measurement approach.

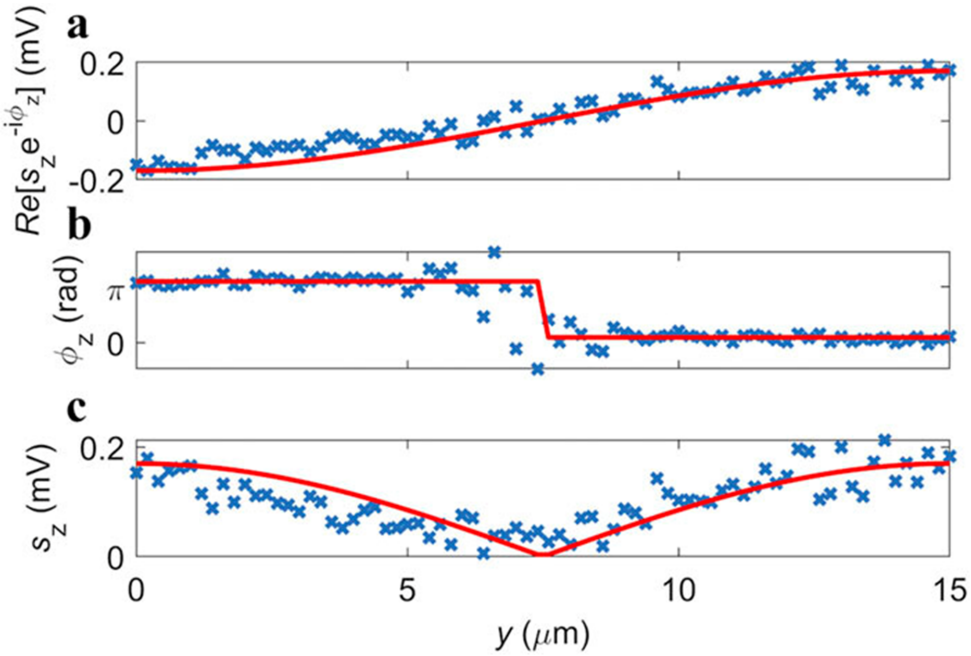

Figure 3.16: (a) Real part $\mathcal{R}[s_z e^{-i\phi_z}]$, (b) phase ϕ_z, and (c) magnitude s_z of the signal component corresponding to the out-of-plane field associated with the plasmonic mode excited in the dipole antenna structure. Blue dots: experimental data obtained from coherent THz-s-SNOM measurements along the long axis (y direction) of the resonator. Red line: corresponding real part, phase, and magnitude values for the out-of-plane field obtained from simulations.

3.8 Conclusion

In summary, coherent THz near-field microscopy was demonstrated using a QCL as both the THz source and the coherent detector. This approach provides a deep sub-wavelength spatial resolution of ~ 35 nm, enabling the high-resolution imaging of individual micro-resonator structures at frequencies beyond the typical ~ 2 THz bandwidth of pulsed THz systems. Through control of the polarization state of the excitation beam, the selective excitation and spatial mapping of in-plane resonant modes supported by SRR and plasmonic dipole antenna structures was demonstrated while suppressing phase retardation effects and reducing the otherwise dominant signal arising from the local material permittivity. Central to this scheme is the imperfectly linear polarized state of the QCL field, which can be exploited to enable sensitive detection of the field scattered from the s-SNOM tip through the SM effect in these lasers. Furthermore, a coherent measurement approach was developed, adapted from coherent far-field THz imaging, to simultaneously resolve both the magnitude and the phase of the scattered field. This approach has been applied, for the first time, to the spatial and coherent mapping of the out-of-plane field associated with THz plasmonic resonances, showing accurate agreement with FEM simulations of these plasmonic modes. The new coherent THz near-field imaging technique can open the way for the future design and optimization of novel THz optoelectronic devices and sensors based on subwavelength resonators and associated metamaterials, as well as the nanoscale mapping of THz plasmons and phonon polaritons in emerging 2D materials.

Chapter 4

Terahertz microscopy of SSPPs on asymmetric planar waveguides

4.1 Introduction

In Chapter 3 it was shown that metamaterials can be designed to support spoof localised surface plasmons. It was shown that the resonant frequency of the free-space beam illuminating the structure depends mainly on the geometry of the structure and the dimensions of its features. Metamaterials also serve as building blocks for the design of plasmonic waveguides. Theoretical studies of metamaterial waveguides in the millimetre-wave frequency regime include periodically corrugated wires [221], wedges [222], channels [223], periodic chains of dominoes [137] or metal-insulator-metal waveguides [224]. Spoof surface plasmon polaritons (SSPPs) have also been demonstrated experimentally to propagate on helically grooved wires [225] and periodic chains of dominoes [226, 227]. SSPPs can also propagate along ultrathin films that can be curved and bent. Initially proposed in [136], conformal surface plasmons (CSPs) are supported by ultrathin films whose propagation adapts to the curvature of the surface. The CSP modes are realised using nearly zero-thickness (e.g. 100 nm) metal strips printed on flexible, ultrathin dielectric films. This allows the design of flexible plasmonic circuits which can be bent, twisted, or folded. When the thickness of this structure approaches infinity, the structure reduces to a 1D array of grooves [228]. Similar to the case of the domino plasmons [226], the mode dispersion is quite insensitive to the thickness of the structure [136]. In addition, CSPs have been shown to exist at microwave, terahertz, and mid-infrared frequencies, and are confined

at a deep subwavelength scale, suffering little radiation losses at sharp edges and corners [136]. Therefore, the CSP waveguides can be wrapped on curved surfaces and objects, which poses advantages over devices integrated on traditional rigid wafer-based substrates [118]. These features make the CSP waveguides promising for applications in plasmonic circuits. One interesting configuration of two coupled CSP waveguides is shown in [229, 230], where the strong coupling between two waveguides results in spoof plasmon bands of negative refractive index. Recent advances on CSP circuitry on ultrathin metal films in the microwave and millimtre-wave frequency regimes have provided a wide range of planar waveguide devices [231], such as multi-band waveguides [232, 233], broadband converters from guided waves to CSPs [234], ultra-wideband beam splitters [235], stripe planar antennas [236], frequency selective devices [237], ultra-wideband and low-loss filters [238–241], 90-degree bends [242], on chip sub-terahertz surface plasmon polariton transmission lines in CMOS [243], spoof plasmon amplification [244], trapping of spoof surface plasmons with corrugation of non-uniform depth [245, 246], stopbands in CSP waveguides with capacitively coupled unit cells [247], multilayer propagation [248], beam steering [249] or second harmonic generation [250]. CSPs have also been shown to suppress interference in compact spaces, which potentially solves the challenge of signal integrity [239]. CSPs propagating in structures with non-rectangular grooves have also been studied [251, 252].

In this work, a metamaterial waveguide is proposed that supports terahertz-frequency planar surface plasmons (PSPs), which are a specific type of spoof surface plasmon polaritons (SSPPs). They are called PSPs because the nearly-zero thickness structure which supports CSPs is now placed on a rigid substrate such as silicon. Initially, the structure was designed in ANSYS HFSS and its dispersion relation was obtained using an eigen-mode solver. Next, a waveguide with finite length was simulated using excitation ports at the two ends of the structure to launch and detect the SSPPs propagating on the waveguide. The out-of-plane electric field E_z was visualised and its amplitude and propagation length values were obtained. The S_{21} Parameters, the cut-off frequency, and the reflection coefficient of the waveguide structure were also obtained. Furthermore, the waveguide was simulated using a free-space beam which showed a different coupling of light to SSPPs on the waveguide compared to the simulations with an excitation port. The effects of varying the beam direction, the polarisation and the angle of incidence were investigated. A grating structure has been designed and optimised to improve the coupling strength of light to SSPPs on the waveguide. The structures

were then fabricated on a silicon substrate using photo-lithographic and metallic deposition techniques. A QCL was used to illuminate the structures with an incident frequency of 3.45 THz and the s-SNOM system was used to measure the out-of-plane electric field E_z. The results from the simulations and the experiments are directly compared and show a good agreement between the two. The results in this chapter show successful mapping of the spatial distribution of the electric field associated with the THz-frequency SSPPs propagating on the PSP waveguide with sub-wavelength resolution for the first time.

4.2 Design of PSP waveguide structures

The waveguide has a comb-shape as shown in Fig. 4.1 (a, inset) and consists of metal strips of thickness t and width w, in which a periodic array of grooves is patterned. This structure design is adapted from [136] where experimental results of this structure were reported at microwave frequencies. The period of the array is d which is treated as the unit length, and the width of the groove is a. The material used to form the plasmonic waveguide was gold and it was placed on a silicon substrate with a dielectric constant of $\varepsilon = 11.65$. This value was obtained experimentally using THz-TDS on the float-zone (FZ) silicon substrate. The dispersion relation for the fundamental mode of the TM-polarised waves propagating along the x-direction with momentum k_x was numerically calculated using the eigenmode solver in ANSYSS HFSS and is presented in Fig. 4.1 (a). A unit cell of the waveguide was considered, periodic boundaries were used in the x-direction and PEC boundaries in the y-direction. By sweeping the phase difference $\Delta\theta$ of the EM fields at the opposite boundaries in the x-direction from 0° to 180°, the eigen-frequencies of the spoof surface plasmon polaritons (SSPPs) are calculated within the first Brillouin zone [253]. The dispersion relation of the PSP waveguide deviates significantly from the light line as shown in Fig. 4.1 a, indicating that the corrugated metal supports the propagation of confined modes. The dispersion curve exhibited SPP-like behaviour, presenting an asymptote controlled mainly by the parameters h and t. For $t \to \infty$, the initial mode appears at $\omega_c = \frac{\pi c}{2h}$, which dictates the asymptote frequency of the PSP mode [136]. The electric field points along the $z-$direction (see Fig. 4.1 (b)) and the magnetic field is directed along the $x-$direction. As t decreases, the magnetic field remains unquantised in the $x-$direction. This is why the dispersion relation is insensitive to the metal thick-

ness [136]. The parameter d dictates the cut-off frequency of the waveguide. The smaller the value of the period d, the greater the value of the waveguide cut-off frequency. In addition, the parameter a also affects the cut-off frequency of the waveguide. A greater value of a leads to a higher cut-off frequency and a lower value of a leads to a lower cut-off frequency.

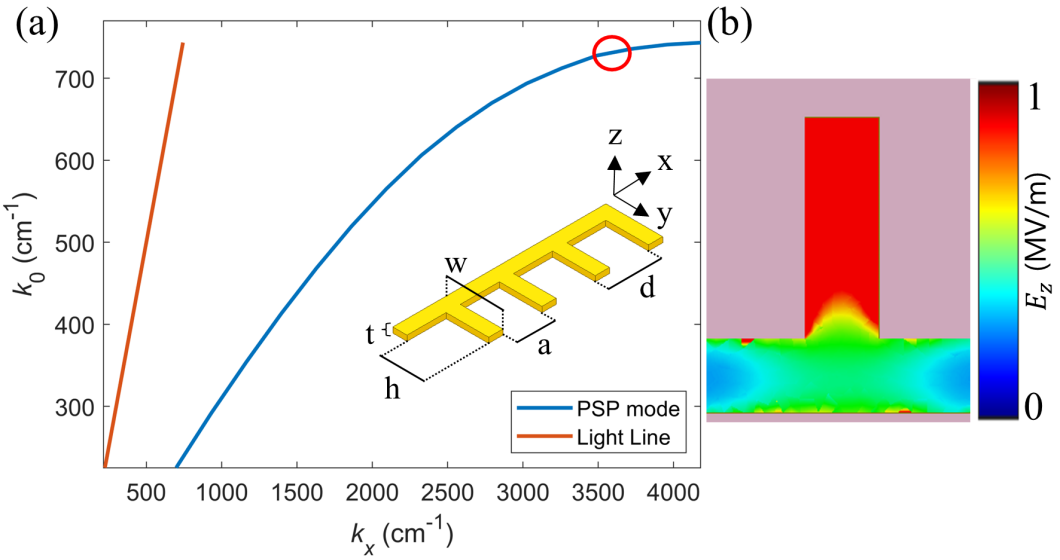

Figure 4.1: Dispersion relation and local field distribution of the comb-shaped PSP waveguide. (a) Dispersion relation for the fundamental PSP mode. (inset) Geometric parameters of the structure, with w = 1.07d, a = 0.73d and h = 0.8d, where d = 7.5 µm. The waveguide material was gold with thickness of 100 nm resting on a silicon substrate with thickness of 50 µm. (b) Amplitude (modulus) of the electric field in the z-direction of a unit cell (normalised) obtained using FEM.

The radiation emitted from the QCL in the experimental system is 3.45 THz. Therefore, the waveguide was designed with parameter values that allow the free-space beam to launch SSPPs on the surface of the waveguide with deep subwavelength confinement. The values of w and h were set to provide deep sub-wavelength confinement with the SSPP wave-vector being much greater than the one of the incident beam with frequency 3.45 THz. The waveguide was designed this way in order to increase the amplitude of the SSPP component obtained experimentally using the s-SNOM system. However, there is a trade-off between strong field confinement and propagation length [136]. The waveguide was designed with period $d = 7.5$ µm, groove width $a = 5.5$ µm, width $w = 8$ µm, height $h = 6$ µm, and thickness $t = 0.1$ µm. The cut-off frequency of the waveguide was $f_c \approx 3.6$ THz.

The wave-vector of the SSPP (k_x) is related to the parameter $\Delta\theta$ whose value is obtained from the eigen-mode simulation for an incident frequency of $f_0 = 3.45$. The relation between the two parameters is $k_x = (\pi\Delta\theta)/(180\,d)$ which yields a value of $k_x = 3500$ cm^{-1}. The SSPP wavelength λ_{SP} is related to the SSPP wave-vector according to the relation: $\lambda_{SP} = 2\pi/k_x$. This leads to a value of $\lambda_{SP} = 18$ µm, corresponding to $\sim \lambda_0/5$.

4.3 Simulation using excitation ports

To calculate the out-of-plane electric field E_z and the S_{21} Parameters of a finite waveguide, a new simulation environment was setup in ANSYS HFSS. The asymmetric PSP waveguide was designed with length of 208 µm and 27 repetitions of the unit cell with periodicity $d = 7.5$ µm. Two wave ports were used at the beginning ($x = 0$) and the end ($x = 208$) µm of the waveguide to launch SSPs on the structure and also obtain the S_{21} Parameters. Open boundaries were used for the simulation using the radiation boundary in HFSS. A schematic diagram of the simulation setup showing the waveports which excite and detect the SSPPs coupled on the waveguide is presented in Fig. 4.2.

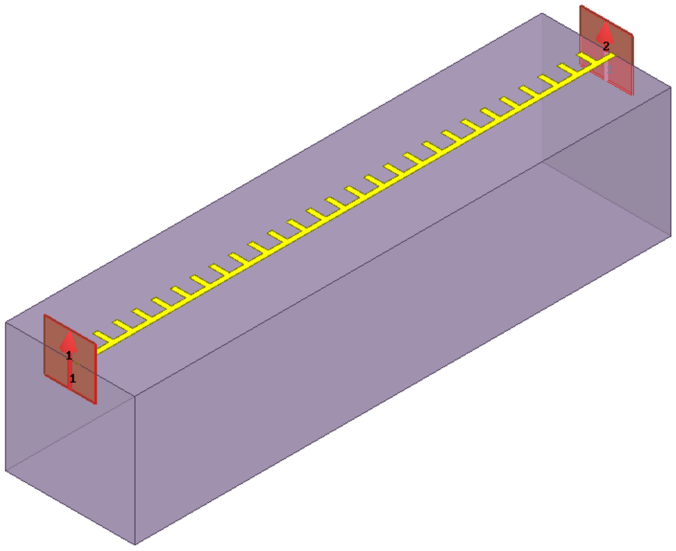

Figure 4.2: Simulation setup of the PSP waveguide using two waveports to launch (port 1) and detect (port 2) the SSPPs propagating on its surface.

The real component of the out-of-plane electric field on the surface of the waveguide is shown in Fig. 4.3, for an excitation frequency of 3.45 THz. From the figure it can be observed that the electric field oscillates from $(+E_z)$ to $(-E_z)$ along the $x-$direction. This can be seen by the variation of the phase of the electric field across the structure. In addition, the electric field decays with distance x, owing to the propagation losses that occur due to ohmic losses in the metal.

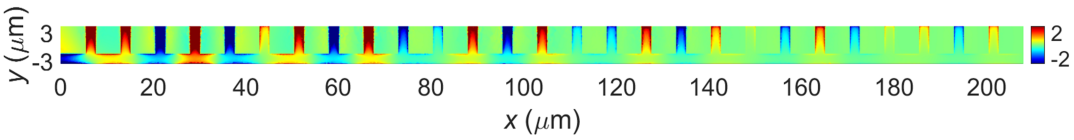

Figure 4.3: Real part of the out-of-plane electric-field component E_z (MV/m) confined on the surface of the asymmetric waveguide with length, $L = 208$ µm.

In order to quantify the field strength associated with the SSPPs as they propagate along the waveguide, the average electric-field E_z was spatially averaged within each bar of the waveguide. These averaged values were then plotted as discrete points as a function of the distance x along the waveguide, as shown in Fig. 4.4. Each average value was assigned at the centre point of its respective bar in the x direction. To determine the wavelength and propagation length of the SSPPs the data in Fig. 4.4 was numerically fit to the equation 4.1. The SSPPs are modeled as propagating waves bound to the surface of the metallic waveguide layer, which has an out-of-plane electric field E_z, wave-vector k_x, and propagation length L_p. A time-independent, single-mode sinusoidal function is used to fit the data with amplitude E_0 which represents the electric field value at $x = 0$, wave-vector k_x which represents the SSPP wave-vector, and phase θ. The sinusoidal function is multiplied by an exponentially decaying function to model the decay of the SPPs as they propagate along the structure with propagation length L_p.

$$E_z = E_0 \cos(k_x\, x - \theta)\, \exp\left(\frac{-x}{L_p}\right), \tag{4.1}$$

The parameter values obtained from this fitting procedure are: $E_0 = 11$ MV/m, $k_x = 3350$ cm^{-1}, $\theta = 1.2$ rad, and $L_p = 75$ µm. The value of E_0 which is measured in MV/m is arbitrary since it depends on the excitation field strength set in the simulation environment. In addition, the wavelength of the SSPP is calculated to be $\lambda_{SP} = 2\pi/k_x \approx 18.75$ µm. This concurs with the SSPP wavelength obtained from the dispersion relation shown in Fig. 4.1 a, which predicts a wavelength value

of $\lambda_{SP} = 18$ µm at 3.45 THz. The small difference in the wavelengths between the two simulations is attributed to the finite meshing of the simulations and the error tolerance of the simulation software. In addition, the electric field within each bar in not uniformly distributed and therefore the data points in Fig. 4.4 do not fully capture the level of detail as compared to the eigen-mode solver simulations. Figure 4.4 demonstrates that Eq. 4.1 fits the simulation data very nicely.

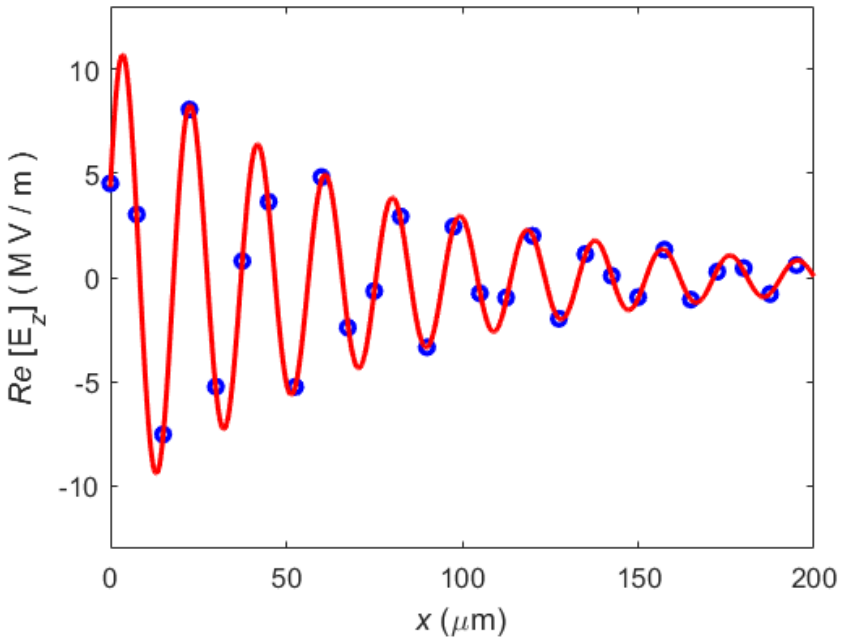

Figure 4.4: Analysis of the SSPP coupled on the PSP waveguide. The data were extracted from the simulation and the average field value of each bar was calculated. The extracted values of the fitting parameters yield: $E_0 = 11$ MV/m, $k_x = 3350$ cm^{-1}, $\theta = 1.2$ rad, and $L_p = 75$ µm.

To obtain the S_{21} Parameters of the PSP waveguide, a waveguide was simulated with length $L = 73$ µm consisting 9 repetitions of the unit cell, which is smaller than the propagation length of the SSPP. The real part of the out-of-plane electric field coupled on the surface of the waveguide is shown in Fig. 4.5. From the figure it can again be observed that the electric field oscillates from $(+E_z)$ to $(-E_z)$ along the $x-$direction. This can be seen by the variation of the phase of the electric field across the structure.

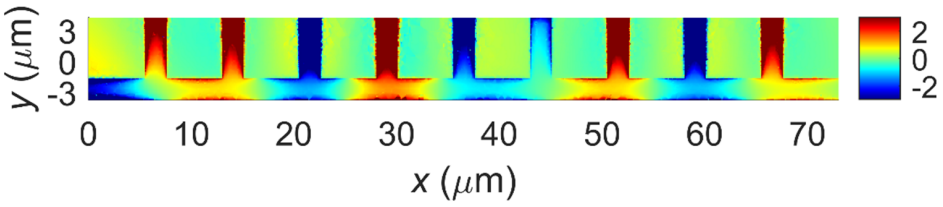

Figure 4.5: Real part of the out-of-plane electric-field component E_z (MV/m) confined on the surface of the asymmetric waveguide with length, $L = 73$ µm.

The S_{21} Parameters obtained for the waveguide with length of 73 µm is shown in Fig. 4.6. It is observed that at frequency of 3.45 THz, the transmitted power has been attenuated by ~ 10 dB. A cut-off frequency of $f_c \approx 3.6$ THz is observed, where the transmitted power is attenuated by ~ 25 dB. The effect of the cut-off frequency arises due the nature of the waveguide which behaves as an optical low-pass filter. For incident frequencies which lead to the SSPP wave-vector $k_x > \pi/d$, the Bragg reflection regime is entered, in which no propagating mode exists, and a guided wave entering the waveguide decays owing to optical reflection [254].

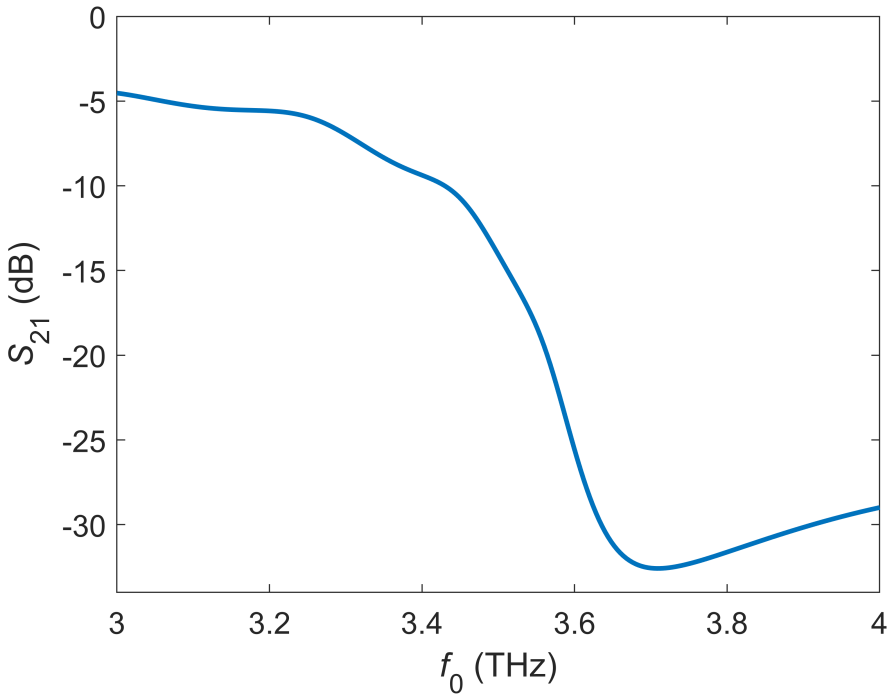

Figure 4.6: S_{21} Parameters of the asymmetric waveguide with length $L = 73$ µm.

4.4 Reflection of SSPPs in waveguide structures

When the length of the waveguide is 73 µm, it is observed from Fig. 4.5 that a significant amount of energy reaches the end of the waveguide. Due to the impedance mismatch experienced by the SSPP at this boundary, a reflection will occur, causing a portion of the SSPP to propagate back towards the energy source. This leads to the formation of a standing wave due to interference between incident and reflected propagating SSPPs. The reflected SSPP will affect the out-of-plane electric field E_z along the waveguide. To determine the reflection coefficient R, three simulations were run with three different lengths of the waveguide: 70 µm; 73 µm; and 75 µm. This difference of 5 µm in the waveguide length corresponds to a $\sim \lambda_{SP}/4$ change based on the calculated SSPP wavelength $\lambda_{SP} \approx 18.75$ µm. The change in the waveguide length changes the phase of the SSPP when it reaches the end of the waveguide. In turn, this affects the size of the final field maximum, due to constructive and destructive interference that occurs between the incident and reflected SSPPs. This field maximum oscillates from a maxima when the waveguide length $L = n\lambda_{SP}/4$ to a minima when the waveguide length $L = n\lambda_{SP}/2$, where n is an integer and the period of the field maximum is λ_{SP}. The amount by which the field maximum changes will depend on the reflection coefficient R. By matching the amount the field maximum changes in the simulations with Eq. 4.2 the value of R can be determined. This equation describes the out-of-plane electric field component E_z as a standing wave consisting an incident and a reflected wave:

$$E_z = E_0 \left(\sin\left(\frac{2\pi}{\lambda_{SP}} + \theta\right) \exp\left(\frac{-x}{L_p}\right) + R \sin\left(2\pi \frac{2L - x}{\lambda_{SP}} + \theta\right) \exp\left(\frac{-(2L - x)}{L_p}\right)\right), \tag{4.2}$$

where E_0 is the amplitude of the SSPP, λ_{SP} is the wavelength of the SSPP, θ is the phase of the SSPP launched at $x = 0$, L_p is the propagation length, and L is the length of the waveguide. Equation 4.2 is used to fit the data obtained from the simulations for the three different lengths of 70 µm; 73 µm; and 75 µm. For small values of R, the three lengths demonstrate almost the same out-of-plane electric field E_z distribution. For large values of R, the electric field E_z varies significantly at the end of the waveguide for the three different lengths. Therefore, the value of R was determined by changing its value to fit the simulation data using Eq. 4.2. Figure 4.7 shows how the Eq. 4.2 fits the simulation data for the three different waveguide lengths and with a reflection coefficient $R = 0.3$, or 30% in each case.

This value will be important for interpreting simulation data in following chapters.

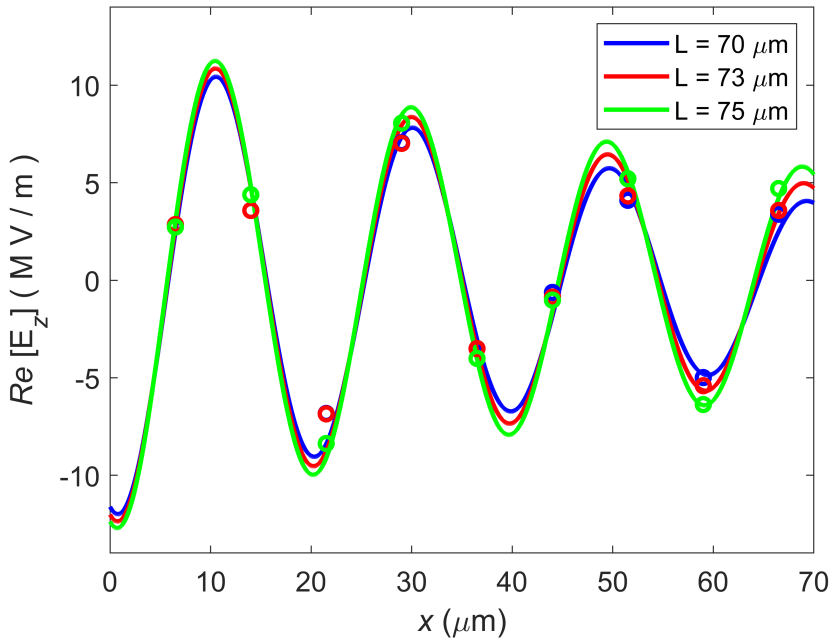

Figure 4.7: Fits of the simulation data for the asymmetric waveguide with lengths: $L = 70$ µm; $L = 73$ µm; and $L = 75$ µm, using Eq. 4.2. The SSPP wavelength used to fit the data was $\lambda_{SP} = 19.4$ µm and the propagation length was $L_p = 75$ µm. By varying the reflection coefficient R to fit the simulation data, a value of $R = 0.3$ was determined.

4.5 Free-space excitation under normal incidence

4.5.1 Parallel Polarisation

In this section the excitation of SSPPs on PSP waveguides using a free-space beam is studied, and the effect of the beam polarisation is investigated. A simulation environment was created in ANSYS HFSS to simulate the PSP waveguide illuminated with a free-space beam. The design parameters of the waveguide are identical to those in Section 4.2. The structure was placed on a silicon substrate with thickness $t = 50$ µm and a dielectric constant of $\varepsilon_r = 11.65$. To define the simulation boundaries, perfectly-matched layers (PML) were used to absorb reflections of the incident and scattered fields at the boundaries of the simulation. Hence, the PML boundaries resemble a free-space simulation in infinite space. Furthermore, an incident plane wave was defined above the structure originating at a distance of $2\,\lambda_0 = 174$ µm away from the silicon substrate and frequency of 3.45 THz propagating towards the waveguide under normal incidence and with its electric field polarisation parallel to the waveguide axis ($x-$direction). Fig. 4.8 shows the direction and the polarisation of the free-space beam.

The free-space simulations of the PSP waveguide demonstrated a different behaviour to the simulations in which the structure was excited using an excitation port at the start ($x = 0$) of the waveguide. This is because when a free-space beam is used, SSPPs may be excited at both ends of the waveguide. For a waveguide shorter than a few propagation lengths, the two SSPPs launched at the two ends of the structure will meet at its centre. To analyse the coupling of SSPPs on the surface of the structure using a free-space beam, a structure with length $L = 208$ µm was simulated using the described free-space simulation setup. This waveguide length ensures that only minimal energy reaches the opposite end. The coupling strength of the free-space beam to SSPPs on the waveguide is compared for the two ends of the waveguide in which SSPPs are launched. Due to the symmetry of the structure, it is expected that the coupling strength and the propagation length of the SSPPs would be identical on both sides. The real part of the out-of-plane electric field component E_z obtained from the simulations is shown in Fig. 4.9 (a). From the figure, it is observed that two separate SSPPs are launched at each end of the waveguide, oscillating from maxima ($+E_z$) to minima ($-E_z$), and propagating towards the centre of the waveguide, as expected. Furthermore, these results show that a free-space beam with parallel polarisation to the waveguide axis can be used

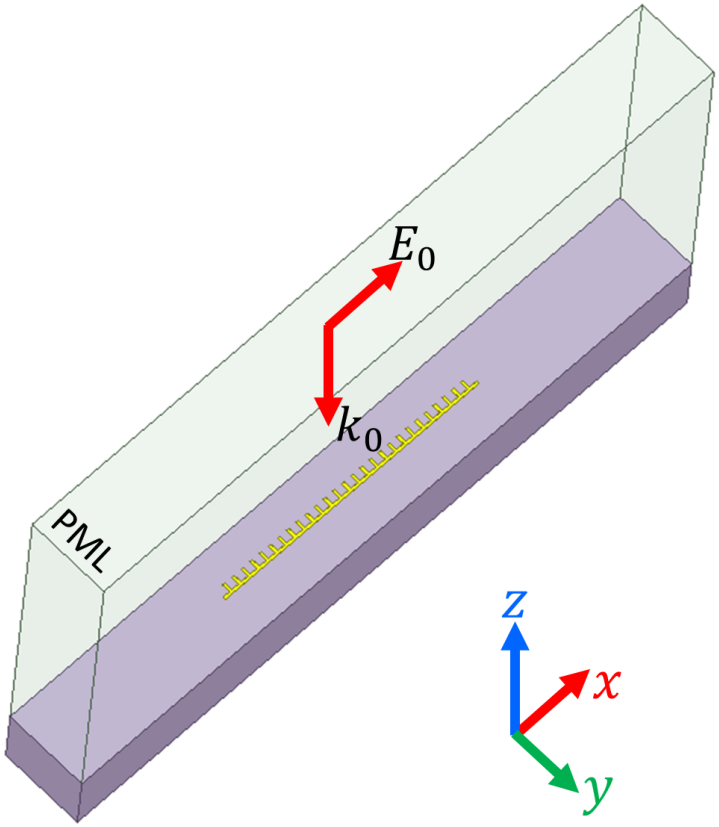

Figure 4.8: Simulation setup of the asymetric waveguide structure placed on a silicon substrate. The incident wave is defined 174 µm above the waveguide. E_0 illustrates the polarisation orientation and k_0 illustrates the direction of the free-space beam propagating towards the waveguide under normal incidence.

to excite SSPPs on the designed PSP waveguide. The out-of-plane electric field E_z is shown to be weakest at the centre of the waveguide. This is due to the finite propagation length of the SSPPs which has been predicted to be 75 µm from the simulations which use a waveport excitation. The interference between the two SSPPs is expected to be strongest at the centre of the waveguide. Furthermore, the incident beam with parallel polarisation causes the individual bars to be polarised along the polarisation direction, causing an additional spatial variation of the field on the surface of each bar. However, the average value of the electric field on each bar caused by that variation would result to zero, therefore this effect will not affect the analysis of the SSPPs launched on the waveguide.

To further analyse the electric field associated with the SSPPs launched on the waveguide, an average value of the electric field was obtained for each bar.

Furthermore, the waveguide was split into two parts, the left part and the right part. The SSPPs launched on the two parts of the waveguide are treated as two separate waves, the left wave and the right wave. Equation 4.1 is used to fit the data of each wave. In this way, the coupling strength of the free-space beam on both ends of the asymmetric PSP waveguide can be compared. The out-of-plane electric field on the left part of the waveguide, along with a fit to Eq. 4.1 is shown in Fig. 4.9 (b). The out-of-plane electric field on the right part of the waveguide, along with a fit to Eq. 4.1 is shown in Fig. 4.9 (c). In the latter case the variable x was substituted for $(L - x)$, where L is the length of the waveguide.

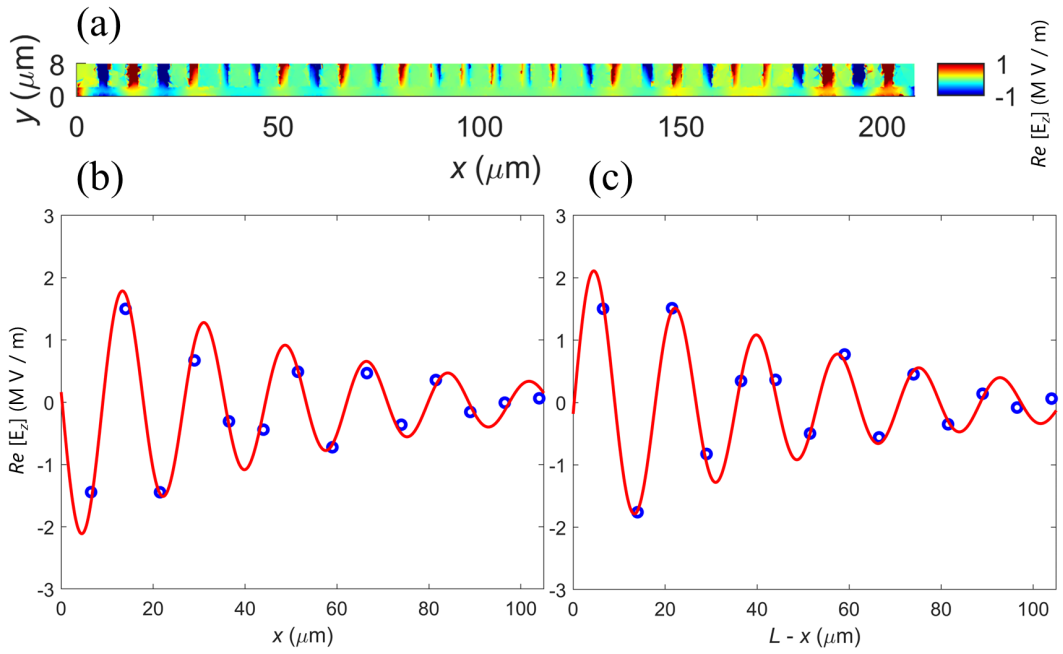

Figure 4.9: **(a)** SSPPs coupled on the surface of the waveguide using a free-space beam normally incident to the waveguide with polarisation parallel to the waveguide axis. Two separate SSPPs are launched at each end of the waveguide and meet at its centre. **(b)** SSPP launched on the left part of the waveguide. Blue data points: Average value of the out-of-plane electric field E_z on the surface of each bar. Red line: Fit of the simulation data using Eq. 4.1. The determined fitting parameters are: $E_0 = 2.3$ MV/m, $k_x \approx 3550$ cm^{-1}, $\theta = -1.5$ rad, and $L_p = 54$ µm. **(c)** SSPP launched on the right part of the waveguide. Blue data points: Average value of the out-of-plane electric field E_z on the surface of each bar. Red line: Fit of the simulation data using Eq. 4.1. The determined fitting parameters are: $E_0 = 2.3$ MV/m, $k_x \approx 3550$ cm^{-1}, $\theta = 1.64$ rad, and $L_p = 54$ µm.

From the analysis, it is observed that the two SSPPs have identical values of the amplitude, wave-vector, and propagation length, which is expected due to the symmetry of the structure. Furthermore, a 180° phase shift is observed between the two SSPPs, which is also expected for this beam polarisation. The wave-vector determined by the free-space beam simulation $k_x = 3575$ cm^{-1} is slightly greater than the wave-vector determined by the simulations using a waveport $k_x \approx 3600$ cm^{-1}. The difference between the two wave-vectors is small and it can be attributed to ANSYS HFSS tolerance margin. However, the propagation length determined by the free-space simulations yields a value of $L_p = 54$ µm, which is noticeably lower than the propagation length obtained by the simulations using a waveport $L_p = 75$ µm. This difference could be attributed to the interference between the SSPPs launched on the left and right part of the waveguide which is expected to be strongest at the centre of the waveguide. In this respect the value of $L_p = 54$ µm does not represent the true propagation length of each SSPP but is an effective value observed due to this interference.

4.5.2 Perpendicular Polarisation

The free-space beam simulations of the CSP waveguide were also run for an incident wave with frequency of 3.45 THz propagating towards the waveguide under normal incidence and its electric field polarisation perpendicular to the waveguide axis (y-direction). The simulation setup is identical to the one presented in Section 4.5.1. Figure 4.10 shows the direction and the polarisation of the free-space beam. In this polarisation orientation, the illuminated beam again causes the individual bars of the structure to be polarised along the polarisation direction. This causes an additional spatial variation of the electric field with a maxima ($+E_z$) and minima ($-E_z$) at the two ends of each bar, resembling the behaviour of the dipole antennas presented in Chapter 3. This effect results in a positive (or negative) offset to the average out-of-plane electric field on each bar. The offset was removed in the analysis to fit the extracted data using Eq. 4.1. The real part of the out-of-plane electric field compoment E_z is shown in Fig. 4.11 (a). From the figure, it is observed that two separate SSPPs are launched at each end of the waveguide, oscillating from a maxima ($+E_z$) to a minima ($-E_z$), and propagating towards the centre of the waveguide. These results show that a free-space beam with polarisation perpendicular to the waveguide axis can also excite SSPPs on the surface of the structure. Due to the initial phase of the SSPPs on the two

ends of the bar, the instantaneous out-of-plane electric field E_z on the surface of the structure seems to be strongest at $x \approx 30$ µm. However, the amplitude of the electric field is strongest at $x = 0$, as it can be seen from the fits in Fig. 4.11 (b) and (c).

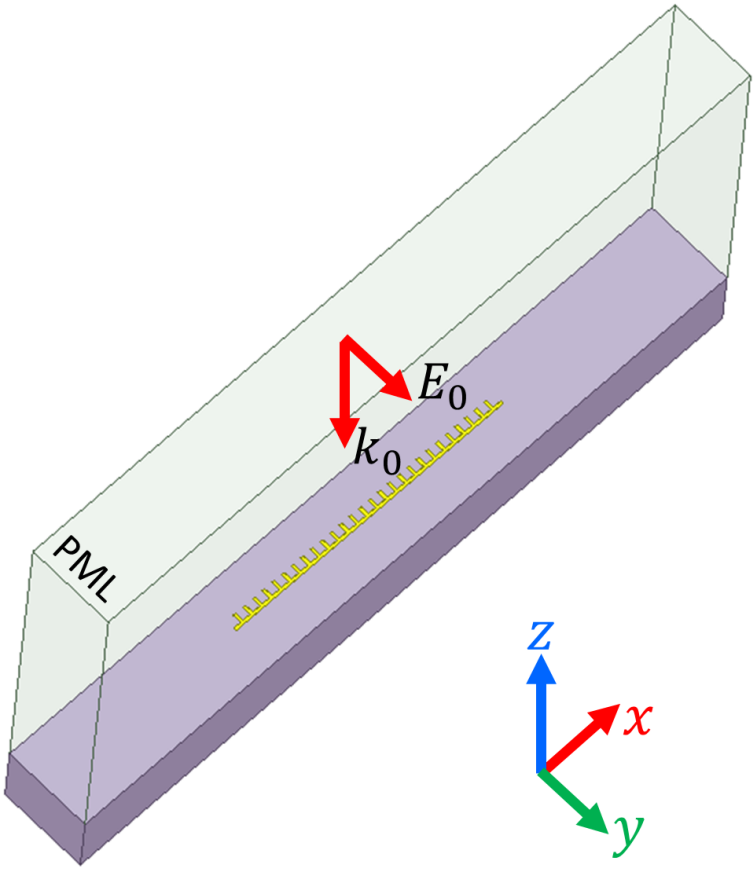

Figure 4.10: Simulation setup of the asymetric waveguide structure placed on a silicon substrate. The incident wave is defined 174 µm above the waveguide. E_0 illustrates the polarisation orientation and k_0 illustrates the direction of the free-space beam propagating towards the waveguide under normal incidence.

In this polarisation orientation, the comparison between the SSPPs launched on the opposite ends of the waveguide shows that the parameters of the two SSPPs have identical values, as expected. Equation 4.1 does not fit the data very well in the centre of the waveguide in Fig. 4.11 (b) and (c), and this is again due to the interference between the SSPPs. The comparison of the SSPP parameters obtained from the two different polarisation orientations shows that the SSPPs launched on the waveguide by an incident wave with polarisation perpendicular to

the waveguide axis are seen to have a lower amplitude compared to the amplitude of the SSPPs in the parallel orientation (see Section 4.5.1).

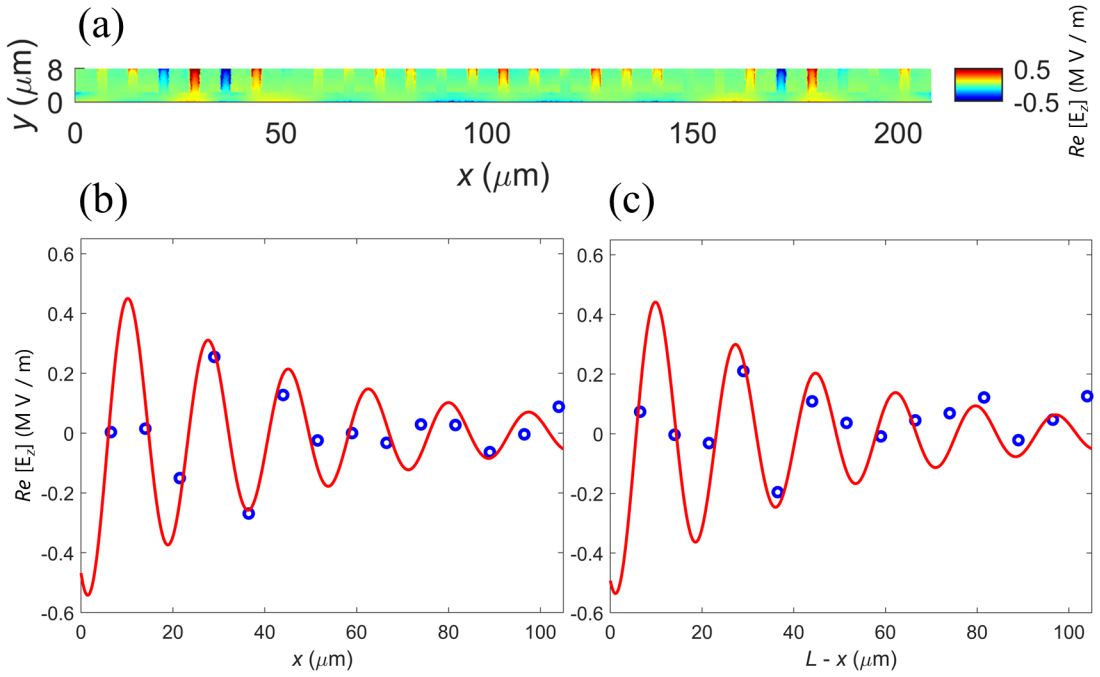

Figure 4.11: **(a)** SSPPs coupled on the surface of the waveguide using a free-space beam normally incident to the waveguide with polarisation perpendicular to the waveguide axis. Two separate SSPPs are launched at each end of the waveguide and meet at its centre. **(b)** SSPP launched on the left part of the waveguide. Blue data points: Average value of the out-of-plane electric field E_z on the surface of each bar. Red line: Fit of the simulation data using Eq. 4.1. The determined fitting parameters are: $E_0 = 0.56$ MV/m, $k_x = 3600$ cm^{-1}, $\theta = -2.58$ rad, and $L_p = 47$ µm. **(c)** SSPP launched on the right part of the waveguide. Blue data points: Average value of the out-of-plane electric field E_z on the surface of each bar. Red line: Fit of the simulation data using Eq. 4.1. The fitting parameters are: $E_0 = 0.56$ MV/m, $k_x = 3600$ cm^{-1}, $\theta = -2.68$ rad, and $L_p = 47$ µm.

This shows that the coupling strength of the incident beam to SSPPs on the structure is weaker for a perpendicular polarisation compared to the coupling strength observed for a parallel polarisation to the waveguide axis. This is because in order to launch a SSPP on the surface of the waveguide, there are two conditions which need to be fulfilled: the photon momentum should point along the direction of the waveguide ($x-$direction), and an electric field component that is out-of-plane ($z-$direction). The first condition is fulfilled by diffraction at the edge of the waveguide. In the case of parallel polarisation, the second condition is naturally satisfied by the beam component that is diffracted along the waveguide ($x-$) axis. This is not the case for the perpendicular polarisation as the beam diffracted along the waveguide axis is still polarised along the $y-$direction. Theoretical studies of the PSP waveguide at frequencies $\sim$ 1 THz, and experimental studies of the PSP waveguide at $\sim$ 10 GHz reported in [255, 256] have shown that the PSP waveguide can sustain broadband terahertz waves in two orthogonal directions. Hence, the PSP waveguide can support two SSPP modes, one with its field pointing predominantly along the $z-$direction, and one with its field pointing predominantly along the $y-$direction. The perpendicular polarisation geometry should only excite the SSPP mode pointing along the $y-$direction, however Fig. 4.11 clearly shows that an electric field pointing in the $z-$direction (E_z) propagates along the surface of the structure. One possible explanation for this is that the electric field pointing in the $y-$direction can also couple in the $z-$direction. This could also explain why the coupling strength of light to SSPPs is weaker when the perpendicular polarisation geometry is used. Moreover, the wave-vector and propagation length values for the two different polarisation orientations are almost identical. This shows that a free-space beam with normal incidence to the waveguide can excite SSPPs in both polarisation orientations with the same parameters but different coupling strengths.

4.6 Free-space excitation under oblique incidence

4.6.1 Parallel Polarisation

The PSP waveguide was then simulated using a free-space beam with frequency $f_0 = 3.45$ THz and an oblique angle of incidence to the surface of the waveguide. The angle of incidence was set to $\theta_i = 54^o$ with respect to the surface normal to match the angle of the experimental s-SNOM system. The simulation environ-

ment described in Section 4.5.1 was used. In this simulation, the free-space beam propagates in the $x-z$ plane, towards the waveguide ($z-$direction), and in the direction of the waveguide axis ($x-$direction). Therefore, the incident beam has both in-plane and out-of-plane components of the photon momentum which will affect how SSPPs are launched on the waveguide. A diagram of the simulation setup for an obliquely incident beam on the waveguide propagating in the $x-z$ plane is shown in Fig. 4.12.

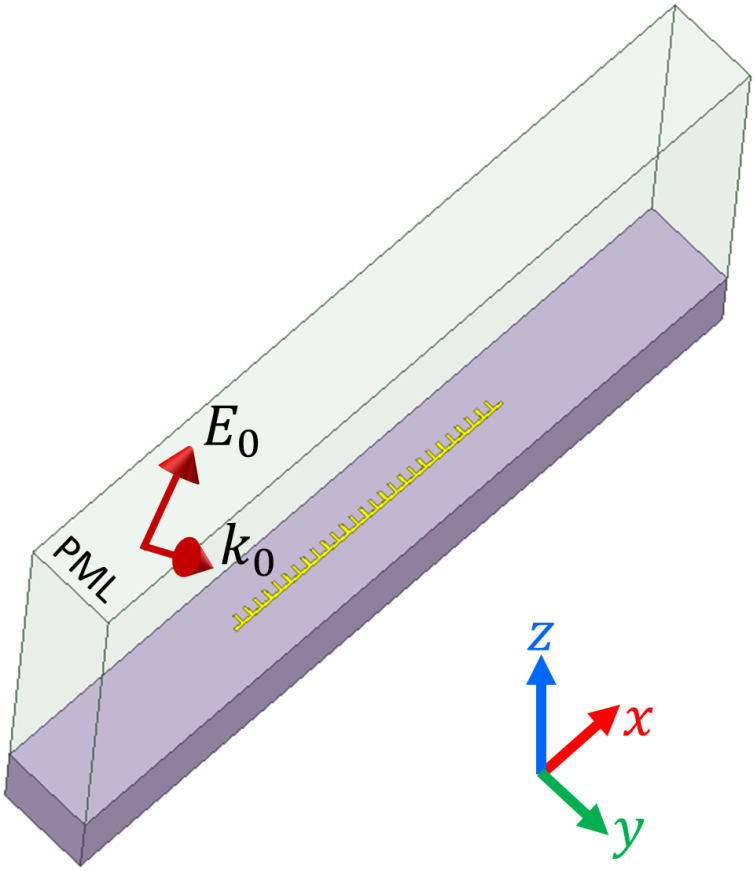

Figure 4.12: Simulation setup of the asymetric waveguide structure placed on a silicon substrate. The incident wave is defined 174 µm above the waveguide. E_0 illustrates the polarisation orientation and k_0 illustrates the direction of the free-space beam propagating towards the waveguide under oblique incidence.

Furthermore, the beam polarisation also oscillates in the $x-z$ plane and it is perpendicular to the beam direction. Due to the angle of incidence, the polarisation is not parallel to the waveguide axis, but it oscillates in the direction of the waveguide axis with an angle of $\theta_p = 36^o$ relative to the surface normal. The

polarisation will also have two components in the out-of-plane (z) and in-plane (x) direction, which also affect how SSPPs are launched on the waveguide. This geometry of incident beam and polarisation is referred to as parallel polarisation hereafter.

The free-space simulations of the PSP waveguide under oblique incidence demonstrated some significant differences when compared with the free-space simulations with parallel polarisation under normal incidence (see Section 4.5.1). Figure 4.13 presents the out-of-plane electric field assosiated with the SSPPs coupled on the waveguide with a free-space beam obliquely incident at a 54° angle relative to the surface normal and with parallel polarisation. In this simulation, two separate SSPPs are launched at the opposite ends of the waveguide, as in the case of the free-space simulations under normal incidence. However, in this case, the phase of the incident beam varies along the waveguide axis due to the incident angle, and the phases of the two SSPPs are different in each end of the waveguide. Furthermore, a different out-of-plane electric field E_z variation is observed on the waveguide when it is compared to the free-space beam simulations under normal incidence. This field variation occurs on a length scale on the order of ~ 100 µm, which is comparable to the incident wavelength. This occurs due to the incident angle which leads to the free-space beam reaching the waveguide at a different phase along the waveguide axis. The simulation is measuring the beam that is reflected from the metal, with the field due to the SSPPs superimposed on that. To analyse the coupling of the free-space beam to SSPPs on the waveguide, the out-of-plane field E_z in each bar was spatially averaged and shown in Fig. 4.14.

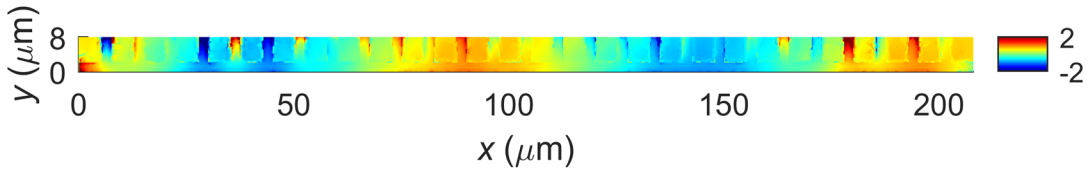

Figure 4.13: Real component of the out-of-plane field E_z (MV/m) on the waveguide. The incident wave has an incident angle of $\theta_i = 54^o$ relative to the surface normal, with its polarisation parallel to the waveguide axis. A spatial variation of the out-of-plane electric field E_z is observed on the waveguide with one cycle being equal to $\lambda_0/\sin(54^o) = 109$ µm.

From Fig. 4.14, it is clearly seen that simulations measure the reflection of the incident beam with different phases along the waveguide and the SSPPs are

superimposed on this field. The phase of the incident beam varies by one cycle over a distance $\lambda_0/\sin(54^o) = 109$ µm. The results from this simulation show that the oblique beam causes this ~ 109 µm variation due to reflection of the incident beam. This makes the simulations difficult to interpret. Furthermore, this oblique incidence is expected to cause a different problem in the experiments, which is the retardation effect (see Section 4.11.2).

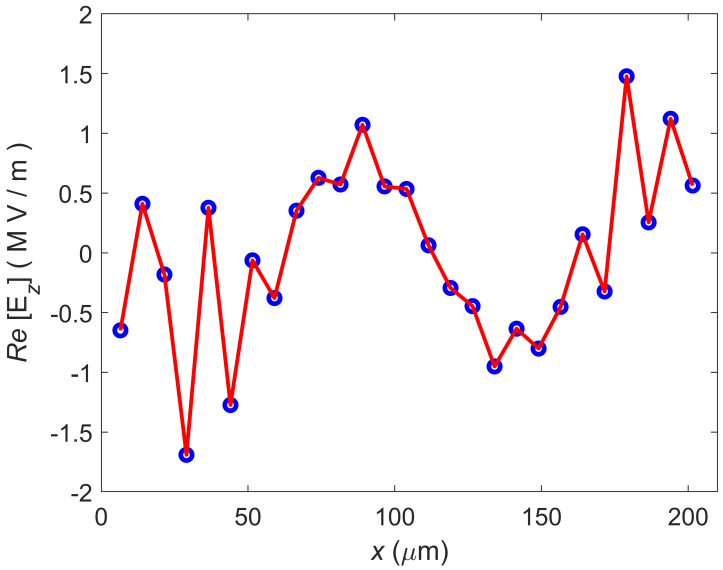

Figure 4.14: Spatially averaged values of the out-of-plane electric field E_z. The phase of the incident beam varies along the waveguide with one cycle over a distance of 109 µm. The simulation calculates the reflected field on the surface of the waveguide along with the SSPPs which are superimposed on the reflected beam.

4.6.2 Perpendicular Polarisation

Another simulation of the waveguide was run with an obliquely incident wave on the waveguide, a frequency $f_0 = 3.45$ THz, and an incident angle $\theta_i = 54^o$. In this simulation, the free-space beam propagates in the $y-z$ plane, towards the waveguide ($z-$ direction), and in the direction which is perpendicular to the waveguide axis ($y-$ direction) as shown in Fig. 4.15.

The simulation environment is described in Section 4.5.1. The incident beam also has two components of the photon momentum just as in the simulation presented in Section 4.6.1. However, in this case the beam propagates in a direction

which is perpendicular to the waveguide axis. The direction of propagation of the beam in the $y-z$ plane leads to the phase of the incident wave illuminating the waveguide being identical along the waveguide axis. Therefore, the two separate SSPPs launched on the opposite ends of the waveguide are expected to have the same phase. The long-range variation (109 µm per cycle) of the out-of-plane field E_z observed in Fig. 4.13 and Fig. 4.14 is not present in this case.

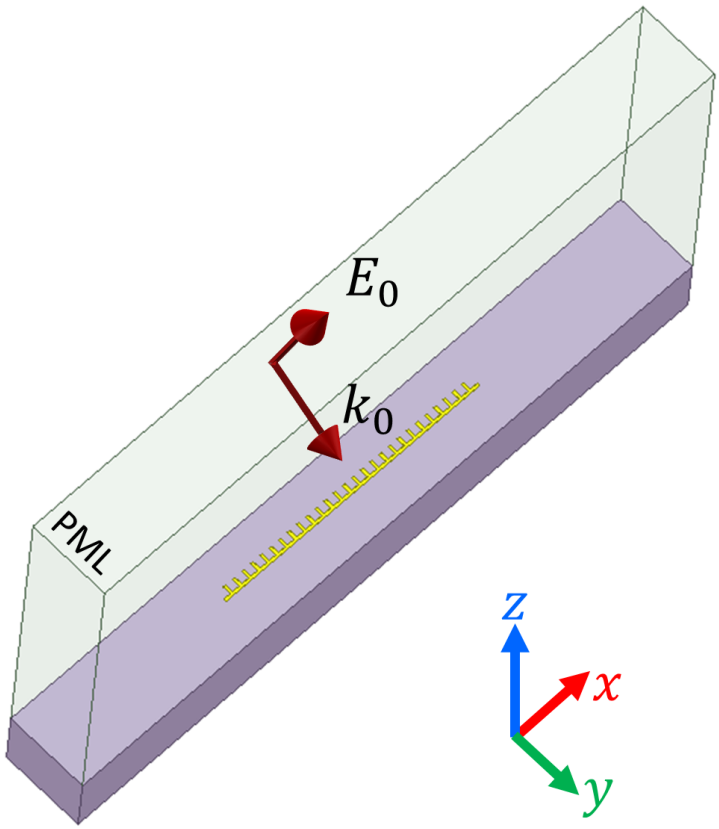

Figure 4.15: Simulation setup of the asymetric waveguide structure placed on a silicon substrate. The incident wave is defined 174 µm above the waveguide. E_0 illustrates the polarisation orientation and k_0 illustrates the direction of the free-space beam propagating towards the waveguide under oblique incidence.

This can be observed in Fig. 4.16 (a). Furthermore, there are electric field components of the incident beam along the $y-$ and $z-$ direction, and the component along the $y-$direction will polarise the bars, as seen in Fig. 4.11. This field variation can be removed by subtracting the offset from the spatially averaged values as shown in Fig. 4.16 (b) and (c). This geometry of incident beam and polarisation is referred to as perpendicular polarisation hereafter.

Figure 4.16 shows that an SSPP amplitude of $E_0 = 0.42$ MV/m is observed on each end of the waveguide. The free-space simulation with normal incidence and with perpendicular polarisation yields an SSPP amplitude of $E_0 = 0.56$ MV/m on each end of the waveguide. This comparison shows that, when the polarisation of the illuminating beam is perpendicular to the waveguide axis, a free-space beam under normal incidence offers a stronger coupling of light to SSPPs on the waveguide when compared to an obliquely incident beam.

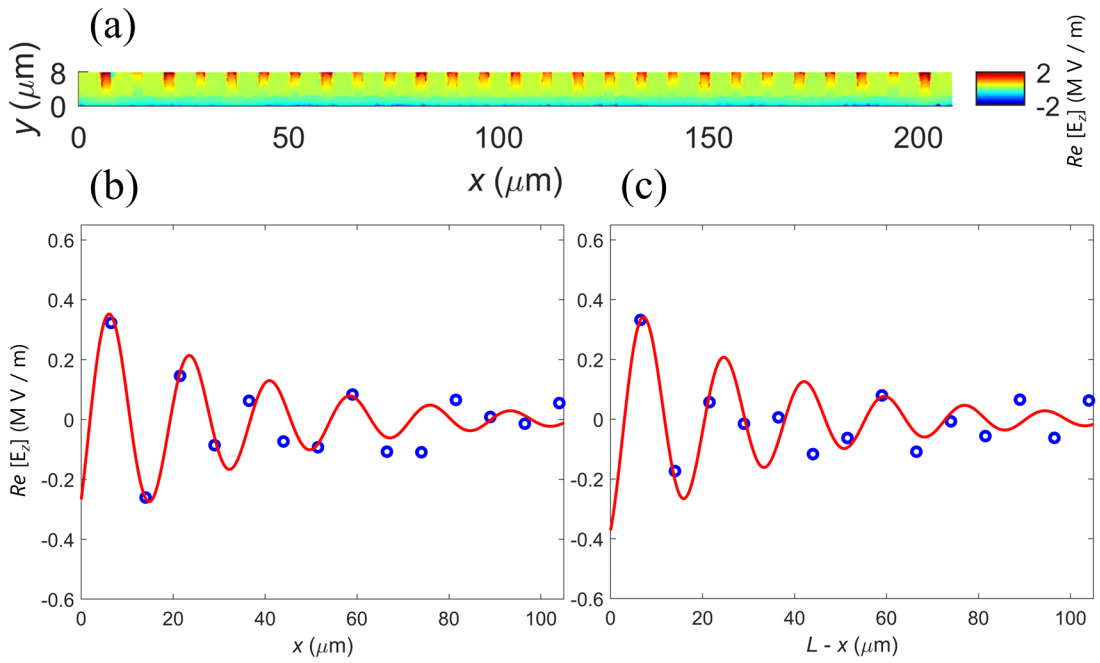

Figure 4.16: **(a)** SSPPs coupled on the surface of the waveguide using a free-space beam obliquely incident on the waveguide propagating in the $y-z$ plane with two polarisation components oscillating in the $y-$ and $z-$ plane. Two separate SSPPs are launched at each end of the waveguide and meet at its centre. **(b)** SSPP launched on the left part of the waveguide. Blue data points: Average value of the out-of-plane electric field E_z on the surface of each bar. Red line: Fit of the simulation data using Eq. 4.1. The determined fitting parameters are: $E_0 = 0.42$ MV/m, $k_x = 3600$ cm^{-1}, $\theta = 2.26$ rad, and $L_p = 35$ µm. **(c)** SSPP launched on the right part of the waveguide. Blue data points: Average value of the out-of-plane electric field E_z on the surface of each bar. Red line: Fit of the simulation data using Eq. 4.1. The fitting parameters are: $E_0 = 0.42$ MV/m, $k_x = 3600$ cm^{-1}, $\theta = 2.66$ rad, and $L_p = 35$ µm.

From the fits in Fig. 4.16 (a) and (b), the value of the propagation length is found to be $L_p = 35$ µm. This value is considerably smaller than the value obtained from the fit to the simulation data with a waveport excitation of the SSPP shown in Fig 4.4, which was $L_p = 75$ µm. A similarly smaller value of L_p was also observed in the case of a normally-incident illuminating beam (Section 4.5). This difference in the values of the propagation length can be attributed to the interference between the SSPPs launched on the opposite ends of the waveguide which meet at the centre of the waveguide. The interference between the SSPPs can be observed also from Fig. 4.16 (a) and (b). The fits of the two SSPPs show that the fitting equation does fit the data well at the two ends of the waveguide, but it does not fit the data well at the centre of the waveguide. This observation can also be attributed to the interference between the SSPPs launched on the opposite ends of the waveguide which meet at the centre of the waveguide.

These simulation results show that the perpendicular polarisation geometry presents a lower level of complexity in the analysis of SSPPs which allows for a more accurate study and analysis of SSPPs coupled on the waveguide using the experimental s-SNOM system. However, the former illuminating beam direction and polarisation orientation yields a weaker coupling of light to SSPPs on the waveguide. Hence, a technique which would improve the coupling of light to SSPPs using this free-space beam direction and polarisation would be highly desirable. In Section 4.6, it was mentioned that various techniques exist to account for the momentum mismatch between the photon momentum of the incident wave and the momentum of the SSPP. Therefore, in order to improve the coupling strength of the light to SSPPs on the waveguide, a grating structure has been designed which is presented in the next section.

4.7 Design of a grating structure to improve the coupling of light to SSPPs

4.7.1 Grating design

In the previous section it was shown that a free-space beam can be used to directly excite SSPPs on the waveguide. However, the experimental geometry of the s-SNOM system which matches that shown in Fig. 4.15 provides the weakest coupling of light to SSPPs on the waveguide. In order to improve the coupling of the incident beam to SSPPs, gratings can be employed to provide the momentum mismatch for the light to be coupled to SSPPs on the waveguide [257]. The optimum grating period that provides perfect momentum matching for an incident wave to launch SSPPs on the waveguide can be calculated using Eq. 4.3:

$$k_z = k_0 \sin\theta_i + q\mathbf{k}\,, \tag{4.3}$$

where k_z is the in-plane component of the photon momentum after interacting with the grating, k_0 is the free-space beam wave-vector, q is the diffraction order, $\mathbf{k} = 2\pi/\alpha$, and α is the grating period. In order to provide the momentum mismatch between the free-space beam and the SSPP wave-vector, the in-plane component of the photon momentum after interacting with the grating has to be equal to the SSPP wave-vector; $k_z = k_{SP}$. By setting k_z to match the momentum of SSPPs k_{SP} and $q = 1$, this gives:

$$\frac{2\pi}{\lambda_{SP}} = \frac{2\pi}{\lambda_0}\sin\theta_i + \frac{2\pi}{\alpha}\,. \tag{4.4}$$

In the s-SNOM system, the free-space beam has a wavelength of $\lambda_0 = 87$ µm and an angle of $\theta_i = 54^o$ relative to the surface normal. The eigen-mode simulation presented in Section 4.3 shows that the SSPP wavelength is $\lambda_{SP} = 18$ µm. Based on that wavelength, the optimum grating period for the parallel polarisation geometry (Fig. 4.12) is $\alpha \approx 21.5$ µm. For the perpendicular polarisation geometry (Fig. 4.15), the angle $\theta_i = 0^o$, and the grating period for this case is $\alpha = 18$ µm. However, the simulations with a free-space beam presented in Section 4.5 yielded a wave-vector of $k_x \approx 3600$ cm^{-1}, which converts to a wavelength of $\lambda_{SP} \approx 17.5$ µm. Based on this wavelength, the optimum grating period for an incident wave with oblique incidence to the waveguide is $\alpha \sim 20$ µm for the parallel polarisation geometry and $\alpha \sim 17.5$ µm for the perpendicular polarisation geometry. Therefore, the grating

structure was designed with period $\alpha = 20$ µm which is a good compromise for all solutions. A diagram of the grating structure is shown in Fig. 4.17. The length of the grating structure was set to $L_g \approx \lambda_0$ µm, and the length of each slit was set to $L_s = 25$ µm. The parameter g_{off} defines the distance between the waveguide and the first slit of the grating structure.

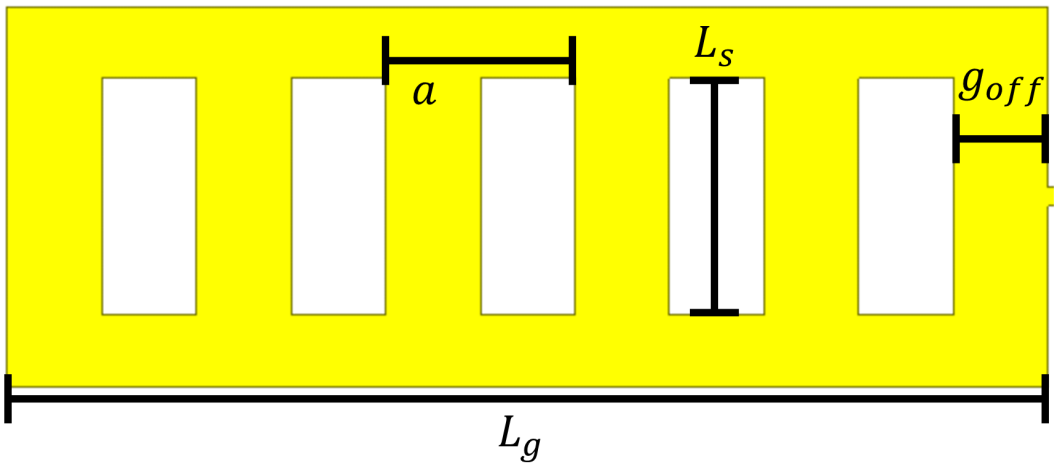

Figure 4.17: Schematic diagram of the grating structure with period $a = 20$ µm, length $L_g \approx 87$ µm, offset $g_{off} = 10$ µm, and slit length $L_s = 25$ µm.

The grating structure integrated with the PSP waveguide placed on a silicon substrate with dielectric constant $\varepsilon_r = 11.65$ is shown in Fig. 4.18.

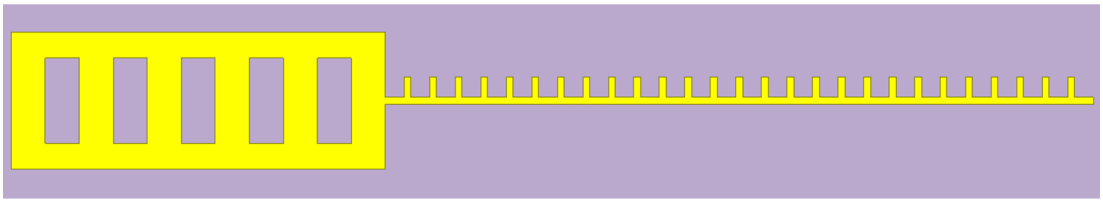

Figure 4.18: Schematic diagram of the grating structure inegrated with the CSP asymmetric waveguide. The period of the grating is $\alpha = 20$ µm and the length of the waveguide is $L = 208$ µm.

4.7.2 Grating period optimisation for an illuminating beam with normal incidence and parallel polarisation

In order to verify that the optimum grating period is $\alpha \approx 20$ µm, the grating structure integrated with the waveguide was simulated with different grating periods from 2 µm to 20 µm with a step of 2 µm. The simulation environment is described in Section 4.5.1. An illuminating beam with frequency $f_0 = 3.45$ THz was normally incident on the waveguide with its polarisation orientation parallel to the waveguide axis. The length of the grating structure was $L_g \approx 87$ µm, and the slit length was $L_s = 25$ µm for all different grating periods. The grating offset was set to $g_{off} = \alpha/2$ for each grating period. The amplitude of the out-of-plane field E_z, determined from a similar fitting procedure to that described in Sections 4.5 and 4.6, are presented in Fig. 4.19.

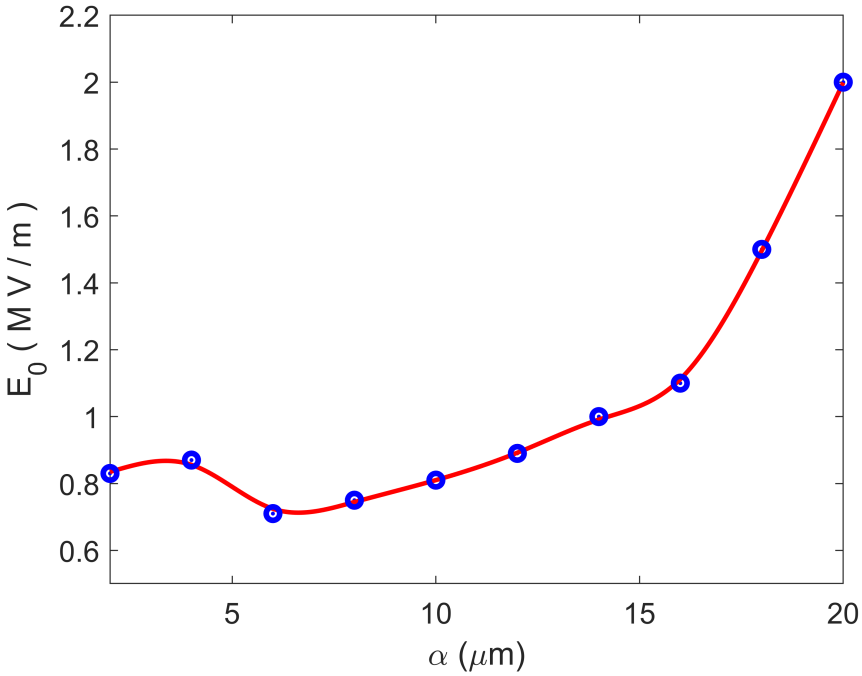

Figure 4.19: Relationship between the grating period α and the amplitude of the out-of-plane electric field E_z coupled on the left part of the waveguide, which is integrated with the grating structure. Blue data points: Amplitude of the SSPP coupled on the left part of the waveguide. Red line: Smoothing fit function used to aid visualisation of the graph.

From Fig. 4.19, it is observed that the strongest coupling of light to SSPPs on the waveguide occurs for a grating period of $\alpha = 20$ µm. These results verify the theoretical calculation of the grating period using Eq. 4.3. In addition, the amplitude of the SSPP which is coupled on the left part of the waveguide due to the grating structure shown a non-linear decay as the grating period reduces from 20 µm to 6 µm. Due to the finite length of the grating L_g, the grating momentum is actually a distribution centered on the value $2\pi/\alpha$. For this reason a non-zero value of the SSPP amplitude is observed for all grating periods that are not exactly $\alpha = 20$ µm. This non-linear relationship between the grating period and the SSPP amplitude changes when the grating period becomes smaller than 6 µm, as a small increase is observed in the coupling strength of light to SSPPs on the waveguide for a grating period of 4 µm. However, this increase is small when compared with the coupling strength which occurs at a grating period of 20 µm.

4.7.3 Grating offset optimisation for an illuminating beam with normal incidence and parallel polarisation

To further improve the coupling strength of the illuminating beam to SSPPs on the waveguide, further simulations were ran to optimise the value of the grating offset g_{off}. The simulation environment is identical to the one described in Section 4.5.1. In these simulations, the grating period was fixed to $\alpha = 20$ µm. An illuminating beam with frequency $f_0 = 3.45$ THz was normally incident on the waveguide with its polarisation orientation parallel to the waveguide axis. The length of the grating structure was $L_g \approx 87$ µm, and the slift length was $L_s = 25$ µm for all different values of the grating offset. The grating structure was integrated with the waveguide as shown in Fig. 4.18, and simulated with different grating offsets from 0 µm to 10 µm with a step of 1 µm. The results from these simulations are presented in Fig. 4.20.

From Fig. 4.20, it is observed that the strongest coupling of light to SSPPs on the waveguide occurs for a grating offset of $g_{off} = 0$ µm. The SSPP coupled on the left part of the waveguide which is where the grating structure is placed yields an amplitude of $E_z = 2.65$ MV/m. When the grating offset is 0 µm, the grating structure is not united with the waveguide. A gap of 10 µm exists between the waveguide and the grating structure. From the simulation with no gratings and polarisation parallel to the waveguide axis presented in Section 4.5.1, the SSPP amplitude is 2.1 MV/m. This comparison shows that the grating structure with

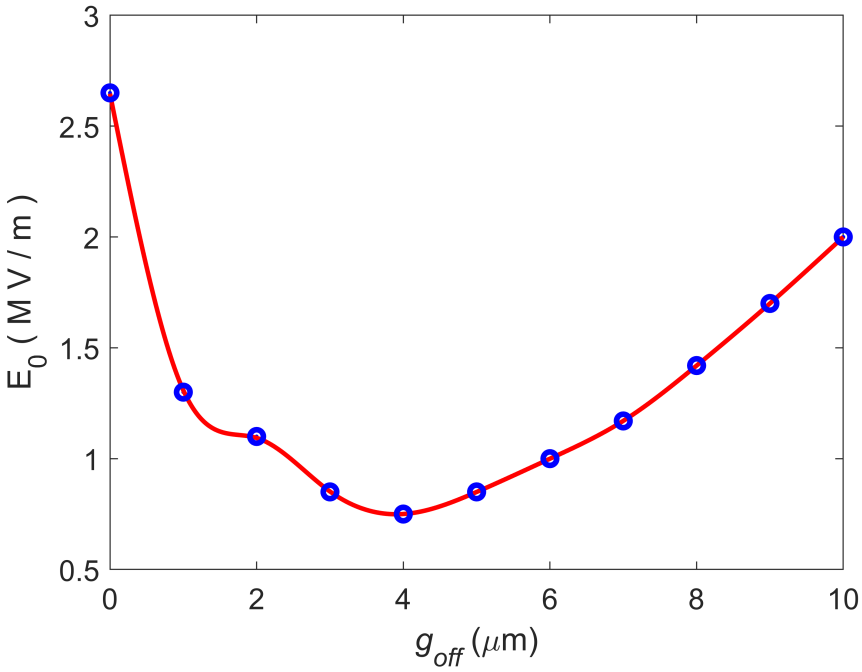

Figure 4.20: Relationship between the grating offset g_{off} and the amplitude of the out-of-plane electric field E_z coupled on the left part of the waveguide, which is integrated with the grating structure. Blue data points: Amplitude of the SSPP coupled on the left part of the waveguide. Red line: Smoothing fit function.

period $\alpha = 20$ µm and grating offset $g_{off} = 0$ µm has improved the coupling strength of light to SSPPs on the waveguide. When the grating offset $g_{off} = 1$ µm, the coupling strength of the illuminating beam to SSPPs on the waveguide decays significantly, from an amplitude of $E_z \sim 2.65$ MV/m to $E_z \sim 1.4$ MV/m. The grating offset which provides the weakest coupling of light to SSPPs on the waveguide is $g_{off} = 4$ µm, which yields a SSPP amplitude of $E_z \approx 0.8$ MV/m. For a grating offset of $g_{off} = 10$ µm, the amplitude of the SSPP on the left part of the waveguide which is integrated with the grating structure is $E_z = 2$ MV/m. This SSPP ammplitude is lower than the SSPP amplitude obtained by a grating offset of $g_{off} = 0$ µm, and it is almost equal to the SSPP amplitude obtained from the simulation with parallel polarisation and no gratings presented in Section 4.5.1.

4.7.4 Grating period optimisation for a beam with oblique incidence and perpendicular polarisation

In the experimental s-SNOM system, the illuminating beam is obliquely incident on the waveguide with an incident angle of $\theta_i = 54^o$. Therefore, it is important to optimise the grating period and the grating offset to provide maximum coupling strength of light to SSPPs for an incident angle of $\theta_i = 54^o$. From the simulations presented in Section 4.6.1, it was observed that for an illuminating beam propagating in the $x-z$ plane, towards the waveguide and in the direction of the waveguide with a polarisation oscillating also in the $x-z$ plane, a long-range variation with one cycle over a distance of 109 µm is observed on the out-of-plane electric field E_z coupled on the waveguide due to the change in phase that the illuminating beam experiences along the waveguide axis. This adds an additional level of complexity which makes it more difficult to study and analyse the light coupled to SSPPs on the waveguide in a simulation environment. In addition, the perpendicular polarisation geometry introduces an additional level of complexity experimentally due to retardation effects, which is different to the long-range variation observed in the simulations. For this reason, the grating period and the grating offset were optimised for an illuminating beam obliquely incident on the waveguide propagating in the $y-z$ plane with its polarisation also oscillating in the $y-z$ plane (geometry shown in Fig. 4.15).

In order to verify the optimum grating period for this direction and polarisation of the illuminating beam, the grating structure integrated with the waveguide was simulated with different grating periods from 2 µm to 20 µm with a step of 2 µm. The simulation environment is described in Section 4.5.1. The length of the grating structure was $L_g \approx 87$ µm, and the slit length was $L_s = 25$ µm for all different grating periods. The grating offset was set to $g_{off} = \alpha/2$ for each grating period. The results from these simulations are presented in Fig. 4.21.

From Fig. 4.21, it is observed that the strongest coupling of light to SSPPs on the waveguide occurs for a grating period of $\alpha = 6$ µm. As for normal incidence, the finite grating length means the grating momentum is a distribution centered around $2\pi/\alpha$. The oblique geometry means the $q = 1$ diffracted beam will have components of momentum along all of x, y, and z directions, so the coupling of light to SSPPs on the waveguide isn't intuitive to understand quantitatively in this case. For this reason the grating period $\alpha = 6$ µm appears to be the optimum value instead of $\alpha = 20$ µm. The SSPP amplitude for $\alpha = 6$ µm is

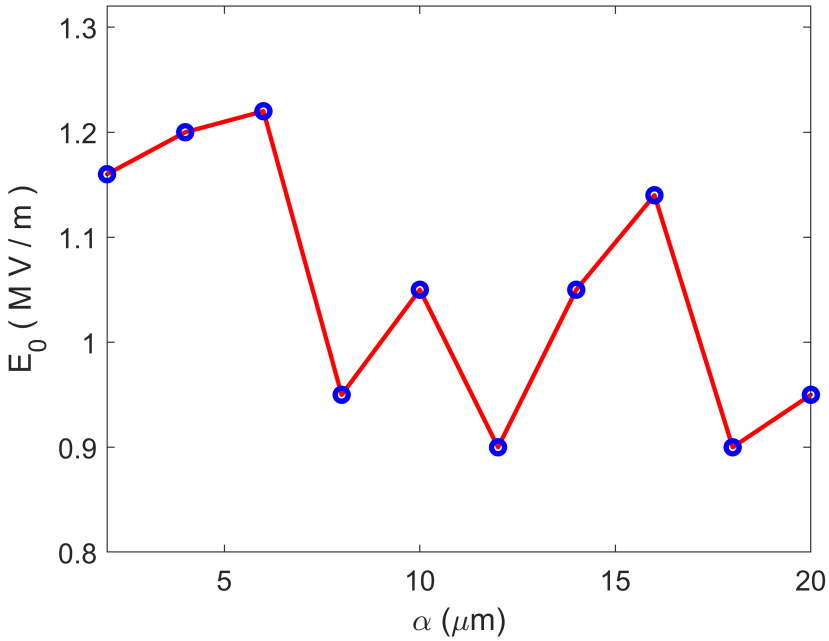

Figure 4.21: Relationship between the grating period α and the amplitude of the out-of-plane electric field E_z coupled on the left part of the waveguide, which is integrated with the grating structure. Blue data points: Amplitude of the SSPP coupled on the left part of the waveguide. Red line: Guide to the eye.

$E_z \approx 1.25$ MV/m, which is greater than $E_z \approx 1$ MV/m obtained for $\alpha = 20$ µm. However, the difference in coupling strength between the two grating periods is not significant. Furthermore, the grating structure with period $\alpha = 6$ µm has increased the coupling strength of light to SSPPs on the waveguide significantly when compared with the coupling strength of light to SSPPs for an illuminating beam with oblique incidence and perpendicular polarisation with no gratings (see Section 4.6.2). The SSPP amplitude obtained from the simulation with no gratings is $E_z = 0.42$ MV/m. This shows that the presence of the grating structure has improved the coupling strength of light to SSPPs by a factor of ~ 3 for this oblique illumination geometry. The weakest coupling of light to SSPPs occurs for a grating period of $\alpha = 12$ µm where the SSPP amplitude is $E_z \approx 0.87$ MV/m. Nevertheless, this SSPP amplitude is still greater than the SSPP amplitude obtained from the simulation with no gratings by a factor of 2. These results are crucial for the experimental study and investigation of SSPPs on the waveguide. By improving the coupling strength of light to SSPPs on the experimental system, the analysis

of the SSPPs observed experimentally and the comparison between experimental and simulation data becomes more accurate.

4.7.5 Grating offset optimisation for a beam with oblique incidence and perpendicular polarisation

In order to obtain the optimum value of the grating offset g_{off} for a period $\alpha = 20$ µm, simulations were ran with an illuminating beam with frequency $f_0 = 3.45$ THz obliquely incident on the waveguide with perpendicular polarisation. The simulation environment is identical to the one described in Section 4.5.1. The grating period was fixed to $\alpha = 20$ µm. The length of the grating structure was $L_g \approx 87$ µm and the length of each slit was $L_s = 25$ µm for all values of the grating offset g_{off}. The grating structure was integrated with the waveguide as shown in Fig. 4.18, and simulated with different grating offsets from 0 µm to 10 µm with a step of 1 µm. The results from these simulations are presented in Fig. 4.22.

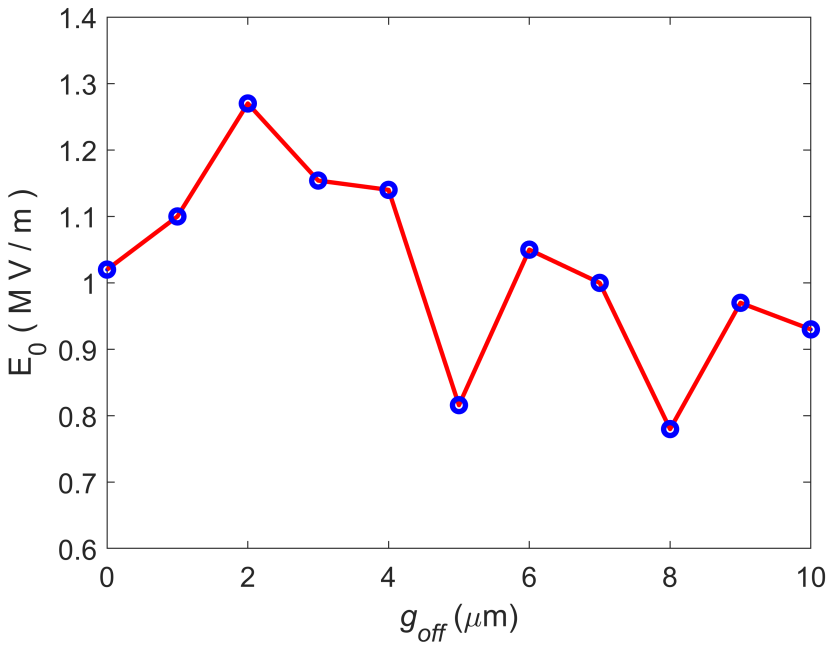

Figure 4.22: Relationship between the grating offset g_{off} and the amplitude of the out-of-plane electric field E_z coupled on the left part of the waveguide, which is integrated with the grating structure. Blue data points: Amplitude of the SSPP coupled on the left part of the waveguide. Red line: Guide to the eye.

From Fig. 4.22, it is observed that the strongest coupling of light to SSPPs on the waveguide occurs for a grating offset $g_{off} = 2$ µm for this oblique illumination geometry. These results differ from the results obtained for an illuminating beam normally incident on the waveguide with polarisation parallel to the waveguide axis (see Section 4.7.3). In this simulation, the highest SSPP amplitude occurs when the grating offset $g_{off} = 2$ µm which yields a value of $E_z = 1.3$ MV/m. This value is greater than the SSPP amplitude $E_z \approx 1$ MV/m obtained for a grating offset of $g_{off} = 0$ µm whereas in the simulation presented in Section 4.7.3, the highest SSPP amplitude occurred when the grating offset was $g_{off} = 0$ µm. Furthermore, the grating structure with period $\alpha = 20$ µm shows an improvement to the coupling strength of light to SSPPs on the waveguide for all values of g_{off} when compared to the coupling strength for oblique illumination and no gratings (Section 4.6.2). The highest amplitude $E_z = 1.3$ MV/m obtained when $g_{off} = 2$ µm which increases the amplitude by a factor of ~ 3.

4.7.6 Discussion

This section presented the design of a grating structure based on Eq. 4.3 and a range of simulations to obtain the optimum values of the period α and the offset g_{off} which provide the strongest coupling of light to SSPPs. The grating structure was optimised for two different scenarios; an illuminating beam with normal incidence on the waveguide with parallel polarisation, and an illuminating beam with oblique incidence propagating in the $y - z$ plane with its polarisation also oscillating in that plane.

The results from the former scenario which matches the experimental geometry of the s-SNOM system showed that the optimum grating period was $\alpha = 20$ µm when the grating offset was set to $g_{off} = \alpha/2$, and the optimum grating offset value was $g_{off} = 0$ µm when the period was fixed at $\alpha = 20$ µm. In this scenario, the presence of a grating structure increased the coupling strength of light to SSPPs when compared to the coupling strength obtained from the simulation with the equivalent beam direction and polarisation but with no gratings. The increase in SSPP amplitude was from of $E_z = 2.3$ MV/m to $E_z = 2.65$ MV/m.

The results from the latter scenario showed that the optimum grating period was $\alpha = 6$ µm when the grating offset was set to $g_{off} = \alpha/2$, and the optimum grating offset value was $g_{off} = 2$ µm when the period was fixed at $\alpha = 20$ µm. In this scenario, the presence of a grating structure also increased the coupling

strength of light to SSPPs when compared to the coupling strength obtained from the simulation with the equivalent beam direction and polarisation but with no gratings. The grating structure with period $\alpha = 6$ µm yielded a SSPP amplitude of $E_z = 1.25$ MV/m, and the grating structure with period $\alpha = 20$ µm and $g_{off} = 2$ µm yield an amplitude of $E_z = 1.3$ MV/m. Both grating designs provide a stronger coupling of light to SSPPs when compared to the coupling strengh with no gratings, which was found to be $E_z = 0.42$ MV/m.

4.8 Free-space excitation under normal incidence using a grating structure

In this section and Section 4.9, the coupling of a free-space beam to SSPPs on the waveguide incorporating optimised grating structures is investigated in further detail. The out-of-plane field distributions of SSPPs are visualised and compared for gratings with 6 µm and 20 µm period, for both parallel and perpendicular polarisation, and for both normal (this Section) and oblique incidence (Section 4.9). In each case the simulation setup is identical to the one described in Section 4.5.1. Two separate SSPPs are launched on the opposite ends of the waveguide. The grating structure is integrated with the waveguide as shown in Fig. 4.18. Thus, the SSPP on the left-hand side (LHS) is launched by the interaction of the incident beam with the grating structure. The SSPP on the right-hand side (RHS) is launched directly by the free-space beam interacting with the edge of the waveguide. In the first instance the polarisation of the incident beam is parallel with the axis of the waveguide, for the case in which the beam is normally incident on the grating. Although the illuminating beam with normal incidence does not match the experimental setup, these simulations allow a simple direction comparison of the coupling strength of light to SSPPs on the waveguide with and without gratings. These simulations also provide insight to the effect of polarisation orientation.

4.8.1 Parallel polarisation - Grating period 6 µm

Firstly, the simulation results of the waveguide integrated with a grating structure which has a period of $\alpha = 6$ µm are presented. The real part of the out-of-plane field E_z is shown in Fig. 4.23 (a). It is clearly observed that the SSPP launched on the end which is connected to the grating has a much lower amplitude compared to

the SSPP launched on the other side of the grating. To analyse the field associated with the SSPPs launched on the waveguide, an average value of the electric field was obtained for each bar. Equation 4.1 was used to fit the data of each SSPP, as shown in Fig. 4.23 (b) and (c). In this way, the amplitude of the SSPPs launched on the opposite ends of the waveguide can be compared.

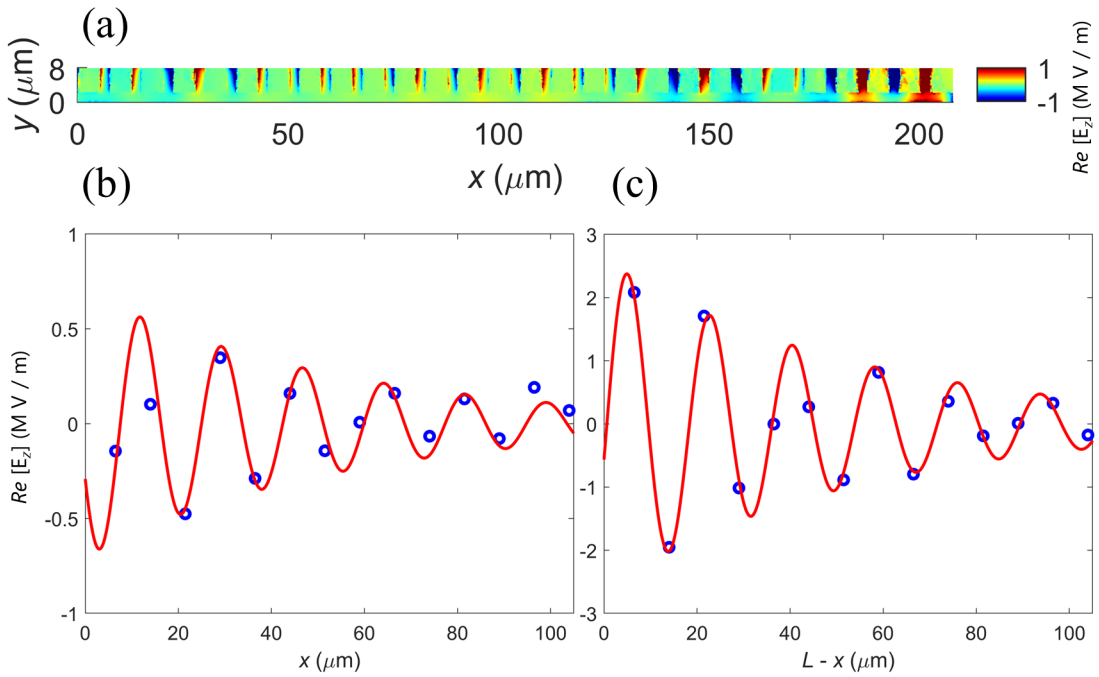

Figure 4.23: **(a)** SSPPs coupled on the surface of the waveguide using a grating structure with period $\alpha = 6$ µm, and a free-space beam normally incident to the waveguide with polarisation parallel to the waveguide axis. Two separate SSPPs are launched at each end of the waveguide and meet at its centre. **(b)** SSPP launched on the LHS. Blue data points: Average value of the out-of-plane electric field E_z on the surface of each bar. Red line: Fit of the simulation data using Eq. 4.1. The determined fitting parameters are: $E_0 = 0.7$ MV/m, $k_x \approx 3600$ cm^{-1}, $\theta = -2$ rad, and $L_p = 54$ µm. **(c)** SSPP launched on the RHS. Blue data points: Average value of the out-of-plane electric field E_z on the surface of each bar. Red line: Fit of the simulation data using Eq. 4.1. The determined fitting parameters are: $E_0 = 2.6$ MV/m, $k_x \approx 3540$ cm^{-1}, $\theta = 1.8$ rad, and $L_p = 54$ µm.

From the analysis, the obtained SSPP amplitude launched from the grating structure on the LHS is $E_z = 0.7$ MV/m which is much lower than the SSPP amplitude launched directly from the free-space beam on the RHS which has a

value of $E_z = 2.6$ MV/m. This analysis agrees with the results presented in Fig. 4.19 which demonstrates the relationship between the grating period and the SSPP amplitude for an illuminating beam normally incident on the gratings. Moreover, the amplitude obtained for the RHS $E_z = 2.6$ MV/m is slightly larger than the amplitude obtained for the RHS in Section 4.5.1 (with no grating on the LHS) which yielded a value of $E_z = 2.3$ MV/m. This difference in amplitudes can be attributed to the fact that the SSPP launched from the grating with 6 µm period has a lower amplitude than the SSPP without a grating which leads to a weaker interaction with the SSPP launched on the RHS.

4.8.2 Parallel polarisation - Grating period 20 µm

Next, the simulation results of the waveguide integrated with a grating structure which has a period of $\alpha = 20$ µm and grating offset $g_{off} = 10$ µm are presented. The real part of the out-of-plane electric field E_z is shown in Fig. 4.24. The results show that the SSPP launched by the gratings on the LHS yields a lower amplitude when compared to the amplitude of the SSPP launched directly by the free-space beam on the RHS. To analyse the electric field associated with the SSPPs launched on the waveguide, an average value of the electric field was obtained for each bar. Equation 4.1 was used to fit the data of each SSPP, as shown in Fig. 4.24 (b) and (c). In this way, the amplitude of the SSPPs launched on the opposite ends of the waveguide can be compared.

From the analysis, the obtained SSPP amplitude launched from the gratings tructure on the LHS is $E_z = 2$ MV/m which is lower than the SSPP amplitude $E_z = 2.6$ MV/m launched directly from the free-space beam on the RHS. This analysis agrees with the results presented in Fig. 4.19 which demonstrates the relationship between the grating period and the SSPP amplitude for an illuminating beam normally incident on the gratings. Moreover, the amplitude obtained for the RHS $E_z = 2.6$ MV/m is slightly larger than the amplitude obtained for the RHS in Section 4.5.1 $E_z = 2.3$ MV/m, where the SSPPs were launched with no gratings on both ends of the waveguide. This difference in amplitude on the RHS can be attributed to the fact that the SSPP launched from the grating with 20 µm period has a lower amplitude which leads to a weaker interaction with the SSPP launched on the RHS. One notable difference observed between the simulation presented in Section 4.5.1 and this simulation, is that the SSPPs in Section 4.5.1

had a phase difference of π. The simulations presented in this section show that the two SSPPs launched on the two ends of the waveguide have an identical phase of $\theta = 1.8$ rad. The change in the phase of the SSPP launched on the LHS also affects the interaction between the two SSPPs.

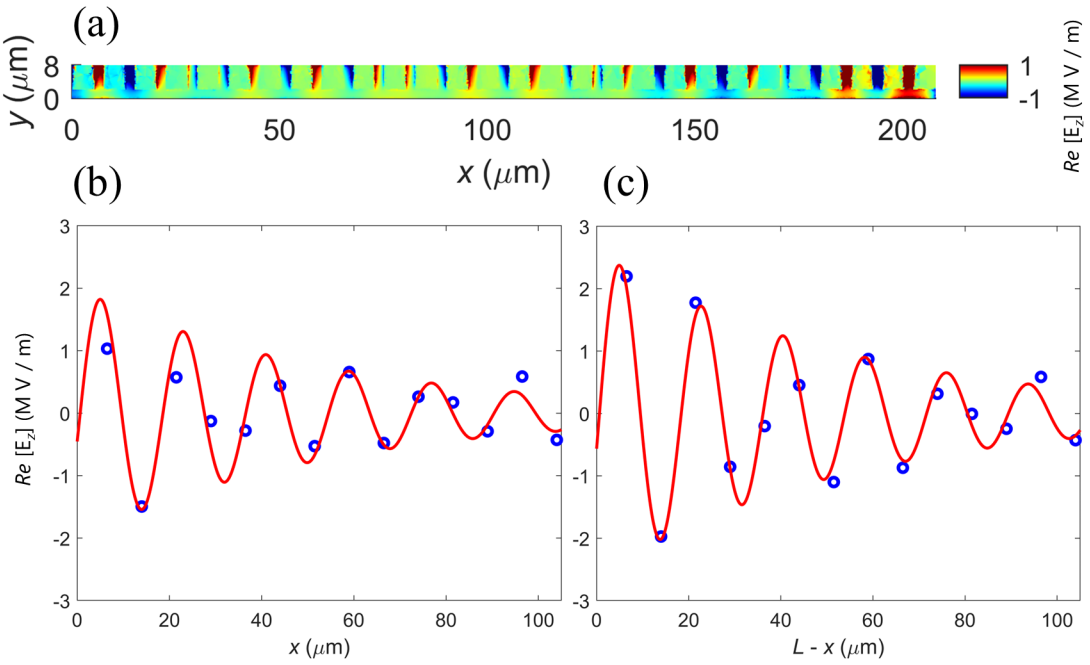

Figure 4.24: **(a)** SSPPs coupled on the surface of the waveguide using a grating structure with $\alpha = 20$ µm, $g_{off} = 10$ µm, and a free-space beam normally incident on the waveguide with polarisation parallel to the waveguide axis. Two separate SSPPs are launched at each end of the waveguide and meet at its centre. **(b)** SSPP launched on the LHS. Blue data points: Average value of the out-of-plane electric field E_z on the surface of each bar. Red line: Fit of the simulation data using Eq. 4.1. The determined fitting parameters are: $E_0 = 2$ MV/m, $k_x \approx 3500$ cm^{-1}, $\theta = 1.8$ rad, and $L_p = 54$ µm. **(c)** SSPP launched on the RHS. Blue data points: Average value of the out-of-plane electric field E_z on the surface of each bar. Red line: Fit of the simulation data using Eq. 4.1. The determined fitting parameters are: $E_0 = 2.6$ MV/m, $k_x \approx 3550$ cm^{-1}, $\theta = 1.8$ rad, and $L_p = 54$ µm.

4.8.3 Perpendicular Polarisation - Grating period 6 µm

The coupling of a free-space beam to SSPPs on the waveguide is investigated incorporating grating structures with 6 µm when the illuminating beam is normally incident on the gratings and its polarisation is perpendicular to the waveguide axis (Fig. 4.10). The real part of the out-of-plane field E_z is shown in Fig. 4.25 (a). To analyse the electric field associated with the SSPPs, an average value of the electric field was obtained for each bar. The SSPPs on the LHS and RHS with a fit to Eq. 4.1 are shown in Fig. 4.25 (b) and (c).

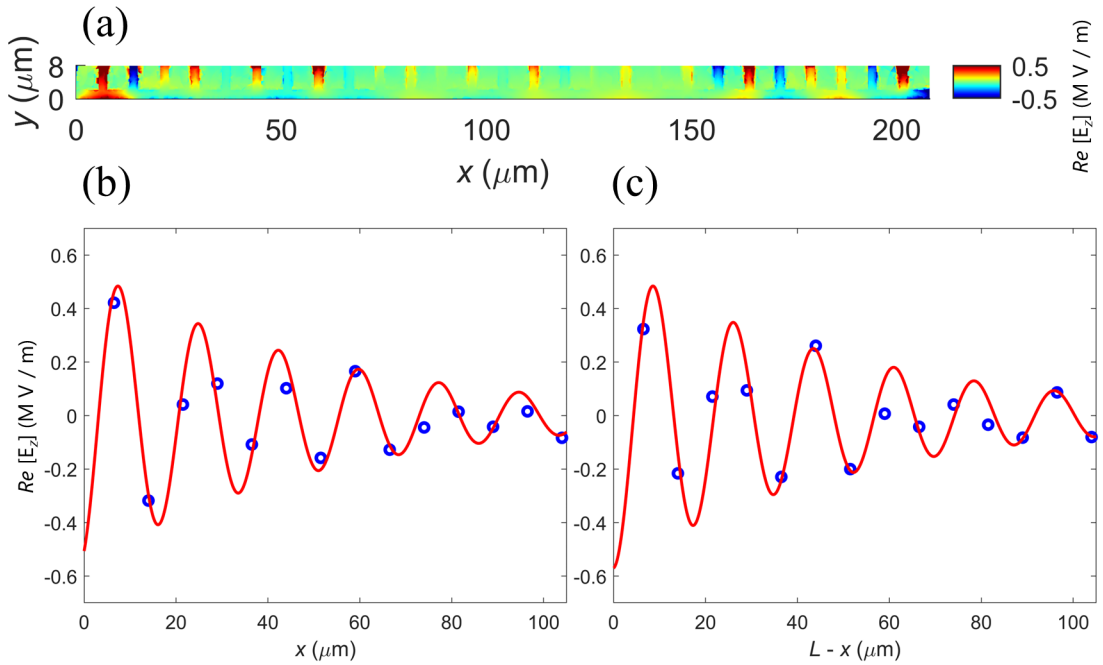

Figure 4.25: **(a)** SSPPs coupled on the surface of the waveguide using a grating structure with period $\alpha = 6$ µm, and a free-space beam normally incident to the waveguide with polarisation perpendicular to the waveguide axis. **(b)** SSPP launched on the LHS. Blue data points: Average value of the SSPP on each bar. Red line: Fit of the data using Eq. 4.1. The determined fitting parameters are: $E_0 = 0.56$ MV/m, $k_x \approx 3600$ cm^{-1}, $\theta = 2.7$ rad, and $L_p = 54$ µm. **(c)** SSPP launched on the RHS. Blue data points: Average value of SSPP on each bar. Red line: Fit of the data using Eq. 4.1. The determined fitting parameters are: $E_0 = 0.56$ MV/m, $k_x \approx 3600$ cm^{-1}, $\theta = \pi$ rad, and $L_p = 54$ µm.

From the analysis, the amplitudes of the SSPPs launched on the two ends of the waveguide have equal values of $E_z = 0.56$ MV/m. This value is equal to the SSPP amplitude obtained in Section 4.5.2 where an illuminating beam was normally incident on the waveguide and no grating structure was used. This shows that for this illumination geometry, the grating structure with period $\alpha = 6$ µm does not improve the coupling strength of light to SSPPs.

4.8.4 Perpendicular Polarisation - Grating period 20 µm

The coupling of a free-space beam to SSPPs on the waveguide is investigated incorporating grating structures with 20 µm for a normally incident beam on the gratings and perpendicular polarisation to the waveguide axis. The real part of the out-of-plane electric field E_z is shown in Fig. 4.26 (a). The SSPPs on the LHS and RHS with a fit to Eq. 4.1 are shown in Fig. 4.26 (b) and (c).

The grating structure with period 20 µm shows a weaker coupling of light to SSPPs on the waveguide ($E_0 = 0.42$ MV/m) compared to the grating structure with 6 µm ($E_0 = 0.56$ MV/m) when the polarisation is perpendicular to the direction of the waveguide. This trend is also observed from the simulations presented in Fig. 4.21 where the grating period α was optimised for an illuminating beam with oblique incidence on the waveguide with perpendicular polarisation. Conversely, when the polarisation is parallel to the direction of the waveguide, the grating structure with a period of 20 µm shows stronger coupling than the grating structure with a period of 6 µm. These results show that the optimum grating period of $\alpha = 20$ µm calculated using Eq. 4.3 is valid only for the case of parallel polarisation to the waveguide axis. This is because the polarisation orientation affects how light interacts with the grating structure and how SSPPs are launched on the waveguide. The results also confirm that an illuminating beam with normal incidence and perpendicular polarisation to the waveguide axis provides a much weaker coupling of light to SSPPs compared to an illuminating beam with normal incidence and parallel polarisation. The results also agree with the ones in Section 4.5 were the parallel polarisation geometry also provided a stronger coupling of light to SSPPs compared to the perpendicular polarisation geometry. This may relate to the discussion in Section 4.5.2 that the PSP waveguide can sustain two orthogonal SSPP modes, and their coupling to the PSP waveguide is affected by whether there is an electric field component in the $z-$direction in the diffracted beam.

Furthermore, the amplitude of the SSPPs on the RHS can be compared for the simulations with 6 µm and 20 µm. The amplitude on the RHS in the simulation with grating period 6 µm has a value of $E_0 = 0.56$ MV/m. This value is identical to the SSPP amplitude on the RHS obtained from the simulation in Section 4.5.2 (with no grating on the LHS). However, in the simulation with a grating period of 20 µm the SSPP amplitude on the RHS is $E_0 = 0.68$ MV/m. A possible explanation for this is that the amplitude on the LHS for 20 µm grating period is weaker ($E_0 = 0.42$ MV/m) compared to the amplitude on the LHS for 6 µm grating period ($E_0 = 0.56$ MV/m). A lower amplitude on the LHS leads to a weaker interaction between the SSPPs launched on the opposite ends of the waveguide.

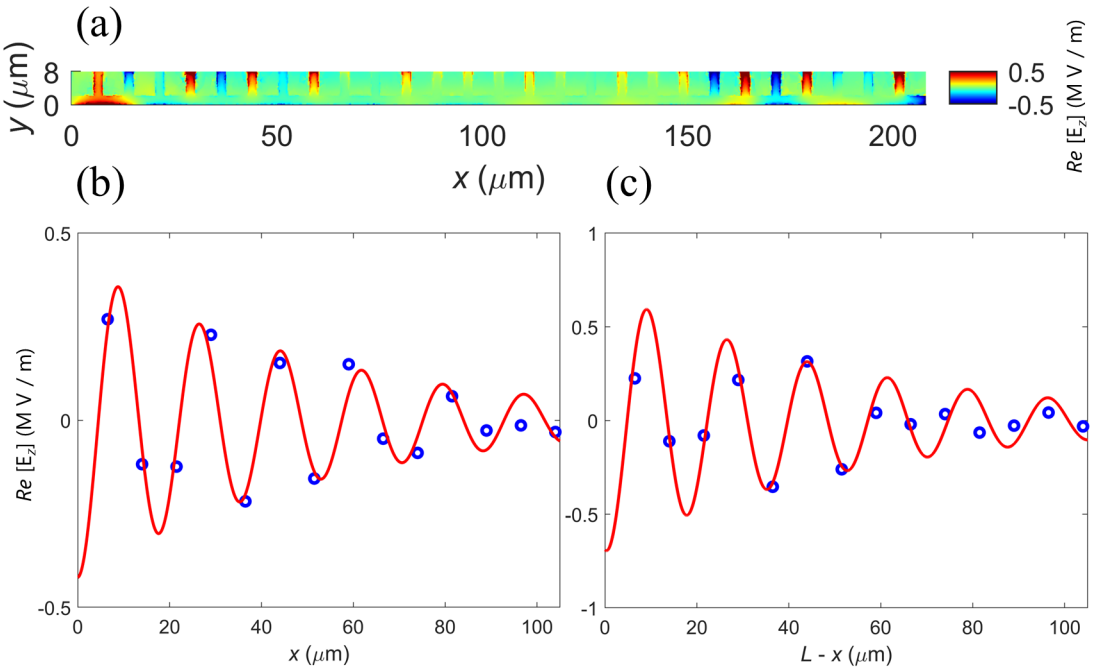

Figure 4.26: **(a)** SSPPs coupled on the surface of the waveguide using a grating structure with period $\alpha = 20$ µm, and a free-space beam normally incident to the waveguide with polarisation perpendicular to the waveguide axis. **(b)** SSPP launched on the LHS. Blue data points: Average value of the SSPP on each bar. Red line: Fit of the data using Eq. 4.1. The determined fitting parameters are: $E_0 = 0.42$ MV/m, $k_x \approx 3600$ cm^{-1}, $\theta \approx \pi$ rad, and $L_p = 54$ µm. **(c)** SSPP launched on the RHS. Blue data points: Average value of SSPP on each bar. Red line: Fit of the data using Eq. 4.1. The determined fitting parameters are: $E_0 = 0.68$ MV/m, $k_x \approx 3600$ cm^{-1}, $\theta = 3.3$ rad, and $L_p = 54$ µm.

4.9 Free-space excitation under oblique incidence using a grating structure

In this section, the coupling of a free-space beam to SSPPs on the waveguide is investigated incorporating grating structures with period of 6 µm, 20 µm with a grating offset of 10 µm, and 20 µm with a grating offset of 2 µm. These designs were found to provide optimum coupling in Section 4.7. The illuminating beam is obliquely incident on the gratings with an incidence angle of $\theta_i = 54^o$, and propagates in the $y - z$ plane with its polarisation also oscillating in that plane (Fig. 4.15). The free-space beam direction and polarisation matches the free-space beam of the experimental s-SNOM system. The results of these simulations will be compared to the results obtained experimentally for this waveguide structure in Section4.10.

4.9.1 Perpendicular Polarisation - Grating period 6 µm

Firstly, the coupling of a free-space beam to SSPPs on the waveguide is investigated incorporating grating structures with 6 µm. The real part of the out-of-plane electric field E_z is shown in Fig. 4.25 (a). From the figure, it is observed that two separate SSPPs are launched on the opposite ends of the waveguide, and propagating towards the centre of the waveguide. To analyse the electric field associated with the SSPPs launched on the waveguide, an average value of the electric field was obtained for each bar. The SSPPs on the LHS and RHS with a fit to Eq. 4.1 are shown in Fig. 4.25 (b) and (c).

The amplitude of the SSPP obtained on the LHS of the waveguide is $E_0 = 1.25$ MV/m which agrees with the simulations presented in Fig. 4.21. It can therefore be seen that the grating structure with 6 µm period has significantly improved the coupling strength of light to SSPPs when compared to the coupling strength observed with no grating (presented in Section 4.6.2) where the SSPP amplitude was $E_0 = 0.42.$ MV/m. These results provide confidence that the presence of the gratings in the experimental s-SNOM system will also improve the coupling strength of light to SSPPs on the waveguide.

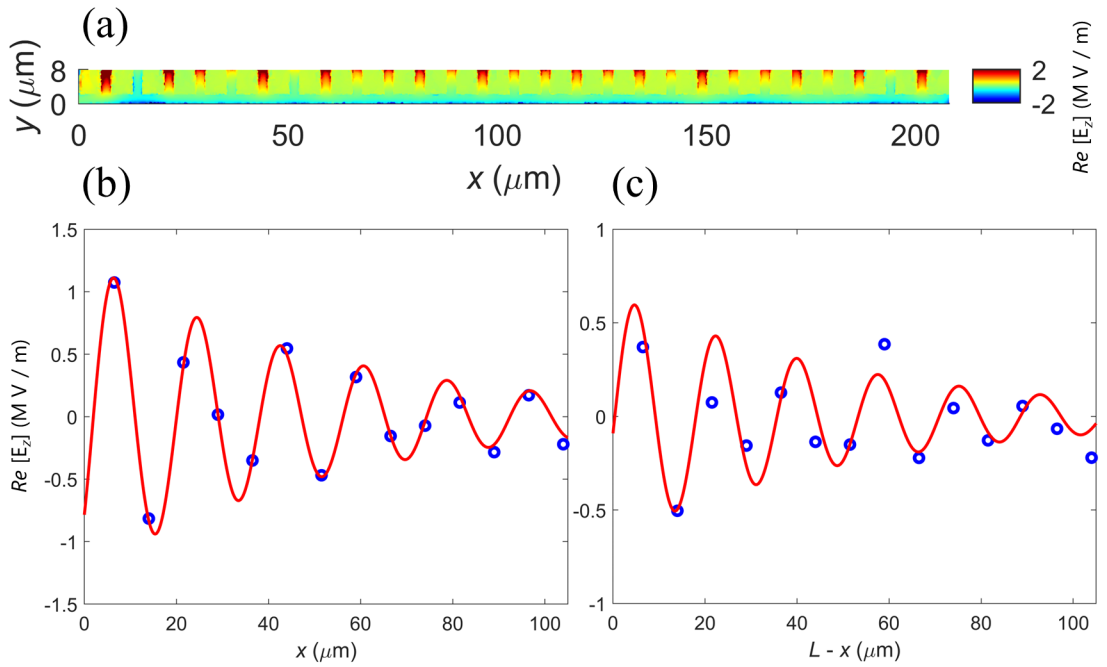

Figure 4.27: **(a)** SSPPs coupled on the surface of the waveguide using a grating structure with period $\alpha = 6$ µm, and a free-space beam obliquely incident on the waveguide with polarisation perpendicular to the waveguide axis. Two separate SSPPs are launched at each end of the waveguide and meet at its centre. **(b)** SSPP launched on the LHS. Blue data points: Average value of the out-of-plane electric field E_z on the surface of each bar. Red line: Fit of the simulation data using Eq. 4.1. The determined fitting parameters are: $E_0 = 1.25$ MV/m, $k_x \approx 3500$ cm^{-1}, $\theta = 2.25$ rad, and $L_p = 54$ µm. **(c)** SSPP launched on the RHS. Blue data points: Average value of the out-of-plane electric field E_z on the surface of each bar. Red line: Fit of the simulation data using Eq. 4.1. The determined fitting parameters are: $E_0 = 0.65$ MV/m, $k_x \approx 3550$ cm^{-1}, $\theta = 1.7$ rad, and $L_p = 54$ µm.

4.9.2 Perpendicular Polarisation - Grating period 20 µm and offset 10 µm

The coupling of a free-space beam to SSPPs on the waveguide is investigated incorporating a grating structure with period $\alpha = 20$ µm and $g_{off} = 10$ µm. The real part of the out-of-plane electric field E_z is shown in Fig. 4.28 (a). To analyse the electric field associated with the SSPPs launched on the waveguide, an average value of the electric field was obtained for each bar. The SSPPs on the LHS and RHS with a fit to Eq. 4.1 are shown in Fig. 4.28 (b) and (c).

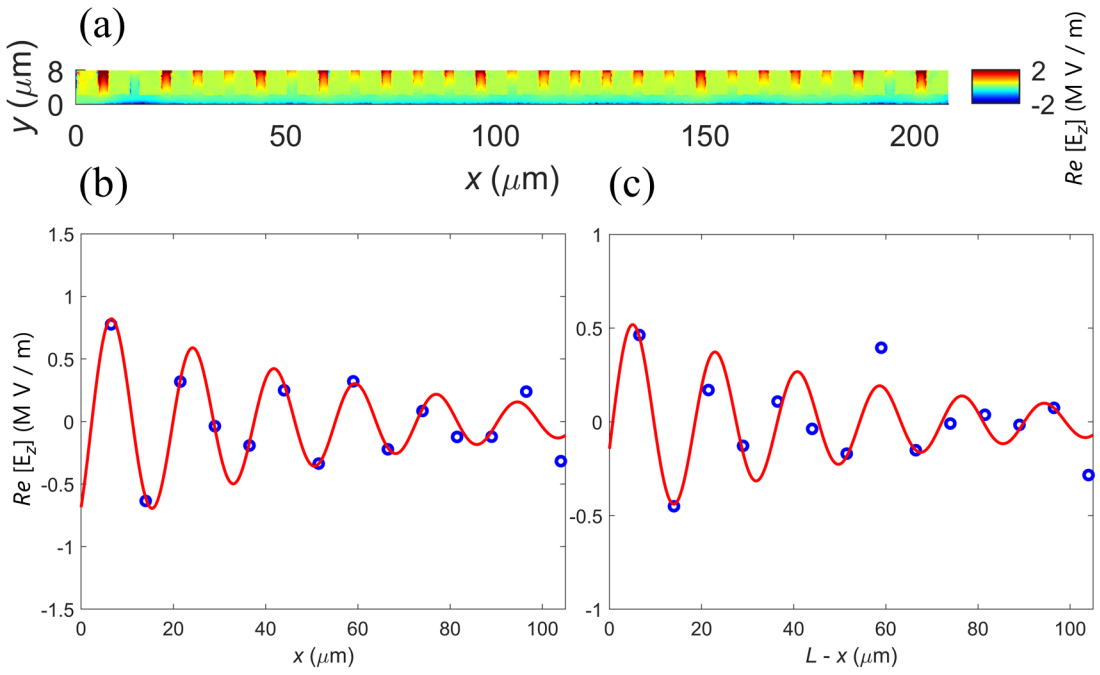

Figure 4.28: **(a)** SSPPs coupled on the surface of the waveguide using a grating structure with $\alpha = 20$ µm, $g_{off} = 10$ µm, and a free-space beam obliquelly incident on the waveguide with polarisation perpendicular to the waveguide axis. Two SSPPs are launched at each end of the waveguide and meet at its centre. **(b)** SSPP launched on the LHS. Blue data points: Average value of the out-of-plane electric field E_z on the surface of each bar. Red line: Fit of the simulation data using Eq. 4.1. The determined fitting parameters are: $E_0 = 0.95$ MV/m, $k_x \approx 3550$ cm^{-1}, $\theta = 2.4$ rad, and $L_p = 54$ µm. **(c)** SSPP launched on the RHS. Blue data points: Average value of the out-of-plane electric field E_z on the surface of each bar. Red line: Fit of the simulation data using Eq. 4.1. The determined fitting parameters are: $E_0 = 0.57$ MV/m, $k_x \approx 3550$ cm^{-1}, $\theta = 1.83$ rad, and $L_p = 54$ µm.

The obtained amplitude of the SSPP on the LHS of the waveguide is $E_0 = 0.95$ MV/m which agrees with the simulations presented in Fig. 4.21. The grating structure with $\alpha = 20$ µm and $g_{off} = 10$ µm has also improved the coupling strength of light to SSPPs when compared to the coupling strength observed for the same illumination geometry but without a grating (as presented in Section 4.6.2) where the SSPP amplitude was $E_0 = 0.42$ MV/m. However, the coupling strength is weaker when compared to the case with a grating structure with $\alpha = 6$ µm where the SSPP amplitude on the LHS is $E_0 = 1.25$ MV/m. It should be noted here that a waveguide with a grating structure where $\alpha = 20$ µm and $g_{off} = 10$ µm is also worth fabricating and measuring experimentally to compare the coupling strength of light to SSPPs on the waveguide for each grating period using the s-SNOM system.

4.9.3 Perpendicular Polarisation - Grating period 20 µm and offset 2 µm

The coupling of a free-space beam to SSPPs on the waveguide is investigated incorporating a grating structure with period $\alpha = 20$ µm and $g_{off} = 2$ µm. The real part of the out-of-plane electric field E_z is shown in Fig. 4.29 (a). To analyse the electric field associated with the SSPPs launched on the waveguide, an average value of the electric field was obtained for each bar. The SSPPs on the LHS and RHS with a fit to Eq. 4.1 are shown in Fig. 4.29 (b) and (c). The obtained amplitude of the SSPP on the LHS of the waveguide is $E_0 = 1.35$ MV/m, which is the highest amplitude obtained when compared to the other simulations with $\alpha = 6$ µm, and $\alpha = 20$ µm and $g_{off} = 10$ µm. These results show that this grating structure has increased the SSPP amplitude launched on the LHS by a factor of 3 when compared with the amplitude observed for this illumination geometry when no grating is present (Section 4.6.2). The simulations in Section 4.7.5 where the optimisations of the grating period and offset were presented also showed that the strongest coupling strength of light to SSPPs on the waveguide occurs when $\alpha = 20$ µm and $g_{off} = 2$ µm. Based on these results, the waveguide will also be fabricated using this grating structure and measured experimentally in Section 4.10.

The amplitude of the SSPP on the RHS of the waveguide is $E_0 = 0.7$ MV/m, which is higher than the amplitudes obtained for a grating with $\alpha = 6$ µm, and $\alpha = 20$ µm and $g_{off} = 10$ µm. This shows a trend that as the SSPP amplitude

on the LHS increases, the amplitude on the RHS with no gratings also increases. This could be attributed to the fact that a larger amplitude on the LHS leads to a stronger interference between the two SSPPs.

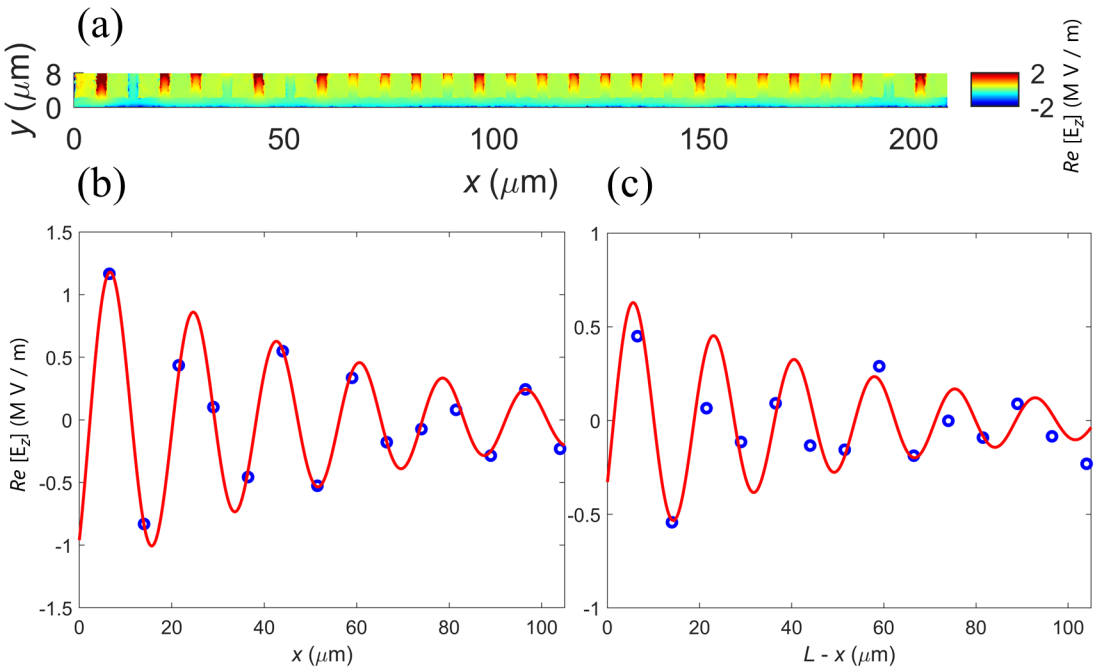

Figure 4.29: **(a)** SSPPs coupled on the surface of the waveguide using a grating structure with $\alpha = 20$ µm, $g_{off} = 2$ µm, and a free-space beam obliquely incident on the waveguide with polarisation perpendicular to the waveguide axis. Two SSPPs are launched at each end of the waveguide and meet at its centre. **(b)** SSPP launched on the LHS. Blue data points: Average value of the out-of-plane electric field E_z on the surface of each bar. Red line: Fit of the simulation data using Eq. 4.1. The determined fitting parameters are: $E_0 = 1.35$ MV/m, $k_x \approx 3500$ cm^{-1}, $\theta = 2.4$ rad, and $L_p = 54$ µm. **(c)** SSPP launched on the RHS. Blue data points: Average value of the out-of-plane electric field E_z on the surface of each bar. Red line: Fit of the simulation data using Eq. 4.1. The determined fitting parameters are: $E_0 = 0.7$ MV/m, $k_x \approx 3600$ cm^{-1}, $\theta = 2$ rad, and $L_p = 54$ µm.

4.10 Fabrication of asymmetric PSP waveguides

Based on the simulation results presented in the previous sections, three different designs of the asymmetric PSP waveguide were fabricated with design parameters presented in Section 4.2, a length $L = 73$ µm incorporating grating structures with periods $\alpha = 6$ µm, $\alpha = 20$ µm and an offset $g_{off} = 10$ µm, and $\alpha = 20$ µm and an offset $g_{off} = 2$ µm. The length of the grating structure was $L_g \approx 90$ µm and the length of each slit was $L_s = 25$ µm. A float-zone silicon substrate was used which has high resistance ($R > 10,000\,\Omega$ cm). The area of the substrate was 15 $\times$ 15 mm and the thickness was 500 ± 50 µm. The asymmetric PSP waveguides were lithographically patterned using a maskless aligner (MLA 150). Two layers of photoresist were used; firstly a lift-off resist was used to ensure that the edges of the metallic structurers would be smooth after the lift-off process. Secondly, a S1805 photoresist was used. After the photolithography process, the samples were placed in an electron-beam evaporator for the metal deposition. The layer thicknesses that were used in this step were titanium 5 nm (Ti) and gold 100 nm (Au). The samples were then placed in a microposit remover for the lift-off process. The fabricated waveguides with gratings of periods 6 µm, 20 µm and $g_{off} = 10$ µm, and 20 µm and $g_{off} = 2$ µm are shown in Fig. 4.30, 4.31, and 4.32 respectively.

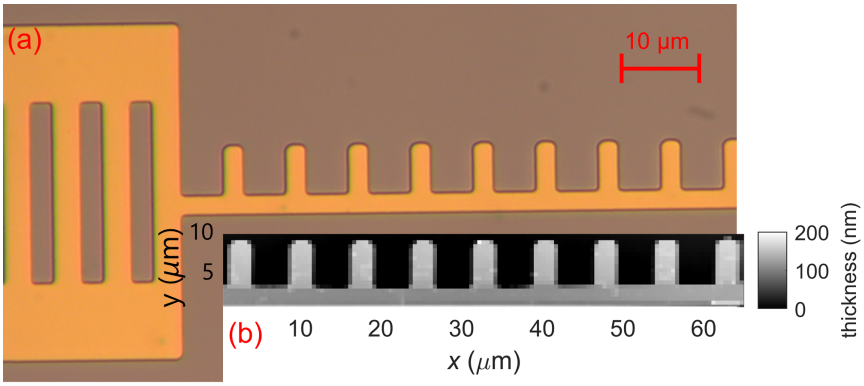

Figure 4.30: (a) Optical, and (b) AFM images of the asymmetric waveguide with length of 73 µm and grating period of 6 µm.

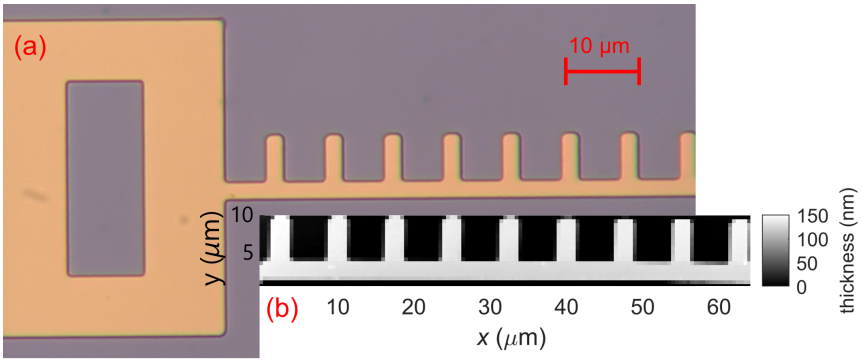

Figure 4.31: (a) Optical, and (b) AFM images of the asymmetric waveguide with length of 73 µm and grating period of 20 µm with a grating offset of 10 µm.

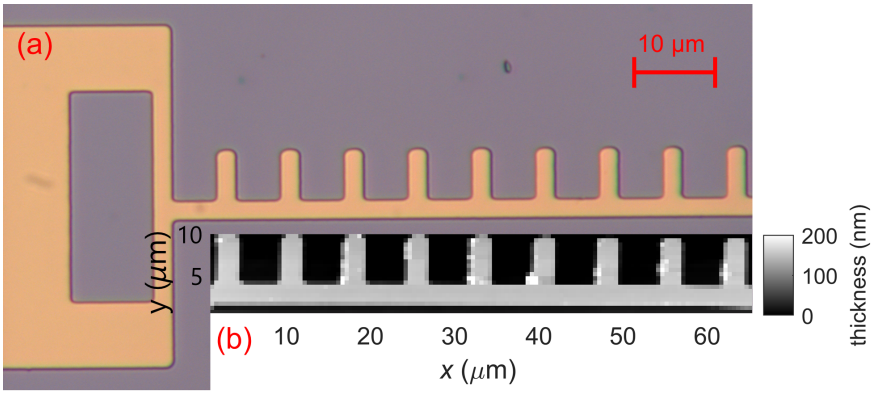

Figure 4.32: (a) Optical, and (b) AFM images of the asymmetric waveguide with length of 73 µm and grating period of 20 µm with a grating offset of 2 µm.

4.11 Experimental Results

4.11.1 THz-s-SNOM system

In order to experimentally confirm the excitation of SSPPs in the designed waveguide structures and investigate their properties, the spatial distribution of the out-of-plane field was measured using THz-s-SNOM. The experimental system setup is identical to the one described in Chapter 3. The QCL was cooled using a continuous-flow L–He cryostat and maintained at a heat sink temperature of 20 ± 0.01 K. A current source was used to drive the laser with a dc current of 420 mA, the QCL voltage was 6.4 V and the emitted power was ∼ 1 mW. Emission from the

QCL was focused to the vertically aligned tip of the s-SNOM system at an angle of $\sim 54^{o}$ relative to the surface normal. Unlike in the measurements presented in Chapter 3, s-SNOM measurements of the waveguide using an s-polarised incident beam are not presented in this chapter. The HWP was used to acquire measurements of the structures but the amplitude of the self-mixing voltage obtained was too small to adequately distinguish from the voltage noise floor. Therefore, for these measurements the free-space beam has a polarisation parallel to the probe axis (p-polarised). When the polarisation of the illuminating beam is parallel to the probe axis, the s-SNOM signal contains a sizable contribution that depends only on the local material properties of the sample (see Chapter 3), as well as a component due to the out-of-plane field associated with the SSPP. To remove the component contributed by the metal, the spatially-averaged value of the total measured signal is removed in the post-processing part of the analysis. This process is equivalent to that employed in Chapter 3, whereby the constant signal σ_{ε} is subtracted according to Eq. 3.5. The time constant used for these measurements is $\tau_s = 50$ ms, the pixel size in the axis of the waveguide ($x-$direction) is 330 nm, and the pixel size in the ($y-$direction) is 250 nm. To isolate the signal component arising from the near-field interaction between the probe and the sample, the microscope probe was operating in a tapping mode and the QCL terminal voltage was demodulated at harmonics of the tip tapping frequency ($\Omega \sim 80$ kHz) using a lock-in amplifier. The tapping amplitude of the tip was set to $A_{tip} \sim 200$ nm, which yields a spatial resolution of ~ 200 nm. The SM signal, arising from the field scattered from the s-SNOM tip and reinjected to the laser cavity, was derived from the $n = 2$ harmonic of the demodulated QCL terminal voltage after amplification using an ac-coupled low-noise voltage amplifier. By raster-scanning the sample in two dimensions, images with deep sub-wavelength resolution were obtained.

4.11.2 Parallel Polarisation

In this section, the excitation and mapping of SSPPs on the waveguide with grating periods of 6 µm is investigated. The beam is obliquely incident on the sample and the polarisation is parallel to the waveguide axis (Fig. 4.12). Due to the illumination orientation in this experiment, there are retardation effects observed on the out-of-plane field on the waveguide. This is because the phase of the excitation at each end of the waveguide will vary as the sample is scanned along the $x-$direction. This explains the variation of the signal over a long length-scale

seen in this data. The spatial distribution of the self-mixing voltage signal along the waveguide obtained experimentally using the s-SNOM system is shown in Fig. 4.33. To analyse the electric field associated with the SSPPs launched on the two ends of the waveguide, an average value of the self-mixing voltage was obtained for each bar. The spatially-averaged signal recorded for each bar, following subtraction of the constant offset arising from the sample permittivity, is shown in Fig. 4.34.

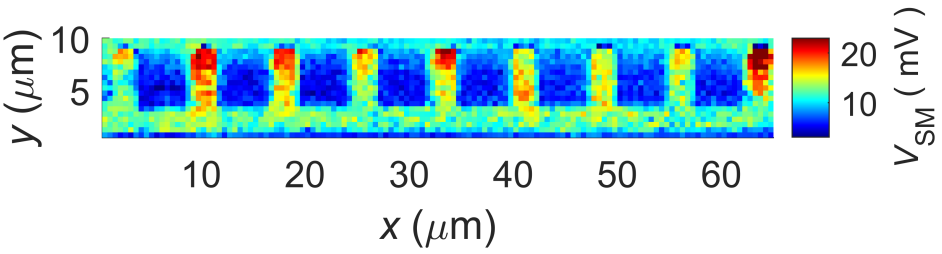

Figure 4.33: s-SNOM image ($n = 2$) of the waveguide where $\alpha = 6$ µm. The incident beam with $\lambda_0 = 87$ µm has a polarisation parallel to the waveguide axis.

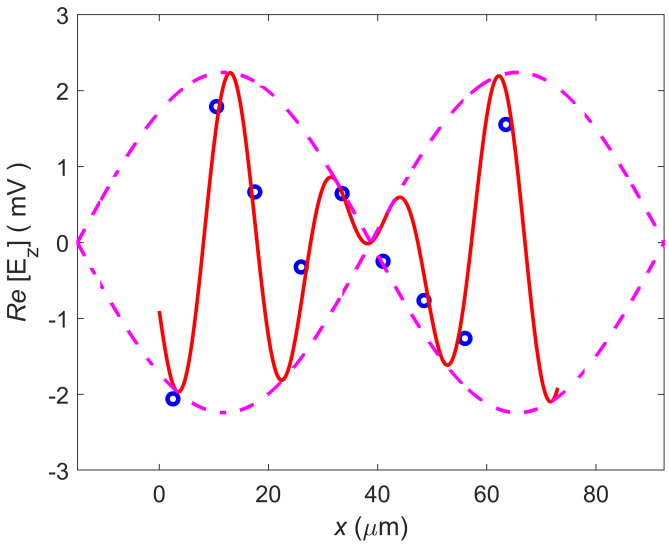

Figure 4.34: SSPPs launched on the opposite ends of the waveguide. Blue data points: Average value of the out-of-plane electric field on the surface of each bar. Red line: Fit of the data using Eq. 4.10. The fitting parameters are: $E_0 = 1.1$ mV, $k_{SP} = 3200$ cm^{-1}, $\theta_a = -0.88$ rad, $\theta_b = -1$ rad, and $\theta_i = 0.9425$ rad (54°). Magenta line: Retardation effects observed in the measured SM voltage due to the illumination orientation.

To explain the data from this experiment, a derivation of an equation is presented for the out-of-plane electric field as a function of distance along the waveguide axis (x) which accounts for the SSPPs launched from each end of the waveguide and the variation of their phase with the measurement position x. For the case of simplicity, this derivation does not account for any exponential decay of the SSPPs propagating from each end of the waveguide, and it assumes that the amplitude of the SSPPs launched from each end are equal. The purpose of this derivation is to illustrate the origin of the variation of the signal over a long length-scale observed in the data by modelling the total out-of-plane field as the summation of two SSPPs with equal amplitude E_0 and wavevector k_{sp} launched from opposite ends of the waveguide with phases θ_1 and θ_2:

$$E_z = E_0 \sin(k_{SP}x + \theta_1) + E_0 \sin(k_{SP}(L - x) + \theta_2), \tag{4.5}$$

where, due to the scanning of the sample in the stationary incident beam, the phases θ_1 and θ_2 vary with x according to:

$$\theta_1 = \theta_{01} - \frac{2\pi}{\lambda_0} x \sin(\theta_i), \tag{4.6}$$

and

$$\theta_2 = \theta_{01} + \frac{2\pi L \sin(\theta_i)}{\lambda_0} - \frac{2\pi}{\lambda_0} x \sin(\theta_i) = \theta_{02} - \frac{2\pi}{\lambda_0} x \sin(\theta_i), \tag{4.7}$$

where θ_{01} and θ_{02} are constants, and θ_i is the angle of incidence of the beam. Applying trigonometric identities to Eq. 4.5 gives:

$$E_z = 2E_0 \sin\left(\frac{k_{SP}L}{2} + \frac{\theta_1 + \theta_2}{2}\right) \cos\left(k_{SP}x - \frac{k_{SP}L}{2} + \frac{\theta_1 - \theta_2}{2}\right), \tag{4.8}$$

and then substituting Eq. 4.6 and Eq. 4.7 into Eq. 4.8 gives:

$$E_z = 2E_0 \sin\left(\frac{k_{SP}L}{2} + \frac{\theta_{01} + \theta_{02}}{2} - \frac{2\pi}{\lambda_0} x \sin\theta_i\right) \cos\left(k_{SP}x - \frac{k_{SP}L}{2} + \frac{\theta_{01} - \theta_{02}}{2}\right). \tag{4.9}$$

Finally, gathering constant phase terms and writing these as θ_a and θ_b gives:

$$E_z = 2E_0 \sin\left(\frac{-2\pi x \sin\theta_i}{\lambda_0} + \theta_a\right) \cos(k_{SP}x + \theta_b). \tag{4.10}$$

Equation 4.10 shows that the out-of-plane electric field E_z oscillates along x with wave-vector k_{SP}, but it is also modulated by an envelope function that varies with x along a longer length-scale. This effective wavelength of this variation is $\lambda_0/\sin(\theta_i) \approx 109$ µm. This equation is used to fit the data obtained from the experiments with this illumination geometry. From Fig. 4.34 it can be observed that the fit using Eq. 4.10 fits the experimental data obtained from Fig. 4.33 remarkably well (i.e. the envelope function in Eq 4.10 causes the long-range variation of E_z seen in the data.). This analysis demonstrates that the illuminating beam with oblique incidence on the waveguide causes retardation effects on the out-of-plane electric field. In addition, it is observed that the wave-vector value of $k_{SP} = 3200$ cm^{-1} is very similar to the wave-vector value obtained in the simulation where the SSPP is launched using a waveport (see Section 4.3) which yielded a value of $k_x = 3350$ cm^{-1}. These results confirm that SSPPs are launched and propagate on the fabricated waveguide with a grating structure of 6 µm.

It was found that Eq. 4.10 does not match the data as well for the case of 20 µm gratings as it does in the case of 6 µm gratings. There are various reason why this occurs. Firstly, the derivation of Eq. 4.10 assumes that the amplitude of the SSPPs launched on the ends of the waveguide are equal. Secondly, the exponential decay of the SSPPs as they propagate along the waveguide has not been included for the purpose of simplification. Furthermore, Eq. 4.10 does not take into account reflections which occur at both ends of the waveguide due to the finite length of the structure which is shorter than the propagation length, $L_p = 75$ µm obtained from the simulation in Section 4.3. These reasons lead to the fitting of the data using Eq. 4.10 not being highly accurate. Finally, this retardation effect adds an additional complexity to analysing the experimental data taken using this geometry, and therefore further measurements will focus on the perpendicular geometry.

4.11.3 Perpendicular Polarisation

In this section, the coupling of the illuminating beam from a QCL to SSPPs on the waveguide with grating periods of 6 µm, 20 µm and $g_{off} = 10$ µm, and 20 µm and $g_{off} = 2$ µm is investigated for a polarisation that is perpendicular to the waveguide axis (see Fig. 4.15). This QCL beam direction and polarisation in this experiment matches the direction and polarisation of the illuminating beam

in the simulation presented in Section 4.7. Firstly, the case for grating period of 6 µm is presented. The spatial distribution of the self-mixing voltage signal along the waveguide obtained experimentally using the s-SNOM system is shown in Fig. 4.35. To analyse the electric field associated with the SSPPs launched on the two ends of the waveguide, an average value of the self-mixing voltage was obtained for each bar, following subtraction of the constant offset arising from the sample permittivity, is shown in Fig. 4.36.

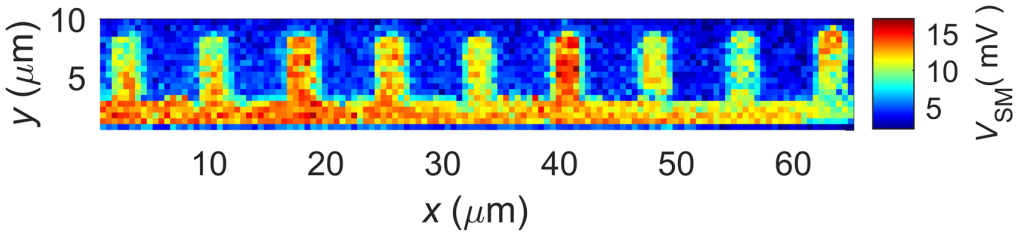

Figure 4.35: s-SNOM image ($n = 2$) of the waveguide where $\alpha = 6$ µm. The incident beam µm has a polarisation perpendicular to the waveguide axis.

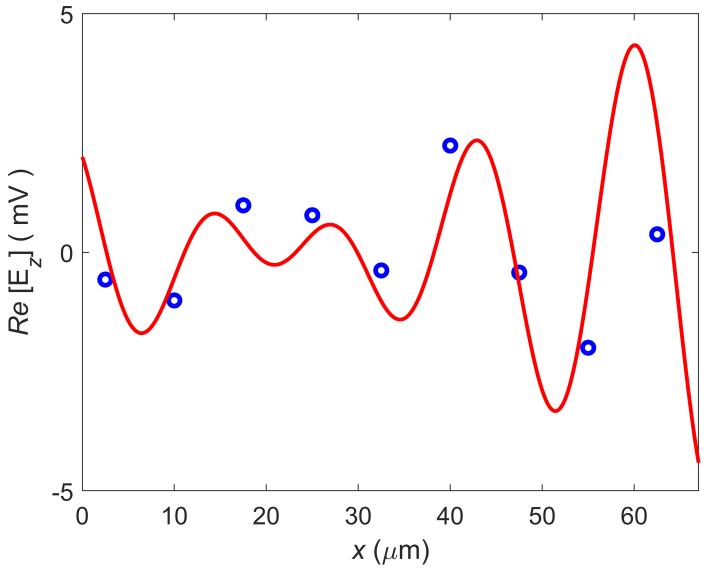

Figure 4.36: SSPPs launched on the opposite ends of the waveguide. Blue data points: Average value of the out-of-plane electric field on the surface of each bar. Red line: Fit of the data using Eq. 4.11. The fitting values are: $E_1 = 6.6$ mV, $E_2 = 9$ mV, $k_{SP} = 3600$ cm^{-1}, $L_p = 95$ µm, $\theta_1 = 2.1$ rad, and $\theta_2 = 3.08$ rad.

To explain the data from this experiment, an equation is presented for the out-of-plane electric field as a function of distance (x) which accounts for both SSPPs launched from each end of the waveguide, their propagation towards the centre, and the attenuation due to the propagation length. This equation differs from Eq. 4.1 because this experimental waveguide is shorter than that simulated, so the interference between the two SSPPs becomes more significant.

$$E_z = E_1 \sin(k_{SP}x + \theta_1)\, e^{-x/L_p} + E_2 \sin(k_{SP}(L-x) + \theta_2)\, e^{-(L-x)/L_p}, \tag{4.11}$$

where E_1 and E_2 are the SSPP amplitudes launched on the side of the grating (LHS) and the RHS respectively, k_{SP} is the wave-vector of the SSPPs, θ_1 and θ_2 are the phases of the SSPPs launched on the LHS and RHS respectively, L_p is the propagation length, and L is the waveguide length.

From Fig. 4.36 it can be observed that the fit using Eq. 4.11 fits the experimental data nicely. The analysis of this experiment demonstrates that the illuminating beam from the QCL with oblique incidence on the sample and perpendicular polarisation to the waveguide axis has launched SSPPs on the two ends of the waveguide, as it was observed in the simulations presented in Section 4.9. Furthermore, the wave-vector obtained experimentally and determined from the fitting procedure $k_{SP} = 3600$ cm cm^{-1} concurs with the wave-vector obtained in the simulation $k_{SP} \approx 3600$ cm^{-1}. One of the differences between the experimental data and the simulation is that the amplitude of the SSPP on the RHS with no gratings ($E_2 = 9$ mV) is greater than the amplitude on the LHS ($E_1 = 6.6$ mV) in the experimental data. The simulation in Section 4.9 showed that the amplitude on the LHS is greater than the one on the RHS. This difference occurs because the fitting equation does not account for reflections, which can significantly affect the values of E_z close to the waveguide ends. This will lead to the fit showing incorrect values of E_1 and E_2. Furthermore, the reflection at the LHS and the RHS have different values of R due to the difference in impedance at the two ends of the waveguide. Nevertheless, the fitting process is useful for confirming that SSPPs are launched from each end, and that they have the expected value of k_{sp}. This design will be directly compared with a free-space simulation which matches the s-SNOM experimental setup in the next section.

Next, the case for grating period of 20 µm and $g_{off} = 10$ µm is presented. The spatial distribution of the self-mixing voltage singal obtained experimentally using the s-SNOM system is shown in Fig. 4.37. To analyse the electric field associated with the SSPPs launched on the two ends of the waveguide, an average value of the self-mixing voltage was obtained for each bar, following subtraction of the constant offset arising from the sample permittivity. The fit to the data using Eq. 4.11 is shown in Fig. 4.38 which again shows that the equation fits the data nicely.

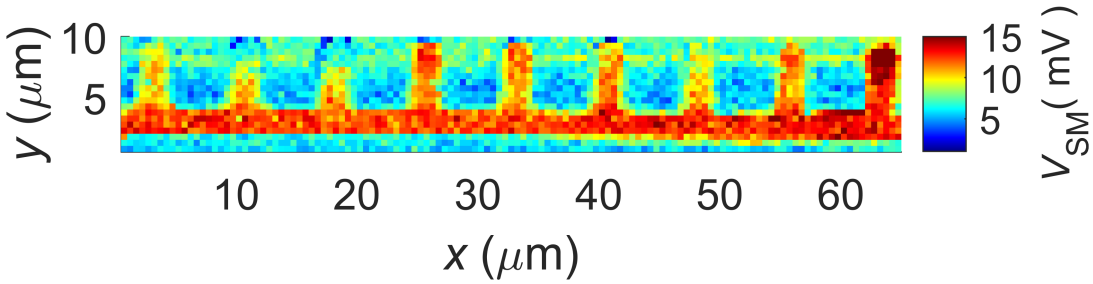

Figure 4.37: s-SNOM image ($n = 2$) of the waveguide with gratings of $\alpha = 20$ µm and $g_{off} = 10$ µm.

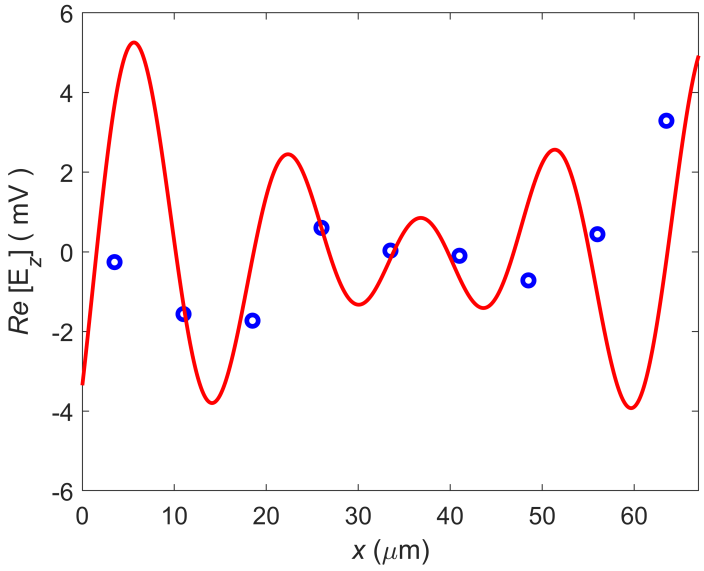

Figure 4.38: SSPPs launched on both ends of the waveguide. Blue data points: Average value of the out-of-plane electric field on the surface of each bar. Red line: Fit of the data using Eq. 4.10. The fitting values are: $E_1 = 10$ mV, $E_2 = 10$ mV, $k_{SP} = 3600$ cm^{-1}, $L_p = 75$ µm, $\theta_1 = -0.65$ rad, and $\theta_2 = -0.37$ rad.

This analysis confirms that the SSPPs observed in simulation (Section 4.7) are also observed experimentally. The wave-vector value obtained experimentally $k_{SP} = 3600$ cm^{-1} again concurs with the wave-vector obtained in Section 4.7. In addition, the phase values obtained from the fitting procedure are different to the ones obtained for a grating of 6 µm, which occurs due to a slightly different optical path length between these measurements.

Furthermore, the case for grating period of 20 µm and $g_{off} = 2$ µm is presented. The sptial distribution of the self-mixing voltage signal obtained experimentally using the s-SNOM system is shown in Fig. 4.39. To analyse the electric field associated with the SSPPs launched on the two ends of the waveguide, an average value of the self-mixing voltage was obtained for each bar, following subtraction of the constant offset arising from the sample permittivity. The fitted data using Eq. 4.11 is shown in Fig. 4.40.

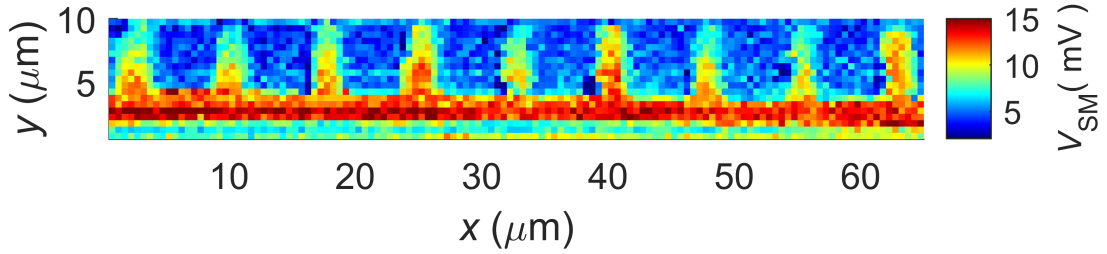

Figure 4.39: s-SNOM image ($n = 2$) of the waveguide with gratings of $\alpha = 20$ µm and $g_{off} = 2$ µm.

Figure 4.40 shows that Eq. 4.11 fits the data very nicely. Two separate SSPPs are launched on the opposite ends of the waveguide with a wave-vector value of $k_{SP} = 3600$ cm^{-1} which matches the wave-vector value obtained in the simulation. In Section 4.12, the experimental results obtained for the waveguide integrated with a grating structure which has a period of 20 µm and $g_{off} = 2$ µm are directly compared with a simulation of the waveguide with this grating structure. In this experiment, the experimental path length was also determined by the optimisation of the self-mixing signal on the waveguide bar at $x = 25$ µm in Fig. 4.39.

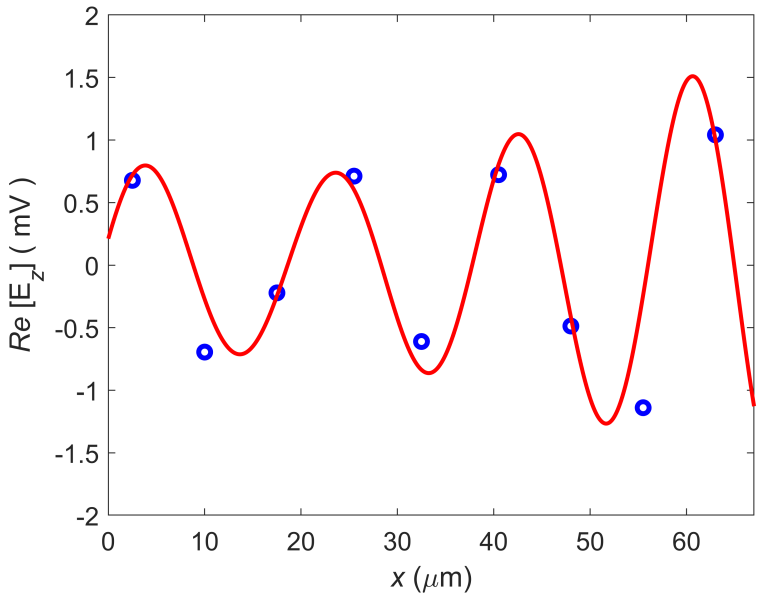

Figure 4.40: SSPPs launched on both ends of the waveguide. Blue data points: Average value of the out-of-plane electric field on the surface of each bar. Red line: Fit of the data using Eq. 4.10. The fitting values are: $E_1 = 1.72$ mV, $E_2 = 2.57$ mV, $k_{SP} = 3600$ cm^{-1}, $L_p = 100$ µm, $\theta_1 = 1$ rad, and $\theta_2 = 2.65$ rad.

4.11.4 Discussion

Overall, the results in this section have confirmed experimentally that the designed waveguides do support SSPPs as predicted, and with the expected wavelength. This is the first experimental observation of THz SSPPs propagating on PSP structures. The simulations in Section 4.9 predicted that the grating structure with period $\alpha = 20$ µm and grating offset $g_{off} = 2$ µm would provide the strongest coupling of light to SSPPs on the waveguide. However, due to the different system alignment between measurements which changes the optical path length and the signal amplitude, it is not possible to confirm this from the experimental data. Moreover, the amplitudes determined from this data are likely not reliable since the model does not account for reflections. Therefore it is necessary to compare the measurements directly with the simulation results.

4.12 Comparison of the experiments with simulations

Due to the complex nature of the SSPP fields supported by these structures with SSPPs launching from both ends of the waveguide, each of which reflect at the opposite ends, and the interference between the two SSPPs, it is necessary to directly compare the measurements with simulations. However, to do this the phase of the excited SSPPs in the simulations need to match that in the experiments. In the experiments, the phase of the coupled SSPPs on the waveguide is determined by the external optical path (cavity) length, whereas in the simulations it is determined by the location of the illuminating beam origin. To achieve this, the length of the waveguide in the simulations was set to $L = 73$ µm in order to match the length of the experimental structure. In each simulation the distance in the $z-$direction between the origin of the illuminating beam and the structure was varied with a step of 5 µm over a 100 µm range. As a result, the phase of the SSPPs in the simulations could be closely matched to the phases obtained in the experiments. The results are presented in this section.

Firstly, the case for grating period of 6 µm is presented. The out-of-plane electric field obtained in the simulation and experimentally is shown in Fig. 4.41. The figure presents a good agreement between the out-of-plane field distributions from the simulation and the experiment. On the RHS part of the waveguide, the experimental data matches the data obtained from the simulation very well. Particularly, the strongest positive field in the experimental image is observed on the waveguide bar at $x \approx 40$ µm. This is also observed in the simulation at $x \approx 45$ µm. Furthermore, a negative field is observed in the simulation on the waveguide bars at $x \approx 35$ µm and $x \approx 60$ µm. This is also observed in the experimental results where the weakest self-mixing voltage is observed on the waveguide bars at $x \approx 35$ µm and $x \approx 55$ µm. However, on the LHS part of the waveguide, the field on the second and third waveguide bars ($x \approx 15$ µm and $x \approx 25$ µm) does not concur for the simulation and the experiment. The field of the second bar in the simulation is strong and positive whereas the field on the second bar in the experiment is weak. The field of the third bar in the simulation is weak and negative whereas the field on the third bar in the experiment is strong.

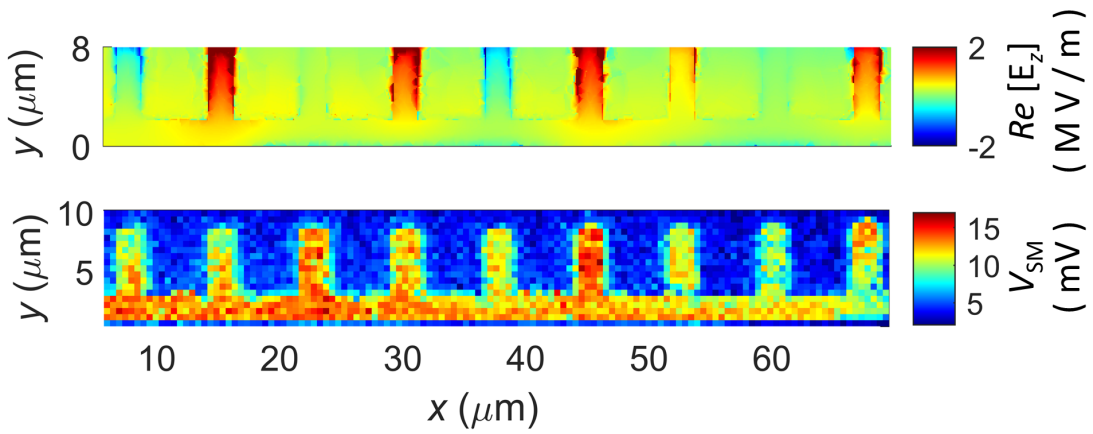

Figure 4.41: Comparison of the out-of-plane electric field obtained in simulation and experimentally for a waveguide with length $L = 73$ µm, and grating period $\alpha = 6$ µm. (upper): data obtained from the simulation, (lower): data obtained experimentally using s-SNOM ($n = 2$).

There are multiple reasons that could be attributed to this discrepancy. Firstly, it has been shown in the literature that the presence of the probe tip has a significant influence on the resulting s-SNOM image [258, 259], due to the near-field interaction between the tip and the sample. Therefore, this observed discrepancy could be due to the presence of the tip. The simulation that was performed to obtain 4.41 (a), did not include a probe tip. To investigate the effects of the tip on the resulting s-SNOM image, further simulations could be performed where the probe tip is included and its effects on the measured field distribution of the SSPPs are studied. To study the effects of the tip in a simulation environment, the field amplitude value of each pixel should be obtained when the probe tip is placed in the near-field of that pixel. Furthermore, the dimensions of the experimental samples deviate slightly from the dimensions of the waveguide designed in the simulation (see Section 4.2). This effect occurs due to the resolution limit of the optical lithography which is $\sim 1 - 2$ µm. The designed width of each bar in simulation is $d - a = 2$ µm, whereas the bars on the fabricated waveguide have a width of ~ 2.4 µm. In addition, the body of the designed waveguide in the simulation is $w - h = 2$ µm, whereas the body of the fabricated waveguide is 2.25 µm. Another reason for this discrepancy is that the illuminating beam from the QCL is not perfectly linearly polarised as it was shown in Chapter 3 unlike the free-space beam in the simulation. As a result, the incident beam contains both parallel and perpendicular electric field components of the polarisation, each of which interact

differently with the grating structure. Therefore, the elliptical beam from the QCL could affect how SSPPs are launched on the waveguide.

To analyse and compare the field associated with the SSPPs in the simulation and experimentally, an average value of the field was obtained for each bar. The simulation and experimental data were normalised and Eq. 4.11 was used to fit the normalised data as shown in Fig. 4.42.

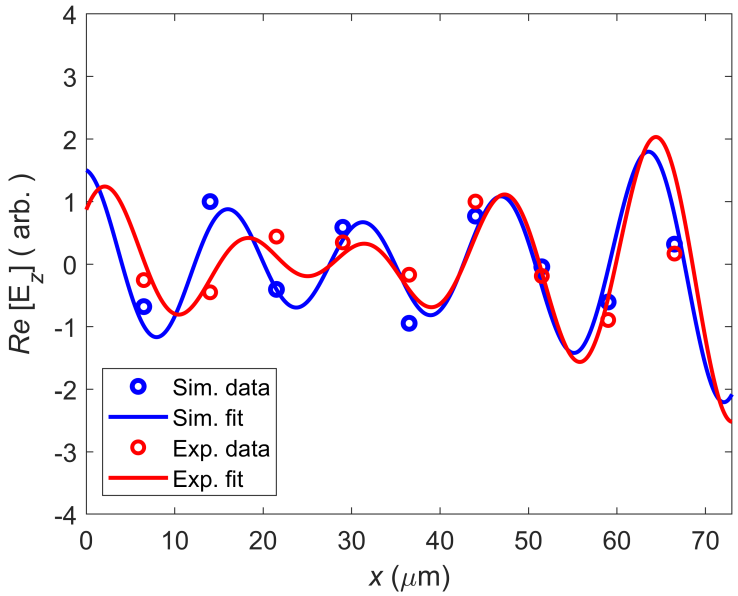

Figure 4.42: Comparison between the out-of-plane electric field E_z on the waveguide obtained from the simulation and experimentally. **Blue data points:** Simulated average value of E_z on each bar. **Blue line:** Fit the simulation data to Eq. 4.11. The fitting values are: $E_1 = 3$ (arb.), $E_2 = 3.55$ (arb.), $k_{SP} = 3600$ cm^{-1}, $L_p = 95$ µm, $\theta_1 = 1.3$ rad, and $\theta_2 = -2.15$ rad. **Red data points:** Experimental average value of E_z on each bar. **Red line:** Fit the experimental data to Eq. 4.11. The fitting values are: $E_1 = 3.2$ (arb.), $E_2 = 4$ (arb.), $k_{SP} = 3600$ cm^{-1}, $L_p = 95$ µm, $\theta_1 = 0.6$ rad, and $\theta_2 = 2.85$ rad.

The fits to the simulation and experimental data using Eq. 4.11 show an excellent agreement on the RHS. The wave-vectors obtained from the fits to the simulation and the experimental data concur and in both cases the value is $k_{SP} = 3600$ cm^{-1}. The propagation length of the SSPPs coupled on the two ends of the waveguide also has the same value of $L_p = 95$ µm for both cases. These results show that the electric field associated with the SSPPs on the waveguide obtained

in simulation has been matched with the field obtained and experimentally.

Next, the case for grating with period $\alpha = 20$ µm and grating offset $g_{off} = 2$ µm is presented. The out-of-plane electric field obtained from the simulation and experimentally is shown in Fig. 4.43.

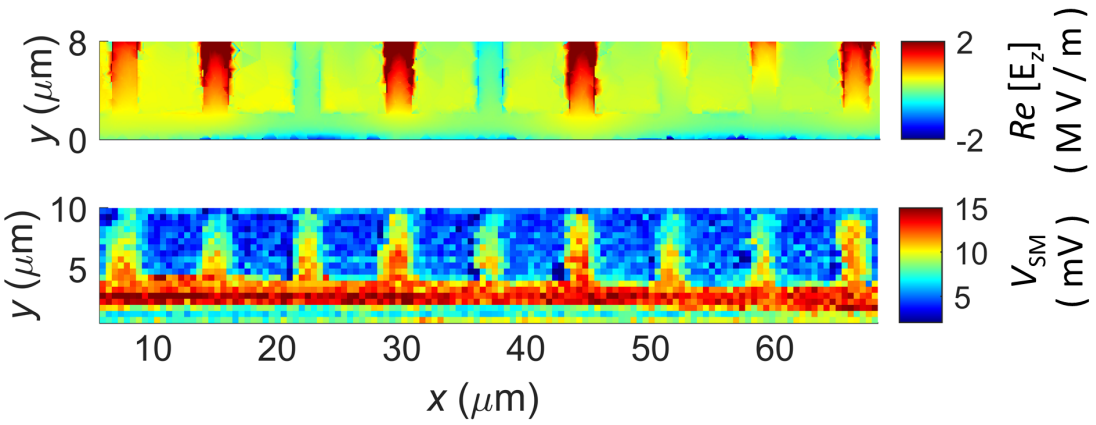

Figure 4.43: Comparison of the out-of-plane electric field obtained in simulation and the experiments for a waveguide with length $L = 73$ µm, grating period $\alpha = 20$ µm, and grating offset $g_{off} = 2$ µm. (upper): data obtained from the simulation, (lower): data obtained experimentally using s-SNOM ($n = 2$).

Figure 4.43 presents a good agreement between the out-of-plane field distributions from the simulation and the experiment. The strongest positive field in the experimental image is observed on the waveguide bars at $x \approx 40$ µm and $x \approx 65$ µm. A strong positive field is also observed in the simulation on the waveguide bars at $x \approx 45$ µm and $x \approx 65$ µm. Furthermore, the most negative field in the simulation is observed on the waveguide bar at $x \approx 35$ µm, where a weak self-mixing voltage on that waveguide bar is also seen experimentally. As observed in the previous case, the field on the second and third waveguide bars ($x \approx 15$ µm and $x \approx 25$ µm) does not concur for the simulation and the experiment. The field of the second bar in the simulation is strong and positive whereas the field on the second bar in the experiment is weak. The field of the third bar in the simulation is weak and negative whereas the field on the third bar in the experiment is strong.

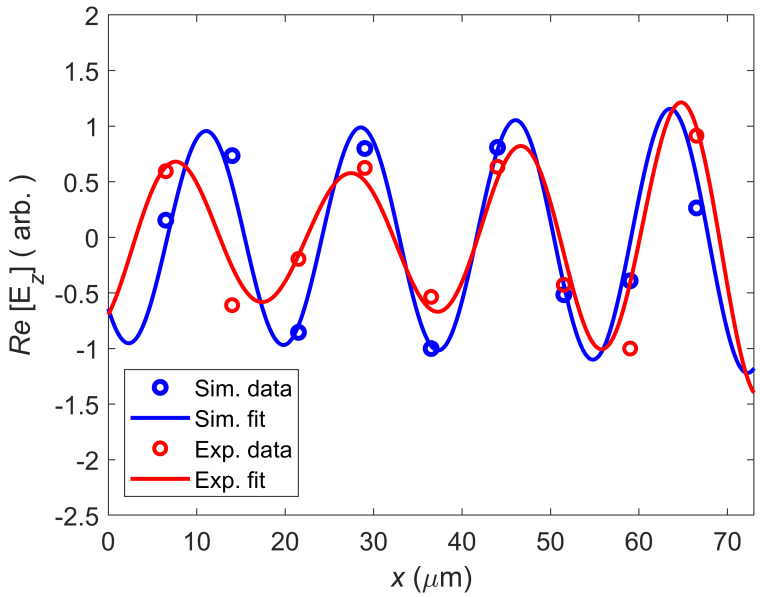

Figure 4.44: Comparison between the out-of-plane electric field E_z on the waveguide obtained from the simulation and experimentally. **Blue data points:** Simulated average value of E_z on each bar. **Blue line:** Fit the simulation data to Eq. 4.11. The fitting values are: $E_1 = 0.5$ (arb.), $E_2 = 1$ (arb.), $k_{SP} = 3600$ cm^{-1}, $L_p = 95$ µm, $\theta_1 = -2.35$ rad, and $\theta_2 = -1.84$ rad. **Red data points:** Experimental average value of E_z on each bar. **Red line:** Fit the experimental data to Eq. 4.11. The fitting values are: $E_1 = 1.5$ (arb.), $E_2 = 2$ (arb.), $k_{SP} = 3600$ cm^{-1}, $L_p = 95$ µm, $\theta_1 = -0.48$ rad, and $\theta_2 = -1.16$ rad.

The fits to the simulation and experimental data using Eq. 4.11 show an excellent agreement on the RHS. In addition, the wave-vectors obtained from the fits to the simulation and the experimental data concur and in both cases the value is $k_{SP} = 3600$ cm^{-1}.

The propagation length of the SSPPs coupled on the two ends of the waveguide also has the same value of $L_p = 95$ µm for both cases. These values are consistent with the ones obtained for the case of 6 µm grating period. These results show that the electric field associated with the SSPPs on the waveguide obtained in simulation has been matched with the field obtained and experimentally. It can also be observed that the field on the LHS show a slight discrepancy between the simulation and experimental data. This could be attributed to the presence of the probe tip in the near-field of the waveguide, the differences in the physical dimensions of the waveguide between the simulation and the experiment, and

the elliptically polarised free-space beam radiated from the QCL. Since this same discrepancy is seen in both cases with 6 µm and 20 µm grating periods, the most likely reason for this discrepancy is the presence of the probe tip in the near-field of the waveguide.

4.13 Summary

To conclude, this chapter presented the design and simulation of the novel asymmetric PSP waveguide structure which supports SSPPs at THz frequencies. Eigenmode simulations were ran to obtain the SSPP wave-vector for an incident frequency of 3.45 THz. A waveguide with length $L = 208$ µm was simulated to analyse the out-of-plane electric field E_z propagation along the waveguide and obtain its finite propagation length. A waveguide with length $L = 73$ µm was also simulated to obtain the S_{21} Parameters of the waveguide, the cut-off frequency, and investigate the effects of reflections. Next, the waveguide was simulated using a free-space beam which showed a different coupling of light to SSPPs on the waveguide compared to the simulations with an excitation port. The effects of varying the beam direction, the polarisation and the angle of incidence were investigated. The design and optimisation of a grating structure was presented to improve the coupling strength of light to SSPPs on the waveguide. Furthermore, the fabrication process of the waveguide structures and the high resolution microscopy of the out-of-plane field of THz-frequency SSPPs propagating on these structures were presented. The images acquired using s-SNOM were compared directly to the simulations where the phases of the SSPPs in the simulations matched those of the experiments. The comparison between the simulation and experimental data showed a good agreement, which is remarkable given the complexity of the experiments. Therefore, the results show successful mapping of the spatial distribution of the electric field associated with THz-frequency SSPPs propagating on an asymmetric PSP waveguide with sub-wavelength resolution. This is the first time this has been reported.

Chapter 5

Terahertz microscopy of SSPPs on symmetric planar waveguides

5.1 Introduction

In this chapter, a symmetric waveguide which supports planar surface plasmons (PSP) is presented (see Fig. 5.1 (a), inset) in which the two sides of the planar metal strip are symmetrically corrugated by grooves. This waveguide design is based on the asymmetric waveguide (see Chapter 4) and it also supports SSPPs on its surface. Well-confined SSPPs can be supported on either side of the symmetric waveguide. Owing to the thin central strip of the symmetric waveguide, the SSPPs supported by the two sides will interact with each other, and split into two supermodes: even mode (symmetric) (Fig. 5.1 (b)) and odd mode (anti-symmetric) (Fig. 5.1 (c)). If the same values of the design parameters (d, a, w, h, t) are used, the even mode of a straight symmetric waveguide is expected to have a shorter propagation length when compared to that of the asymmetric waveguide [136]. However, the even mode of the symmetric waveguide is less sensitive to bending losses when the waveguide is folded, which makes the waveguide preferable for the design of flexible circuits. Furthermore, the odd mode of the symmetric waveguide shows a weaker confinement on the waveguide but it has a longer propagation length [136]. Theoretical studies of such structures in the sub-millimetre frequency range $(0.1 - 1)$ THz have been reported in [260], where experimental verification of SSPPs was also reported in the microwave frequency range $(1 - 10)$ GHz.

In this chapter, theoretical studies of symmetric PSP waveguides and their experimental verification is reported in the terahertz range (3.45 THz) for the first time. Initially, the structure was designed in ANSYS HFSS and its dispersion relations were obtained using an eigen-mode solver. Next, a waveguide with finite length was simulated using excitation ports at the two ends of the structure to launch and detect the SSPPs propagating on the waveguide. The out-of-plane electric field E_z was visualised and its amplitude and propagation length values were obtained. The S_{21} Parameters, and the cut-off frequency of the waveguide structure were also obtained. Furthermore, the waveguide was simulated with excitation by a free-space beam and perpendicular polarisation which showed a different coupling of light to SSPPs on the waveguide compared to the simulations with an excitation port. The structures were then fabricated on a silicon substrate using photo-lithographic and metallic deposition techniques. A QCL was used to illuminate the structures with an incident frequency of 3.45 THz and the s-SNOM system was used to measure the out-of-plane electric field E_z. The results from the simulations and the experiments are directly compared and show an adequate agreement between the two. The results in this chapter show successful mapping of the spatial distribution of the electric field associated with the THz-frequency SSPPs propagating on the PSP symmetric waveguide with sub-wavelength resolution for the first time.

5.2 Design of PSP symmetric waveguide structures

The waveguide design shown in Fig. 5.1 (a, inset) consists of metal strips of thickness t and width w, in which a periodic array of grooves is patterned. This structure design is adapted from [136]. The period of the array is d which is treated as the unit length, and the width of the groove is a. The material used to form the plasmonic waveguide was gold and it was placed on a silicon substrate with a dielectric constant of $\varepsilon = 11.65$. This value was obtained experimentally using THz-TDS on the float-zone (FZ) silicon substrate. The radiation emitted from the QCL in the experimental system is 3.45 THz. Therefore, the waveguide was designed with parameter values that allow the free-space beam to launch SSPPs on the surface of the waveguide with deep sub-wavelength confinement. The value of the periodicity was set to $d = 7.5$ µm, the value of the groove width was

$a = 5.5$ µm, and the thickness of the waveguide was $t = 0.1$ µm. These parameter values were kept equal to the ones used for the design of the asymmetric structure presented in Chapter 4. The value of the waveguide width w and groove height h were adjusted in order to match the momentum value of the even mode of the symmetric waveguide with the momentum value of the fundamental mode of the asymmetric waveguide $k_{xe}(symmetric) = k_x(asymmetric)$. To achieve this, the value of the waveguide width was set to $w = 7.5$ µm, and the value of the groove height was set to $h = 5.5$ µm. This modification results in a higher propagation length of the symmetric waveguide as will be shown in Section 5.3, but a slightly weaker field confinement.

The dispersion relations of the even and odd modes of the TM-polarised waves propagating along the x-direction with momentum k_{xe} and k_{xo} respectively were numerically calculated using the eigenmode solver in ANSYSS HFSS and are presented in Fig. 5.1 (a). For this calculation a unit cell of the waveguide was considered, periodic boundaries were used in the x-direction and PEC boundaries in the y-direction. By sweeping the phase difference $\Delta\theta$ of the EM fields at the opposite boundaries in the x-direction from 0° to 180°, the eigen-frequencies of the spoof surface plasmon polaritons (SSPPs) are calculated within the first Brillouin zone [253]. The dispersion curves reveal that there are two distinct modes with different asymptotic (plasma) frequencies and slightly different wave-vectors.

The wave-vectors of the even (k_{xe}) and odd (k_{xo}) modes are related to the parameter $\Delta\theta$ whose values are obtained from the eigen-mode simulation for an incident frequency of $f_0 = 3.45$ THz. The relationships between the wave-vectors and $\Delta\theta$ are $k_{xe} = (\pi\Delta\theta_e)/(180\,d)$ and $k_{xo} = (\pi\Delta\theta_o)/(180\,d)$ which yield values of $k_{xe} = 3500$ cm^{-1} and $k_{xo} = 2440$ cm^{-1}. The SSPP wavelengths of the even λ_e and odd λ_o modes are related to their corresponding SSPP wave-vectors according to the relations: $\lambda_e = 2\pi/k_{xe}$ and $\lambda_o = 2\pi/k_{xo}$. This leads to values of $\lambda_e = 18$ µm, and $\lambda_o = 25.75$ µm, corresponding to $\sim \lambda_0/5$ and $\sim \lambda_0/3.4$ respectively.

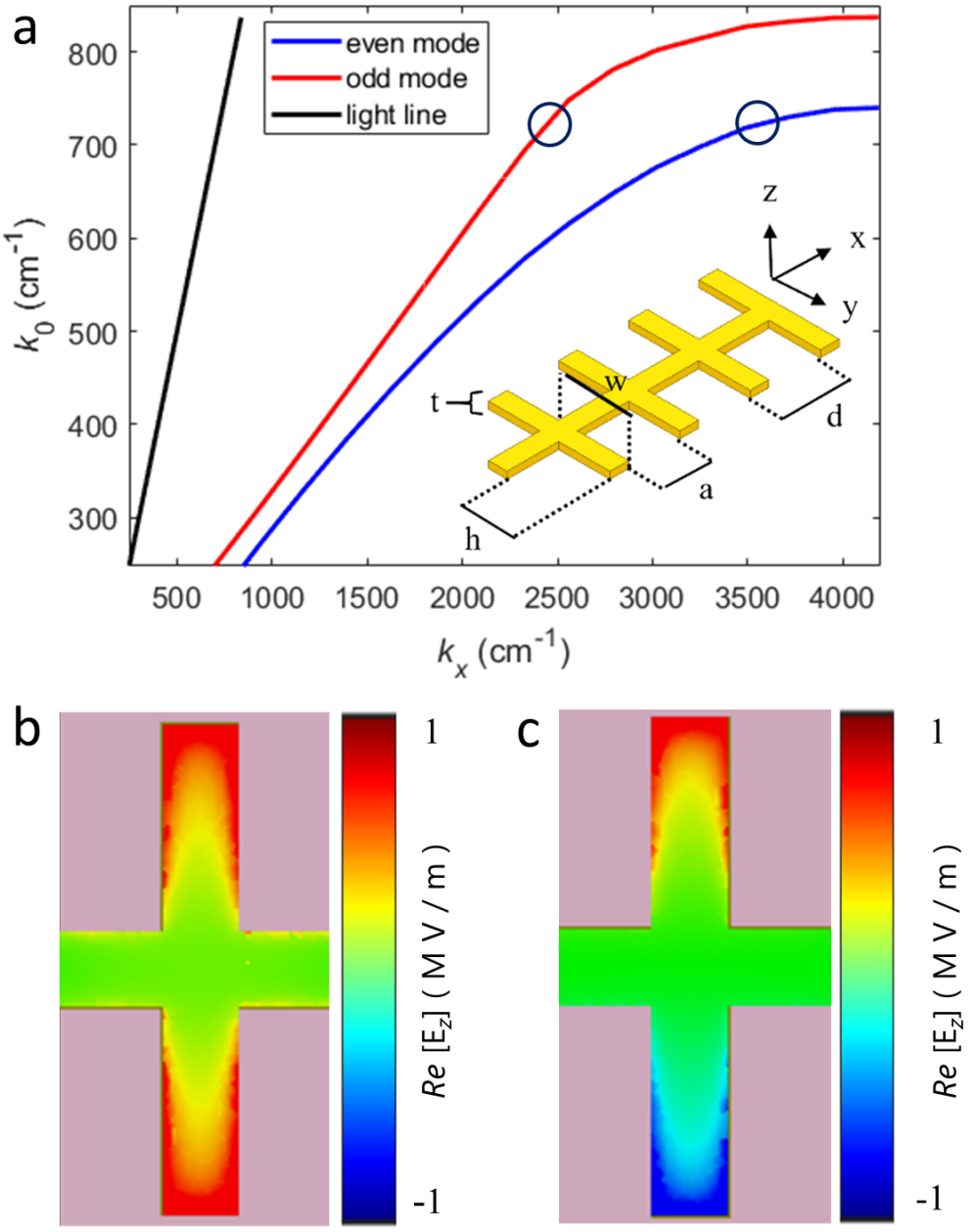

Figure 5.1: Dispersion relation and local field distribution of the symmetric PSP waveguide. (a) Dispersion relation for the even (blue) and odd (red) PSP modes. (inset) Geometric parameters of the structure, with $w = d$, $a = 0.73d$, and $h = 0.73d$, where $d = 7.5$ µm. The assigned material on the waveguide was gold with thickness of 100 nm, and it was placed on a silicon substrate with thickness of 50 µm. (b) Real component of the SSPP even mode (normalised), and (c) real component of the SSPP odd mode (normalised) obtained using FEM.

5.3 Simulation using excitation ports

To calculate the out-of-plane electric field E_z and the S_{21} Parameters of a finite waveguide, a new simulation environment was setup in ANSYS HFSS. The symmetric PSP waveguide was designed with length of 208 µm and 27 repetitions of the unit cell with periodicity $d = 7.5$ µm. Two wave ports were used at the beginning ($x = 0$) and the end ($x = 208$) µm of the waveguide to launch SSPPs on the structure and also obtain the S_{21} Parameters. Open boundaries were used for the simulation using the radiation boundary in HFSS. The real component of the out-of-plane electric field on the surface of the waveguide is shown in Fig. 5.2, for an excitation frequency of 3.45 THz.

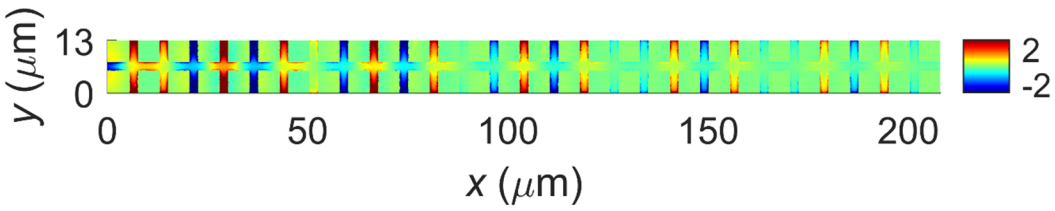

Figure 5.2: Real part of the out-of-plane electric-field component E_z (MV/m) confined on the surface of the symmetric waveguide with length, $L = 208$ µm.

In order to quantify the field strength associated with the SSPPs as they propagate along the waveguide, the average electric-field E_z was spatially averaged within each bar of the waveguide. These averaged values were then plotted as discrete points as a function of the distance x along the waveguide, as shown in Fig. 5.3. Each average value was assigned at the centre point of its respective bar in the x direction. To determine the wavelength and propagation length of the SSPPs the data in Fig. 5.3 was numerically fit to the equation 4.1. The SSPPs are modeled as propagating waves bound to the surface of the metallic waveguide layer, which has an out-of-plane electric field E_z, wave-vector k_x, phase θ, and propagation length L_p. The parameter values obtained from this fitting procedure are: $E_0 = 6.7$ MV/m, $k_x = 3350$ cm^{-1}, $\theta = 1.2$ rad, and $L_p = 83$ µm. The value of E_0 which is measured in MV/m is arbitrary since it depends on the excitation field strength set in the simulation environment. In addition, the wavelength of the SSPP is calculated to be $\lambda_{SP} = 2\pi/k_x \approx 18.75$ µm. This concurs with the SSPP wavelength of the even mode obtained from the dispersion relation shown in Fig. 5.1 a, which predicts a value $\lambda_{SP} = 18$ µm at 3.45 THz. It should be noted

here that the symmetric structure supports both even and odd SSPP modes, however at an incident frequency $f_0 = 3.45$ THz the even mode is dominant and a single mode component is sufficient to fit the data extracted from the simulations. Figure 5.3 demonstrates that Eq. 4.1 fits the simulation data very nicely.

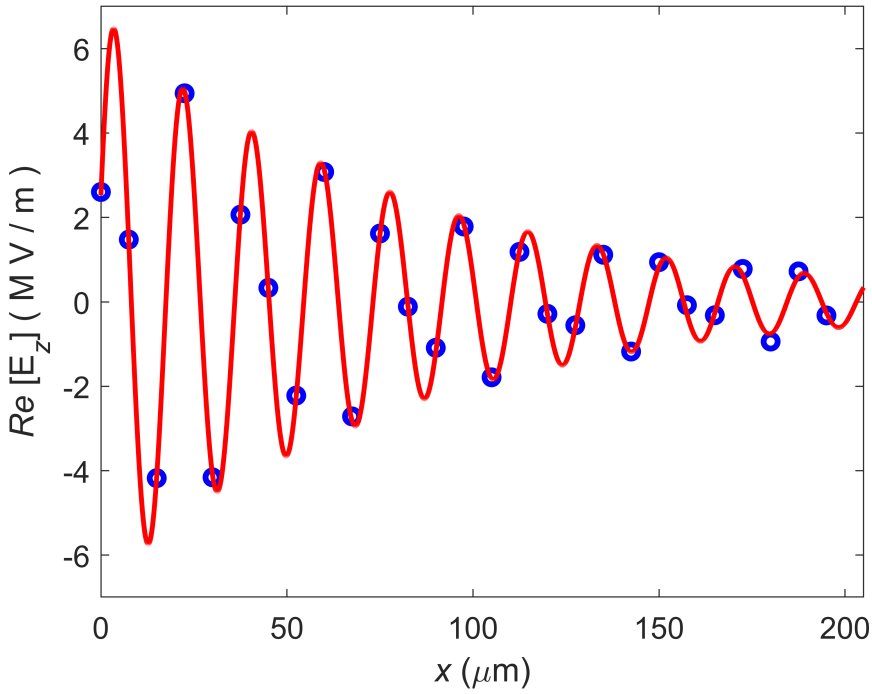

Figure 5.3: Analysis of the SSPP coupled on the symmetric waveguide. The data were extracted from the simulation and the average value of each bar was calculated. The extracted values of the fitting parameters yield: $E_0 = 6.7$ MV/m, $k_x = 3350$ cm^{-1}, $\theta = 1.2$ rad, and $L_p = 83$ µm.

To obtain the S_{21} Parameters of the PSP waveguide, a waveguide was simulated with length $L = 73$ µm consisting 9 repetitions of the unit cell, which is smaller than the propagation length of the SSPP. The real part of the out-of-plane electric field coupled on the surface of the waveguide is shown in Fig. 5.4. The S_{21} Parameters obtained for the waveguide with length of 73 µm is shown in Fig. 5.5.

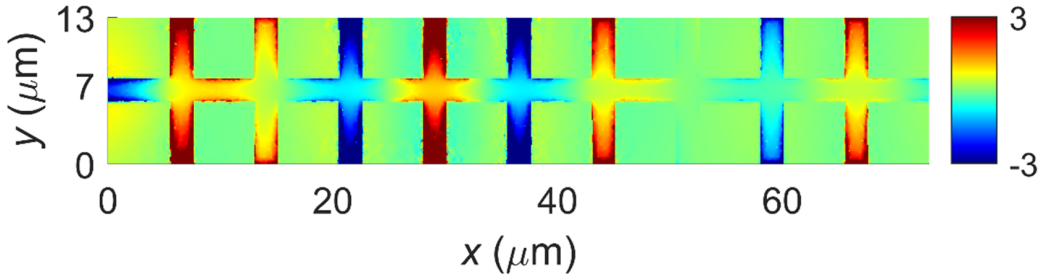

Figure 5.4: Real part of the out-of-plane electric-field component E_z (MV/m) confined on the surface of the asymmetric waveguide with length, $L = 73$ µm.

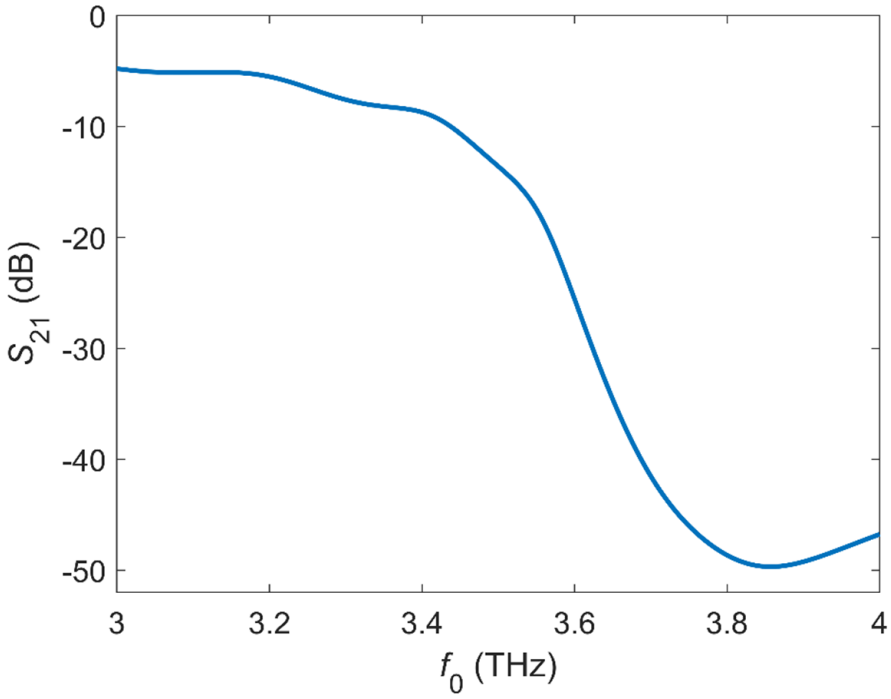

Figure 5.5: S_{21} Parameters of the symmetric waveguide with length $L = 73$ µm.

From Fig. 5.5, it is observed that at frequency of 3.45 THz, the transmitted power has been attenuated by $\sim$ 10 dB. A cut-off frequency of $f_c \approx 3.7$ THz is observed, where the transmitted power is attenuated by $\sim$ 45 dB. The effect of the cut-off frequency arises due the nature of the waveguide which behaves as an optical low-pass filter. For incident frequencies which lead to the SSPP wave-vector $k_x > \pi/d$, the Bragg reflection regime is entered, in which no propagating mode exists, and a guided wave entering the waveguide decays owing to optical reflection [254].

5.4 Free-space excitation under oblique incidence using a grating structure

In this section, the coupling of a free-space beam to SSPPs on the waveguide is investigated incorporating grating structures with periods $\alpha = 6$ µm, and $\alpha = 20$ µm with a grating offset $g_{off} = 10$ µm. Since the value of k_{xe} is identical to the value of k_x of the asymmetric waveguide (see Section 4.2), the same grating designs have been used in this Chapter. The illuminating beam is obliquely incident on the gratings with an incidence angle of $\theta_i = 54^o$, and propagates in the $y-z$ plane with its polarisation also oscillating in that plane. The free-space beam direction and polarisation matches the free-space beam of the experimental s-SNOM system. To describe the out-of-plane field associated with the SSPPs, an equation was used to fit the SSPPs coupled on the waveguide using a free-space beam. This equation differs from Eq. 4.1 which was used to fit the SSPPs in the simulation using wave-ports (see section 5.3). When the SSPPs are excited using wave-ports, the first-order (even) mode ($k_{xe} \approx 3350$) cm^{-1} appears to be the dominant mode and the second-order (odd) mode ($k_{xo} \approx 2440$) appears to be very weak. In contrast, when the SSPPs are excited using a free-space beam and a grating structure, the diffraction of light at the side of the waveguide leads to a scattered light with a range of momentum values, but with the same frequency of 3.45 THz. Furthermore, the free-space beam in this geometry has polarisation components along both $y-$ and $z-$directions. Therefore, it can be expected that a free-space beam excites SSPPs on the waveguide in a different way when compared with the wave-port simulation. In fact, it is found that both even and odd modes can be excited efficiently using a free-space beam, as is shown below. As such the out-of-plane field associated with SSPPs on the the surface of the symmetric

waveguide is better described by the equation:

$$E_z = E_e \cos(k_{xe}\, x + \theta_e) \exp\left(\frac{-x}{L_e}\right) + E_o \cos(k_{xo}\, x + \theta_o) \exp\left(\frac{-x}{L_o}\right) , \qquad (5.1)$$

where E_e and E_o are the electric field strengths (MV/m) of the even and odd modes, k_{xe} and k_{xo} are the wave-vectors of the even and odd modes, θ_e and θ_o are the phases of the even and odd modes, and L_e and L_o are the propagation lengths of the even and odd modes, respectively.

5.4.1 Perpendicular Polarisation - Grating period 6 µm

Firstly, the coupling of a free-space beam to SSPPs is investigated for a waveguide incorporating a grating structure with period $\alpha = 6$ µm. The real part of the out-of-plane electric field E_z is shown in Fig. 5.6 (a). In this simulation the grating structure is placed on the LHS. From the figure, it is observed that two separate SSPPs are launched on the opposite ends of the waveguide which propagate towards the centre of the waveguide. To analyse the electric field associated with the SSPPs launched on the waveguide, an average value of the electric field was obtained for each bar. Only the bars of the upper part of the waveguide were considered (7.5 µm to 13 µm in the $y-$direction in Fig. 5.6 (a)). This is because the propagation of the SSPPs on the two sides of the waveguide is expected to be identical as it was shown in Fig. 5.2. The out-of-plane field on the LHS and RHS with a fit to Eq. 5.1 are shown in Fig. 5.6 (b) and (c).

The fit to the out-of-plane field on the grating side (LHS) shows that the amplitudes of the even $E_e = 1$ MV/m and odd $E_o = 0.95$ MV/m modes are almost equal when the period of the grating structure is $\alpha = 6$ µm. This shows that the excitation of SSPPs on the waveguide by a free-space beam differs from that observed in the wave-ports simulation (section 5.3), and justifies the choice to use Eq. 5.1 rather than Eq. 4.1. Furthermore, the values of the wavelengths of the even and odd modes are determined from the fit to be $\lambda_e \sim 18$ µm and $\lambda_o \sim 25.75$ µm which concur with the values obtained from the dispersion relation (see Fig. 5.1 (a)). The initial phase of the two modes are different from each other. This shows that the two modes do not have the same phase when they are launched at the beginning of the waveguide. It is also observed that the propagation lengths of the two modes have different values. This agrees with the waveguide theory, which shows that the odd mode has a longer propagation length on the symmetric waveguide [136].

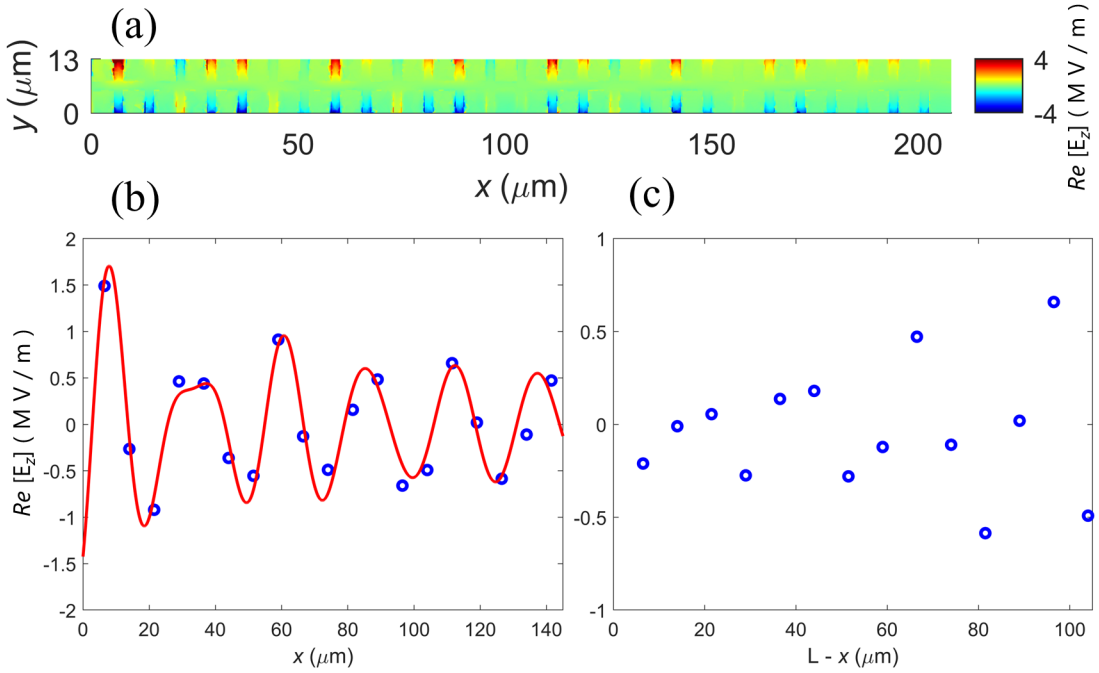

Figure 5.6: (a) SSPPs coupled on the surface of the waveguide using a grating structure with period $\alpha = 6$ µm, and a free-space beam obliquely incident on the waveguide with perpendicular polarisation. Two separate SSPPs are launched at each end of the waveguide and meet at its centre. (b) SSPP launched on the LHS. Blue data points: Average value of the out-of-plane electric field E_z on the surface of each bar. Red line: Fit to the simulation data using Eq. 5.1 The determined fitting parameters are: $E_e = 1$ MV/m, $E_o = 0.95$ MV/m, $k_{xe} = 3500$ cm^{-1}, $k_{xo} = 2440$ cm^{-1}, $\theta_e = -2.65$ rad, $\theta_o = -2.2$ rad, $L_e = 40$ µm, and $L_o = 250$ µm. (c) SSPP launched on the RHS. Blue data points: Average value of the out-of-plane electric field E_z on the surface of each bar. The coupling of SSPPs on the LHS of the waveguide is much stronger than the coupling of SSPPs on the RHS.

The field associated with the SSPPs launched from the side with no gratings (RHS) is much weaker than that of the SSPPs launched on the side with the gratings (LHS). This is illustrated in Fig. 5.6 (c), which shows a very weak out-of-plane field at the RHS end of the waveguide ($L-x \sim 0$) and a stronger field towards the center ($L-x \sim 100$ µm). That shows that the SSPPs coupled from the grating side dominate on the surface of the waveguide. These results provide confidence that the presence of the gratings with 6 µm period in the s-SNOM system will also improve the coupling strength of light to SSPPs on the waveguide.

5.4.2 Polarisation Perpendicular - 20 µm gratings

The coupling of a free-space beam to SSPPs on the waveguide is also investigated using a grating structure with period $\alpha = 20$ µm and grating offset $g_{off} = 10$ µm. The real part of the out-of-plane electric field E_z is shown in Fig. 5.7 (a). To analyse the electric field associated with the SSPPs launched on the waveguide, an average value of the electric field was obtained for each bar on the upper part of the waveguide. The SSPPs on the LHS and RHS with a fit to Eq. 5.1 are shown in Fig. 5.7 (b) and (c).

From the simulation results, it is observed that the amplitude of the even mode $E_e = 2.3$ MV/m is almost twice as strong as the amplitude of the odd mode $E_o = 1.2$ MV/m when the period of the grating structure is $\alpha = 20$ µm, and the grating offset is $g_{off} = 10$ µm. As in the case of 6 µm grating period, both even and odd modes are excited by the free-space beam. However, the even mode seems to be excited more efficiently for gratings with $\alpha = 20$ µm and $g_{off} = 10$ µm. Furthermore, the values of the wavelengths of the even and odd modes obtained from the fits are ~ 18 µm and ~ 25.75 µm which concur with the values obtained from the dispersion relation (see Fig. 5.1). The initial phase of the two modes are different from each other. This shows that the two modes do not have the same phase when they are launched at the beginning of the waveguide. It is also observed that the propagation lengths of the two modes have different values. This agrees with the waveguide theory, which shows that the odd mode has a weaker confinement but a longer propagation length on the symmetric waveguide [136].

The field associated with the SSPPs launched from the side with no gratings (RHS) is much weaker than that of the SSPPs launched on the side with the gratings (LHS). This is illustrated in Fig. 5.7 (c), which shows a weak out-of-plane field at the RHS end of the waveguide ($L - x \sim 0$) and a stronger field towards the center ($L - x \sim 100$ µm). That shows that the SSPPs coupled from the grating side dominate on the surface of the waveguide. These results provide confidence that the presence of the gratings with $\alpha = 20$ µm and $g_{off} = 10$ µm in the s-SNOM system will also improve the coupling strength of light to SSPPs on the waveguide. From the simulations, it was found that in both cases the presence of the grating structure increases the coupling strength of light to SSPPs on the waveguide.

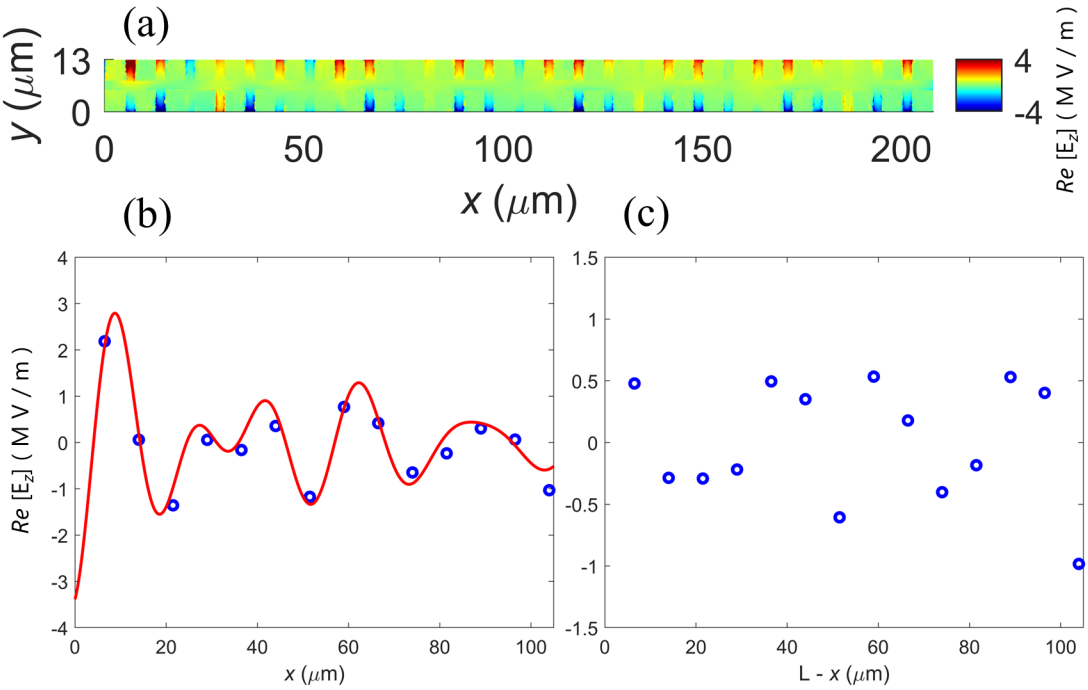

Figure 5.7: (a) SSPPs coupled on the surface of the waveguide using a grating structure with period $\alpha = 20$ µm, offset $g_{off} = 10$ µm, and a free-space beam obliquely incident on the waveguide with perpendicular polarisation. Two separate SSPPs are launched at each end of the waveguide and meet at its centre. (b) SSPP launched on the LHS. Blue data points: Average value of the out-of-plane electric field E_z on the surface of each bar. Red line: Fit to the simulation data using Eq. 5.1 The determined fitting parameters are: $E_e = 2.3$ MV/m, $E_o = 1.2$ MV/m, $k_{xe} = 3500$ cm^{-1}, $k_{xo} = 2440$ cm^{-1}, $\theta_e = -2.9$ rad, $\theta_o = -2.75$ rad, $L_e = 40$ µm, and $L_o = 150$ µm. (c) SSPP launched on the RHS. Blue data points: Average value of the out-of-plane electric field E_z on the surface of each bar. The coupling of SSPPs on the LHS of the waveguide is much stronger than the coupling of SSPPs on the RHS.

5.5 Fabrication of symmetric PSP waveguides

Two different designs of the symmetric PSP waveguide were fabricated with design parameters presented in section 5.2, a length $L = 73$ µm incorporating grating structures with periods $\alpha = 6$ µm, and $\alpha = 20$ µm with an offset $g_{off} = 10$ µm. The length of the grating structure was $L_g \approx 90$ µm and the length of each slit was $L_s = 25$ µm. A float-zone silicon substrate was used which has high resistance ($R > 10,000\,\Omega$ cm). The area of the substrate was 15×15 mm and the thickness was 500 ± 50 µm. The fabrication process has been described in Chapter 4 (see section 4.10). The fabricated waveguides with grating periods $\alpha = 6$ µm, and $\alpha = 20$ µm with offset $g_{off} = 10$ µm, are shown in Fig. 5.8, and 5.9 respectively.

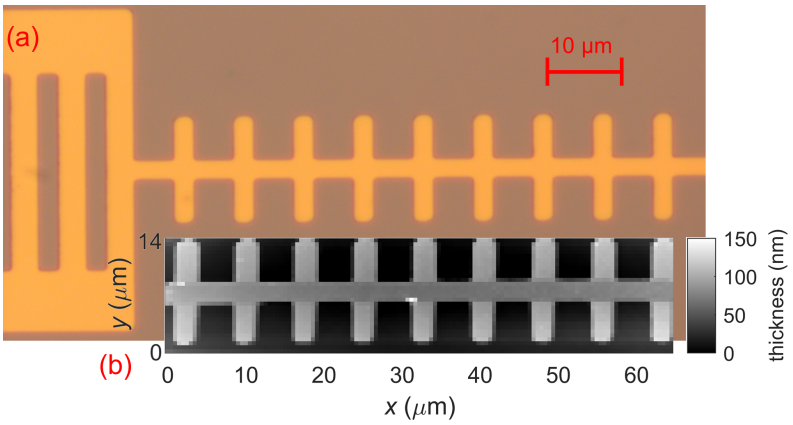

Figure 5.8: (a) optical, and (b) AFM images of the fabricated waveguide with $L = 73$ µm, and $\alpha = 6$ µm.

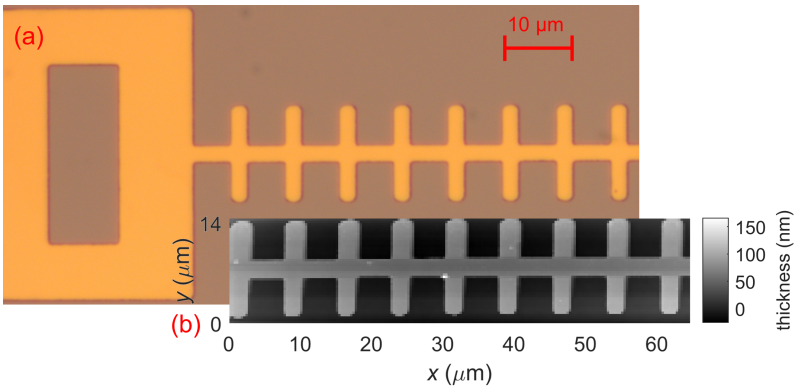

Figure 5.9: (a) optical, and (b) AFM images of the fabricated waveguide with $L = 73$ µm, $\alpha = 20$ µm, and $g_{off} = 10$ µm.

5.6 THz-s-SNOM of SSPPs on symmetric PSP waveguides

In this section, the coupling of the illuminating beam from a QCL to SSPPs on the waveguide with grating periods $\alpha = 6$ µm, and $\alpha = 20$ µm with grating offset $g_{off} = 10$ µm is investigated for a polarisation that is perpendicular to the waveguide axis (see Fig. 4.15). The QCL beam direction and polarisation in this experiment matches the direction and polarisation of the illuminating beam in the simulation presented in section 5.4. The experimental s-SNOM system setup is described in Chapter 4 (see section 4.11.1). Firstly, the case for grating period of 6 µm is presented. The spatial distribution of the self-mixing voltage signal (harmonic $n = 2$) along the waveguide obtained experimentally using the s-SNOM system is shown in Fig. 5.10. From the figure, it can be observed that the signal is much weaker in the bottom half of the waveguide ($0-6$ µm in the $y-$direction). This occurs due to a resonance being setup on the bars where the length of the structure in the $y-$direction (13 µm) is similar to the length of the DAs (15 µm) presented in Chapter 3, and the width of the bars ($x-$direction) is identical to the width of the DAs (2 µm). Furthermore, the oblique illumination causes retardation effects along the $y-$direction. To analyse the electric field associated with the SSPPs launched on the two ends of the waveguide, an average value of the self-mixing voltage was obtained for each bar on the upper part of the waveguide ($8-14$ µm in the $y-$direction), following subtraction of the constant offset arising from the sample permittivity, is shown in Fig. 5.11.

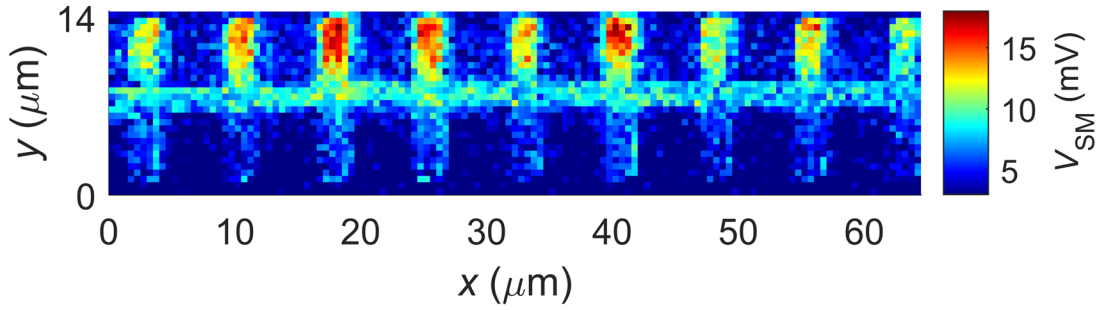

Figure 5.10: s-SNOM image (harmonic $n = 2$) of the symmetric waveguide with 6 µm gratings. The illuminating beam with $\lambda_0 = 87$ µm has a polarisation perpendicular to the waveguide axis.

To interpret the data from this experiment, an equation is presented for the out-of-plane electric field as a function of distance (x) which accounts for both SSPPs launched from each end of the waveguide, the propagation towards the centre, and the attenuation due to the finite propagation length. This equation differs from Eq. 5.1 because this experimental waveguide is shorter than that simulated, so the interference between the SSPPs launched from each end of the waveguide becomes more significant. In this case the out-of-plane field E_z is described by:

$$\begin{aligned} E_z = {} & E_{e1}\sin(k_{xe}x + \theta_{e1})\, e^{-x/L_e} + E_{e2}\sin(k_{xe}(L-x) + \theta_{e2})\, e^{-(L-x)/L_e} \\ & + E_{o1}\sin(k_{xo}x + \theta_{o1})\, e^{-x/L_o} + E_{o2}\sin(k_{xo}(L-x) + \theta_{o2})\, e^{-(L-x)/L_o}, \end{aligned} \tag{5.2}$$

where E_{e1} and E_{e2} are the SSPP amplitudes of the even modes launched from the side of the waveguide with the grating (LHS) and the RHS, E_{o1} and E_{o2} are the SSPP odd modes launched from the LHS and the RHS, k_{xe} and k_{xo} are the wave-vectors of the SSPP even and odd modes, θ_{e1}, θ_{e2}, θ_{o1}, and θ_{o2} are their respective phases, L_e and L_o are the propagation lengths of the even and odd modes, and L is the length of the waveguide. In order to simplify the analytical expression, reflections have not been considered at this stage.

One could notice that Eq. 5.2 has many free parameters, which makes the fit less statistically significant. To simplify the fit, the amplitude of the even and odd modes launched from the side of the waveguide with the gratings (LHS) were set to equal values ($E_{e1} = E_{o1}$), and the even and modes launched on the other side of the grating were also set to equal values ($E_{e2} = E_{o2}$). From Fig. 5.11 it can be observed that the fit using Eq. 5.2 fits the data reasonably well. From the fitting process, it can be seen that the SSPP modes are all equal, $E_{e1} = E_{o1} = E_{e2} = E_{o2} = 2$ mV. The simulation of the symmetric waveguide with grating period $\alpha = 6$ µm in section 5.4.1 also showed that the even and odd modes launched from the side of the waveguide with the gratings (LHS) have equal amplitudes. However, the simulation in section 5.4.1 showed that the SSPP modes launched on the other side of the waveguide (RHS) are very weak. This difference between the simulation and experimental results can be attributed to the reflections which occur in the waveguide which are not taken into account in this fit. Nevertheless, the fitting process is useful for confirming that SSPPs are launched from each end, and that they have the expected values of the even and odd mode wave-vectors, k_{xe} and k_{xo}. The even and odd mode wave-vectors obtained experimentally and determined from the fitting procedure $k_{xe} = 3600$ and $k_{xo} = 2650$ cm^{-1} respectively, concur

with the wave-vectors obtained from the dispersion relations (Section 5.2) which yielded values of $k_{xe} = 3600$ and $k_{xo} = 2400$ cm^{-1} respectively. The analysis of this experiment demonstrates that the illuminating beam from the QCL with oblique incidence on the sample and perpendicular polarisation to the waveguide axis has launched SSPPs on the two ends of the waveguide, just as it was observed in the simulations presented in section 5.4.1. This design will be directly compared with a free-space simulation which matches the s-SNOM experimental setup in the next section.

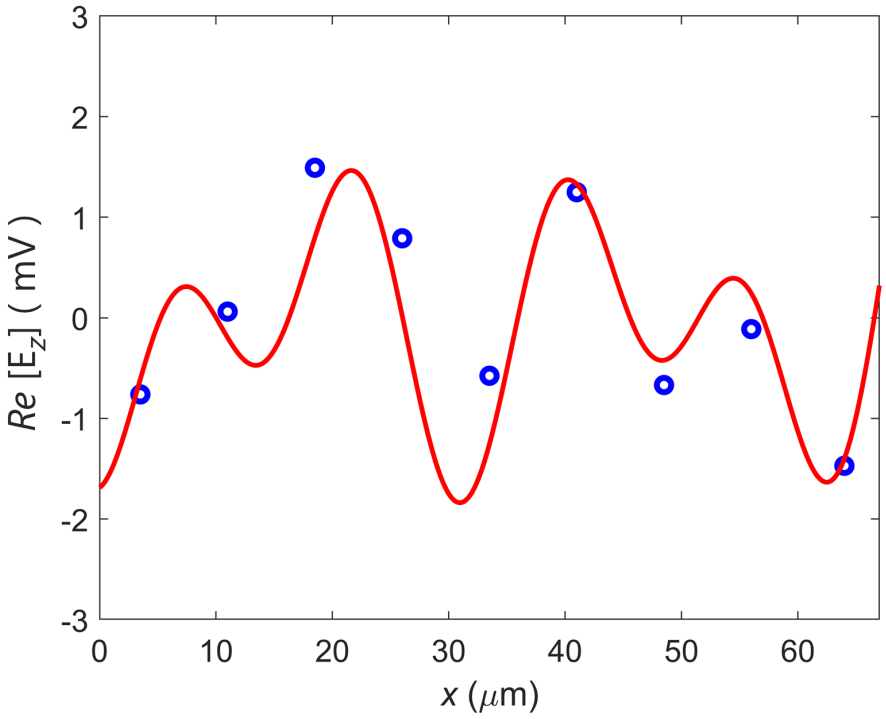

Figure 5.11: SSPPs launched on both ends of the waveguide. Blue data points: Average value of the out-of-plane electric field on the surface of each bar. Red line: Fit to the data using Eq. 5.2. The fitting values are: $E_{e1} = 2$ mV, $E_{e2} = 2$ mV, $E_{o1} = 2$ mV, $E_{o2} = 2$ mV, $k_{xe} = 3600$ cm^{-1}, $k_{xo} = 2650$ cm^{-1}, $\theta_{e1} = -2.78$ rad, $\theta_{e2} = -0.7$ rad, $\theta_{o1} = 2.3$ rad, $\theta_{o2} = -0.3$ rad, $L_e = 83$ µm, and $L_o = 78$ µm.

Next, the case for grating period $\alpha = 20$ µm and grating offset $g_{off} = 10$ µm is presented. The spatial distribution of the self-mixing voltage obtained experimentally using the s-SNOM system is shown in Fig. 5.12. To analyse the electric field associated with the SSPPs launched on the two ends of the waveguide, an average value of the self-mixing voltage was obtained for each bar, following subtraction of the constant offset arising from the sample permittivity. The fit to the data using Eq. 5.2 is shown in Fig. 5.13.

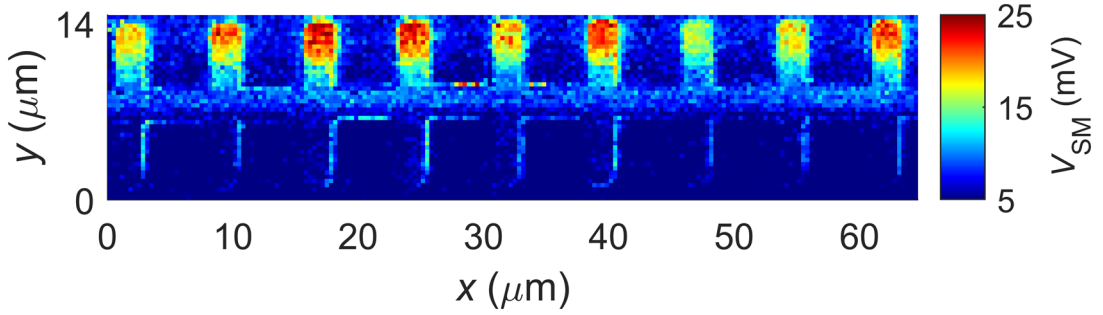

Figure 5.12: s-SNOM image (harmonic $n = 2$) of the symmetric waveguide with grating period $\alpha = 20$ µm, and offset $g_{off} = 10$ µm.

To simplify the fit, the amplitude of the even and odd modes launched from the side of the gratings (LHS) were again set to equal values ($E_{e1} = E_{o1}$), and the even and modes launched on the other side of the grating were also set to equal values ($E_{e2} = E_{o2}$). From the fitting process, it can be seen that the SSPP modes are all equal, $E_{e1} = E_{o1} = E_{e2} = E_{o2} = 2$ mV. As for the $\alpha = 6$ µm case, these fits indicate equal amplitudes of the SSPPs launched from the LHS and RHS, whereas the simulations in Section 5.4.2 indicated much weaker amplitudes on the RHS. Again, this can be explained by the fact that reflections are not considered in Eq. 5.2. Nevertheless, the fitting process is useful for confirming that SSPPs are launched from each end, and that they have the expected values of the even and odd mode wave-vectors, k_{xe} and k_{xo}. Specifically, the even and odd mode wave-vectors obtained experimentally and determined from the fitting procedure $k_{xe} = 3500$ and $k_{xo} = 2600$ cm^{-1} respectively, concur with the wave-vectors obtained from the dispersion relations (section 5.2) which yielded values of $k_{xe} = 3600$ and $k_{xo} = 2400$ cm^{-1} respectively. This analysis confirms that the SSPPs observed in simulation (section 5.4.2) are also observed experimentally. This design will also be directly compared with a free-space simulation which matches the s-SNOM experimental setup in the next section.

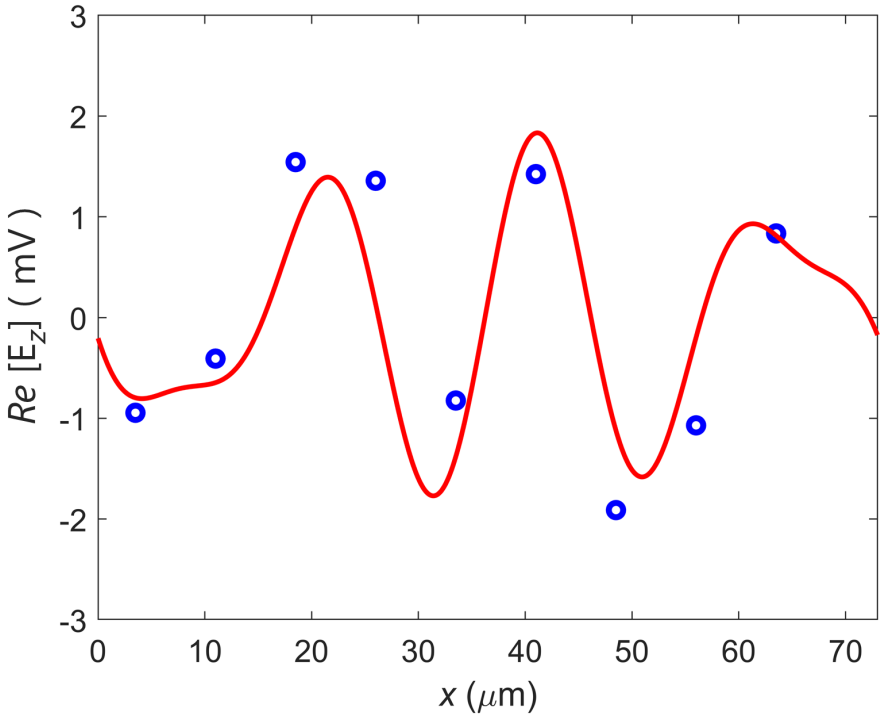

Figure 5.13: SSPPs launched on both ends of the waveguide. Blue data points: Average value of the out-of-plane electric field on the surface of each bar. Red line: Fit to the data using Eq. 5.2. The fitting values are: $E_{e1} = 2$ mV, $E_{e2} = 2$ mV, $E_{o1} = 2$ mV, $E_{o2} = 2$ mV, $k_{xe} = 3500$ cm^{-1}, $k_{xo} = 2600$ cm^{-1}, $\theta_{e1} = \pi$ rad, $\theta_{e2} = 0$ rad, $\theta_{o1} = 0.8$ rad, $\theta_{o2} = -2.6$ rad, $L_e = 83$ µm, and $L_o = 50$ µm.

5.7 Comparison of the experiments with simulations

Due to the complex nature of the SSPP fields supported by these structures with SSPPs launching from both ends of the waveguide, each of which reflect at the opposite ends, and the interference between the four SSPPs, it is necessary to directly compare the measurements with simulations. However, to do this the phase of the excited SSPPs in the simulations need to match that in the experiments. In the experiments, the phase of the coupled SSPPs on the waveguide is determined by the external optical path (cavity) length, whereas in the simulations it is determined by the location of the illuminating beam origin. To achieve this, the length of the waveguide in the simulations was set to $L = 73$ µm in order to match the length of the experimental structure. In each simulation the distance in the $z-$direction between the origin of the illuminating beam and the structure was varied with a step of 5 µm over a 100 µm range. As a result, the phase of the SSPPs in the simulations could be closely matched to the phases obtained in the experiments. The results are presented in this section.

Firstly, the case for grating period of 6 µm is presented. The out-of-plane electric field obtained in the simulation and experimentally is shown in Fig. 5.14. The figure presents a reasonable agreement between the out-of-plane field distributions from the simulation and the experiment. On the RHS part of the waveguide, the experimental data matches the data obtained from the simulation quite well. Particularly, the strongest positive field in the experimental image is observed on the waveguide bar at $x \approx 40$ µm (i.e. the fourth bar from the RHS). This is also observed in the simulation at $x \approx 45$ µm (i.e. the fourth bar from the RHS). Furthermore, a negative field is observed in the simulation on the waveguide bars at $x \approx 35$ µm (i.e. the fifth bar from the RHS) and $x \approx 55$ µm (i.e. the third bar from the RHS). This is also observed in the experimental results where a weaker self-mixing voltage is observed on the waveguide bars at $x \approx 35$ µm (i.e. the fifth bar from the RHS) and $x \approx 50$ µm (i.e. the third bar from the RHS). However, on the LHS part of the waveguide, the field on the first and third waveguide bars ($x \approx 7.5$ µm and $x \approx 22.5$ µm) does not concur for the simulation and the experiment. The field of the first bar in the simulation is strong and positive whereas the field on the first bar in the experiment is weak. The field of the third bar in the simulation is weak and negative whereas the field on the third bar in the

experiment is strong.

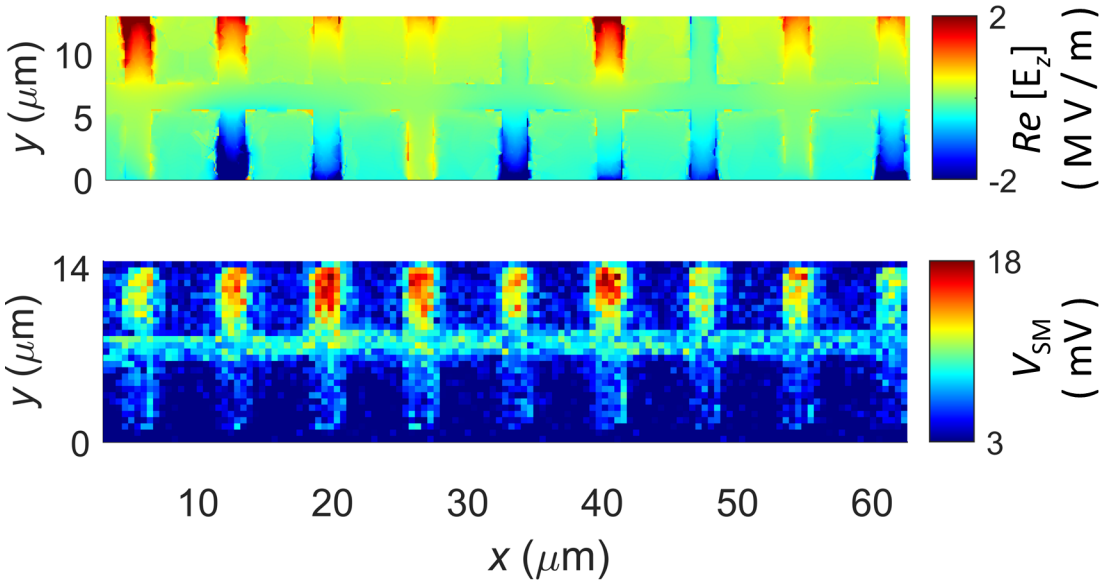

Figure 5.14: Comparison of the out-of-plane electric field obtained in simulation and experimentally with length $L = 73$ µm. (upper): data obtained from the simulation, (lower): data obtained experimentally using s-SNOM ($n = 2$).

There are multiple reasons that could be attributed to this discrepancy. Firstly, as discussed in Section 4.12, the presence of the probe tip in the near-field of the waveguide affects the resulting s-SNOM image, due to the near-field interaction between the tip and the sample. Therefore, this observed discrepancy could be due to the presence of the tip. To investigate the effects of the tip on the resulting s-SNOM image, further simulations could be performed where the probe tip is included and its effects on the measured field distribution of the SSPPs are studied. Furthermore, the dimensions of the experimental samples deviate slightly from the dimensions of the waveguide designed in the simulation (see section 5.2). This effect occurs due to the resolution limit of the optical lithography which is $\sim 1-2$ µm. The designed width of each bar in simulation is $d - a = 2$ µm, whereas the bars on the fabricated waveguide have a width of ~ 2.4 µm. In addition, the body of the designed waveguide in the simulation is $w - h = 2$ µm, whereas the body of the fabricated waveguide is 2.2 µm. Another reason for this discrepancy is that the illuminating beam from the QCL is not perfectly linearly polarised as it was shown in Chapter 3 unlike the free-space beam in the simulation. As a result, the incident beam contains both parallel and perpendicular electric field components

of the polarisation, each of which interact differently with the grating structure. Therefore, the elliptical beam from the QCL could affect how SSPPs are launched on the waveguide.

To further analyse and compare the field associated with the SSPPs in the simulation and experimentally, an average value of the field was obtained for each bar. The simulation and experimental data were normalised and Eq. 5.2 was used to fit the normalised data as shown in Fig. 5.15.

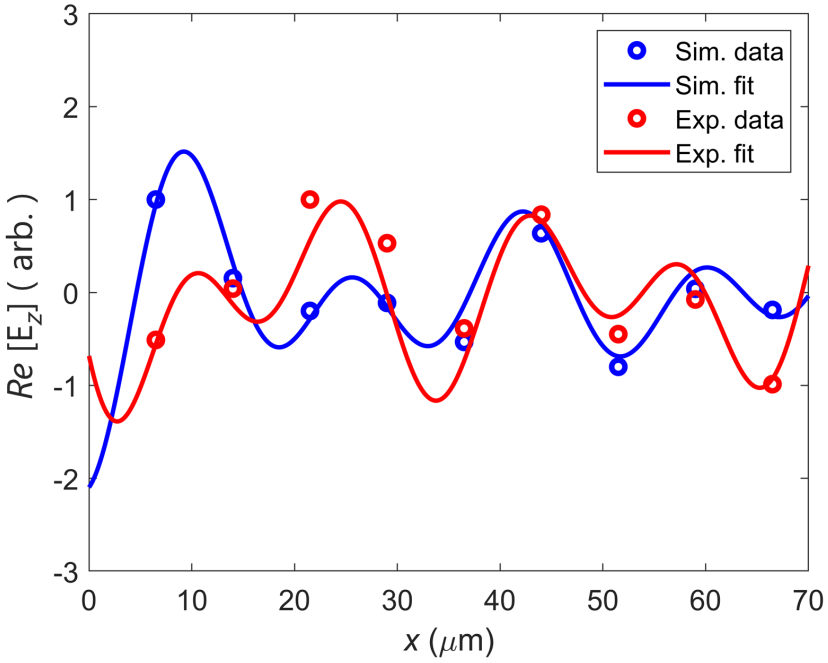

Figure 5.15: Comparison between the out-of-plane field on the waveguide obtained from the simulation and experimentally. **Blue data points:** Simulated average value of E_z on each bar. **Blue line:** Fit the simulation data to Eq. 5.2. The fitting values are: $E_{e1} = 1.2$ (arb.), $E_{e2} = 0.53$ (arb.), $E_{o1} = 1.2$ (arb.), $E_{o2} = 0.53$ (arb.), $k_{xe} = 3550$ cm^{-1}, $k_{xo} = 2400$ cm^{-1}, $\theta_{e1} = \pi$ rad, $\theta_{e2} = 0$ rad, $\theta_{o1} = -2.85$ rad, $\theta_{o2} = 0.37$ rad, $L_e = 100$ µm, and $L_o = 50$ µm. **Red data points:** Experimental average value of E_z on each bar. **Red line:** Fit to the experimental data using Eq. 5.2. The fitting values are: $E_{e1} = 1.7$ (arb.), $E_{e2} = 1$ (arb.), $E_{o1} = 1.7$ (arb.), $E_{o2} = 1$ (arb.), $k_{xe} = 3600$ cm^{-1}, $k_{xo} = 2700$ cm^{-1}, $\theta_{e1} = 2.7$ rad, $\theta_{e2} = 0.14$ rad, $\theta_{o1} = 1.1$ rad, $\theta_{o2} = 0.6$ rad, $L_e = 50$ µm, and $L_o = 50$ µm.

The fits to the simulation and experimental data using Eq. 5.2 show an adequate agreement on the RHS. The amplitudes of the SSPP even and odd modes launched on the grating side of the waveguide (LHS) are greater than the ampltidues of the even and odd modes launched from the other side of the waveguide (RHS). The even and odd mode wave-vectors obtained from the fit to the simulation data are $k_{xe} = 3550$ cm^{-1} and $k_{xo} = 2400$ cm^{-1} , which concur with the values obtained from the fit to the experimental data, $k_{xe} = 3600$ cm^{-1} and $k_{xo} = 2700$ cm^{-1}. These values also agree with the ones obtained from the dispersion relation.

Next, the case for grating with period $\alpha = 20$ µm and grating offset $g_{off} = 10$ µm is presented. The out-of-plane electric field obtained from the simulation and experimentally is shown in Fig. 5.16.

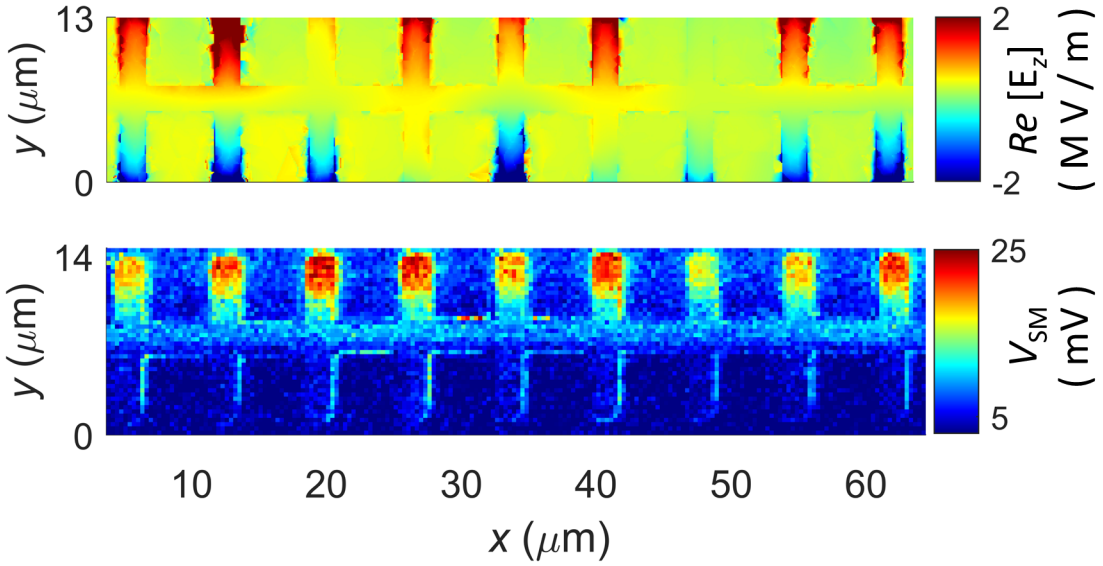

Figure 5.16: Comparison of the out-of-plane electric field obtained in simulation and experimentally with length $L = 73$ µm. (upper): data obtained from the simulation, (lower): data obtained experimentally using s-SNOM ($n = 2$).

Figure 5.16 presents a reasonable agreement between the out-of-plane field distributions from the simulation and the experiment. The strongest positive field in the experimental image is observed on the waveguide bars at $x \approx 25$ µm (i.e. the sixth bar from the RHS) and $x \approx 40$ µm (i.e. the fourth bar from the RHS). A strong positive field is also observed in the simulation on the waveguide bars at $x \approx 30$ µm (i.e. the sixth bar from the RHS) and $x \approx 45$ µm (i.e. the fourth bar from the RHS). Furthermore, a negative field in the simulation is observed on

the waveguide bar at $x \approx 37.5$ µm (i.e. the fifth bar from the RHS), and $x \approx 55$ µm (i.e. the third bar from the RHS), where a weak self-mixing voltage on that waveguide bar is also seen experimentally at $x \approx 32$ µm (i.e. the fifth bar from the RHS), and $x \approx 50$ µm (i.e. the third bar from the RHS). However, the field on the second and third waveguide bars from the LHS does not concur for the simulation and the experiment. The field of the second bar in the simulation is strong and positive whereas the field on the second bar in the experiment is weak. The field of the third bar in the simulation is very weak whereas the field on the third bar in the experiment is strong.

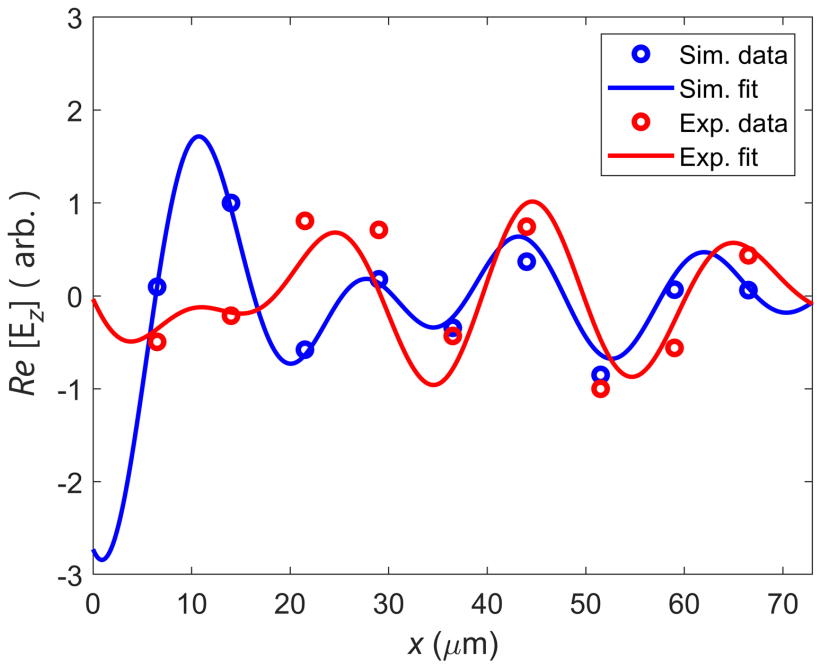

Figure 5.17: Comparison between the out-of-plane electric field E_z on the waveguide obtained from the simulation and experimentally. **Blue data points:** Simulated average value of E_z on each bar. **Blue line:** Fit to the simulation data using Eq. 5.2. The fitting values are: $E_{e1} = 1.8$ (arb.), $E_{e2} = 0.5$ (arb.), $E_{o1} = 1.8$ (arb.), $E_{o2} = 0.5$ (arb.), $k_{xe} = 3500$ cm^{-1}, $k_{xo} = 2700$ cm^{-1}, $\theta_{e1} = \pi$ rad, $\theta_{e2} = 0$ rad, $\theta_{o1} = 2.34$ rad, $\theta_{o2} = -0.12$ rad, $L_e = 79$ µm, and $L_o = 50$ µm. **Red data points:** Experimental average value of E_z on each bar. **Red line:** Fit to the experimental data using Eq. 5.2. The fitting values are: $E_{e1} = 0.95$ (arb.), $E_{e2} = 0.4$ (arb.), $E_{o1} = 0.95$ (arb.), $E_{o2} = 0.4$ (arb.), $k_{xe} = 3500$ cm^{-1}, $k_{xo} = 2700$ cm^{-1}, $\theta_{e1} = 2.8$ rad, $\theta_{e2} = 0.6$ rad, $\theta_{o1} = 0.85$ rad, $\theta_{o2} = -1$ rad, $L_e = 150$ µm, and $L_o = 50$ µm.

The fits to the simulation and experimental data using Eq. 5.2 (Fig. 5.17) show an adequate agreement on the RHS. The amplitudes of the SSPP even and odd modes launched on the grating side of the waveguide (LHS) are greater than the ampltidues of the even and odd modes launched from the other side of the waveguide (RHS). The even and odd mode wave-vectors obtained from the fit to the simulation data are $k_{xe} = 3500$ cm^{-1} and $k_{xo} = 2700$ cm^{-1}, which concur with the even and odd mode wave-vectors obtained from the fit to the experimental data, $k_{xe} = 3500$ cm^{-1} and $k_{xo} = 2700$ cm^{-1}. These values also agree with the ones obtained from the dispersion relation. It can also be observed that the field on the LHS show a slight discrepancy between the simulation and experimental data. This could be attributed to the presence of the probe tip in the near-field of the waveguide, differences in the physical dimensions of the waveguide between the simulation and the experiment, and the elliptically polarised free-space beam radiated from the QCL, as discussed previously.

5.8 Summary

To conclude, this chapter presented the design and simulation of the novel symmetric PSP waveguide structure which supports SSPPs at THz frequencies. Eigenmode simulations were ran to obtain the SSPP wave-vectors of the even and odd modes for an incident frequency of 3.45 THz. A waveguide with length $L = 208$ µm was simulated to analyse the out-of-plane electric field E_z propagation along the waveguide and obtain its finite propagation length. A waveguide with length $L = 73$ µm was also simulated to obtain the S_{21} Parameters of the waveguide, and the cut-off frequency. Next, the waveguide was simulated using a free-space beam with perpendicular polarisation which showed a different coupling of light to SSPPs on the waveguide compared to the simulations with an excitation port. Furthermore, the fabrication process of the waveguide structures and the high resolution microscopy of the out-of-plane field of THz-frequency SSPPs propagating on these structures were presented. The images acquired using s-SNOM were compared directly to the simulations where the phases of the SSPPs in the simulations matched those of the experiments. The comparison between the simulation and experimental data showed an adequate agreement, which is considered successful given the complexity of the experiments. Therefore, the results show successful mapping of the spatial distribution of the electric field associated with THz-frequency SSPPs propagating on an asymmetric PSP waveguide with sub-wavelength resolution. This is the first time this has been reported.

Chapter 6

Terahertz microscopy of directional couplers

6.1 Introduction

Recent advances in the field of plasmonics have motivated scientists to realise compact nanophotonic integrated circuits (ICs), where the compact size of electronic circuits can be combined with the operational bandwidth of plasmonic circuits. In order to realise compact devices, several essential components such as single-mode waveguides, waveguide bends and splitters, waveguide crossings, and wavelength-selective components for filtering and separation of wavelengths are necessary. Such wavelength-selective components are essential in the realisation of demultiplexing components, and one structure that can be used to realise such devices is a directional coupler (DC) [261]. The possibility of realising wavelength-dependent components and directional coupling with plasmonic waveguides has been investigated recently by several research groups [262–270]. In this Chapter, the potential to realise different functional plasmonic components at terahertz frequencies is investigated, such as DCs based on the asymmetric PSP waveguides described in Chapter 4.

Initially, a unit cell of the DC structure was designed in ANSYS HFSS and its dispersion relations were calculated using an eigen-mode solver. Next, a DC structure with finite length was simulated using excitation ports, placed at the edge of the excitation region (Fig. 6.1) and at the two ends of the structure to launch and detect the SSPPs propagating on the waveguide. The effects of varying the gap size, g on the SSPP energy distribution between the two waveguides

in the interaction region (Fig. 6.1) were explored using two models, one based on a phenomenological analysis, and one using supermode analysis [261]. The S_{21} Parameters, and the cut-off frequency of the waveguide structure were obtained. Furthermore, the waveguide was simulated using a free-space beam and perpendicular polarisation which showed a different coupling of light to SSPPs on the waveguide compared to the simulations with wave-ports. The structures were then fabricated on a silicon substrate using electron-beam lithography and metal deposition techniques. A QCL was used to illuminate the structures with an incident frequency of 3.45 THz and the s-SNOM system was used to measure the out-of-plane electric field E_z. The results from the experiments are presented in Section 6.7 and are compared with theoretical expectations.

6.2 Principle of operation of DC structures

The DC structures designed and investigated in this Chapter consist of three sections: the excitation region, the interaction region (IR), and the S-bend region (Fig. 6.1). The operating principle of these structures is as follows: SSPPs are launched at the edge of the first waveguide, which is known as the excitation region. The interaction region consists of two parallel straight PSP asymmetric waveguides (WG1 and WG2), where the distance between them is g, and the length of the parallel interaction region is L. The purpose of the interaction region is to distribute the energy of the SSPPs between the two waveguides in a controlled manner, i.e. by controlling the values of the parameters g and L. In the end of each straight waveguide, an S-bend waveguide is connected to spatially separate the SSPPs propagating on each waveguide. When two identical waveguides are close to each other, there are two modes supported by the entire structure; the even and odd modes at $f_0 = 3.45$ THz. The wave-vectors of the even and odd modes vary with frequency f_0 and gap size g. For the even mode, the value of g has little influence on the wave-vector value k_{xe}. However, for the odd mode, the value of the wave-vector k_{xo} becomes larger with increasing g at the same frequency. Thus, the difference between the two modes is larger for DCs with a smaller gap size g. The difference between the wave-vectors of the two modes at the same frequency will lead to a phase difference between the modes after propagating a distance L [261]:

$$\Delta\phi = (k_{xe} - k_{xo})\, L. \tag{6.1}$$

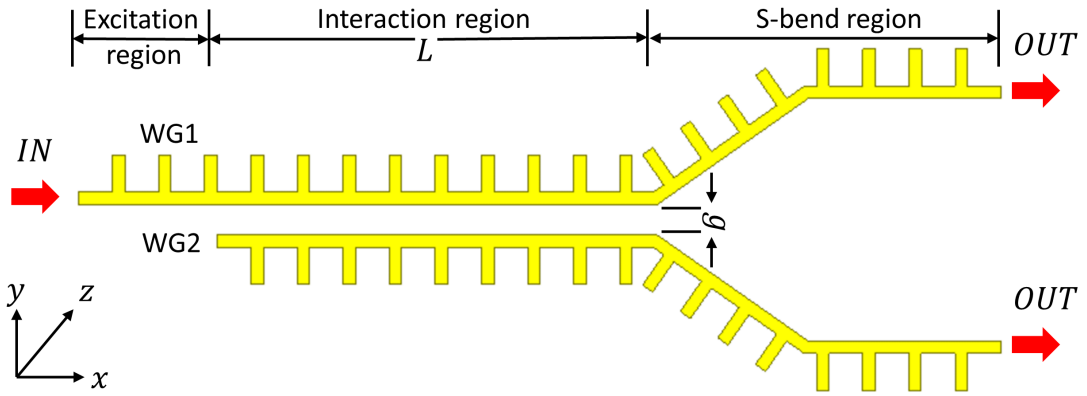

Figure 6.1: Schematic of the designed DC structure showing the three regions. The SSPPs are launched on the edge of WG1, and couple on the WG2 when they reach the interaction region. The SSPPs are then separated in the S-bend region.

This phase difference between the even and odd modes affects how the energy is distributed between the two waveguides in the IR. The electric fields on WG1 and WG2 associated with the even mode are always in-phase (Fig. 6.2 (a)) whereas the fields associated with the odd mode are always out-of-phase (Fig. 6.2 (b)).

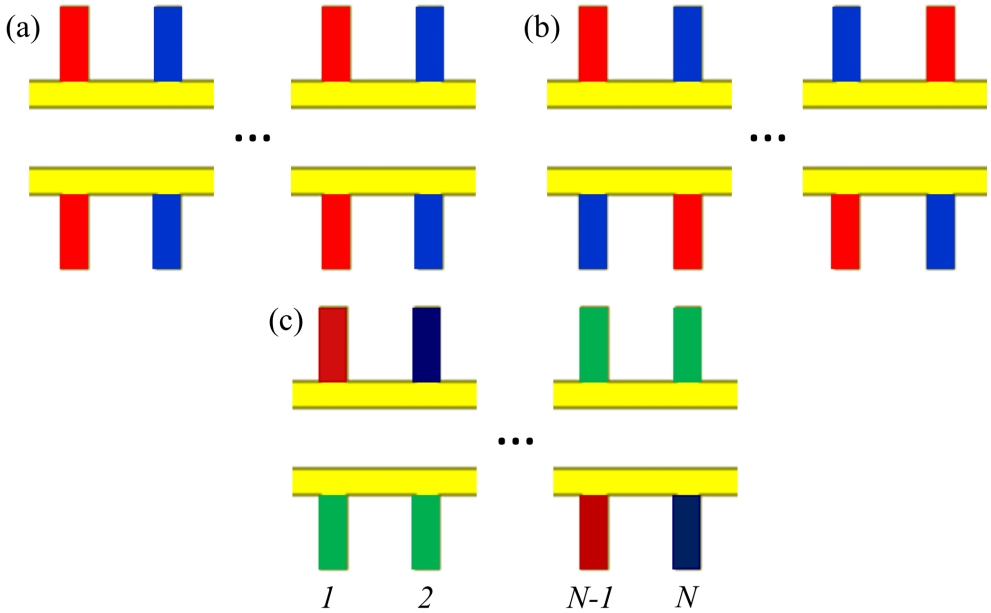

Figure 6.2: (a) Fields associated with the even mode on the IR are always in-phase. (b) Fields associated with the odd mode on the IR are always out-of-phase. (c) The total field is the sum of the even and odd modes. Red bars indicate positive field, blue bars indicate negative field, and green bars indicate a null field.

The fields associated with even and odd modes in each bar interfere either constructively or destructively, causing the energy associated with the SSPPs to be distributed in either WG1 or WG2. As the SSPPs propagate on the IR in the $x-$direction, for certain values of x, the even and odd modes will be exactly in-phase ($\Delta\theta = \theta_{e1} - \theta_{o1} = 0^{o}$). This leads to the sum of the fields on WG1 to reach a maxima, and the sum of the fields on WG2 to be at a null. This is shown in Fig. 6.2 (c) where bar 1 is positive and bar 2 is negative in WG1, whereas the field of both bars is at a null in WG2. In this case, the total energy on the IR remains on WG1. Conversely, for other values of x, the even and odd modes will be exactly out-of-phase ($\Delta\theta = \theta_{e1} - \theta_{o1} = 180^{o}$). This leads to the sum of the fields on WG1 to be at a null, and the sum of the fields on WG2 to reach a maxima. This is also shown in Fig. 6.2 (c) where bar $N-1$ is positive and bar N is negative in WG2, whereas the field at both bars is at a null in WG1. In this case, the total energy on the IR transfers to WG2. The total energy will transfer to WG2 for a certain value of the coupling length L_c which can be expressed as [261]:

$$L_c = \frac{\pi}{k_{xe} - k_{xo}}. \tag{6.2}$$

6.3 Design of DC structures

The DC structure design shown in Fig. 6.1 consists of two asymmetric PSP waveguides separated by a distance, g, and consists of three regions: the excitation region, the interaction region, and the S-bend region. The excitation of SSPPs on the structure occurs at the start of WG1 and the length of the region is 22.5 µm. This region ensures that the wave-port (in simulations) or gratings (in experimental devices) located at the beginning of WG1 launches SSPPs only on WG1 and there is no unwanted excitation of SSPPs from the wave-port or the gratings on WG2. The interaction region has a length of $L = L_c = 73$ µm, which is the calculated length over which the total energy shifts from WG1 to WG2 for a distance, $g = 500$ nm (see below). The S-bend region spatially decouples the SSPPs propagating on the structure and allows for the energy distribution on the waveguide to be analysed when varying the distance, g between the two waveguides. The design parameters of each of the constituent asymmetric waveguides (WG1 and WG2) are identical to the one presented in Chapter 4. The waveguides were designed with period $d = 7.5$ µm, groove width $\alpha = 5.5$ µm, width $w = 8$ µm, height $h = 6$ µm, and thickness $t = 0.1$ µm, since these parameters are known from Chapter

4 to support SSPPs in the desired frequency range. The material used to form the DC structure was gold ($t = 100$ nm) and it was placed on a silicon substrate ($t = 50$ µm) with a dielectric constant of $\varepsilon = 11.65$.

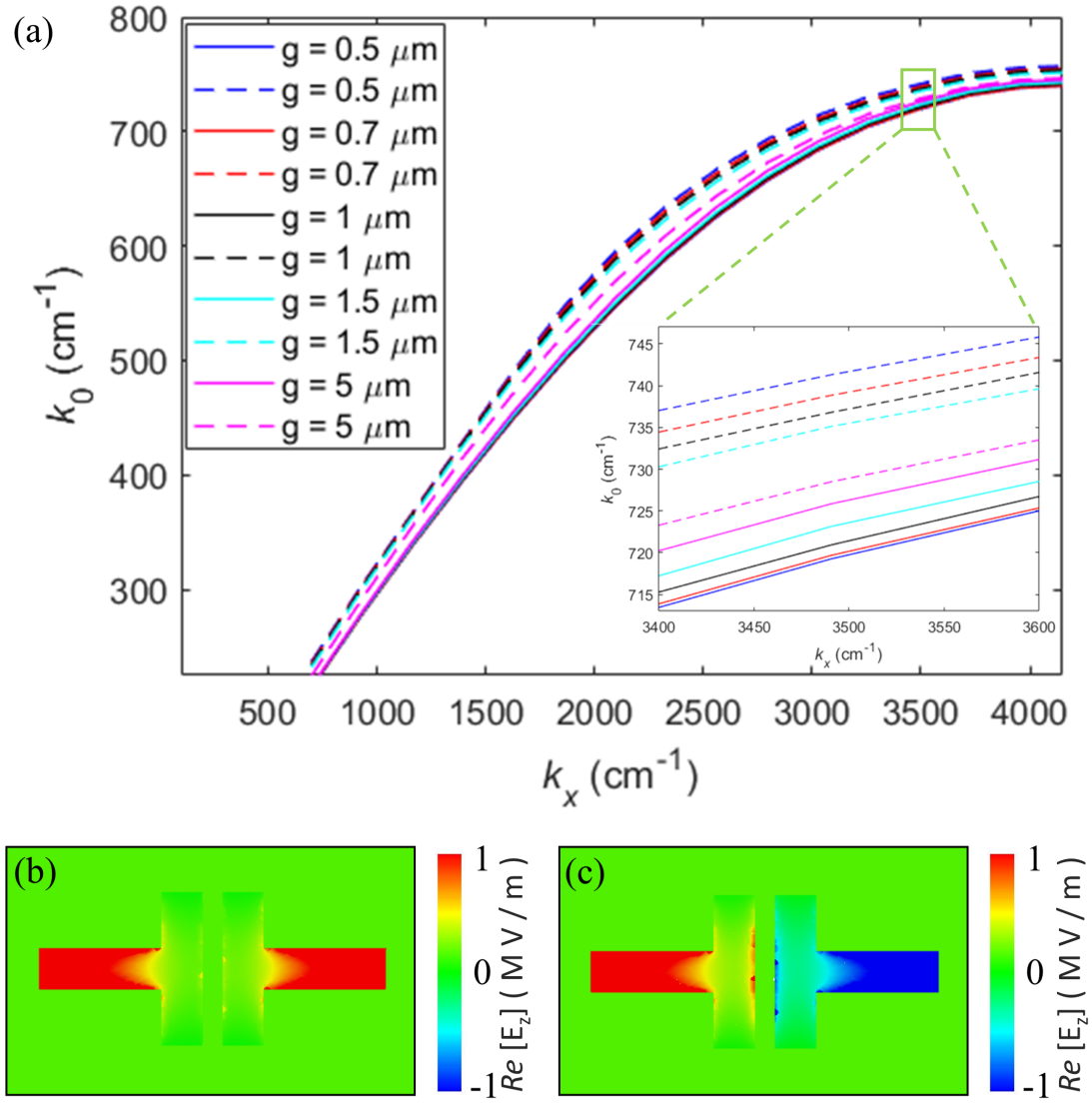

Figure 6.3: Dispersion relation and local field distribution of the DC structure. (a) Dispersion relation for the even (solid lines) and odd (dashed lines) PSP modes. The geometric parameters of the structure are: $w = 1.07d$, $a = 0.73d$, and $h = 0.8d$, where $d = 7.5$ µm. (a, inset) Dispersion relation zoom in. (b) Real part of the out-of-plane electric field, E_z of the SSPP even, and (c) odd modes obtained using FEM for $g = 500$ nm.

The dispersion relations of the even and odd modes of the TM-polarised waves propagating along the $x-$direction with momentum k_{xe} and k_{xo} respectively were numerically calculated using the eigenmode solver in ANSYSS HFSS for gap sizes: $g = 500$ nm, $g = 700$ nm, $g = 1$ µm, $g = 1.5$ µm, and $g = 5$ µm, and are presented in Fig. 6.3 (a). A unit cell of the waveguide was considered, and periodic boundaries were used in the x-direction and PEC boundaries in the y-direction. By sweeping the phase difference $\Delta\theta$ of the EM fields at the opposite boundaries in the x-direction from 0° to 180°, the eigen-frequencies of the spoof surface plasmon polaritons (SSPPs) are calculated within the first Brillouin zone [253]. The real part of the out-of-plane electric field component E_z of the even and odd modes is shown in Fig. 6.3 (b) and Fig. 6.3 (c) respectively.

The wave-vectors of the even (k_{xe}) and odd (k_{xo}) modes are related to the parameter $\Delta\theta$ whose values are obtained from the eigen-mode simulation for an incident frequency of $f_0 = 3.45$ THz. The relationships between the wave-vectors and $\Delta\theta$ are $k_{xe} = (\pi\Delta\theta_e)/(180\,d)$ and $k_{xo} = (\pi\Delta\theta_o)/(180\,d)$ which yield values of $k_{xe} = 3600$ cm^{-1} and $k_{xo} = 3150$ cm^{-1} for $g = 500$ nm. The SSPP wavelengths of the even λ_e and odd λ_o modes are related to their corresponding SSPP wave-vectors according to the relations; $\lambda_e = 2\pi/k_{xe}$ and $\lambda_o = 2\pi/k_{xo}$. This leads to values of $\lambda_e = 17.5$ µm, and $\lambda_o = 20$ µm, corresponding to $\sim \lambda_0/5$ and $\sim \lambda_0/4.3$ respectively. Furthermore, the length L_c of the IR which causes the total energy of the propagating SSPPs to shift from WG1 to WG2 was calculated using Eq. 6.2. Based on the calculated wave-vector values of the even and odd modes, the phase difference $\Delta\phi = \pi$ when the length $L_c = 73$ µm for a gap size, $g = 500$ nm.

6.4 Simulation using excitation ports

To calculate the out-of-plane electric field E_z and the S_{21} Parameters of a finite waveguide, a new simulation environment was setup in ANSYS HFSS. The DC structure was designed with a total length of 160 µm. Three wave ports were used in the simulation, one at the beginning ($x = 0$) of WG1 to launch SSPPs on the structure, and two at the end of WG1 and WG2 ($x = 150$ µm) to obtain the S_{21} Parameters. Open boundaries were used for the simulation using the radiation boundary in HFSS. The magnitude and real component of the out-of-plane electric field on the surface of the DC structure is shown in Fig. 6.4, for an excitation frequency of 3.45 THz and all cases of g.

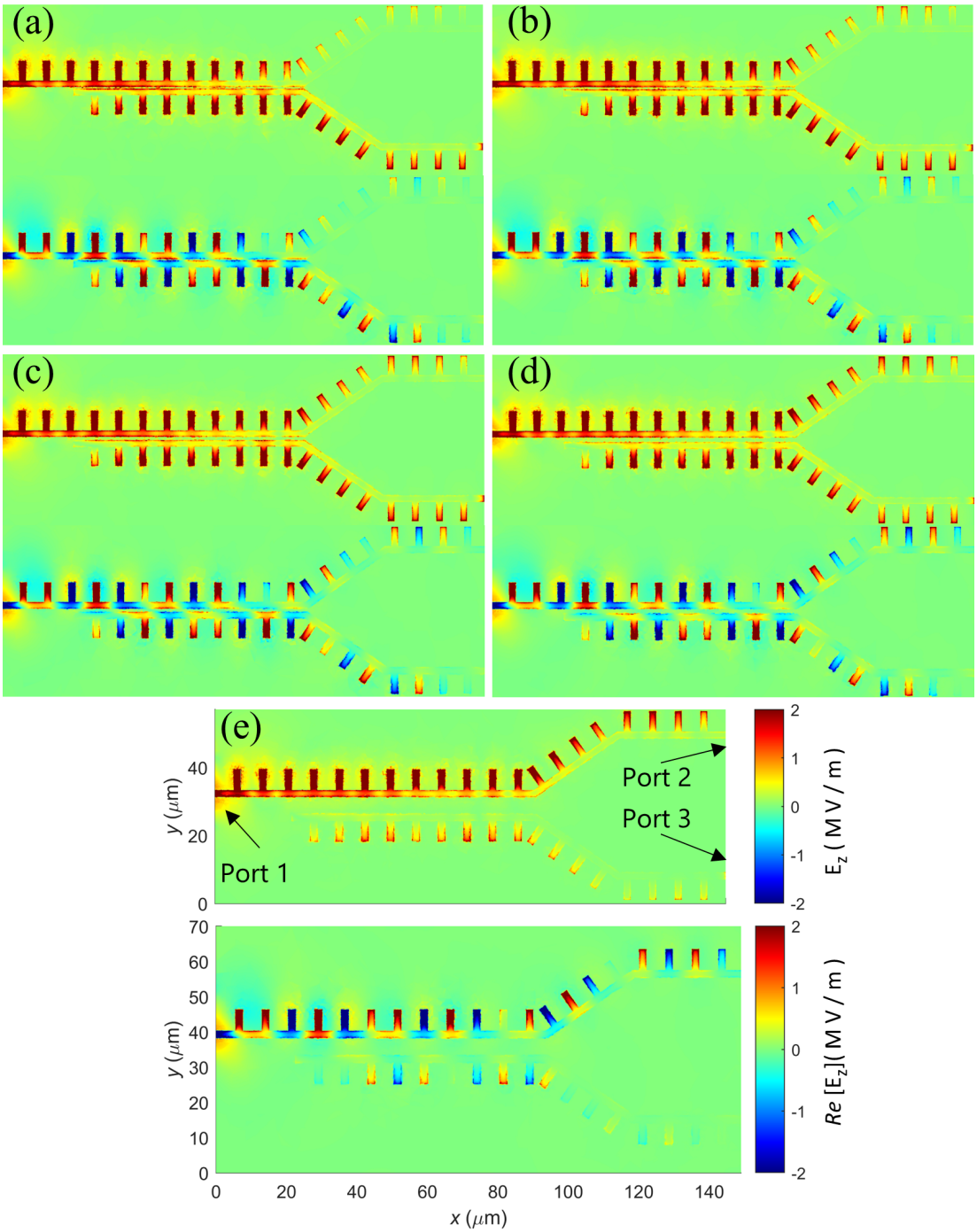

Figure 6.4: Simulated magnitude (upper), and real part of the out-of-plane electric field E_z (lower) on the surface of the DC structure using excitation ports. (a) $g = 500$ nm, (b) $g = 700$ nm, (c) $g = 1$ µm, (d) $g = 1.5$ µm, and (e) $g = 5$ µm.

The S_{21} Parameters have been obtained for SSPPs launched on the excitation region (port 1) and detected at the end of the WG1 S-bend region (port 2), as shown in Fig. 6.5. It is observed that for an incident frequency $f_0 = 3.45$ THz, the transmitted power for a gap size $g = 5$ µm has been attenuated by ~ 25 dB. As the gap size decreases, the power transmitted from port 1 to port 2 also decreases, leading to an attenuation of ~ 40 dB for a gap size $g = 500$ nm. These results concur with the expected behaviour of the DC structure since for $g = 5$ µm most of the energy is expected to remain in WG1, whereas for $g = 500$ nm most of the energy is expected to shift to WG2. A cut-off frequency is observed at an incident frequency $f_c \approx 3.5$ THz. The effect of the cut-off frequency arises due the nature of the structure which behaves as an optical low pass filter. For incident frequencies which lead to the SSPP wave-vector $k_x > \pi/d$, the Bragg reflection regime is entered, in which no propagating mode exists, and a guided wave entering the waveguide decays owing to optical reflection [254].

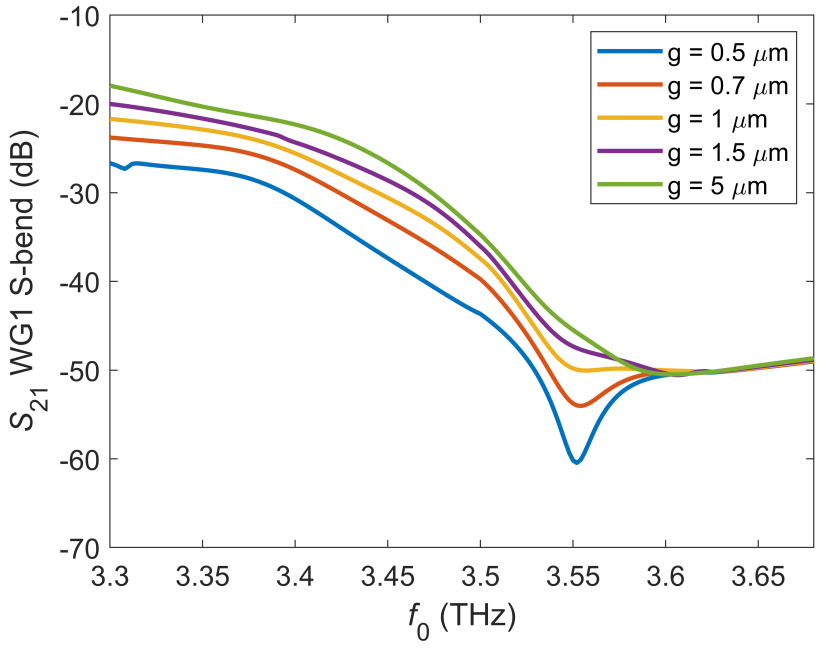

Figure 6.5: S_{21} Parameters of the DC structure for SSPPs launched in the excitation region and detected in the end of the WG1 S-bend region.

Furthermore, the S_{31} Parameters have been obtained for SSPPs launched on the excitation region (port 1) and detected at the end of the WG2 S-bend region (port 3), as shown in Fig. 6.6. It is observed that for an incident frequency $f_0 = 3.45$

THz, the transmitted power for a gap size $g = 5$ µm has been attenuated by ~ 50 dB. As the gap size decreases, the power transmitted from port 1 to port 3 increases, leading to an attenuation of ~ 25 dB for a gap size $g = 500$ nm. These results show the opposite behaviour to the S_{21} Parameters for WG1 and also concur with the expected behaviour of the DC structure since for $g = 5$ µm most of the energy is expected to remain in WG1, whereas for $g = 500$ nm most of the energy is expected to shift to WG2. A cut-off frequency is also observed at an incident frequency $f_c \approx 3.5$ THz.

The S_{21} and S_{31} parameters also concur with the magnitude plots in Fig. 6.4. Fig. 6.4 shows how the energy of the SSPPs gets split between WG1 and WG2 according to the gap size. For values of $g = 500$ nm and $g = 700$ nm, Fig. 6.4 shows that most of the energy shifts from WG1 to WG2. For values of $g = 1$ µm and $g = 1.5$ µm, Fig. 6.4 shows that the SSPP energy is split between WG1 and WG2. For a value of $g = 5$ µm, Fig. 6.4 shows that almost all of the energy remains in WG1. These results concur with the expected behaviour of the DC.

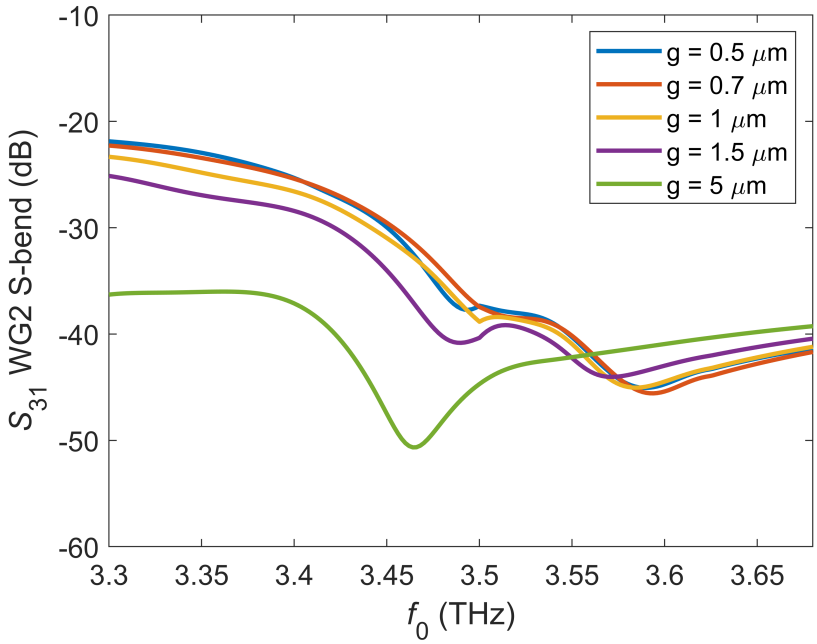

Figure 6.6: S_{31} Parameters of the DC structure for SSPPs launched in the excitation region and detected in the end of the WG2 S-bend region.

6.4.1 Phenomenological Analysis

Interaction Region

Due to the coupling between the two waveguides, the description of SSPPs propagating on the DC structures is more complex than for the asymmetric and symmetric waveguides presented in Chapters 4 and 5. Nevertheless, initially, a simple phenomenological model describing the field associated with the SSPPs on the DC structures is presented in this Section. The purpose of this phenomenological analysis is to to quantify in simple terms how the field amplitude of SSPPs changes due to the exchange of energy between waveguides as the SSPPs propagate through the interaction region of the DC structure.

In order to quantify the field strength associated with the SSPPs as they propagate along the waveguide, the average electric-field E_z was spatially averaged within each bar of the structure for all cases of g. These averaged values were then plotted as discrete points as a function of the distance x along the waveguide. Each average value was assigned at the centre point of its respective bar in the x direction. In Chapter 4, the SSPPs propagating on an asymmetric waveguide under no coupling ($g \rightarrow \infty$) were modeled as propagating waves bound to the surface of the waveguide, with an amplitude E_0, wave-vector k_x, a phase θ. and propagation length L_p.

By analogy the SSPPs propagating within the IR of WG1 of the DC structures can be modeled by a sinusoidal function which attenuates with distance from the origin of the IR (here defined as $x = 0$) using the expression:

$$E_z = E_0 \cos(k_x x + \theta) e^{-x/L_{eff}}. \tag{6.3}$$

The parameter L_{eff} accounts for the propagation length of the SSPPs, L_p, and also for the loss of energy due to coupling of the SSPPs with the WG2 in the IR. The fit of Eq. 6.3 to the simulation data of the IR of WG1 is shown in Fig. 6.7.

Furthermore, the SSPPs propagating on the IR of WG2 are also modelled by a sinusoidal function, but in this case the SSPP experiences an effective gain instead of a decay due to the exchange of energy from WG1 to WG2. This effective gain occurs due to the coupling of the two waveguides and is quantified using the variable L_g. The variable, L_g also accounts for the losses due to the propagation length, L_p. The simulation data of the SSPPs propagating on the IR of WG2 was numerically fit to Eq. 6.4, as shown in Fig. 6.8.

$$E_z = E_0 \cos(k_x x + \theta) e^{x/L_g}. \tag{6.4}$$

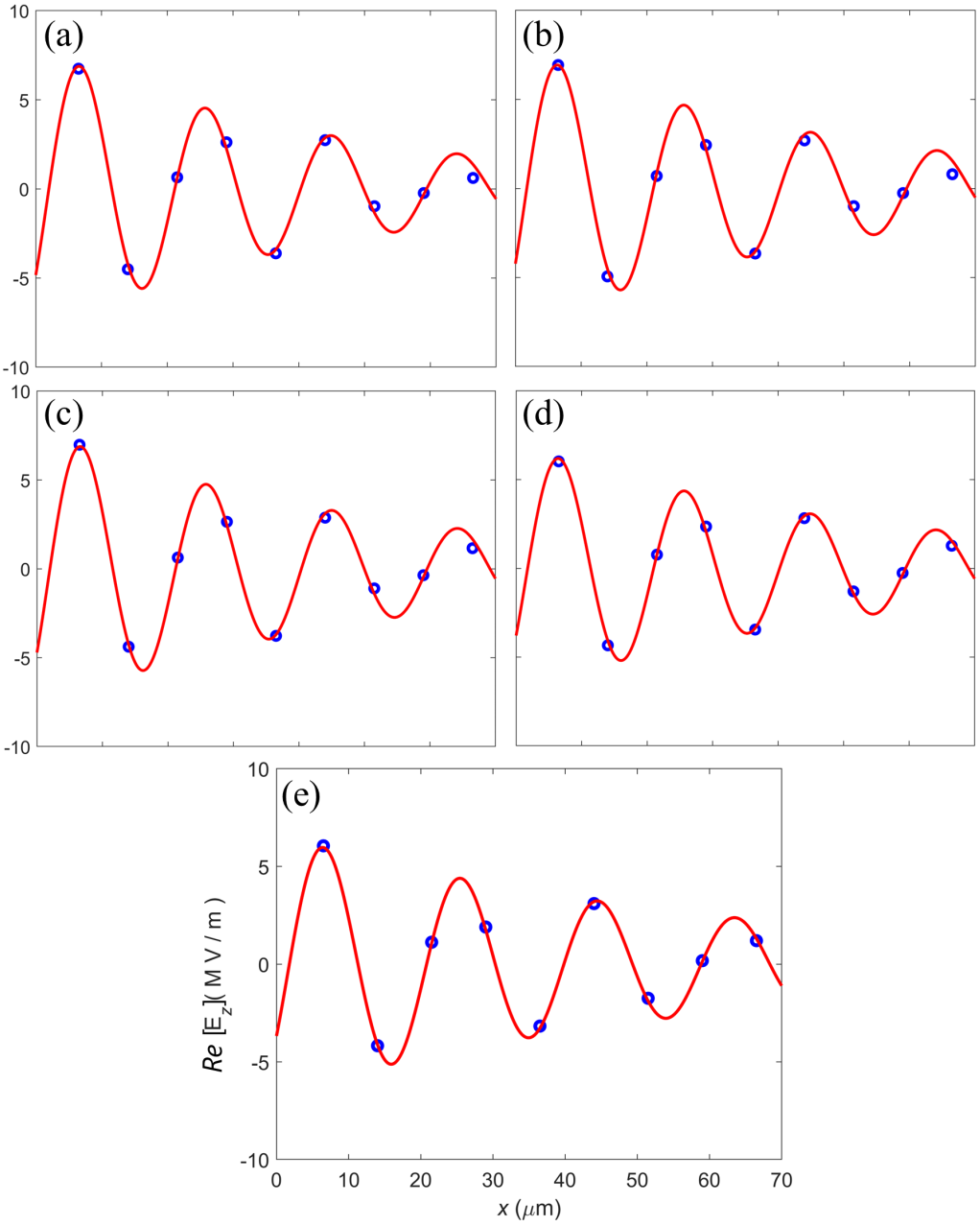

Figure 6.7: Analysis of the SSPPs coupled on the WG1 IR. (a) $g = 500$ nm. $E_0 = 8$ MV/m, $k_x = 3280$ cm^{-1}, $\theta = -2.2$ rad, and $L_{eff} = 46$ µm. (b) $g = 700$ nm. $E_0 = 7.9$ MV/m, $k_x = 3260$ cm^{-1}, $\theta = -2.1$ rad, and $L_{eff} = 49$ µm. (c) $g = 1$ µm. $E_0 = 7.8$ MV/m, $k_x = 3270$ cm^{-1}, $\theta = -2.2$ rad, and $L_{eff} = 52$ µm. (d) $g = 1.5$ µm. $E_0 = 6.95$ MV/m, $k_x = 3270$ cm^{-1}, $\theta = -2.15$ rad, and $L_{eff} = 55$ µm. (e) $g = 5$ µm. $E_0 = 6.6$ MV/m, $k_x = 3300$ cm^{-1}, $\theta = -2.15$ rad, and $L_{eff} = 63$ µm.

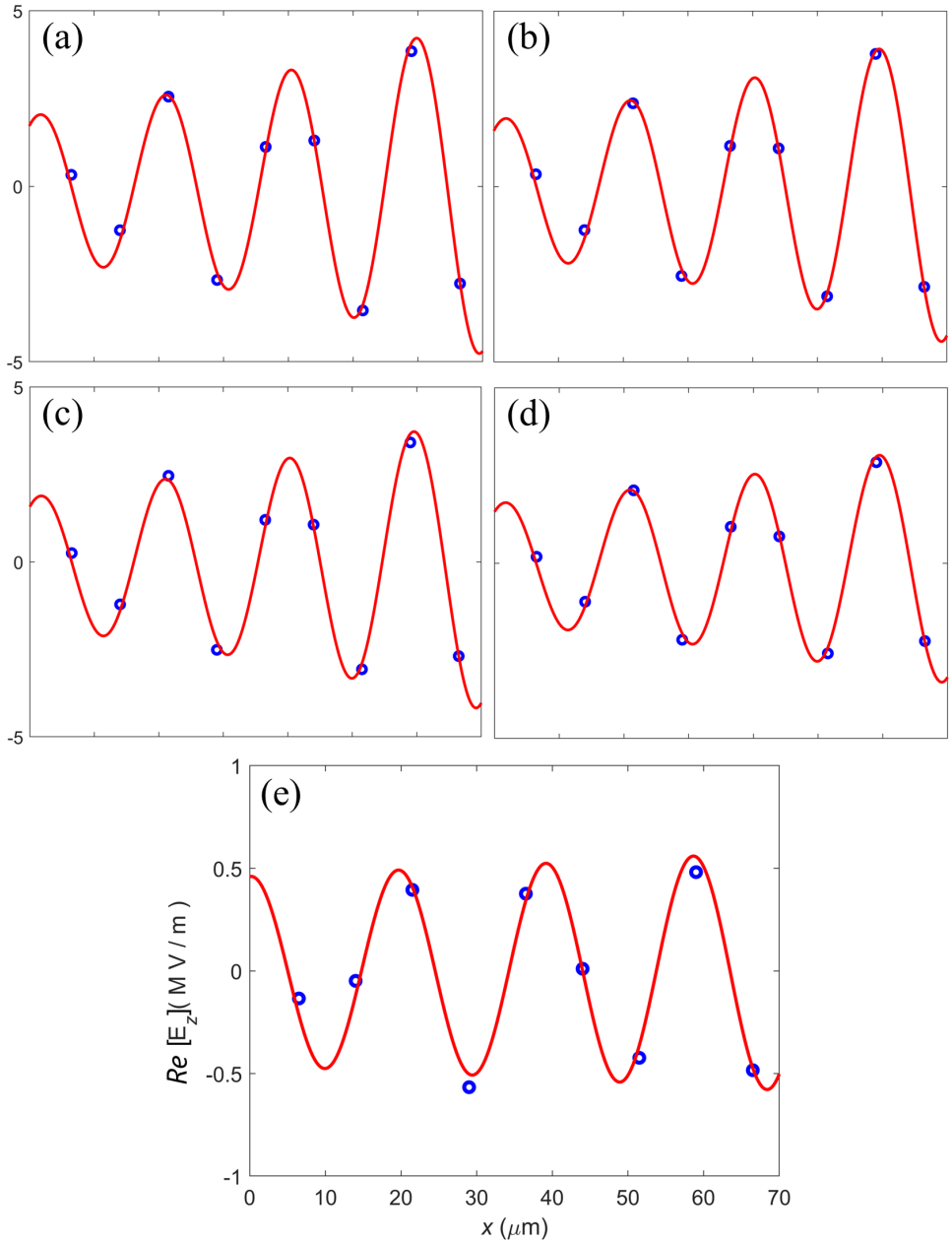

Figure 6.8: Analysis of the SSPPs coupled on the WG2 IR. (a) $g = 500$ nm. $E_0 = 2$ MV/m, $k_x = 3250$ cm^{-1}, $\theta = -0.54$ rad, and $L_g = 80$ µm. (b) $g = 700$ nm. $E_0 = 1.9$ MV/m, $k_x = 3270$ cm^{-1}, $\theta = -0.58$ rad, and $L_g = 82$ µm. (c) $g = 1$ µm. $E_0 = 1.85$ MV/m, $k_x = 3260$ cm^{-1}, $\theta = -0.55$ rad, and $L_g = 85$ µm. (d) $g = 1.5$ µm. $E_0 = 1.7$ MV/m, $k_x = 3265$ cm^{-1}, $\theta = -0.53$ rad, and $L_g = 100$ µm. (e) $g = 5$ µm. $E_0 = 0.46$ MV/m, $k_x = 3225$ cm^{-1}, $\theta = 0$ rad, and $L_g = 300$ µm.

Figure 6.9 shows the relationship between the gap size, g and the effective propagation length, L_{eff} obtained from the fits to the simulation data for the SSPPs propagating on the WG1 IR. The effective propagation length of the propagating SSPPs on the WG1 IR increases as the gap size increases. This is a phenomenological analysis which embeds the behaviour of the coupling between the two waveguides on the propagation length. The propagation length of the asymmetric waveguide under no coupling with another waveguide has been shown to be $L_p = 75$ µm (see section 4.3). At $g = 5$ µm, the propagation length has been calculated to be $L_{eff} = 63$ µm, which approaches the value of $L_p = 75$ µm. This result agrees with the expectation that as the gap size increases, the effective propagation length approaches the value of the propagation length of the asymmetric waveguide under no coupling with another waveguide ($L_{eff} \rightarrow L_p$). Conversely, for smaller gap sizes, L_{eff} is seen to decrease due to the exchange of SSPP energy to WG2 within the IR. At $g = 500$ nm, the propagation length shows the lowest value which is calculated to be $L_{eff} = 46$ µm.

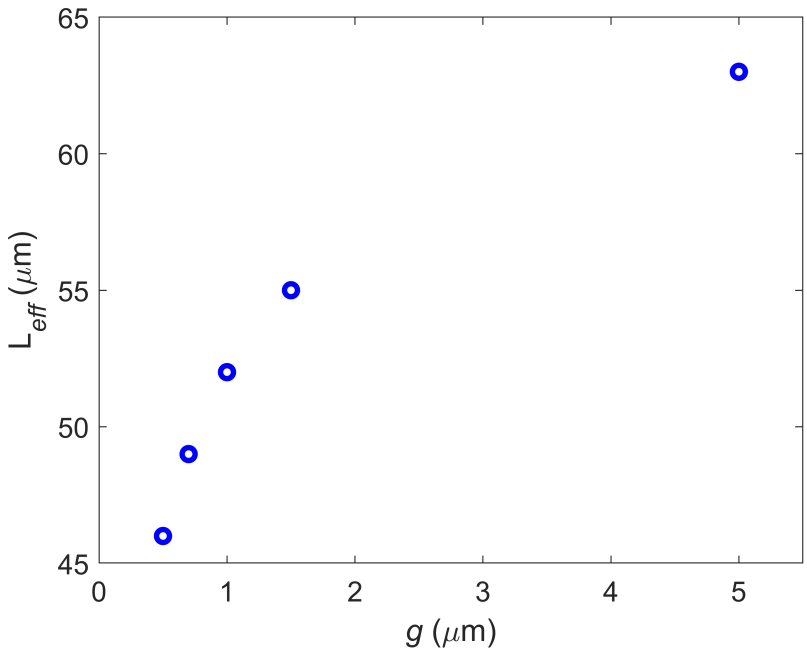

Figure 6.9: Analysis of L_{eff} on the WG1 IR as a function of g.

Figure 6.10 shows the relationship between the gap size, g and the effective gain length, L_g obtained from the fits to the simulation data for the SSPPs propagating on the WG2 IR. In this case, the SSPP experiences an effective gain instead of a gradual decay. The smaller the value of the effective gain length, L_g, the stronger the gain that the SSPP experiences. In Fig. 6.10, it can be seen that for a gap size, $g = 500$ nm, the effective gain length has its lowest value ($L_g = 80$ µm) indicating strongest gain, whereas for $g = 5$ µm, the effective gain length has its highest value ($L_g = 300$ µm) indicating lowest gain. This variation of the effective gain length, L_g is the opposite to that observed in WG1 and agrees with the expected behaviour of the DC structure, the transfer of energy from WG1 to WG2 is expected to be stronger for smaller gaps.

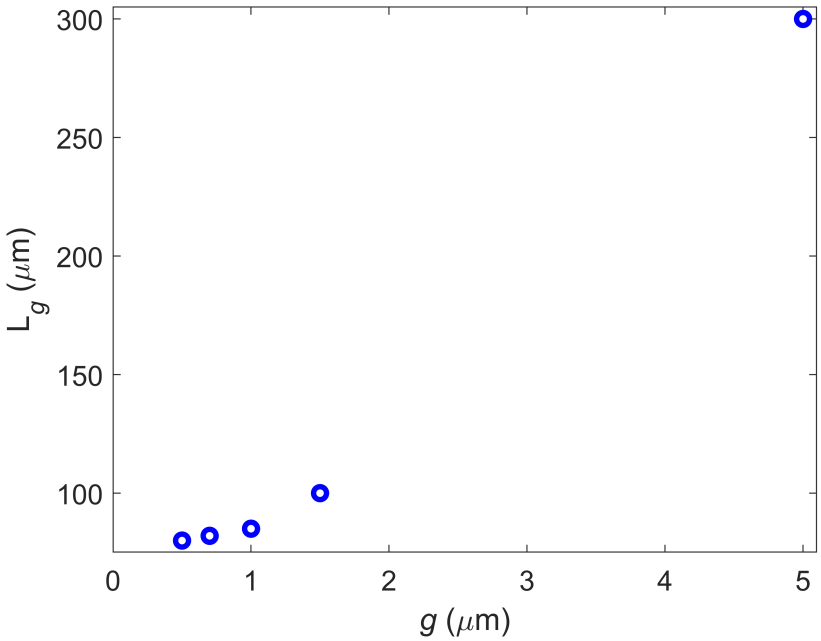

Figure 6.10: Analysis of L_g on the WG2 IR as a function of g.

Figure 6.11 shows the relationship between the amplitude of the SSPP (E_0) at the origin of the WG1 IR ($x = 0$) as a function of gap size, g. The values of E_0 were extracted from the numerical fits to the simulation data of the SSPPs propagating on the WG1 IR shown in Fig. 6.7. Figure 6.12 shows the relationship between the amplitude of the SSPP (E_0) at the origin of the WG2 IR ($x = 0$) as a function of gap size, g. The values of E_0 were extracted from the numerical fits to the simulation data of the SSPPs propagating on the WG2 IR shown in Fig. 6.8.

Figure 6.11 shows that the amplitude, E_0 of the SSPP propagating on the WG1 IR decreases as the gap size, g increases. When the gap size, $g = 500$ nm, the energy of the SSPP is large at the origin of the WG1 IR ($E_0 = 8$ MV/m), whereas when $g = 5$ µm, the energy of the SSPP is lower at the origin of the WG1 IR ($E_0 = 6.6$ MV/m). Similarly, Fig. 6.12 shows that the amplitude, E_0 of the SSPP propagating on the WG2 IR also decreases as the gap size, g increases. When the gap size, $g = 500$ nm, the energy of the SSPP is large at the origin of the WG2 IR ($E_0 = 2$ MV/m), whereas when $g = 5$ µm, the energy of the SSPP is lower at the origin of the WG2 IR ($E_0 = 0.46$ MV/m). This decrease in amplitude observed in both Fig. 6.11 and Fig. 6.12 could occur due to the change in phase difference between the even and odd modes at the start of the IR ($x = 0$) as the gap size changes. In this analysis, the even and odd modes are modelled by a single wave-vector, k_x, therefore the change in the phase difference is embedded in the amplitude of the SSPP, E_0.

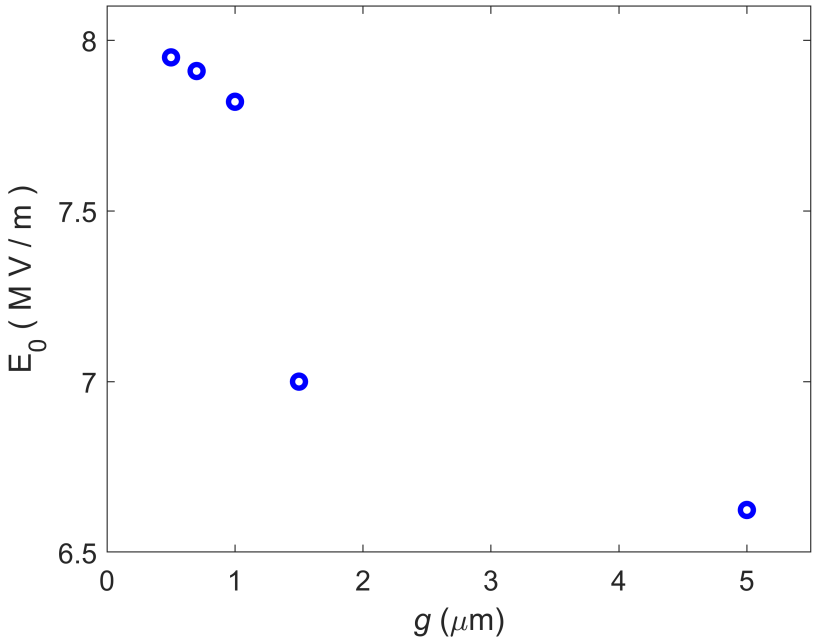

Figure 6.11: Analysis of E_0 on the WG1 IR as a function of g.

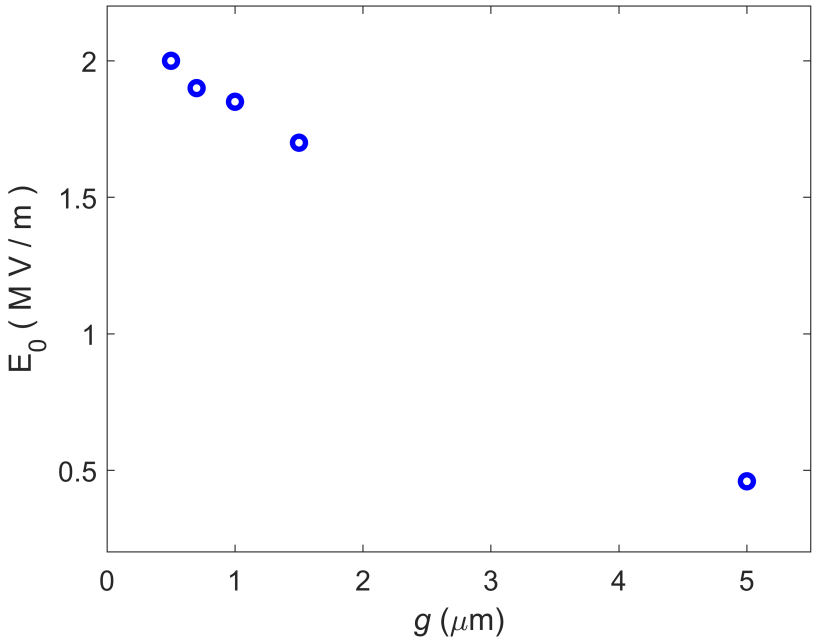

Figure 6.12: Analysis of E_0 on the WG2 IR as a function of g.

S-bend regions

The SSPPs propagating on the interaction region, are spatially separated in the S-bend region. When the SSPPs propagate on the S-bend region, they do not experience any coupling between the two waveguides. Therefore, the SSPPs behave in the same manner as seen in Chapter 4; SSPPs propagate on an asymmetric waveguide and are modeled as propagating waves bound to the surface of the metallic waveguide layer, with an amplitude E_0 at the origin of the S-bend region ($x = 0$), wave-vector k_x, phase θ, and propagation length L_p. In this case, the propagation length L_p only accounts for the losses as the SSPP propagates along the waveguide. Therefore, Eq. 4.1 was used to fit the simulation data of the SSPPs propagating on the WG1 and WG2 S-bend regions. In this analysis, the propagation length for WG1 and WG2 S-bend regions was kept constant at $L_p = 33$ µm. This value is considerably lower than the propagation length of the asymmetric waveguide found in Chapter 4; $L_p = 75$ µm. This is because in this case the S-bend region is comprised of two bends which cause additional losses when compared with a straight asymmetric waveguide. The fits to the simulation data of the SSPPs propagating on the WG1 and WG2 S-bend regions are shown in

Fig. 6.13 and Fig. 6.14 respectively. The wave-vector of the SSPPs propagating on the S-bend regions was found to be $k_x = 3600$ cm^{-1} from all the fits, as expected.

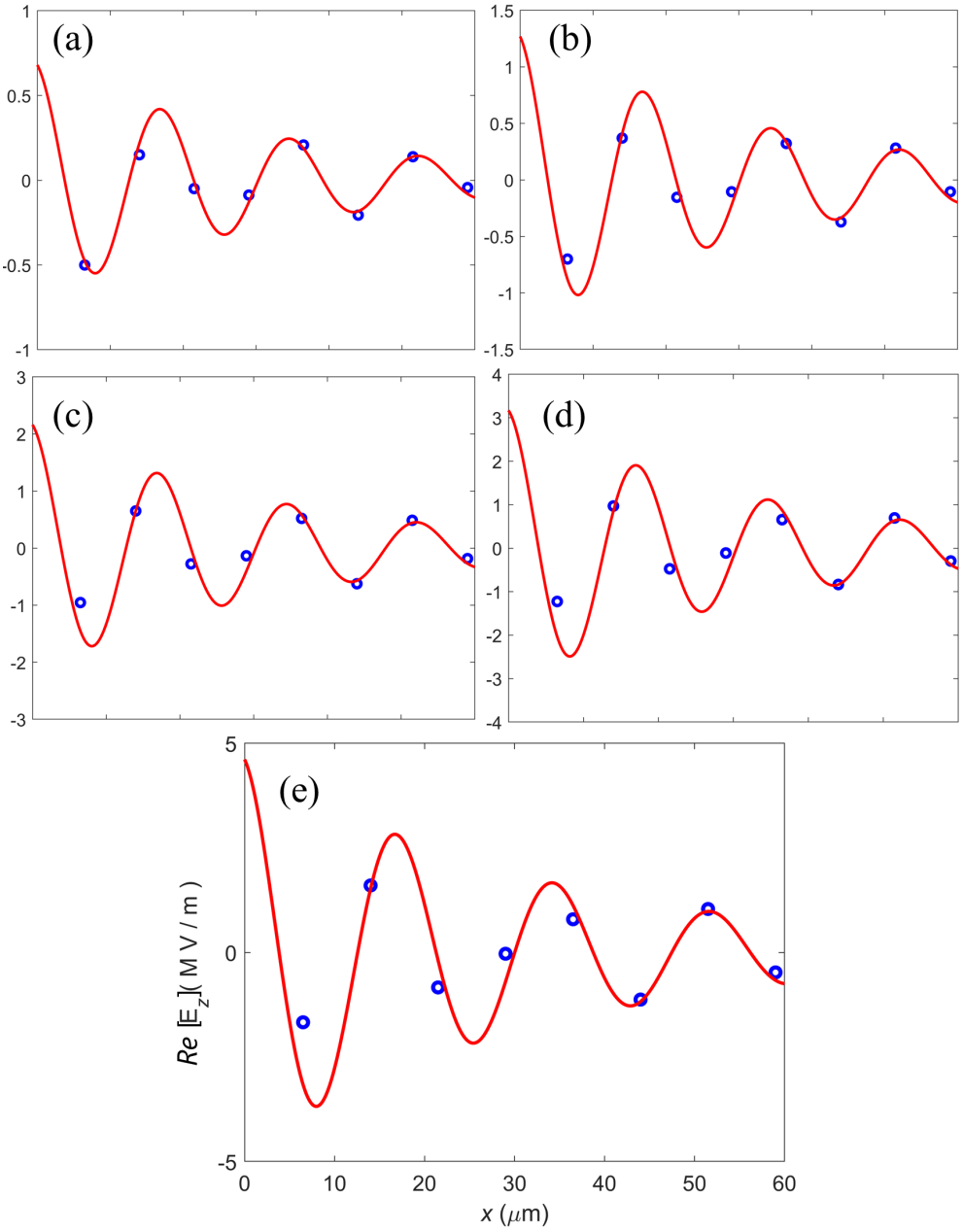

Figure 6.13: Analysis of the SSPPs coupled on the WG1 S-bend. (a) $g = 500$ nm. $E_0 = 0.7$ MV/m, $k_x = 3550$ cm^{-1}, $\theta = 0.24$ rad. (b) $g = 700$ nm. $E_0 = 1.3$ MV/m, $k_x = 3570$ cm^{-1}, $\theta = 0.22$ rad. (c) $g = 1$ µm. $E_0 = 2.2$ MV/m, $k_x = 3570$ cm^{-1}, $\theta = 0.18$ rad. (d) $g = 1.5$ µm. $E_0 = 3.2$ MV/m, $k_x = 3570$ cm^{-1}, $\theta = 0.14$ rad. (e) $g = 5$ µm. $E_0 = 4.7$ MV/m, $k_x = 3600$ cm^{-1}, $\theta = 0.19$ rad.

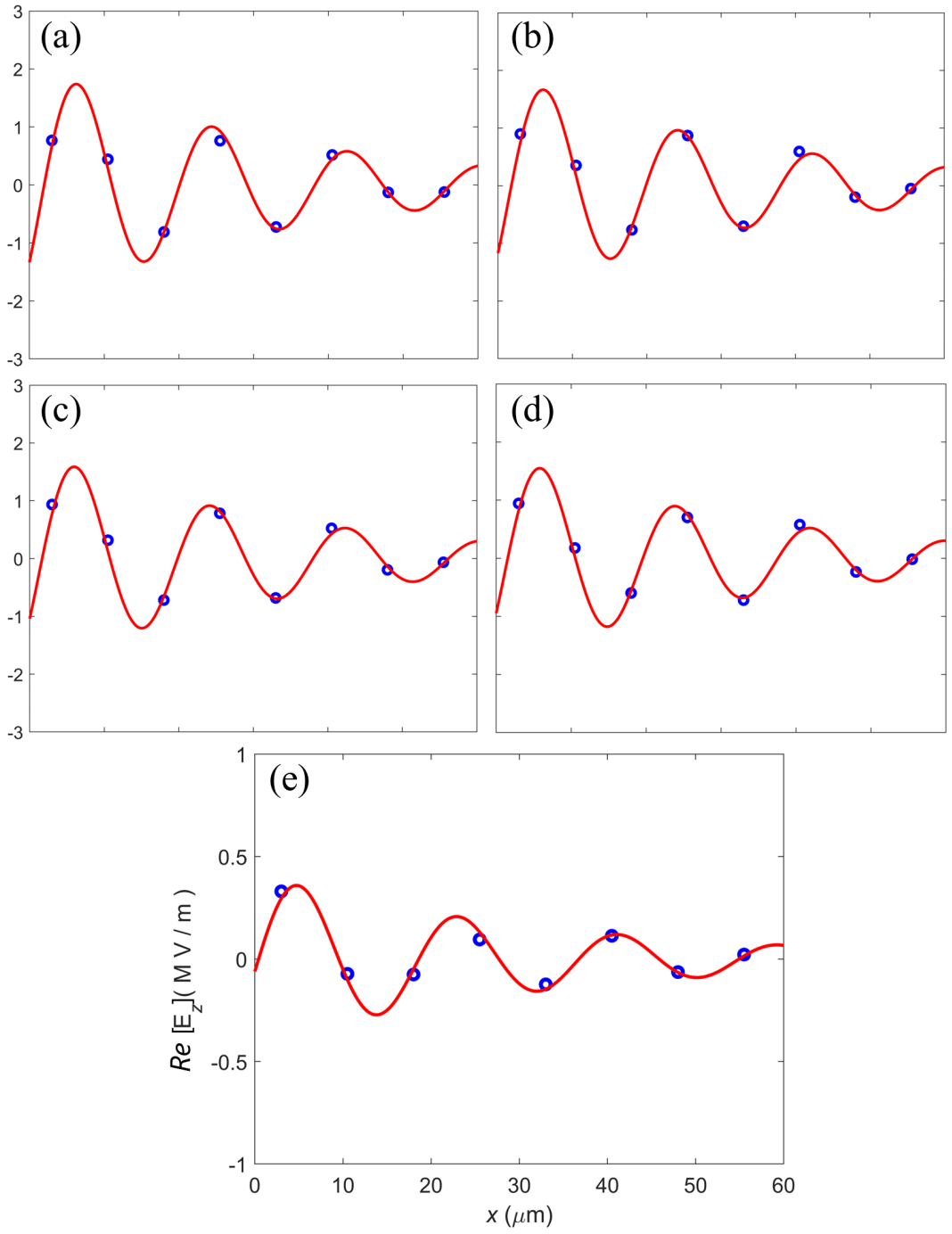

Figure 6.14: Analysis of the SSPPs coupled on the WG2 S-bend. (a) $g = 500$ nm. $E_0 = 2.3$ MV/m, $k_x = 3470$ cm^{-1}, $\theta = 2.8$ rad. (b) $g = 700$ nm. $E_0 = 2.25$ MV/m, $k_x = 3480$ cm^{-1}, $\theta = 2.9$ rad. (c) $g = 1$ µm. $E_0 = 2.15$ MV/m, $k_x = 3460$ cm^{-1}, $\theta = 2.9$ rad. (d) $g = 1.5$ µm. $E_0 = 2$ MV/m, $k_x = 3485$ cm^{-1}, $\theta = 3$ rad. (e) $g = 5$ µm. $E_0 = 0.46$ MV/m, $k_x = 3460$ cm^{-1}, $\theta = -3$ rad.

The fitted amplitude, E_0 (at $x = 0$) of the SSPP propagating on the WG1 S-bend region, indicates the energy of the SSPP which reaches the WG1 S-bend region. This value depends on the value of the gap size, g. It is expected that the smallest amount of energy (smallest amplitude, E_0) reaching the WG1 S-bend will occur for $g = 500$ nm, as almost the total energy is expected to be transferred to WG2. The highest amplitude is expected to be reached at $g = 5$ µm because the energy is expected to mostly remain in WG1. Figure 6.15 confirms these expectations and the amplitude follows a non-linear increase as the gap increases.

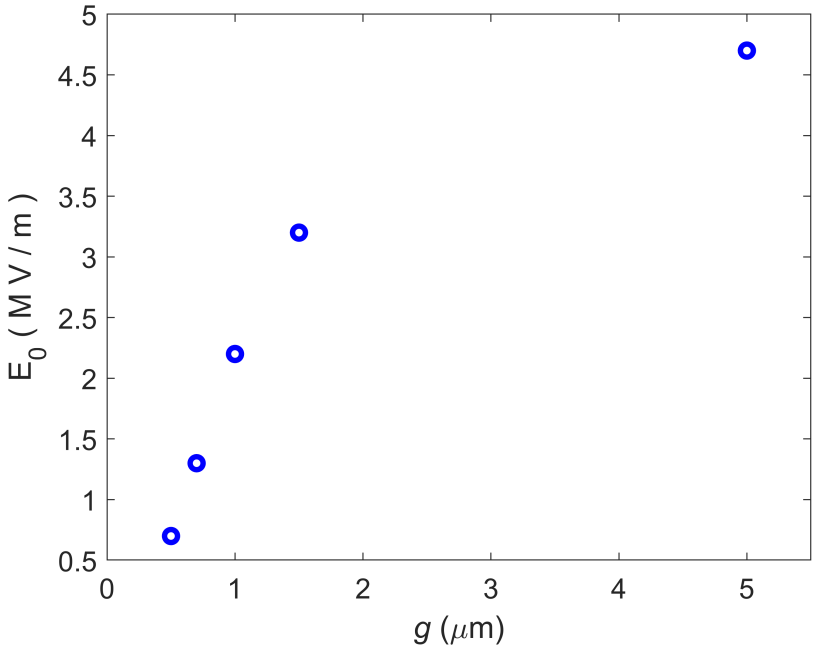

Figure 6.15: Analysis of E_0 as a function of g for the WG1 S-bend.

The relationship between the amplitude, E_0 (at $x = 0$) of the propagating SSPP on the WG2 S-bend and the gap size, g is expected to show a decrease in amplitude as the gap increases. This is because most of the energy is expected to transfer from WG1 to WG2 for a gap size, $g = 500$ nm. As the gap increases, the coupling between WG1 and WG2 is expected to reduce, hence less energy is expected to transfer to WG2. Figure 6.16 shows this decrease in amplitude on the WG2 S-bend as the gap increases, which is opposite to the increases observed in WG1, as expected.

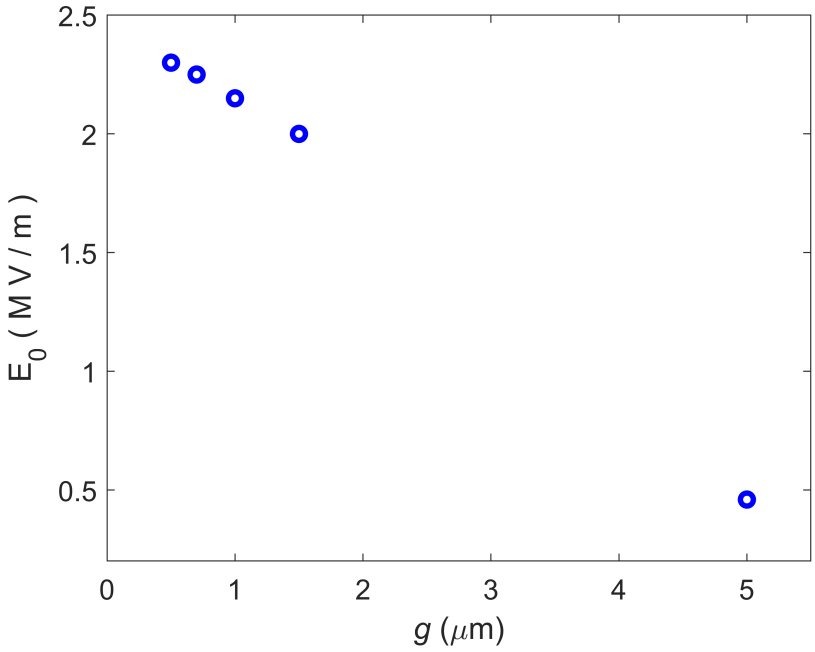

Figure 6.16: Analysis of E_0 as a function of g for the WG2 S-bend.

6.4.2 Supermode Analysis

To further investigate the effect of varying the gap size, g on the SSPPs propagating on the DC structure, the supermode analysis was also applied [261]. As before, SSPPs are excited at the excitation region (Fig. 6.1). These SSPPs are expected to behave in the same manner as those seen in the asymmetric waveguides (Chapter 4); they are characterised by a single wave-vector and they will decay as they propagate along WG1. When the decayed SSPPs reach the start of the IR ($x = 0$) they can excite even and odd modes in the DC structure. It can be expected that the total energy of the excited modes will be distributed primarily in WG1 at $x = 0$ i.e. the even and odd modes will be approximately in-phase. As these modes propagate, energy will be transferred to WG2 but the modes will also decay according to the waveguide losses.

The electric fields associated with the even mode, expressed as a function of distance x, for each of WG1 and WG2, can be approximated as:

$$E_{1e} = E_e \sin\left(k_{xe}x + \theta_e\right) \exp\left(\frac{-x}{L_e}\right) \tag{6.5}$$

$$E_{2e} = E_e \sin\left(k_{xe}x + \theta_e\right) \exp\left(\frac{-x}{L_e}\right) \tag{6.6}$$

For simplicity it is assumed that the amplitudes in WG1 and WG2, E_e are equal. The fields oscillate at a frequency $f = 3.45$ THz, and with a wavelength $\lambda_e = 2\pi/k_{xe}$, and the fields on WG1 and WG2 are in-phase.

The electric fields associated with the odd mode, expressed as a function of distance x, for each of WG1 and WG2, can be approximated as:

$$E_{1o} = E_o \sin\left(k_{xo}x + \theta_o\right) \exp\left(\frac{-x}{L_o}\right) \tag{6.7}$$

$$E_{2o} = -E_o \sin\left(k_{xo}x + \theta_o\right) \exp\left(\frac{-x}{L_o}\right) \tag{6.8}$$

The odd modes have a different wavelength to the even mode, $\lambda_o = 2\pi/k_{xo}$, and in this case the fields on WG1 and WG2 are out-of-phase.

The total field expressed as a function of distance x, for each of WG1 and WG2, is obtained by summing the fields associated with the even (Eq. 6.5 and Eq. 6.6) and odd (Eq. 6.7 and Eq. 6.8) modes:

$$E_1 = E_e \sin\left(k_{xe}x + \theta_e\right) \exp\left(\frac{-x}{L_e}\right) + E_o \sin\left(k_{xo}x + \theta_o\right) \exp\left(\frac{-x}{L_o}\right) \tag{6.9}$$

$$E_2 = E_e \sin\left(k_{xe}x + \theta_e\right) \exp\left(\frac{-x}{L_e}\right) - E_o \sin\left(k_{xo}x + \theta_o\right) \exp\left(\frac{-x}{L_o}\right) \tag{6.10}$$

To further simplify the analysis, it is assumed that $L_e = L_o = L$, and $E_e = E_o = E$. This gives:

$$E_1 = 2E \sin\left(\frac{(k_{xe}+k_{xo})x}{2} + \frac{\theta_e+\theta_o}{2}\right) \cos\left(\frac{(k_{xe}-k_{xo})x}{2} + \frac{\theta_e-\theta_o}{2}\right) \exp\left(\frac{-x}{L}\right) \tag{6.11}$$

$$E_2 = 2E \cos\left(\frac{(k_{xe}+k_{xo})x}{2} + \frac{\theta_e+\theta_o}{2}\right) \sin\left(\frac{(k_{xe}-k_{xo})x}{2} + \frac{\theta_e-\theta_o}{2}\right) \exp\left(\frac{-x}{L}\right) \tag{6.12}$$

And rewriting $\frac{k_{xe}+k_{xo}}{2} = k_x$ and $\frac{k_{xe}-k_{xo}}{2} = \Delta k$:

$$E_1 = 2E \sin\left(k_x x + \frac{\theta_e+\theta_o}{2}\right) \cos\left(\Delta k.x + \frac{\theta_e-\theta_o}{2}\right) \exp\left(\frac{-x}{L}\right) \tag{6.13}$$

$$E_2 = 2E \cos\left(k_x x + \frac{\theta_e+\theta_o}{2}\right) \sin\left(\Delta k.x + \frac{\theta_e-\theta_o}{2}\right) \exp\left(\frac{-x}{L}\right) \tag{6.14}$$

In each of these equations, the first trigonometric function represents the oscillation of the SSPP field and the second trigonometric function represents the (time-independent) envelope function that describes the energy distribution between WG1 and WG2. It can be seen that when $\theta_e - \theta_o = 0$ (i.e. the even and odd modes are in-phase at $x = 0$) then $E_2 = 0$ at $x = 0$ (indicating that all the energy associated with the SSPPs is distributed in WG1). When $\theta_e - \theta_o = \pi$ (i.e. the even and odd modes are out-of-phase) then $E_1 = 0$ at $x = 0$ (indicating that all the energy associated with the SSPPs is distributed in WG2). For intermediate values of $\theta_e - \theta_o$ the energy is distributed between WG1 and WG2.

Equations 6.13 and 6.14 were used to fit the simulation data for WG1 and WG2, as shown in Fig. 6.17 and Fig. 6.18 respectively. Since there are a lot of free parameters in these equations, it was necessary to reduce the number of fitting parameters. Therefore the following parameters were fixed: $L_p = 83$ µm which is the value of the propagation length obtained from the wave-port simulation of the PSP symmetric structures (see Section 5.3), and the electric field, $E = 8$ was kept constant for the even and odd modes for all gap sizes. The value of $E = 8$ MV/m was determined by first running fits with E as a free parameter and then taking an average value of the fitted values. The total energy in the system does not change with gap size, g; it is only how the energy is distributed between WG1 and WG2 that changes, and that is controlled by Δk and the phase difference ($\Delta\theta = \theta_e - \theta_o$).

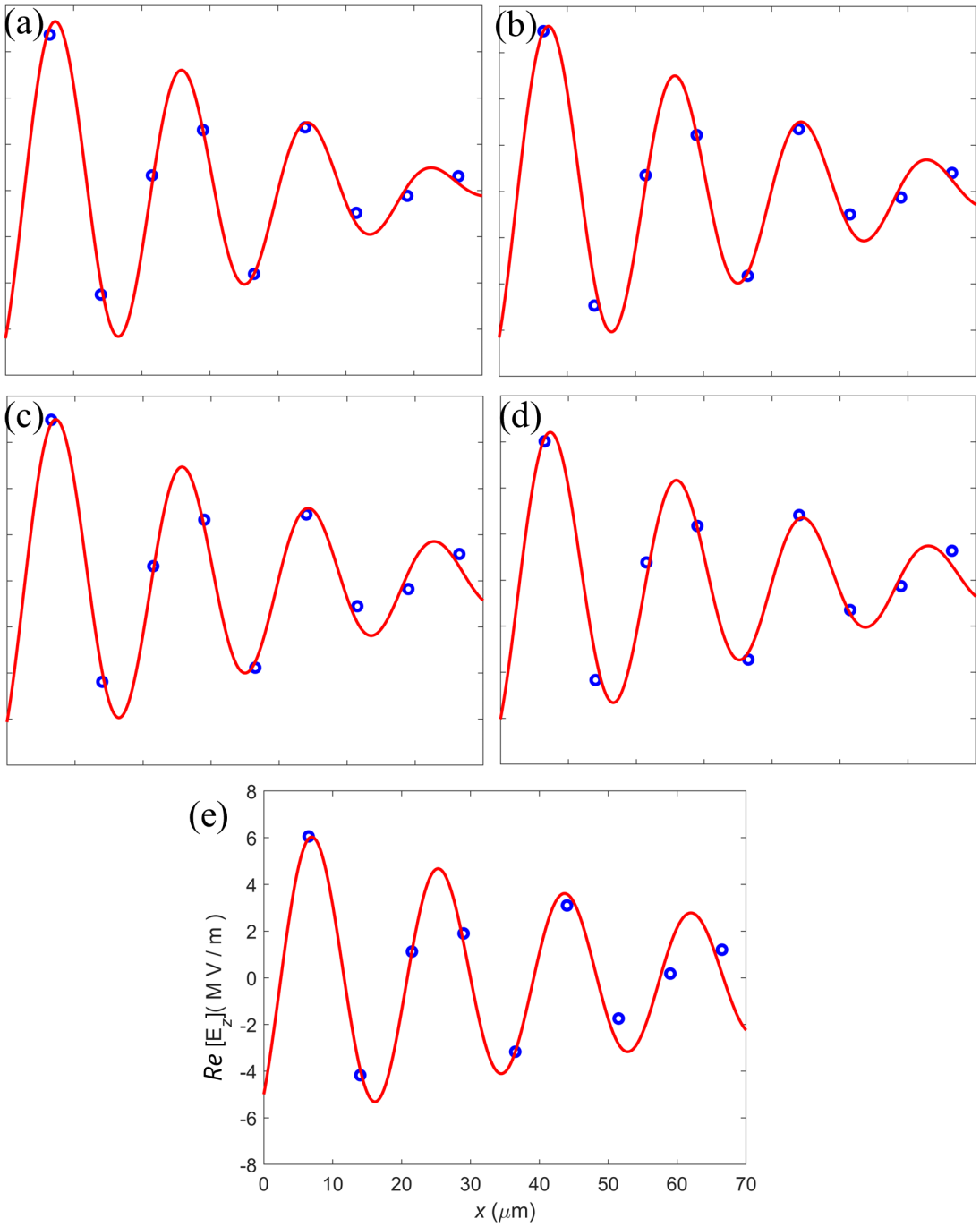

Figure 6.17: Supermode analysis of the SSPPs coupled on the surface of the WG1 interaction region. (a) gap, $g = 500$ nm, (b) gap, $g = 700$ nm, (c) gap, $g = 1$ µm, (d) gap, $g = 1.5$ µm, (e) gap, $g = 5$ µm.

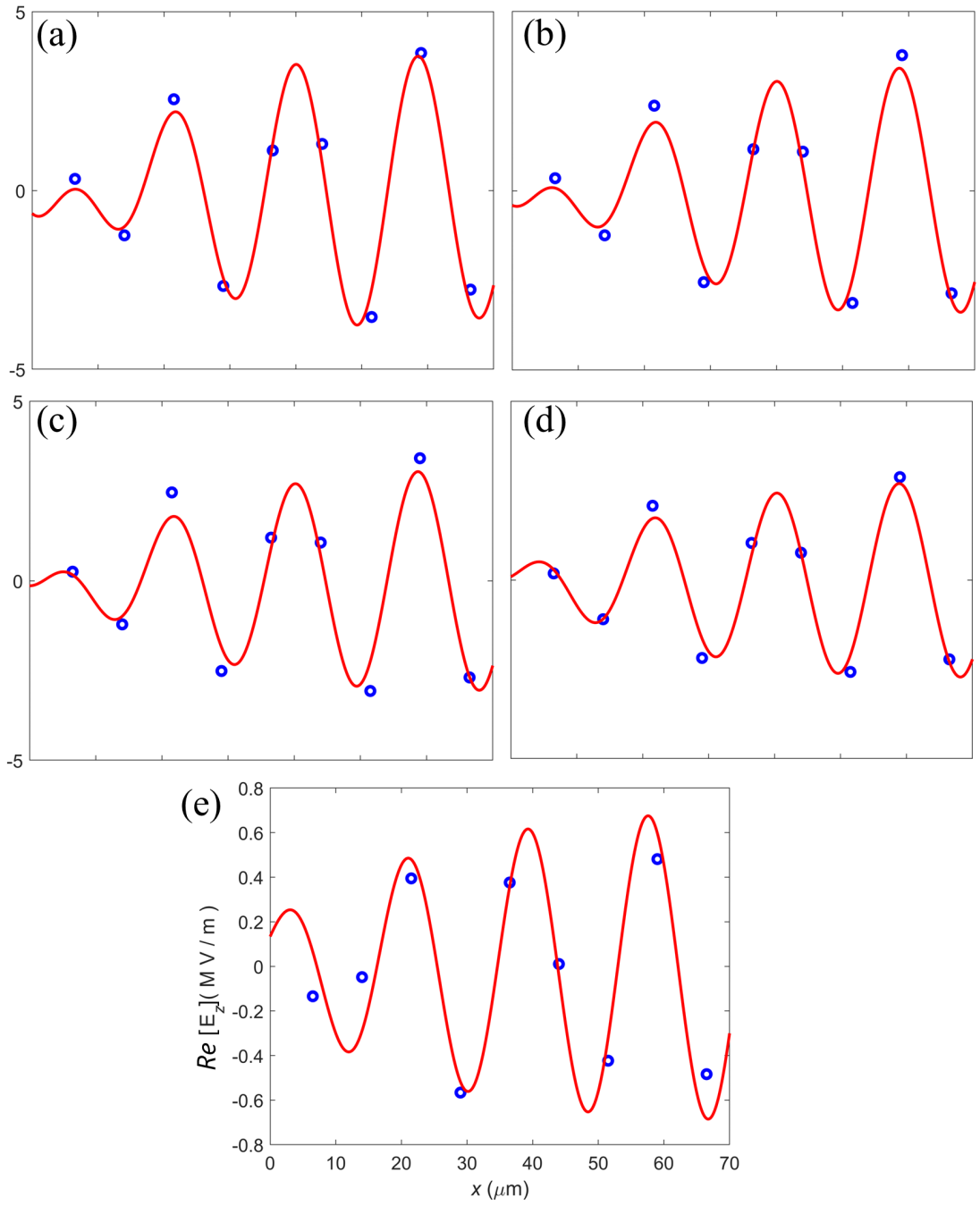

Figure 6.18: Supermode analysis of the SSPPs coupled on the surface of the WG2 interaction region. (a) gap, $g = 500$ nm, (b) gap, $g = 700$ nm, (c) gap, $g = 1$ µm, (d) gap, $g = 1.5$ µm, (e) gap, $g = 5$ µm.

The values of the coupling coefficient Δk and phase difference $\Delta\theta$ obtained from the fits shown in Figures 6.17 and 6.18 are shown in Figures 6.19 and 6.20.

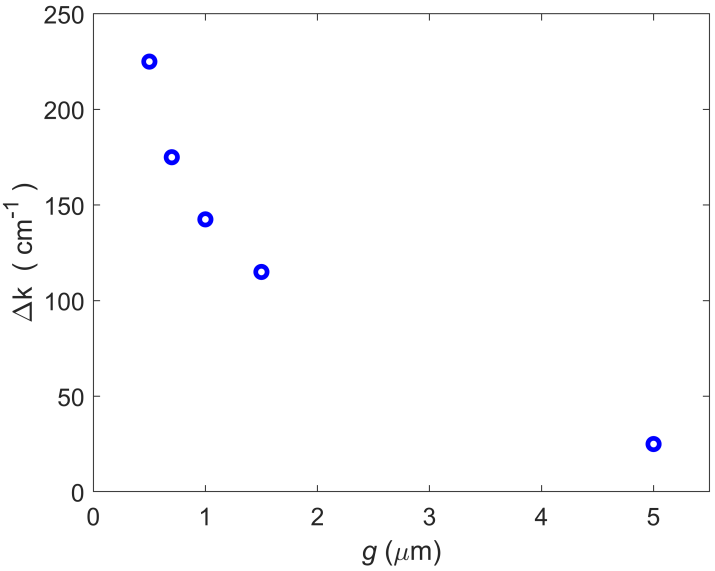

Figure 6.19: Variation of the parameter Δk as a function of g in WG1 and WG2 IR using supermode analysis.

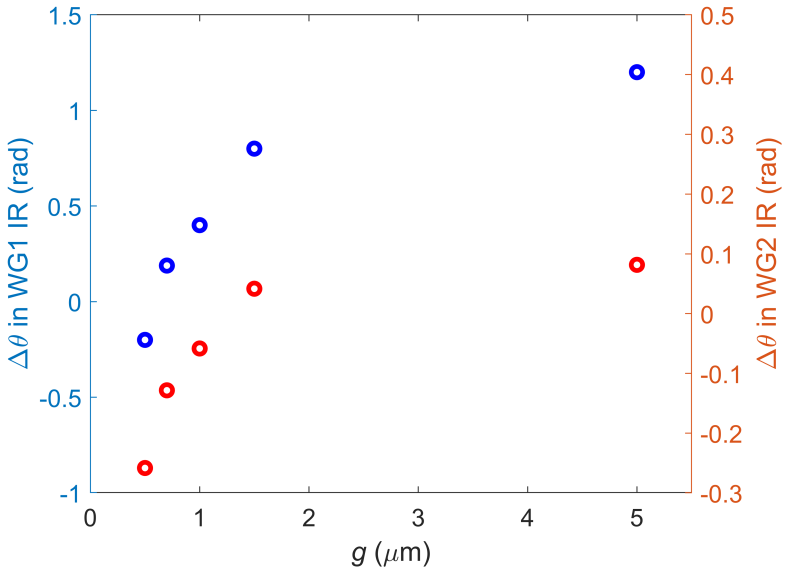

Figure 6.20: Variation of the parameter $\Delta\theta$ as a function of g in WG1 and WG2 IR using supermode analysis.

From Fig. 6.17 and Fig. 6.18, it can be seen that Equations 6.13 and 6.14 fit the simulation data very well. The variation of Δk as a function of gap size, g in the IR observed in Fig. 6.19 for WG1 and WG2 follows a trend which concurs with the calculated dispersion relations for the even and odd modes in these structures. Namely, for small values of g, the difference in the wave-vector values between the even and odd modes is large (see Fig. 6.3). As g increases, the difference in the wave-vector values between the even and odd modes becomes smaller. This means that the coupling length gets larger according to Eq. 6.2. This pattern is clearly observed in Fig. 6.19. The relation between Δk and g is analogous to the relations between the effective propagation length, L_{eff}, and g for WG1, and between the effective gain, L_g, and g for WG2 obtained from the phenomenological analysis (see Figures 6.9 and 6.10).

In theory, the values of Δk obtained from the simulation results for WG1 and WG2 (Fig. 6.19) should be equal for the same value of g. From the analysis, they were found to be equal and also concur with the wave-vector values obtained from the dispersion relations. This similarity is observed despite the various assumptions made in this supermode analysis, for example the assumptions that $L_e = L_o = L$ and $E_e = E_o = E$, and the fixed values of these parameters used in the fits. The results show that the variation of Δk as a function of g behaves as expected, with the energy associated with the SSPPs transferring from WG1 to WG2 over shorter distances as the gap size decreases.

Figure 6.20 shows the variation of the phase difference, $\Delta\theta$ as a function of gap size, g, for WG1 and WG2. The phase difference determined from the simulation data for WG1 is close to zero for small values of g, and it increases as g increases. From Eq. 6.13, $\Delta\theta = \theta_e - \theta_o \approx 0$ leads to the cosine term approaching unity when $x = 0$, which shows that all the energy remains in WG1 at the start if the interaction region, as expected. The phase difference determined from the simulation data for WG2 is also lower than zero for small values of g and greater than zero for $g > 1.5$ µm. Likewise, from Eq. 6.14, $\Delta\theta = \theta_e - \theta_o \approx 0$ leads to the sine term to a zero value when $x = 0$, which shows that no energy has transferred to WG2 at the start of the interaction region, as expected.

6.5 Free-space excitation under oblique incidence

6.5.1 Theoretical description of free-space excitation of DC structures

In this section, the coupling of a free-space beam to SSPPs on the DC structure is investigated incorporating grating structures with period $\alpha = 6$ µm. The illuminating beam is obliquely incident on the structure with an angle of incidence $\theta_i = 54^o$, and propagates in the $y-z$ plane with its polarisation also oscillating in the plane (perpendicular polarisation), as shown in Fig. 4.15. The free-space beam direction and polarisation matches the free-space beam of the experimental s-SNOM system. The simulation environment is described in Section 4.5.

This situation is much more complex than the wave-port excitation case since SSPPs can be excited at both edges of both WG1 and WG2. In this case the situation can be described as follows: SSPPs are launched at the excitation region of WG1 by the free-space beam interacting with the grating structure. The SSPPs will behave in the same manner as those seen in the asymmetric structures (Chapter 4); they are characterised by a single wave-vector and they will decay as they propagate along WG1. When the decayed SSPPs reach the start of the interaction region ($x = 0$) they can excite even and odd modes in the DC structure. It can be expected that the total energy of the excited modes will be distributed primarily in WG1 at $x = 0$ i.e. the even and odd modes will be approximately in-phase. As these modes propagate, energy will be transferred to WG2 but the modes will also decay according to the waveguide losses. At the same time waveguide modes can also be excited at the edge of WG2 by the free-space beam. In this case the total energy is expected to be distributed primarily in WG2 at $x = 0$ i.e. the even and odd modes will be approximately out-of-phase. As these modes propagate, energy will be transferred to WG1 but the modes will also decay according to the waveguide losses.

Starting by considering the modes launched from the excitation region of WG1, the situation will be similar to that described for the wave-port excitation (Equations 6.9 and 6.10):

$$E_{1,1} = E_{e1}\sin\left(k_{xe}x + \theta_{e1} + \phi\right)\exp\left(\frac{-x}{L_e}\right) + E_{o1}\sin\left(k_{xo}x + \theta_{o1} + \phi\right)\exp\left(\frac{-x}{L_o}\right) \tag{6.15}$$

$$E_{2,1} = E_{e1}\sin\left(k_{xe}x + \theta_{e1} + \phi\right)\exp\left(\frac{-x}{L_e}\right) - E_{o1}\sin\left(k_{xo}x + \theta_{o1} + \phi\right)\exp\left(\frac{-x}{L_o}\right) \tag{6.16}$$

Here the second subscript number, 1 indicates excitation from WG1. Note that the phase delay ϕ is also included to account for the extra phase accumulated by the SSPPs as they propagate from the grating on WG1 to the start of the interaction region ($x = 0$). To further simplify the analysis, it is assumed that $L_e = L_o = L$, and $E_e = E_o = E_{01}$. This gives:

$$E_{1,1} = 2E_{01}\sin\left(k_x x + \frac{\theta_{e1} + \theta_{o1}}{2} + \frac{\phi}{2}\right)\cos\left(\frac{\Delta k.x}{2} + \frac{\theta_{e1} - \theta_{o1}}{2} + \frac{\phi}{2}\right)\exp\left(\frac{-x}{L}\right) \tag{6.17}$$

$$E_{2,1} = 2E_{01}\cos\left(k_x x + \frac{\theta_{e1} + \theta_{o1}}{2} + \frac{\phi}{2}\right)\sin\left(\frac{\Delta k.x}{2} + \frac{\theta_{e1} - \theta_{o1}}{2} + \frac{\phi}{2}\right)\exp\left(\frac{-x}{L}\right) \tag{6.18}$$

Now considering the modes launched from the edge of WG2 the amplitudes of the even and odd modes are also assumed to be equal, $E_e = E_o = E_{02}$. In this case there is no need to account for the phase accumulation, ϕ so the equations are:

$$E_{1,2} = 2E_{02}\sin\left(k_x x + \frac{\theta_{e2} + \theta_{o2}}{2}\right)\cos\left(\frac{\Delta k.x}{2} + \frac{\theta_{e2} - \theta_{o2}}{2}\right)\exp\left(\frac{-x}{L}\right) \tag{6.19}$$

$$E_{2,2} = 2E_{02}\cos\left(k_x x + \frac{\theta_{e2} + \theta_{o2}}{2}\right)\sin\left(\frac{\Delta k.x}{2} + \frac{\theta_{e2} - \theta_{o2}}{2}\right)\exp\left(\frac{-x}{L}\right) \tag{6.20}$$

Since it is expected that the total energy of these excited modes to be distributed primarily in WG2 at $x = 0$, then it is expected that $(\theta_{e2} - \theta_{o2}) \approx \pi$ but the exact value will vary with gap size.

The total field expressed as a function of distance x, for each of WG1 and WG2, is obtained by summing the fields associated with the even and odd modes excited from both WG1 and WG2:

$$\begin{aligned} E_1 = {} & 2E_{01}\sin\left(k_x x + \frac{\theta_{e1} + \theta_{o1}}{2} + \frac{\phi}{2}\right)\cos\left(\frac{\Delta k.x}{2} + \frac{\theta_{e1} - \theta_{o1}}{2} + \frac{\phi}{2}\right)\exp\left(\frac{-x}{L}\right) \\ & + 2E_{02}\sin\left(k_x x + \frac{\theta_{e2} + \theta_{o2}}{2}\right)\cos\left(\frac{\Delta k.x}{2} + \frac{\theta_{e2} - \theta_{o2}}{2}\right)\exp\left(\frac{-x}{L}\right) \end{aligned} \tag{6.21}$$

$$E_2 = 2E_{01}\cos\left(k_x x + \frac{\theta_{e1}+\theta_{o1}}{2} + \frac{\phi}{2}\right)\sin\left(\frac{\Delta k.x}{2} + \frac{\theta_{e1}-\theta_{o1}}{2} + \frac{\phi}{2}\right)\exp\left(\frac{-x}{L}\right) + 2E_{02}\cos\left(k_x x + \frac{\theta_{e2}+\theta_{o2}}{2}\right)\sin\left(\frac{\Delta k.x}{2} + \frac{\theta_{e2}-\theta_{o2}}{2}\right)\exp\left(\frac{-x}{L}\right) \tag{6.22}$$

It should be noted that many of the parameters in these equations are expected to vary with g. For example, as g gets larger it is expected that: $k_x \to k_x$ of the asymmetric structures investigated in Chapter 4, and $\Delta k \to 0$. Also, the phase differences $(\theta_{e1} - \theta_{o1})$, $(\theta_{e2} - \theta_{o2})$, and amplitudes E_{01}, E_{02} will vary with g, which will affect how the energy is distributed between WG1 and WG2.

In principle, the free-space simulation data should approximately be described by Eq. 6.21 and 6.22. Due to the numerous assumptions made in the theory presented for this analysis, it was found that this approach did not adequately describe the simulation data. The analysis approach adopted here is to fit the data to a simpler phenomenological equation that can approximately, but adequately, capture the spatial variation of the field observed in the simulation data, so as to allow easier comparison between data obtained for different gap sizes. Therefore, an equation is used that describes the out-of-plane electric field, E_z as a function of distance (x) from the start of the IR, and which accounts for the propagation of both even and odd SSPP modes on the IR, the coupling of SSPPs between WG1 and WG2, and their attenuation due to their finite propagation length. In this case the out-of-plane field E_z for WG1 and WG2 is described by:

$$E_z = E_e \sin\left(k_{xe}x + \theta_e\right)\exp\left(\frac{-x}{L}\right) + E_o \sin\left(k_{xo}x + \theta_o\right)\exp\left(\frac{-x}{L}\right), \tag{6.23}$$

where E_e and E_o are the amplitudes of the even and odd modes launched at the beginning $(x = 0)$ of the IR, k_{xe} and k_{xo} are the wave-vectors of the even and odd modes, θ_e and θ_o are the phases of the even and odd modes, and L is the propagation length of the even and odd modes.

6.5.2 Simulation of free-space excitation of DC structures under oblique incidence

The real part of the out-of-plane electric field, E_z for all values of the gap size, g is shown in Fig. 6.21.

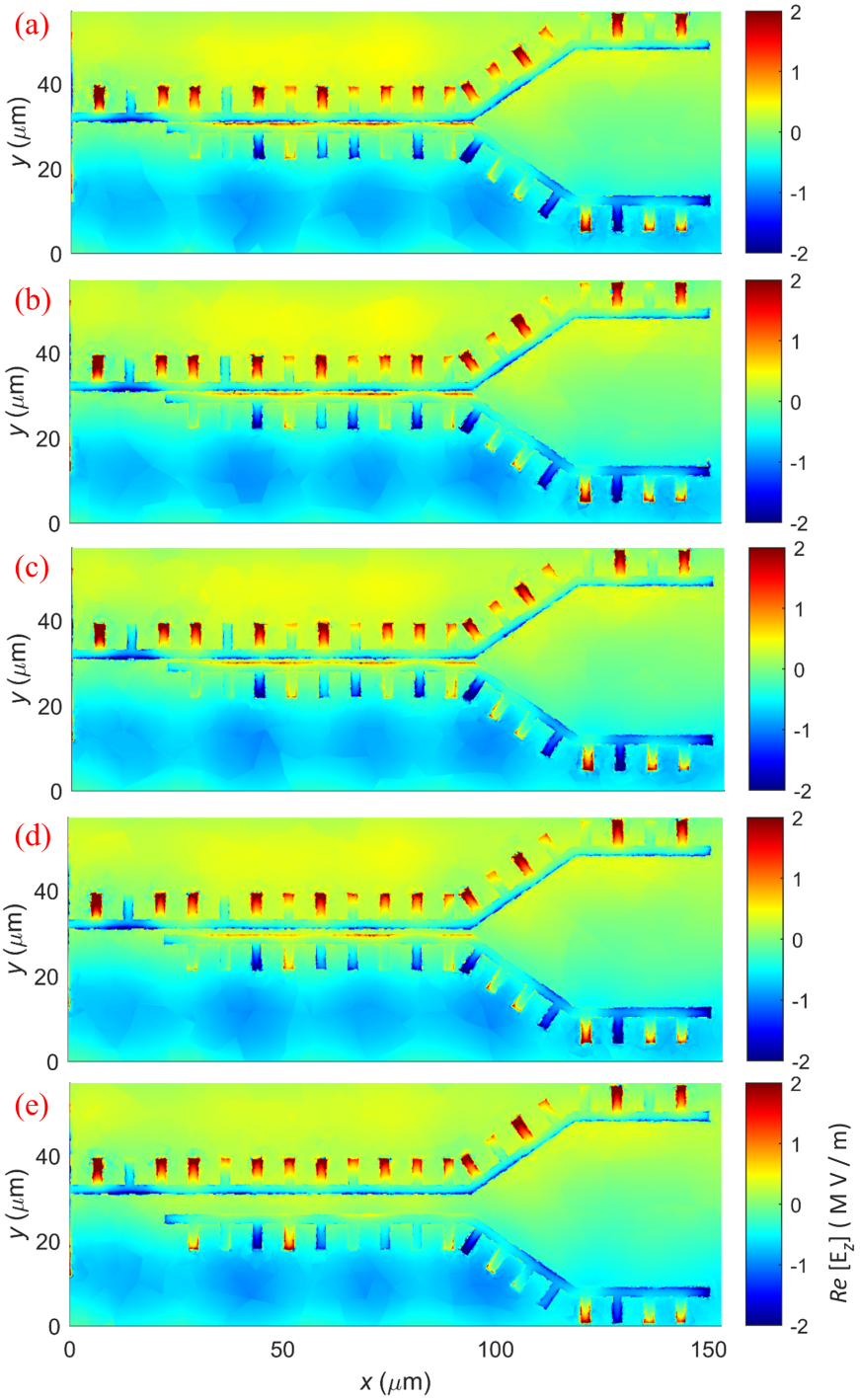

Figure 6.21: Real part of the out-of-plane electric field E_z of the DC structures using a grating structure with period $\alpha = 6$ µm, and a free-space beam with oblique incidence on the structure and perpendicular polarisation. (a) $g = 500$ nm, (b) $g = 700$ nm, (c) $g = 1$ µm, (d) $g = 1.5$ µm, and (e) $g = 5$ µm.

In order to quantify the out-of-plane field associated with the SSPPs as they propagate along the DC structure, the average electric field E_z obtained from the simulations shown in Fig. 6.21 was spatially averaged within each bar of the structure for all cases of g. These averaged values were then plotted as discrete points as a function of the distance x along the waveguide. Each average value was assigned at the centre point of its respective bar in the $x-$direction.

6.5.3 Analysis of IR of the DC structure under free-space excitation

The wave-vector values of the even and odd modes were fixed at the same values as the ones predicted from the dispersion relations (see Fig. 6.3) for each case of g, as shown in Fig. 6.22. The value of the propagation length was also fixed at $L = 83$ µm, which is the same value that was used in the supermode analysis.

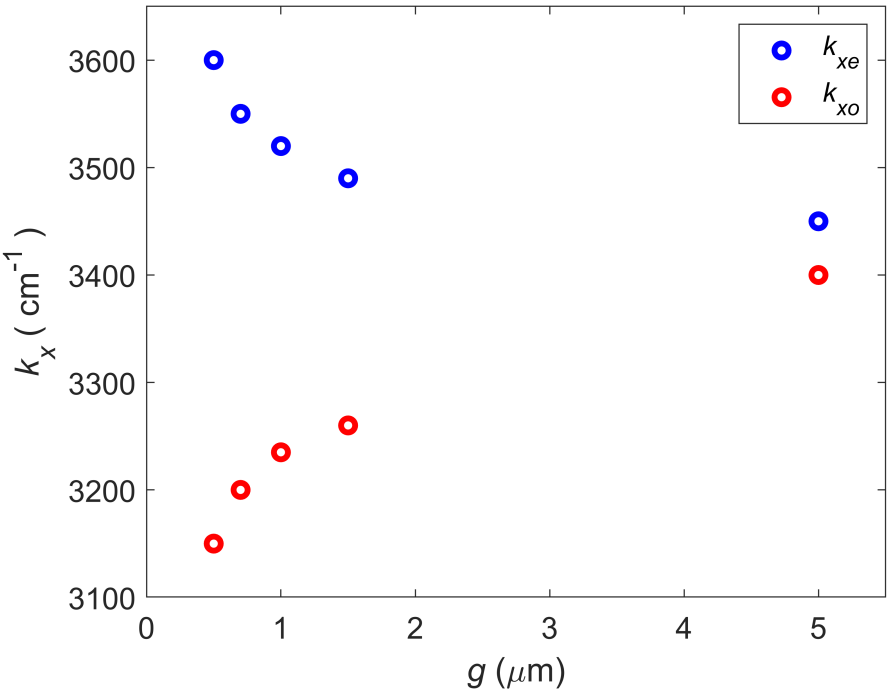

Figure 6.22: Variation of the even (k_{xe}) and odd (k_{xo}) modes as a function of gap size, g. These values were predicted in the dispersion relation.

Figures 6.23 and 6.24 show the averaged values of the out-of-plane electric field, E_z on WG1 and WG2 IR respectively, fitted using Eq. 6.23 for all cases of g.

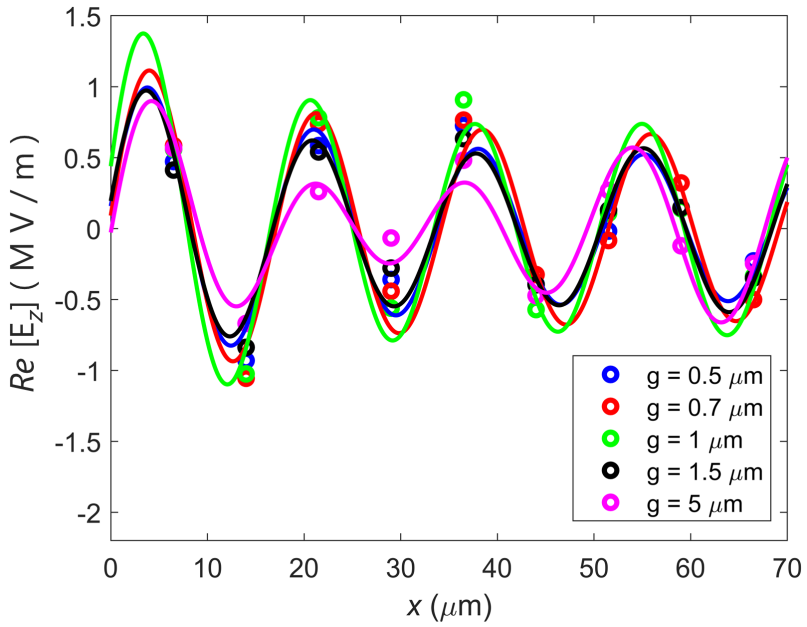

Figure 6.23: SSPPs coupled on the surface of the WG1 interaction region. Data points: Average value of the out-of-plane electric field E_z on each bar for all cases of g. Lines: Fit of the simulation data using Eq. 6.23 for all cases of g.

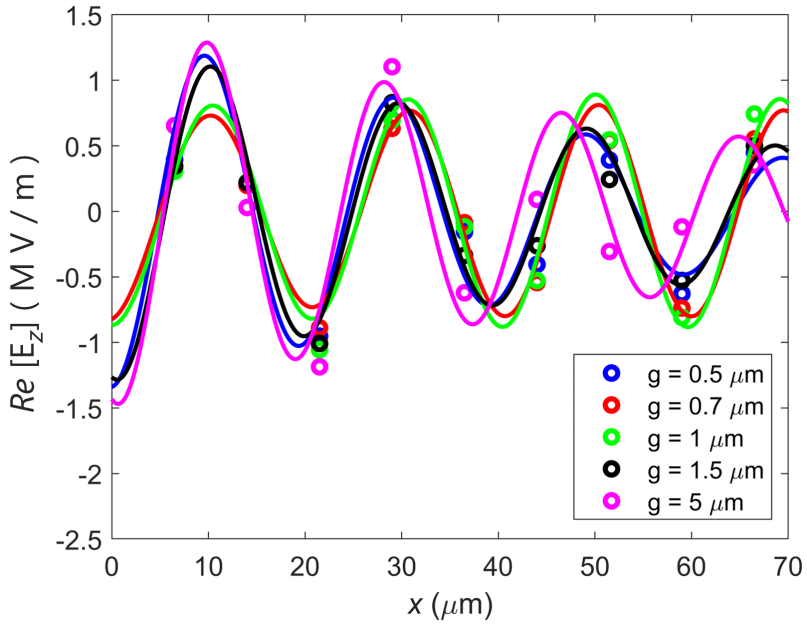

Figure 6.24: SSPPs coupled on the surface of the WG2 interaction region. Data points: Average value of the out-of-plane electric field E_z on each bar for all cases of g. Lines: Fit of the simulation data using Eq. 6.23 for all cases of g.

Figures 6.23 and 6.24 show that Eq. 6.23 fits the data nicely when the wave-vector values of the even and odd modes were fixed at the predicted values of the dispersion relation for each case of g. This shows that expected variation of Δk as a function of g is still be observed in the free-space simulations, despite the fact that the situation in this case is much more complex compared to the simulations where wave-ports are used to launch SSPPs on the DC structure. In this analysis, the SSPPs launched at the start of WG2, and at the end of the S-bends by the free-space beam have not been taken into account.

Furthermore, the field value of the first maxima in E_z for WG1 and the first minima for WG2 (at $x \approx 2.5$ µm) gives an estimate of the sum of amplitudes of the even and odd modes in Eq. 6.23, which describes how the energy is distributed at the start of the interaction region ($x = 0$). Figures 6.25 and 6.26 summarise these values as a function of g for WG1 and WG2 interaction regions respectively. The trends shown in these figures are approximately mirror images of each other, which is what would be expected from conservation of energy, i.e. the total energy at the start of the interaction region ($x = 0$) remains fixed but its distribution between WG1 and WG2 varies with gap size.

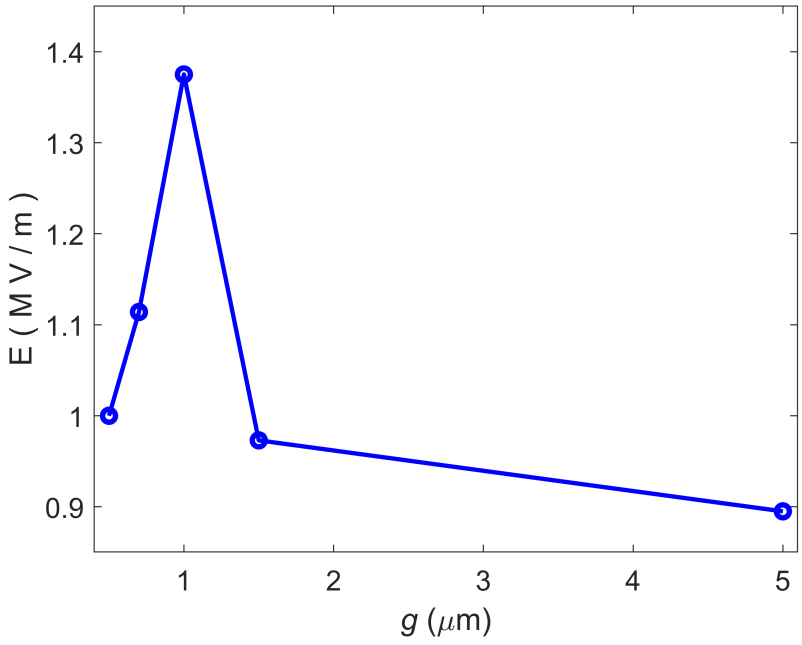

Figure 6.25: Field value of the first maxima in $\mathcal{R}e[E_z]$ for WG1 at $x \approx 2.5$ µm as a function of gap size, g.

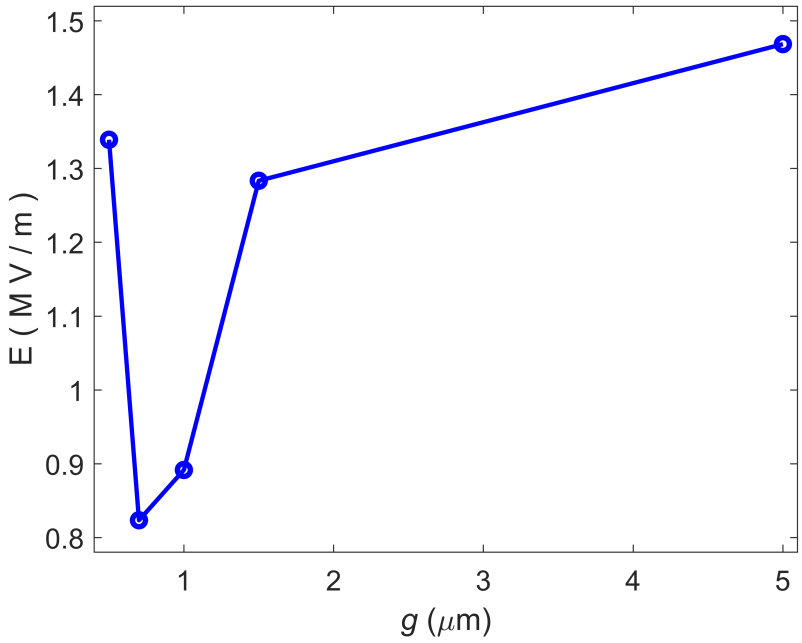

Figure 6.26: Field value of the first minima in $\mathcal{R}e[E_z]$ for WG2 at $x \approx 2.5$ µm as a function of gap size, g.

6.5.4 Analysis of S-bend region of the DC structure under free-space excitation

Under free-space illumination, in addition to the SSPPs launched from the excitation region and the start of the interaction region, SSPPs may also be launched from the end of each S-bend region, which will interfere with the (weaker) forwards propagating modes exiting from the interaction region. The interference will cause standing waves to form in the S-bend region, which will depend on both the amplitude and phase of the modes propagating in each direction, with those of the forwards propagating modes varying with gap size, as seen in Section 6.5.2. The out-of-plane field within the S-bend region of WG1 and WG2 can therefore be approximated as:

$$E_1 = E_{1f}\sin\left(k_x x + \theta_{1f}\right)\exp\left(\frac{-x}{L_p}\right) + E_{1b}\sin\left(-k_x(L_0 - x) + \theta_{1b}\right)\exp\left(\frac{-(L_0 - x)}{L_p}\right) \tag{6.24}$$

$$E_2 = E_{2f}\sin\left(k_x x + \theta_{2f}\right)\exp\left(\frac{-x}{L_p}\right) + E_{2b}\sin\left(-k_x(L_0 - x) + \theta_{2b}\right)\exp\left(\frac{-(L_0 - x)}{L_p}\right), \tag{6.25}$$

where $L_0 = 62$ µm is the total length of the s-bend section, $x = 0$ is now defined the start of the S-bend region, and f, b denotes forward and backward propagating SSPPs respectively. Figure 6.27 shows the averaged values of the out-of-plane electric field, E_z on the surface of the WG1 S-bend region fitted using Eq. 6.24 for all cases of g. Figure 6.28 shows the averaged values of the out-of-plane electric field, E_z on the surface of the WG2 S-bend region fitted using Eq. 6.25 for all cases of g. The value of the propagation length was fixed at $L_p = 60$ µm for all cases of g, whereas the value of the wave-vector, k_x was set as a free parameter.

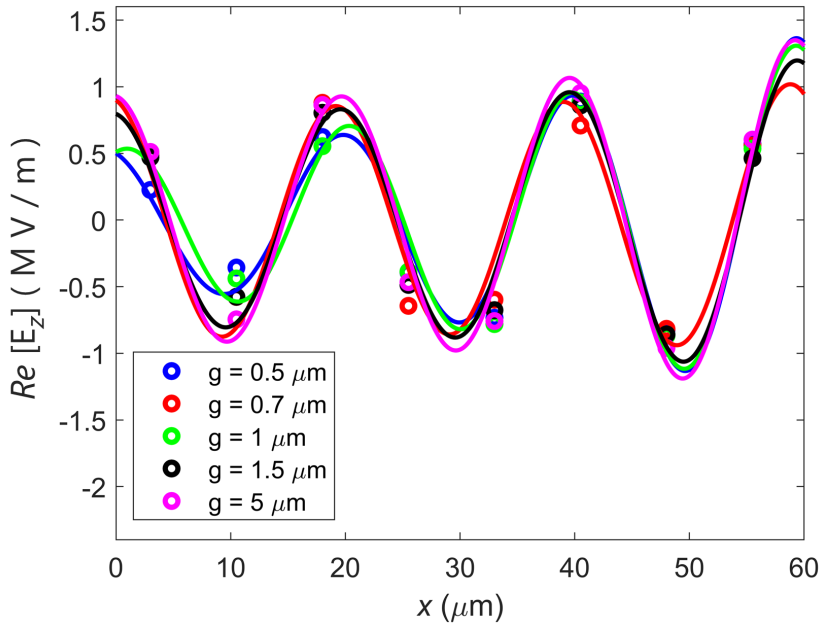

Figure 6.27: SSPPs coupled on the surface of the WG1 S-bend region. Data points: Average value of the out-of-plane electric field E_z on each bar for all cases of g. Lines: Fit of the simulation data using Eq. 6.24 for all cases of g.

It is clear from these figures that SSPPs are launched from both ends of the S-bend region, as expected. There is also a clear trend that the field is strongest

at the end of the S-bend region ($x \sim 60$) µm, which is expected since SSPPs are launched there and the field values here are only weakly affected by the gap size. Conversely at $x = 0$, it can be seen that the gap has a larger effect on the fields. This is expected since the SSPPs which enter the S-bend region from the IR are strongly affected by g, and the highest SSPP amplitude occurs at $x = 0$. However, the SSPPs launched from the end of the S-bend region are not affected by g and their amplitude will be weakest at $x = 0$, due to their finite propagation length.

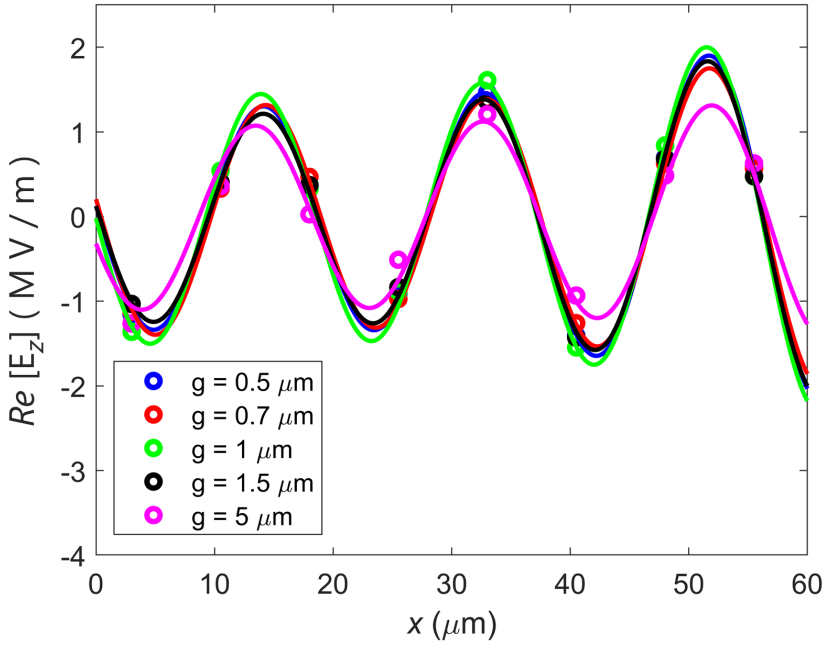

Figure 6.28: SSPPs coupled on the surface of the WG2 S-bend region. Data points: Average value of the out-of-plane electric field E_z on each bar for all cases of g. Lines: Fit of the simulation data using Eq. 6.25 for all cases of g.

6.6 Fabrication of DC structures

DC structures were fabricated for all values of gap size, g with design parameters presented in Section 6.3, an interaction region of length $L_c = 73$ µm, and incorporating a grating structure with period $\alpha = 20$ µm with a grating offset $g_{off} = 10$ µm. The length of the grating structure was $L_g = 90$ µm and the length of each grating slit was $L_s = 25$ µm. A float-zone silicon substrate was used which has high resistance ($R > 10,000\ \Omega$ cm). The area of the substrate was 15×15 mm and the thickness was 500 ± 50 µm. The samples were fabricated using standard

electron-beam lithography (EBL) and metal deposition by Dr Mark C. Rosamond. The layer thicknesses that were used were titanium 2 nm (Ti) and gold 100 nm (Au). The sample was then placed in a microposit remover for the lift-off process. The topography of each sample was acquired using an atomic force microscope (AFM), as shown in Fig. 6.29.

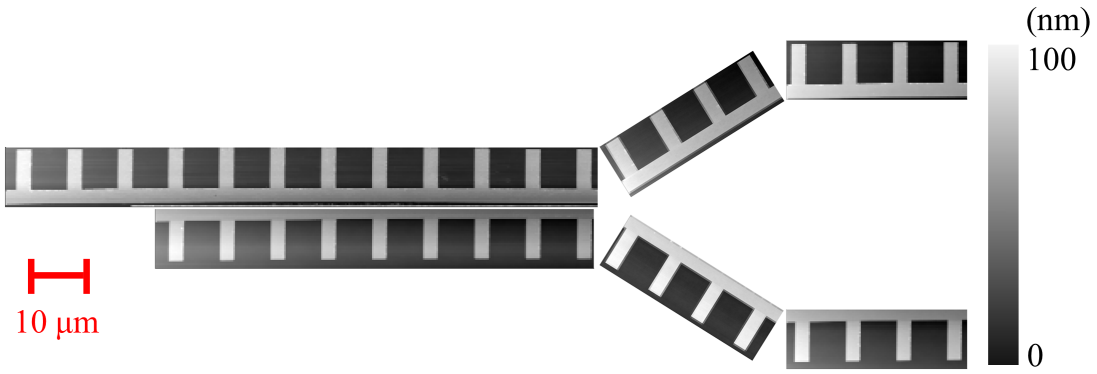

Figure 6.29: AFM image of the DC structure with interaction length $L_c = 73$ µm and a grating period $\alpha = 20$ µm with grating offset $g_{off} = 10$ µm.

6.7 THz-s-SNOM of SSPPs propagating on DC structures

In this section, the coupling of the illuminating beam from a QCL to SSPPs on DC structures with grating period $\alpha = 20$ µm and grating offset $g_{off} = 10$ µm is investigated for a polarisation that is perpendicular to the DC structure axis (see Fig. 4.15). The QCL beam direction and polarisation in this experiment matches the direction and polarisation of the illuminating beam in the simulations presented in Section 6.5.

6.7.1 THz-s-SNOM system

The experimental s-SNOM system setup is described in Chapter 4 (see Section 4.11.1) The time constant used for these measurements was $\tau_s = 50$ ms, the pixel size in the axis of the waveguide ($x-$direction) was 250 nm, and the pixel size in the ($y-$direction) also was 250 nm. To isolate the signal component arising from the near-field interaction between the probe and the sample, the microscope probe

was operating in a tapping mode and the QCL terminal voltage was demodulated at harmonics of the tip tapping frequency ($\Omega \sim 80$ kHz) using a lock-in amplifier. The tapping amplitude of the tip was set to $A_{tip} \sim 200$ nm, which yields a spatial resolution of ~ 200 nm. The SM signal, arising from the field scattered from the s-SNOM tip and reinjected to the laser cavity, was derived from the $n = 2$ harmonic of the demodulated QCL terminal voltage after amplification using an ac-coupled low-noise voltage amplifier. By raster-scanning the sample in two dimensions, images with deep sub-wavelength resolution were obtained, with the QCL emitting light at a frequency $\nu = 3.45$ THz.

6.7.2 Interaction Region

The spatial distribution of the self-mixing voltage signal obtained experimentally within the IR of WG1 and WG2 is shown for all values of g in Figures 6.30 and 6.31, respectively. To analyse the electric field associated with the SSPPs propagating on the interaction region of WG1 and WG2, an average value of the self-mixing voltage was obtained for each bar of WG1 and WG2, following subtraction of the spatially constant signal contribution arising from the sample permittivity, as shown in Fig. 6.32 and Fig. 6.33.

Due to the numerous assumptions made in the theory presented for the analysis of the free-space simulations in Section 6.5, it was found that this approach did not adequately describe the experimental data. This is compounded by additional factors that affect experimental measurements that are not present in the simulations, such as the spatial variation of the intensity of the THz beam spot illuminating the sample, the effects of the s-SNOM tip on the field distribution on the sample, the spatial in-homogeneity in the sample, and the voltage noise and thermal drift of the QCL during the measurements. For these reasons the analysis approach adopted here is to fit the data to a simpler phenomenological equation that can approximately, but adequately, capture the spatial variation of the field observed in the experimental data, so as to allow easier comparison between data obtained for different gap sizes. As such the out-of-plane electric field E_z as a function of distance (x) from the start of the IR is described by the propagation of both even and odd SSPP modes on the IR, the coupling of SSPPs between WG1 and WG2, and their attenuation due to their finite propagation length, according to Eq. 6.23.

In order to simplify the analytical expression, SSPPs coupling from the S-bend regions (RHS) and propagating on the interaction region have not been considered. The parameters k_{xe} and k_{xo} were fixed at the same wave-vector values as the ones predicted by the dispersion relation (Fig. 6.3) for each case of the gap size, g. Figure 6.22 shows this variation of the even and odd mode wave-vector values as a function of g. The fits to Eq. 6.23 for the experimental data obtained from the IR of WG1 and WG2 are shown in Figures 6.32 and 6.33, respectively. The fitting parameters obtained from the analysis of WG1 and WG2 interaction regions are summarised in Table 6.1 and Table 6.2 respectively.

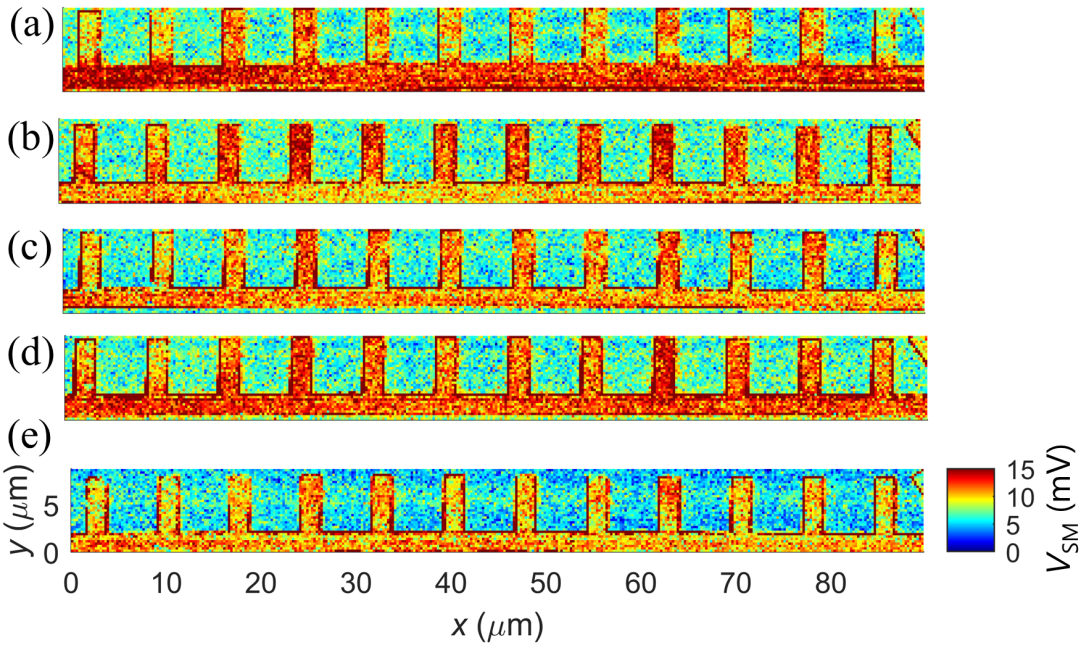

Figure 6.30: s-SNOM images ($n = 2$) of WG1 with $\alpha = 20$ µm and $g_{off} = 10$ µm. The incident beam has a polarisation perpendicular to the waveguide axis. (a) $g = 500$ nm, (b) $g = 700$ nm, (c) $g = 1$ µm, (d) $g = 1.5$ µm, and (e) $g = 5$ µm.

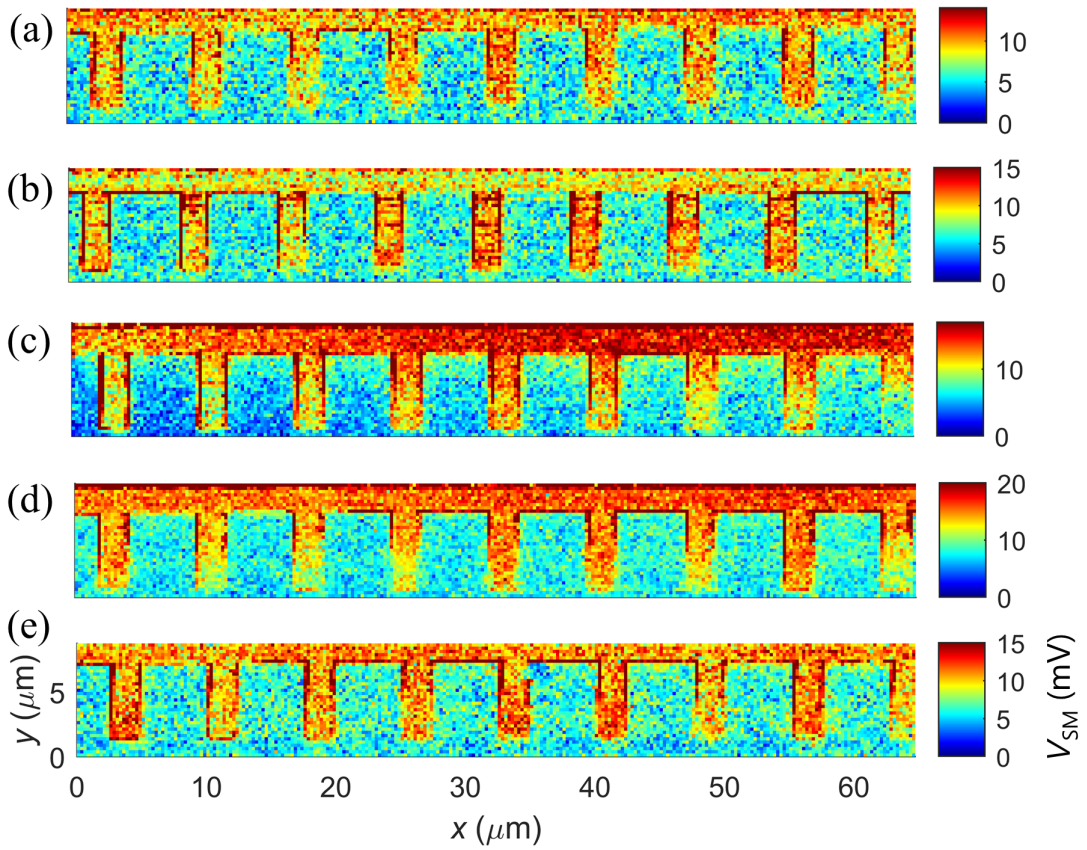

Figure 6.31: s-SNOM images ($n = 2$) of WG2 with $\alpha = 20$ µm and $g_{off} = 10$ µm. The incident beam has a polarisation perpendicular to the waveguide axis. (a) $g = 500$ nm, (b) $g = 700$ nm, (c) $g = 1$ µm, (d) $g = 1.5$ µm, and (e) $g = 5$ µm.

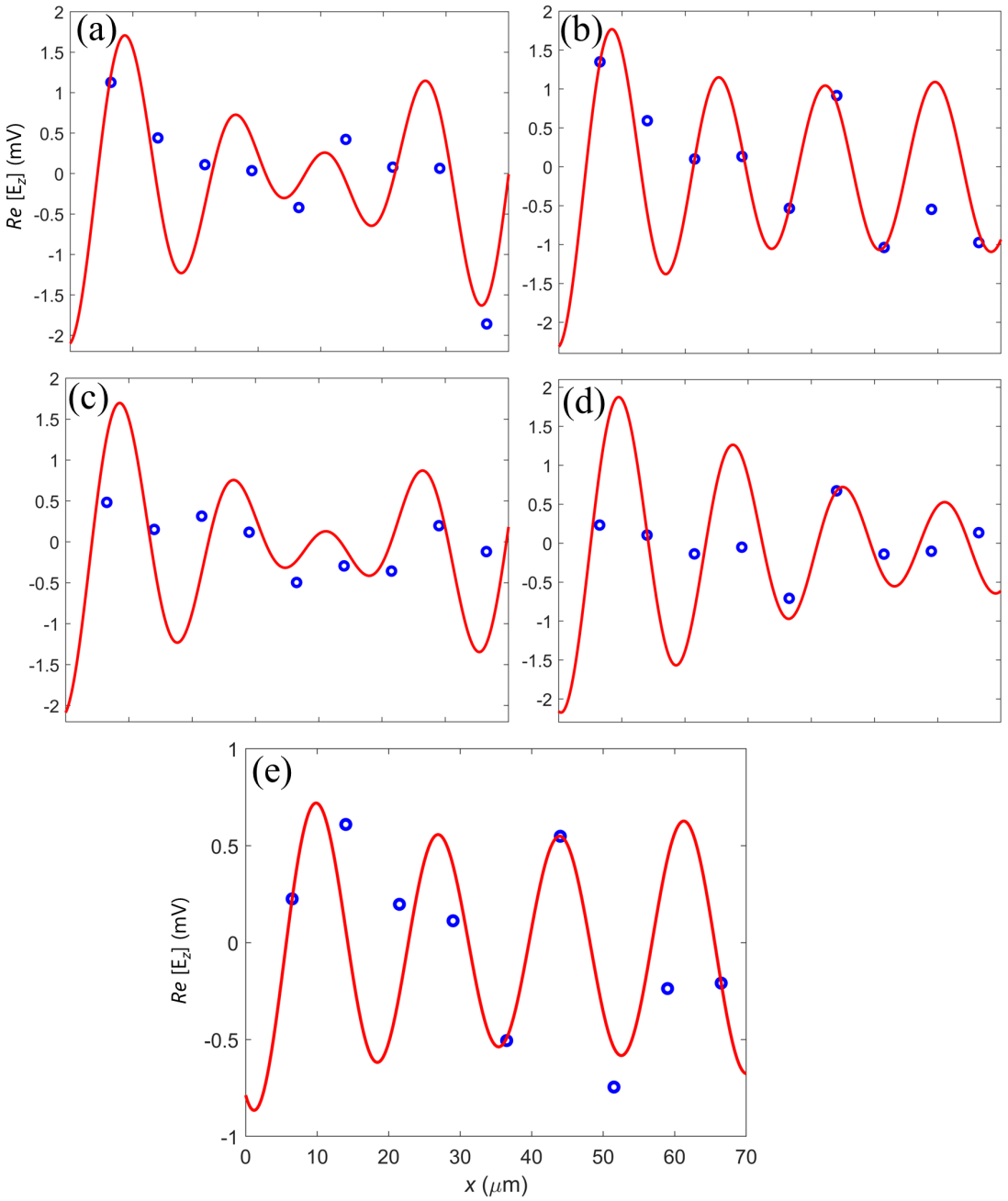

Figure 6.32: Analysis of the SSPPs coupled on the surface of the WG1 IR. (a) gap, $g = 500$ nm, (b) gap, $g = 700$ nm, (c) gap, $g = 1$ µm, (d) gap, $g = 1.5$ µm, (e) gap, $g = 5$ µm.

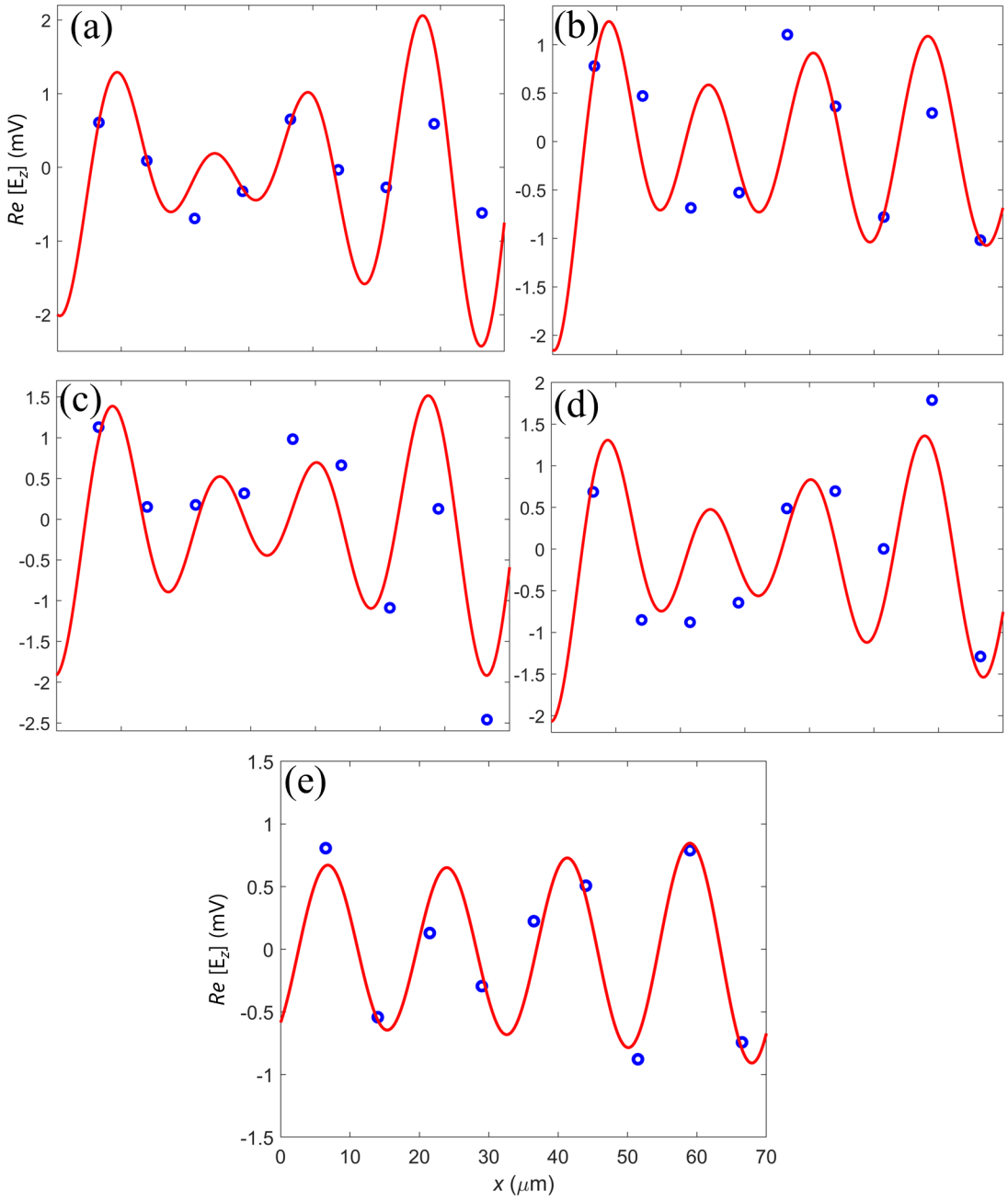

Figure 6.33: Analysis of the SSPPs coupled on the surface of the WG2 IR. (a) gap, $g = 500$ nm, (b) gap, $g = 700$ nm, (c) gap, $g = 1$ µm, (d) gap, $g = 1.5$ µm, (e) gap, $g = 5$ µm.

gap size, g µm	E_e mV	E_o mV	k_{xe} cm^{-1}	k_{xo} cm^{-1}	θ_e rad	θ_o rad	L µm
0.5	1.5	1.29	3600	3150	-0.84	-2.27	10^5
0.7	2.8	1.15	3550	3200	-1.14	2.9	70
1	2	1.9	3520	3235	-0.5	-2.5	10^5
1.5	2	1.45	3490	3260	-1	-2.8	10^3
5	4.45	3.8	3450	3400	-1.4	1.9	150

Table 6.1: Summary of the fitting parameters of WG1 IR.

gap size, g µm	E_e mV	E_o mV	k_{xe} cm^{-1}	k_{xo} cm^{-1}	θ_e rad	θ_o rad	L µm
0.5	2	1.8	3600	3150	-0.9	-2.9	300
0.7	3.2	2.4	3550	3200	-1	2.8	50
1	2.46	2	3520	3235	-2.2	1.8	443
1.5	3.75	3.1	3490	3260	-2.3	1.5	92
5	4	3.3	3450	3400	-2.27	0.9	219

Table 6.2: Summary of the fitting parameters of WG2 IR.

From Fig. 6.32 and Fig. 6.33, it can be seen that Eq. 6.23 fits the data nicely. This analysis proves that SSPPs with even and odd modes are propagating on the DC structure with the predicted wave-vector values from the dispersion relation. Figure 6.32 (a) shows that the field amplitude of the SSPP propagating on WG1 IR is large at $x = 0$, it reduces sharply at the centre of WG1 IR, and it increases at the end of WG1 IR ($x \approx 70$) µm. This indicates that when the gap size, $g = 500$ nm, the energy of the SSPP launched in the excitation region of WG1 transfers to WG2, and the energy of the SSPP launched at the edge of WG2 transfers to WG1. The same pattern is observed in Fig. 6.33 (a). Furthermore, Fig. 6.32 (e) shows that the field amplitude of the SSPP propagating on WG1 IR when the gap size, $g = 5$ µm remains approximately constant throughout the IR. This is expected

due to the difference in wave-vector values between the even and odd modes being smaller ($k_{xe} - k_{xo} = 50$ cm^{-1}), resulting in less transfer of energy between WG1 and WG2. The same pattern is observed in Fig. 6.33 (e), where the SSPP propagates on WG2 IR when the gap size, $g = 5$ µm.

6.7.3 S-bend Region

The spatial distribution of the self-mixing voltage signal along WG1 and WG2 S-bend regions for values of $g = 500$ nm, and $g = 5$ µm obtained experimentally using the s-SNOM system is shown in Fig. 6.34. To analyse the electric field associated with the SSPPs propagating on the S-bend region, an average value of the self-mixing voltage was obtained for each bar of WG1 and WG2, following subtraction of the constant offset arising from the sample permittivity, as shown in Fig. 6.35.

To interpret the data from this experiment, an equation is used that describes the out-of-plane electric field, E_z as a function of distance (x) which accounts for the propagation of SSPPs on the the S-bends region. Since the SSPPs are now spatially separated, the equation models the SSPPs entering S-bend from the IR (LHS in Fig. 6.34) as a single SSPP mode with wave-vector k_x instead of an even and an odd mode. Furthermore, the SSPPs launched from the end of the S-bend (RHS in Fig. 6.34) are now also taken into account since their energy propagating on the S-bends will be non-negligible. The two SSPPs will propagate on the S-bend in opposite directions causing an interference, and will attenuate due to the finite propagation length. In this case, by analogy to Eq. 6.24 used for the analysis of the simulation data in the S-bend region, the out-of-plane field E_z is described by:

$$E_z = E_f \sin\left(k_{xe}\, x + \theta_f\right) \exp\left(\frac{-x}{L_p}\right) + E_b \sin\left(k_x \left(L_0 - x\right) + \theta_b\right) \exp\left(\frac{-(L_0 - x)}{L_p}\right), \tag{6.26}$$

where E_f is the amplitude of the SSPP which enters the S-bend from the IR, E_b is the amplitude of the SSPP launched from the end of the S-bend, k_x is the wave-vector of the SSPP propagating on the S-bend, θ_f and θ_b are the corresponding phases of the SSPPs, $L_0 = 62$ µm is the length of each S-bend, and L_p is the propagation length.

The fits to Eq. 6.26 for the experimental data obtained from the WG1 and WG2 S-bends are shown in Fig. 6.35. The fitting parameters obtained from the analysis of WG1 and WG2 S-bends are summarised in Table 6.3 and Table 6.4 respectively.

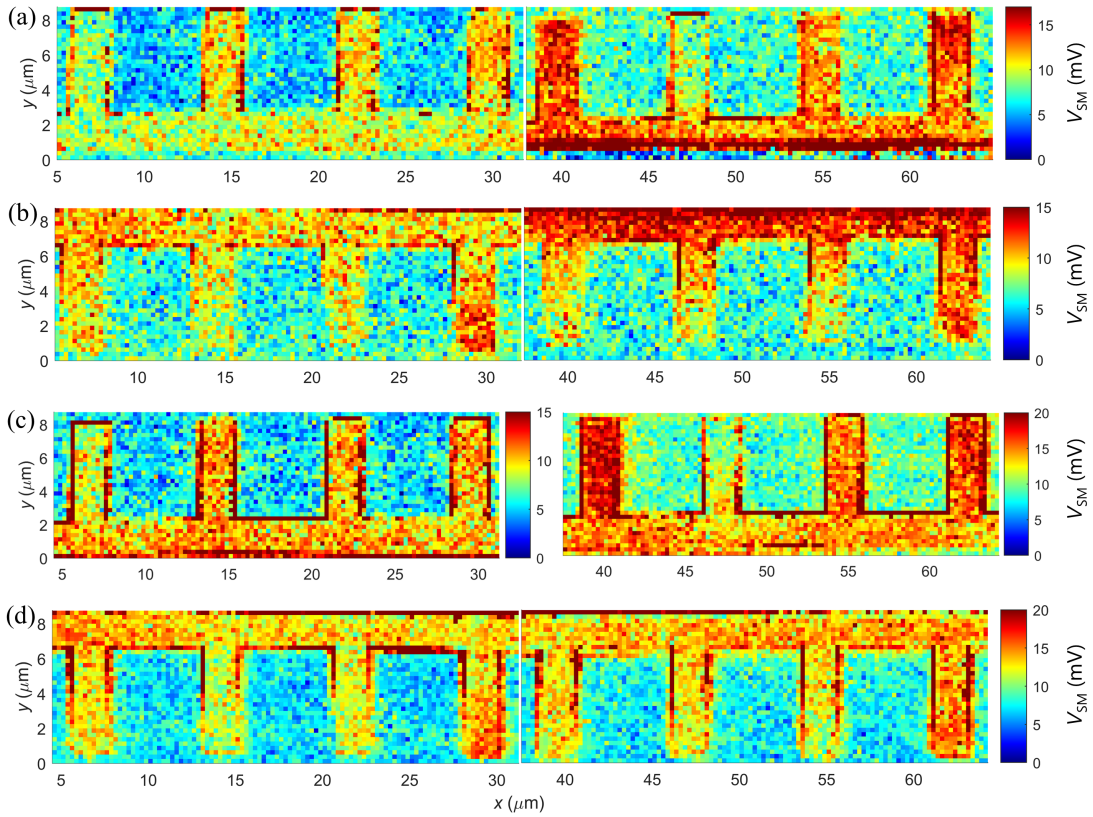

Figure 6.34: s-SNOM images ($n = 2$) of the S-bends with $\alpha = 20$ µm and $g_{off} = 10$ µm. The illuminating beam has a polarisation perpendicular to the waveguide axis. (a) WG1 S-bend with $g = 500$ nm, (b) WG2 S-bend with $g = 500$ nm, (c)WG1 S-bend with $g = 5$ µm, and (d) WG2 S-bend with $g = 5$ µm.

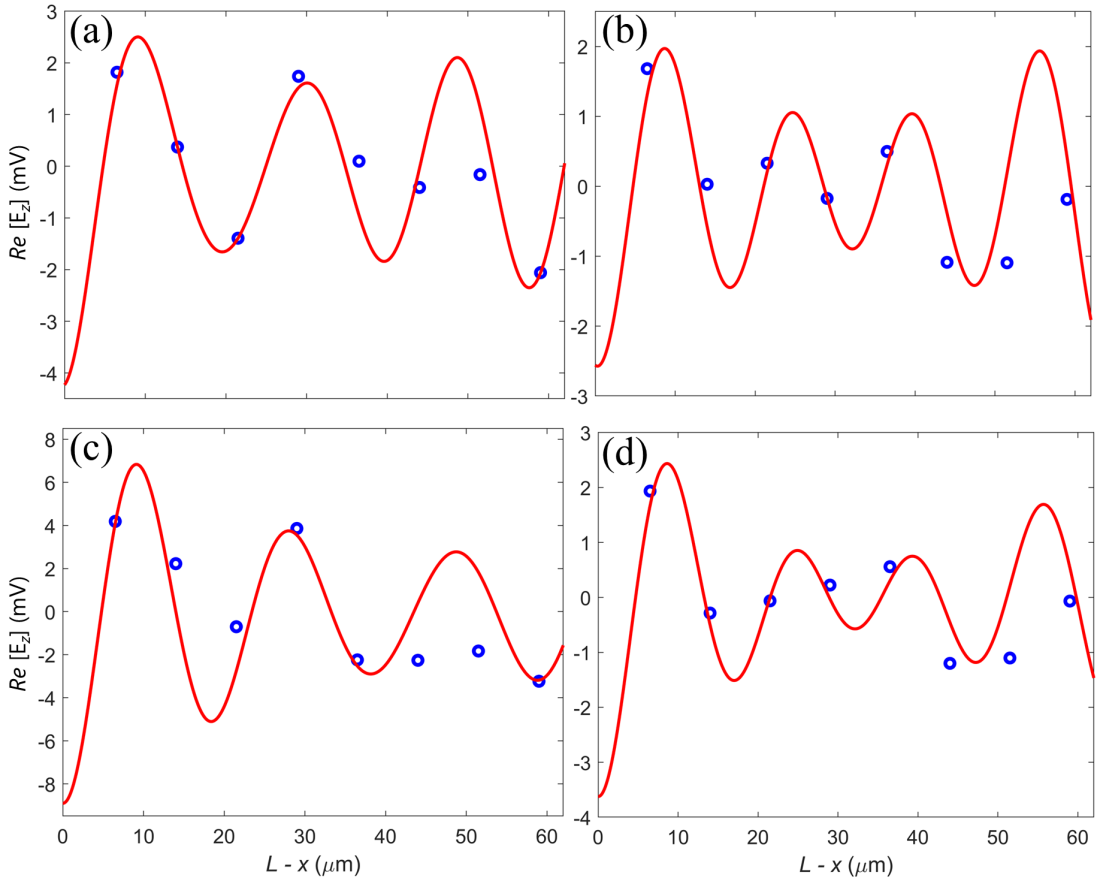

Figure 6.35: Analysis of the SSPPs coupled on the S-bends. (a) WG1 S-bend with $g = 500$ nm, (b) WG2 S-bend with $g = 500$ nm, (c)WG1 S-bend with $g = 5$ µm, and (d) WG2 S-bend with $g = 5$ µm.

gap size, g µm	E_f mV	E_b mV	k_x cm^{-1}	k_{xe} cm^{-1}	θ_f rad	θ_b rad	L_p µm
0.5	3	5	3600	3600	-2.3	-1.8	40
5	7	5	3600	3450	-1.2	-3	40

Table 6.3: Summary of the fitting parameters of WG1 S-bend.

gap size, g µm	E_f mV	E_b mV	k_x cm^{-1}	k_{xe} cm^{-1}	θ_f rad	θ_b rad	L_p µm
0.5	3.9	4	3600	3600	-1.3	-1.8	40
5	3	4	3600	3450	-1	-1.63	40

Table 6.4: Summary of the fitting parameters of WG2 S-bend.

From the fitting parameters in Table 6.3, it can be seen that when the gap size, $g = 500$ nm, the field amplitude of the SSPP launched at the end of the WG1 S-bend ($E_b = 5$ mV) is greater than the amplitude of the SSPP entering the S-bend from the WG1 IR ($E_f = 3$ mV). When the gap size, $g = 5$ µm, the field amplitude of the SSPP launched at the end of the S-bend is still $E_b = 5$ mV, as expected since this SSPP is not affected by the gap size, g, but now the amplitude of the SSPP entering the S-bend from the WG1 IR is greater, $E_2 = 7$ mV, indicating that the energy of the SSPP propagating on the WG1 IR has mostly remained in WG1. Furthermore, from the fitting parameters in Table 6.4, it can be seen that when the gap size, $g = 500$ nm, the field amplitude of the SSPP launched at the end of the S-bend ($E_b = 4$ mV) is almost equal to the field amplitude of the SSPP entering the S-bend region from the WG2 IR ($E_f = 3.9$ mV). The values of E_b are also similar to those obtained from WG1, as expected. When the gap size, $g = 5$ µm, the field amplitude of the SSPP launched at the end of the S-bend is still $E_b = 4$ mV, but the amplitude of the SSPP entering the S-bend from the WG2 IR is now lower, indicating that less energy has been transferred from WG1 to WG2. These results agree well with the expected behaviour of DC structures shown in Section 6.4, which is remarkable given the complexity of this experiment.

6.8 Summary

To conclude, this chapter presented the design, simulation, fabrication and experimental measurements of the novel DC structure which allows the control of the spatial distribution of SSPPs between two spatially separated waveguides, depending on the gap size, g in the IR, and the coupling length of the IR, L_c. Firstly, eigen-mode simulations were performed to obtain the SSPP wave-vectors of the even and odd modes fore each case of g for an incident frequency of 3.45 THz. DC structures were then simulated using wave-port excitation simulations to obtain the S_{21} Parameters, and to analyse the electric field distribution for each value of g using a phenomenological analysis, and the supermode analysis. This analysis confirmed the desired behaviour whereby the energy associated with SSPPs is transferred between waveguides within the interaction region and depending on the gap size, g. Next, DC structures were simulated using a free-space beam which matches the illumination geometry of the experimental THz-s-SNOM system. The coupling of SSPPs on the DC structure presented some significant differences when compared to the wave-port excitation simulations, as SSPPs were also launched at the start of WG2, and the ends of the two S-bends. This further complicated the analysis of the free-space beam simulations, therefore some assumptions were made in order to facilitate the analysis. It was found that the wave-vectors propagating on the DC structure for each case of g concurred with the wave-vectors predicted by the dispersion relations. Furthermore, the experimental data obtained from the measurements using the THz-s-SNOM system was analysed using the same method that was used to analyse the simulation data with a free-space beam. The wave-vector values of the even and odd modes obtained from the experimental data also agreed with the wave-vector values from the dispersion relation. In addition, the analysis of the S-bend region from the experimental data indicated that when $g = 500$ nm most of the energy in WG1 transfers to WG2, whereas when $g = 5$ µm, most of the energy in WG1 remains in WG1, experimentally confirming the expected behaviour of the DC structure. Therefore, the results show successful mapping of the spatial distribution of the electric field associated with THz-frequency SSPP even and odd modes propagating on a DC structure with sub-wavelength resolution. This is the first time this has been reported.

Chapter 7

Future work

7.1 Chapter 2

All the work presented in this thesis was undertaken using a single-mode THz-QCL based on a nine-well hybrid active region design lasing at ~ 3.45 THz, which was processed into a SI-SP ridge waveguide and operated in CW mode. However, the fabrication and use of new QCLs would open-up further opportunities such as higher emission frequencies, allowing investigation of structures exhibiting stronger plasmonic confinement, higher operating temperatures and lower threshold current density, allowing development of cryogenic-free microscopy systems, and new QCL designs tailored to provide larger self-mixing voltage signals leading to better SNR and shorter acquisition times [271].

7.2 Chapter 3

In Chapter 3, the use of s-SNOM employing a THz-frequency QCL is demonstrated for coherently probing the localized field supported by individual micro-resonator structures. There are a number of ways in which these experiments could be expanded. The design of the DA and SRR structures led to the simulation in ANSYS HFSS and mapping of the out-of-plane electric field, E_z using s-SNOM of a dipole resonance (first-order mode) when a terahertz beam with a frequency $f_0 = 3.45$ THz illuminated the structures. However, such structures support higher order modes, such as the quadruple resonance (second-order mode) and even higher order modes. In order to achieve that, the structures would have to be redesigned and simulated in ANSYS HFSS to determine the dimensions which would lead to

these higher-order modes being supported by the SRR and DA structures for an incident frequency $f_0 = 3.45$ THz. The higher-order modes could be mapped using incoherent high-resolution imaging (amplitude images) or coherent high-resolution imaging by employing the swept-frequency technique. Furthermore, the THz-s-SNOM system can be used to investigate other resonators and metamaterials, which could aid their use in a range of applications. Some examples are: the investigation of how surface fields on such structures are affected by the presence of bio-molecules, aiding the development of THz plasmonic sensors, the mapping and investigation of surface plasmons confined on two-dimensional (2D) material structures (e.g. graphene [102] and topological insulators), and the investigation of THz chiral metamaterial for the development of THz modulators [272].

7.3 Chapters 4 and 5

In chapters 4 and 5, novel structures that support propagating THz SSPPs are designed and their operation is confirmed by finite-element method (FEM) simulations and experimentally using THz-s-SNOM. These include asymmetric and symmetric PSP waveguides. These waveguides are realised using nearly zero-thickness metal strips printed on rigid substrates. The free-space simulations of the asymmetric and symmetric PSP waveguides which were used to study the effects of the illumination geometry were based on a structure with length $L = 208$ µm. This length allowed the independent analysis of the SSPPs which were launched from the opposite ends of the waveguides, and it also reduced the interference between the two SSPPs due to the finite propagation length, $L_p = 75$ µm (asymmetric) and $L_p = 83$ µm (symmetric). However, the presented experimental results from the fabricated structures had a length of $L = 73$ µm instead of $L = 208$ µm. This resulted in a strong interference between the SSPPs launched from the two ends of each waveguide, with reflections also occurring at the end of each waveguide, increasing the complexity of the analysis. Another option would be to suppress SSPPs launched from the opposite end of the gratings by designing and investigating different waveguide terminations such as tapered, fanned, or rounded waveguide ends. Furthermore, the structures can be fabricated using electron-beam lithography which can achieve a higher lithographic resolution compared to optical lithography. This will lead to the dimensions of the fabricated structures being equal to the ones defined in simulation. This would facilitate the investigation

of the discrepancies presented between the simulation and experimental results in Chapter 4 and 5. Another difference between the simulations and the experimental setup is the elliptical polarisation of the THz-QCL, which is defined as linear in the simulations. To account for this, the polarisation in the simulation can be modified to include an electric field component oscillating in the minor axis. Another solution would be to place a grid-wire polariser in the experimental system to force the polarisation in only one direction, hence matching the free-space beam of the experimental s-SNOM system with the one in the simulation. However, due to the non-ideal behaviour of the wire-grid polariser at THz frequencies, this would lead to attenuation of the scattered field from the probe tip, reducing the SNR. Further improvements to the experiments include the investigation and design of optimised gratings such as 2D gratings to account for the illuminating beam with oblique incidence in the THz-s-SNOM system, and performing coherent s-SNOM measurements to resolve both the amplitude and phase of the out-of-plane field associated with the SSPPs. The results presented in these Chapters pave the way for further novel research directions, such as investigating SSPPs on CSP waveguides printed on flexible films which can be bent or twisted, altering the dimensions of the waveguides to achieve greater propagation lengths, the introduction of doped layers on the substrate where applying a gate voltage could electrically control the transmission of SSPPs along the waveguide, and also further investigate different metamaterial waveguides such as corrugated wires [221], wedges [222], channels [223], and domino structures [137, 226, 227] at THz frequencies.

7.4 Chapter 6

In Chapter 6, the potential to realise different functional plasmonic components at terahertz frequencies is investigated, such as DCs based on the asymmetric metamaterial waveguides. DCs allow the control of the spatial distribution of SSPPs between two spatially separated waveguides, depending on the gap size, g in the IR, and the coupling length of the IR, L_c. There are a number of ways in which the experiments presented in this Chapter could be improved. Due to the length of the S-bend region, $L = 62$ µm, the SSPPs reaching the S-bends from the interaction region will experience a reflection due to the finite propagation length, $L_p = 75$ µm being greater than the S-bend length ($L_p > L$). In order to avoid reflections and facilitate the analysis, the length of the S-bends needs to be longer than the

propagation lengh (i.e. $L \approx 100$ µm). In addition, the finite beam spot size of the QCL (~ 200 µm) has a Gaussian shape, resulting in the beam intensity incident on the gratings reducing as the waveguide is scanned along. This will affect the out-of-plane field associated with the SSPPs in the region under the tip. This is because during a scan, it is the sample which is displaced, and not the probe tip. To reduce the effect that this has on the experimental data, the overall length of the DC structure has to decrease. Therefore, a DC structure can be redesigned with a lower interaction length ($L_c = 73$ µm $\rightarrow L_c = 40$ µm). This modification in the design would reduce the gap size, g where a total shift in energy would be observed from WG1 to WG2. However, as these structures were fabricated using electron-beam lithography, a narrower distance between the two waveguides (e.g. $L_c \approx 200$ µm) can be achieved physically. Furthermore, the free-space simulations presented a much more complex situation than the wave-port excitation simulations since SSPPs can also be launched at the start of WG2 and the end of the S-bends. To circumvent coupling of light to SSPPs at unwanted regions, different waveguide terminations such as tapered, fanned or rounded waveguide ends can be designed and integrated with DCs, suppressing SSPPs launched at these regions. These solutions could lead to the free-space simulations and measurements to launch SSPPs only from the excitation region, allowing a direct comparison with the wave-port excitation simulations. The results presented in this Chapter pave the way for further novel research directions, such as further investigating active elements based on SSPPs including switches [273–275], amplifiers [244], and frequency mixers [250] at THz frequencies.

References

[1] C. Sirtori, "Bridge for the terahertz gap," *Nature*, vol. 417, no. 6885, pp. 132–133, 2002.

[2] G. Davies and E. Linfield, "Bridging the terahertz gap," *Physics World*, vol. 17, no. 4, pp. 37–41, 2004.

[3] B. S. Williams, "Terahertz quantum cascade lasers," Ph. D. Thesis, Massachusetts Institute of Technology, 2003.

[4] M. Tonouchi, "Cutting-edge terahertz technology," *Nature Photonics*, vol. 1, no. 2, pp. 97–105, 2007.

[5] M. Shur, "Terahertz technology: Devices and applications," in *Proceedings of the 31st European Solid-State Circuits Conference, 2005. ESSCIRC 2005.*, 2005, pp. 13–21.

[6] A. G. Davies, A. D. Burnett, W. Fan, E. H. Linfield, and J. E. Cunningham, "Terahertz spectroscopy of explosives and drugs," *Materials Today*, vol. 11, no. 3, pp. 18–26, 2008.

[7] J. F. Federici, B. Schulkin, F. Huang, D. Gary, R. Barat, F. Oliveira, and D. Zimdars, "THz imaging and sensing for security applications—explosives, weapons and drugs," *Semiconductor Science and Technology*, vol. 20, no. 7, S266–S280, Jun. 2005.

[8] P. H. Siegel, "Terahertz technology in biology and medicine," *IEEE Transactions on Microwave Theory and Techniques*, vol. 52, no. 10, pp. 2438–2447, 2004.

[9] S. M. Kim, F. Hatami, J. S. Harris, A. W. Kurian, J. Ford, D. King, G. Scalari, M. Giovannini, N. Hoyler, J. Faist, and G. Harris, "Biomedical terahertz imaging with a quantum cascade laser," *Applied Physics Letters*, vol. 88, no. 15, p. 153 903, 2006.

[10] P. Dean, N. K. Saat, S. P. Khanna, M. Salih, A. Burnett, J. Cunningham, E. H. Linfield, and A. G. Davies, "Dual-frequency imaging using an electrically tunable terahertz quantum cascade laser," *Optics Express*, vol. 17, no. 23, pp. 20 631–20 641, 2009.

[11] E. Nichols and J. Tear, "Joining the infra-red and electric wave spectra," *The Astrophysical Journal*, vol. 61, p. 17, 1925.

[12] E. Bründermann, H.-W. Hübers, and M. F. Kimmitt, *Terahertz techniques*. Springer, 2012, vol. 151.

[13] D. H. Barker, D. T. Hodges, and T. S. Hartwick, "Far Infrared Imagery," in *Long-Wavelength Infrared*, W. L. Wolfe, Ed., International Society for Optics and Photonics, vol. 0067, SPIE, 1975, pp. 27–36.

[14] D. L. Woolard, R. Brown, M. Pepper, and M. Kemp, "Terahertz frequency sensing and imaging: A time of reckoning future applications?" *Proceedings of the IEEE*, vol. 93, no. 10, pp. 1722–1743, 2005.

[15] A. G. Davies, E. H. Linfield, and M. B. Johnston, "The development of terahertz sources and their applications," *Physics in Medicine and Biology*, vol. 47, no. 21, pp. 3679–3689, Oct. 2002.

[16] A. Gowen, C. O'Sullivan, and C. O'Donnell, "Terahertz time domain spectroscopy and imaging: Emerging techniques for food process monitoring and quality control," *Trends in Food Science Technology*, vol. 25, no. 1, pp. 40–46, 2012.

[17] G. Mourou, C. V. Stancampiano, A. Antonetti, and A. Orszag, "Picosecond microwave pulses generated with a subpicosecond laser-driven semiconductor switch," *Applied Physics Letters*, vol. 39, no. 4, pp. 295–296, 1981.

[18] B. B. Hu and M. C. Nuss, "Imaging with terahertz waves," *Opt. Lett.*, vol. 20, no. 16, pp. 1716–1718, Aug. 1995.

[19] P. Dean, A. Valavanis, J. Keeley, K. Bertling, Y. L. Lim, R. Alhathlool, A. D. Burnett, L. H. Li, S. P. Khanna, D. Indjin, T. Taimre, A. D. Rakić, E. H. Linfield, and A. G. Davies, "Terahertz imaging using quantum cascade lasers—a review of systems and applications," *Journal of Physics D: Applied Physics*, vol. 47, no. 37, p. 374 008, 2014.

[20] R. Chhantyal-Pun, A. Valavanis, J. T. Keeley, P. Rubino, I. Kundu, Y. Han, P. Dean, L. Li, A. G. Davies, and E. H. Linfield, "Gas spectroscopy with integrated frequency monitoring through self-mixing in a terahertz quantum-cascade laser," *Opt. Lett.*, vol. 43, no. 10, pp. 2225–2228, May 2018.

[21] H.-W. Hübers, S. G. Pavlov, A. D. Semenov, R. Köhler, L. Mahler, A. Tredicucci, H. E. Beere, D. A. Ritchie, and E. H. Linfield, "Terahertz quantum cascade laser as local oscillator in a heterodyne receiver," *Opt. Express*, vol. 13, no. 15, pp. 5890–5896, Jul. 2005.

[22] R. F. Kazarinov and R. A. Suris, *Possible amplification of electromagnetic waves in a semiconductor with a superlattice*. 1971, vol. 5, pp. 707–709.

[23] J. Faist, F. Capasso, D. L. Sivco, C. Sirtori, A. L. Hutchinson, and A. Y. Cho, "Quantum Cascade Laser," vol. 264, no. 5158, pp. 553–556, 1994.

[24] R. Köhler, A. Tredicucci, F. Beltram, H. E. Beere, E. H. Linfield, A. G. Davies, D. A. Ritchie, R. C. Iotti, and F. Rossi, "Terahertz semiconductor-heterostructure laser," *Nature*, vol. 417, no. 6885, pp. 156–159, 2002.

[25] L. H. Li, L. Chen, J. R. Freeman, M. Salih, P. Dean, A. G. Davies, and E. H. Linfield, "Multi-Watt high-power THz frequency quantum cascade lasers," *Electronics Letters*, vol. 53, no. 12, pp. 799–800, 2017.

[26] A. Khalatpour, A. K. Paulsen, C. Deimert, Z. R. Wasilewski, and Q. Hu, "High-power portable terahertz laser systems," *Nature Photonics*, vol. 15, no. 1, pp. 16–20, 2021.

[27] M. S. Vitiello and A. Tredicucci, "Tunable emission in thz quantum cascade lasers," *IEEE Transactions on Terahertz Science and Technology*, vol. 1, no. 1, pp. 76–84, 2011.

[28] V. P. Wallace, E. MacPherson, J. A. Zeitler, and C. Reid, "Three-dimensional imaging of optically opaque materials using nonionizing terahertz radiation," *J. Opt. Soc. Am. A*, vol. 25, no. 12, pp. 3120–3133, Dec. 2008.

[29] J. Zeitler, Y. Shen, C. Baker, P. F. Taday, M. Pepper, and T. Rades, "Analysis of coating structures and interfaces in solid oral dosage forms by three dimensional terahertz pulsed imaging," *Journal of Pharmaceutical Sciences*, vol. 96, no. 2, pp. 330–340, 2007.

[30] T. Yasui, T. Yasuda, K.-i. Sawanaka, and T. Araki, "Terahertz paintmeter for noncontact monitoring of thickness and drying progress in paint film," *Appl. Opt.*, vol. 44, no. 32, pp. 6849–6856, Nov. 2005.

[31] J. A. Zeitler, P. F. Taday, D. A. Newnham, M. Pepper, K. C. Gordon, and T. Rades, "Terahertz pulsed spectroscopy and imaging in the pharmaceutical setting - a review," *Journal of Pharmacy and Pharmacology*, vol. 59, no. 2, pp. 209–223, 2007.

[32] Y. C. Shen, P. F. Taday, D. A. Newnham, and M. Pepper, "Chemical mapping using reflection terahertz pulsed imaging," vol. 20, no. 7, S254–S257, Jun. 2005.

[33] B. Fischer, M. Hoffmann, H. Helm, G. Modjesch, and P. U. Jepsen, "Chemical recognition in terahertz time-domain spectroscopy and imaging," vol. 20, no. 7, S246–S253, Jun. 2005.

[34] Y. Watanabe, K. Kawase, T. Ikari, H. Ito, Y. Ishikawa, and H. Minamide, "Component spatial pattern analysis of chemicals using terahertz spectroscopic imaging," *Applied Physics Letters*, vol. 83, no. 4, pp. 800–802, 2003.

[35] V. Wallace, A. Fitzgerald, S. Shankar, N. Flanagan, R. Pye, J. Cluff, and D. Arnone, "Terahertz pulsed imaging of basal cell carcinoma ex vivo and in vivo," *British Journal of Dermatology*, vol. 151, no. 2, pp. 424–432, 2004.

[36] A. J. Fitzgerald, V. P. Wallace, M. Jimenez-Linan, L. Bobrow, R. J. Pye, A. D. Purushotham, and D. D. Arnone, "Terahertz pulsed imaging of human breast tumors," *Radiology*, vol. 239, no. 2, pp. 533–540, 2006, PMID: 16543586.

[37] J. Darmo, V. Tamosiunas, G. Fasching, J. Kröll, K. Unterrainer, M. Beck, M. Giovannini, J. Faist, C. Kremser, and P. Debbage, "Imaging with a terahertz quantum cascade laser," *Opt. Express*, vol. 12, no. 9, pp. 1879–1884, May 2004.

[38] D. R. Chamberlin, P. R. Robrish, W. R. Trutna, G. Scalari, M. Giovannini, L. Ajili, and J. Faist, "Imaging at 3.4 thz with a quantum-cascade laser," *Appl. Opt.*, vol. 44, no. 1, pp. 121–125, Jan. 2005.

[39] P. Dean, M. U. Shaukat, S. P. Khanna, S. Chakraborty, M. Lachab, A. Burnett, G. Davies, and E. H. Linfield, "Absorption-sensitive diffuse reflection imaging of concealed powders using a terahertz quantum cascade laser," *Opt. Express*, vol. 16, no. 9, pp. 5997–6007, Apr. 2008.

[40] M. Ravaro, M. Locatelli, L. Viti, D. Ercolani, L. Consolino, S. Bartalini, L. Sorba, M. S. Vitiello, and P. De Natale, "Detection of a 2.8thz quantum cascade laser with a semiconductor nanowire field-effect transistor coupled to a bow-tie antenna," *Applied Physics Letters*, vol. 104, no. 8, p. 083 116, 2014.

[41] A. A. Danylov, J. Waldman, T. M. Goyette, A. J. Gatesman, R. H. Giles, K. J. Linden, W. R. Neal, W. E. Nixon, M. C. Wanke, and J. L. Reno, "Transformation of the multimode terahertz quantum cascade laser beam into a gaussian, using a hollow dielectric waveguide," *Appl. Opt.*, vol. 46, no. 22, pp. 5051–5055, Aug. 2007.

[42] H. Richter, A. D. Semenov, S. G. Pavlov, L. Mahler, A. Tredicucci, H. E. Beere, D. A. Ritchie, K. S. Il'in, M. Siegel, and H.-W. Hübers, "Terahertz heterodyne receiver with quantum cascade laser and hot electron bolometer mixer in a pulse tube cooler," *Applied Physics Letters*, vol. 93, no. 14, p. 141 108, 2008.

[43] M. Hajenius, P. Khosropanah, J. N. Hovenier, J. R. Gao, T. M. Klapwijk, S. Barbieri, S. Dhillon, P. Filloux, C. Sirtori, D. A. Ritchie, and H. E. Beere, "Surface plasmon quantum cascade lasers as terahertz local oscillators," *Opt. Lett.*, vol. 33, no. 4, pp. 312–314, Feb. 2008.

[44] E. Bründermann, M. Havenith, G. Scalari, M. Giovannini, J. Faist, J. Kunsch, L. Mechold, and M. Abraham, "Turn-key compact high temperature terahertz quantum cascade lasers:" *Opt. Express*, vol. 14, no. 5, pp. 1829–1841, Mar. 2006.

[45] H. Richter, M. Greiner-Bär, S. G. Pavlov, A. D. Semenov, M. Wienold, L. Schrottke, M. Giehler, R. Hey, H. T. Grahn, and H.-W. Hübers, "A compact, continuous-wave terahertz source based on a quantum-cascade laser and a miniature cryocooler," *Opt. Express*, vol. 18, no. 10, pp. 10 177–10 187, May 2010.

[46] A. A. Danylov, T. M. Goyette, J. Waldman, M. J. Coulombe, A. J. Gatesman, R. H. Giles, X. Qian, N. Chandrayan, S. Vangala, K. Termkoa, W. D. Goodhue, and W. E. Nixon, "Terahertz inverse synthetic aperture radar (isar) imaging with a quantum cascade laser transmitter," *Opt. Express*, vol. 18, no. 15, pp. 16 264–16 272, Jul. 2010.

[47] U. S. de Cumis, J.-H. Xu, L. Masini, R. Degl'Innocenti, P. Pingue, F. Beltram, A. Tredicucci, M. S. Vitiello, P. A. Benedetti, H. E. Beere, and D. A. Ritchie, "Terahertz confocal microscopy with a quantum cascade laser source," *Opt. Express*, vol. 20, no. 20, pp. 21 924–21 931, Sep. 2012.

[48] N. Rothbart, H. Richter, M. Wienold, L. Schrottke, H. T. Grahn, and H.-W. Hübers, "Fast 2-d and 3-d terahertz imaging with a quantum-cascade laser and a scanning mirror," *IEEE Transactions on Terahertz Science and Technology*, vol. 3, no. 5, pp. 617–624, 2013.

[49] K. L. Nguyen, M. L. Johns, L. F. Gladden, C. H. Worrall, P. Alexander, H. E. Beere, M. Pepper, D. A. Ritchie, J. Alton, S. Barbieri, and E. H. Linfield, "Three-dimensional imaging with a terahertz quantum cascade laser," *Opt. Express*, vol. 14, no. 6, pp. 2123–2129, Mar. 2006.

[50] X. Yin, B. W.-H. Ng, J. A. Zeitler, K. L. Nguyen, L. F. Gladden, and D. Abbott, "Local computed tomography using a thz quantum cascade laser," *IEEE Sensors Journal*, vol. 10, no. 11, pp. 1718–1731, 2010.

[51] M. S. Vitiello, L. Consolino, S. Bartalini, A. Taschin, A. Tredicucci, M. Inguscio, and P. De Natale, "Quantum-limited frequency fluctuations in a terahertz laser," *Nature Photonics*, vol. 6, no. 8, pp. 525–528, 2012.

[52] M. Ravaro, S. Barbieri, G. Santarelli, V. Jagtap, C. Manquest, C. Sirtori, S. P. Khanna, and E. H. Linfield, "Measurement of the intrinsic linewidth of terahertz quantum cascade lasers using a near-infrared frequency comb," *Opt. Express*, vol. 20, no. 23, pp. 25 654–25 661, Nov. 2012.

[53] D. M. Kane and K. A. Shore, *Unlocking Dynamical Diversity: Optical Feedback Effects on Semiconductor Lasers*. Wiley, 2005.

[54] T. Taimre, M. Nikolić, K. Bertling, Y. L. Lim, T. Bosch, and A. D. Rakić, "Laser feedback interferometry: a tutorial on the self-mixing effect for coherent sensing," *Advances in Optics and Photonics*, vol. 7, no. 3, pp. 570–631, 2015.

[55] G. J. S. P. G. R. King, "Metrology with an optical maser," *New Sci*, vol. 17, p. 180, 1963.

[56] D. A. Kleinman and P. P. Kisliuk, "Discrimination Against Unwanted Orders in the Fabry-Perot Resonator," *Bell System Technical Journal*, vol. 41, no. 2, pp. 453–462, 1962.

[57] C. K. N. P. H. Kogelnick, "Mode Suppression and Single Frequency Operation in Gaseous Optical Masers," *IRE*, vol. 50, pp. 2365–2366, 1962.

[58] H. Bachert and S. Raab, "The Influence of External Optical Coupling on the Threshold Current Density of GaAs Injection Lasers," *Phys. Status Solidi*, vol. 29, pp. 175–178, 1968.

[59] V. N. Morozov, V. V. Nikitin, A. A. Sheronov, and P. N. Lebedev, "Self synchronization of modes in a GaAs semiconductor injection laser," *Sov. J. Exp. Theor. Phys. Lett.*, vol. 6, pp. 256–258, 1968.

[60] R. Lang and K. Kobayashi, "External optical feedback effects on semiconductor injection laser properties," *IEEE Journal of Quantum Electronics*, vol. 16, no. 3, pp. 347–355, 1980.

[61] J. Keeley, "Self-mixing in Terahertz Quantum Cascade Lasers," Ph.D. dissertation, 2016.

[62] P. Rubino, "Near-field Imaging Using Self Mixing in Terahertz frequency Quantum Cascade Lasers," no. August, 2019.

[63] G. Giuliani, M. Norgia, S. Donati, and T. Bosch, "Laser diode self-mixing technique for sensing applications," *Journal of Optics A: Pure and Applied Optics*, vol. 4, no. 6, S283–S294, Nov. 2002.

[64] R. P. Green, J.-H. Xu, L. Mahler, A. Tredicucci, F. Beltram, G. Giuliani, H. E. Beere, and D. A. Ritchie, "Linewidth enhancement factor of terahertz quantum cascade lasers," *Applied Physics Letters*, vol. 92, no. 7, p. 071 106, 2008.

[65] P. Dean, Y. Leng Lim, A. Valavanis, R. Kliese, M. Nikolić, S. P. Khanna, M. Lachab, D. Indjin, Z. Ikonić, P. Harrison, A. D. Rakić, E. H. Linfield, and A. G. Davies, "Terahertz imaging through self-mixing in a quantum cascade laser," *Optics Letters*, vol. 36, no. 13, pp. 2587–2589, 2011.

[66] G. Scalari, L. Ajili, J. Faist, H. Beere, E. Linfield, D. Ritchie, and G. Davies, "Far-infrared ($\lambda \approx$ 87 μm) bound-to-continuum quantum-cascade lasers operating up to 90 k," *Applied Physics Letters*, vol. 82, no. 19, pp. 3165–3167, 2003.

[67] D. Indjin, P. Harrison, R. W. Kelsall, and Z. Ikonić, "Mechanisms of temperature performance degradation in terahertz quantum-cascade lasers," *Applied Physics Letters*, vol. 82, no. 9, pp. 1347–1349, 2003.

[68] S. S. Dhillon, M. S. Vitiello, E. H. Linfield, A. G. Davies, C. H. Matthias, B. John, P. Claudio, M. Gensch, P. Weightman, G. P. Williams, E. Castro-Camus, D. R. S. Cumming, F. Simoens, I. Escorcia-Carranza, J. Grant, L. Stepan, K.-G. Makoto, K. Kuniaki, K. Martin, A. S. Charles, L. C. Tyler, H. Rupert, A. G. Markelz, Z. D. Taylor, P. W. Vincent, J. A. Zeitler, S. Juraj, M. K. Timothy, B. Ellison, S. Rea, P. Goldsmith, B. C. Ken, A. Roger, D. Pardo, P. G. Huggard, V. Krozer, S. Haymen, F. Martyn, R. Cyril, S. Alwyn, S. Andreas, N. Mira, R. Nick, C. Roland, E. C. John, and B. J. Michael, "The 2017 terahertz science and technology roadmap," *Journal of Physics D: Applied Physics*, vol. 50, no. 4, p. 43 001, 2017.

[69] P. Dean, Y. Leng Lim, A. Valavanis, R. Kliese, M. Nikolić, S. P. Khanna, M. Lachab, D. Indjin, Z. Ikonić, P. Harrison, A. D. Rakić, E. H. Linfield, and A. G. Davies, "Terahertz imaging through self-mixing in a quantum cascade laser," *Optics Letters*, vol. 36, no. 13, pp. 2587–2589, 2011.

[70] J. Keeley, P. Dean, A. Valavanis, K. Bertling, Y. L. Lim, R. Alhathlool, T. Taimre, L. H. Li, D. Indjin, A. D. Rakic, E. H. Linfield, and A. G. Davies, "Three-dimensional terahertz imaging using swept-frequency feedback interferometry with a quantum cascade laser," *Optics Letters*, vol. 40, no. 6, p. 994, 2015.

[71] A. D. Rakić, T. Taimre, K. Bertling, Y. L. Lim, P. Dean, D. Indjin, Z. Ikonić, P. Harrison, A. Valavanis, S. P. Khanna, M. Lachab, S. J. Wilson, E. H. Linfield, and A. G. Davies, "Swept-frequency feedback interferometry using terahertz frequency QCLs: a method for imaging and materials analysis," *Optics Express*, vol. 21, no. 19, p. 22 194, 2013.

[72] Y. L. Lim, T. Taimre, K. Bertling, P. Dean, D. Indjin, A. Valavanis, S. P. Khanna, M. Lachab, H. Schaider, T. W. Prow, H. P. Soyer, S. J. Wilson, E. H. Linfield, A. G. Davies, and A. D. Rakić, "High-contrast coherent

terahertz imaging of porcine tissue via swept-frequency feedback interferometry," *Biomed. Opt. Express*, vol. 5, no. 11, pp. 3981–3989, Nov. 2014.

[73] Y. Ren, R. Wallis, D. S. Jessop, R. Degl'Innocenti, A. Klimont, H. E. Beere, and D. A. Ritchie, "Fast terahertz imaging using a quantum cascade amplifier," *Applied Physics Letters*, vol. 107, no. 1, p. 011 107, 2015.

[74] M. Wienold, T. Hagelschuer, N. Rothbart, L. Schrottke, K. Biermann, H. T. Grahn, and H.-W. Hübers, "Real-time terahertz imaging through self-mixing in a quantum-cascade laser," *Applied Physics Letters*, vol. 109, no. 1, p. 11 102, Jul. 2016.

[75] D. Richards, A. Zayats, F. Keilmann, and R. Hillenbrand, "Near-field microscopy by elastic light scattering from a tip," *Philosophical Transactions of the Royal Society of London. Series A: Mathematical, Physical and Engineering Sciences*, vol. 362, no. 1817, pp. 787–805, 2004.

[76] R. Hillenbrand, "Scattering-type Near-field Microscopy: From Nanoscale Infrared Material Recognition to Superlens Studies," in *2007 Conference on Lasers and Electro-Optics - Pacific Rim*, 2007, pp. 1–2.

[77] R. Hillenbrand and F. Keilmann, "Material-specific mapping of metal/semiconductor/dielectric nanosystems at 10 nm resolution by backscattering near-field optical microscopy," *Applied Physics Letters*, vol. 80, no. 1, pp. 25–27, 2002.

[78] A. J. Huber, A. Ziegler, T. Köck, and R. Hillenbrand, "Infrared nanoscopy of strained semiconductors," *Nature Nanotechnology*, vol. 4, p. 153, 2009.

[79] F. Keilmann, A. J. Huber, and R. Hillenbrand, "Nanoscale Conductivity Contrast by Scattering-Type Near-Field Optical Microscopy in the Visible, Infrared and THz Domains," *Journal of Infrared, Millimeter, and Terahertz Waves*, vol. 30, no. 12, pp. 1255–1268, 2009.

[80] J. M. Stiegler, A. J. Huber, S. L. Diedenhofen, J. Gómez Rivas, R. E. Algra, E. P. A. M. Bakkers, and R. Hillenbrand, "Nanoscale Free-Carrier Profiling of Individual Semiconductor Nanowires by Infrared Near-Field Nanoscopy," *Nano Letters*, vol. 10, no. 4, pp. 1387–1392, 2010.

[81] T. Taubner, F. Eilmann, and R. Hillenbrand, "Nanoscale-resolved subsurface imaging by scattering-type near-field optical microscopy," *Optics Express*, vol. 13, no. 22, pp. 8893–8899, 2005.

[82] A. J. L. Adam, "Review of near-field terahertz measurement methods and their applications," *Journal of Infrared, Millimeter, and Terahertz Waves*, vol. 32, no. 8, pp. 976–1019, 2011.

[83] G. Binnig, C. F. Quate, and C. Gerber, "Atomic Force Microscope," *Physical Review Letters*, vol. 56, no. 9, pp. 930–933, 1986.

[84] R. Esteban, R. Vogelgesang, and K. Kern, "Tip-substrate interaction in optical near-field microscopy," *Physical Review B*, vol. 75, no. 19, p. 195 410, 2007.

[85] E. Yoxall, "Applications of Scattering-Type Scanning Near-Field Optical Microscopy in the Infrared," Ph.D. dissertation, 2013.

[86] L. Aigouy, F. X. Andréani, A. C. Boccara, J. C. Rivoal, J. A. Porto, R. Carminati, J. J. Greffet, and R. Mégy, "Near-field optical spectroscopy using an incoherent light source," *Applied Physics Letters*, vol. 76, no. 4, pp. 397–399, 2000.

[87] B. Knoll and F. Keilmann, "Enhanced dielectric contrast in scattering-type scanning near-field optical microscopy," *Optics Communications*, vol. 182, no. 4, pp. 321–328, 2000.

[88] R. Hillenbrand, T. Taubner, and F. Keilmann, "Phonon-enhanced light–matter interaction at the nanometre scale," *Nature*, vol. 418, no. 6894, pp. 159–162, 2002.

[89] R. Hillenbrand and F. Keilmann, "Complex optical constants on a subwavelength scale," *Phys. Rev. Lett.*, vol. 85, pp. 3029–3032, 14 Oct. 2000.

[90] A. Dereux, C. Girard, and J.-C. Weeber, "Theoretical principles of near-field optical microscopies and spectroscopies," *The Journal of Chemical Physics*, vol. 112, no. 18, pp. 7775–7789, 2000.

[91] M. B. Raschke and C. Lienau, "Apertureless near-field optical microscopy: Tip–sample coupling in elastic light scattering," *Applied Physics Letters*, vol. 83, no. 24, pp. 5089–5091, 2003.

[92] B. Knoll and F. Keilmann, "Near-field probing of vibrational absorption for chemical microscopy," *Nature*, vol. 399, no. 6732, pp. 134–137, 1999.

[93] H.-T. Chen, R. Kersting, and G. C. Cho, "Terahertz imaging with nanometer resolution," *Applied Physics Letters*, vol. 83, no. 15, pp. 3009–3011, 2003.

[94] A. Cvitkovic, N. Ocelic, and R. Hillenbrand, "Analytical model for quantitative prediction of material contrasts in scattering-type near-field optical microscopy," *Optics Express*, vol. 15, no. 14, pp. 8550–8565, 2007.

[95] J. Dorfmüller, R. Vogelgesang, R. T. Weitz, C. Rockstuhl, C. Etrich, T. Pertsch, F. Lederer, and K. Kern, "Fabry-Pérot resonances in one-dimensional plasmonic nanostructures," *Nano Letters*, vol. 9, no. 6, pp. 2372–2377, 2009.

[96] M. M. Wiecha, S. Al-Daffaie, A. Bogdanov, M. D. Thomson, O. Yilmazoglu, F. Küppers, A. Soltani, and H. G. Roskos, "Direct Near-Field Observation of Surface Plasmon Polaritons on Silver Nanowires," *ACS Omega*, vol. 4, no. 26, pp. 21 962–21 966, Dec. 2019.

[97] J. Chen, M. Badioli, P. Alonso-González, S. Thongrattanasiri, F. Huth, J. Osmond, M. Spasenović, A. Centeno, A. Pesquera, P. Godignon, A. Zurutuza Elorza, N. Camara, F. J. García, R. Hillenbrand, and F. H. Koppens, "Optical nano-imaging of gate-tunable graphene plasmons," *Nature*, vol. 487, no. 7405, pp. 77–81, 2012.

[98] A. Woessner, M. B. Lundeberg, Y. Gao, A. Principi, P. Alonso-González, M. Carrega, K. Watanabe, T. Taniguchi, G. Vignale, M. Polini, J. Hone, R. Hillenbrand, and F. H. L. Koppens, "Highly confined low-loss plasmons in graphene–boron nitride heterostructures," *Nature Materials*, vol. 14, p. 421, 2014.

[99] M. B. Lundeberg, Y. Gao, A. Woessner, C. Tan, P. Alonso-González, K. Watanabe, T. Taniguchi, J. Hone, R. Hillenbrand, and F. H. L. Koppens, "Thermoelectric detection and imaging of propagating graphene plasmons," *Nature Materials*, vol. 16, no. 2, pp. 204–207, 2017.

[100] Z. Fei, G. O. Andreev, W. Bao, L. M. Zhang, A. S. McLeod, C. Wang, M. K. Stewart, Z. Zhao, G. Dominguez, M. Thiemens, M. M. Fogler, M. J. Tauber, A. H. Castro-Neto, C. N. Lau, F. Keilmann, and D. N. Basov, "Infrared Nanoscopy of Dirac Plasmons at the Graphene–SiO2 Interface," *Nano Letters*, vol. 11, no. 11, pp. 4701–4705, 2011.

[101] Z. Fei, M. D. Goldflam, J.-S. Wu, S. Dai, M. Wagner, A. S. McLeod, M. K. Liu, K. W. Post, S. Zhu, G. C. A. M. Janssen, M. M. Fogler, and D. N. Basov, "Edge and surface plasmons in graphene nanoribbons," *Nano Letters*, vol. 15, no. 12, pp. 8271–8276, 2015, PMID: 26571096.

[102] F. Hu, Y. Luan, Z. Fei, I. Z. Palubski, M. D. Goldflam, S. Dai, J.-S. Wu, K. W. Post, G. C. A. M. Janssen, M. M. Fogler, and D. N. Basov, "Imaging the Localized Plasmon Resonance Modes in Graphene Nanoribbons," *Nano Letters*, vol. 17, no. 9, pp. 5423–5428, Sep. 2017.

[103] G. X. Ni, A. S. McLeod, Z. Sun, L. Wang, L. Xiong, K. W. Post, S. S. Sunku, B. Y. Jiang, J. Hone, C. R. Dean, M. M. Fogler, and D. N. Basov, "Fundamental limits to graphene plasmonics," *Nature*, vol. 557, no. 7706, pp. 530–533, 2018.

[104] Q. Guo, C. Li, B. Deng, S. Yuan, F. Guinea, and F. Xia, "Infrared nanophotonics based on graphene plasmonics," *ACS Photonics*, vol. 4, no. 12, pp. 2989–2999, 2017.

[105] O. Mitrofanov, W. Yu, R. Thompson, Y. Jiang, Z. Greenberg, J. Palmer, I. Brener, W. Pan, C. Berger, W. de Heer, and Z. Jiang, "Terahertz near-field imaging of surface plasmon waves in graphene structures," *Solid State Communications*, vol. 224, pp. 47–52, 2015.

[106] P. Alonso-González, A. Y. Nikitin, Y. Gao, A. Woessner, M. B. Lundeberg, A. Principi, N. Forcellini, W. Yan, S. Vélez, A. J. Huber, K. Watanabe, T. Taniguchi, F. Casanova, L. E. Hueso, M. Polini, J. Hone, F. H. Koppens, and R. Hillenbrand, "Acoustic terahertz graphene plasmons revealed by photocurrent nanoscopy," *Nature Nanotechnology*, vol. 12, no. 1, pp. 31–35, 2017.

[107] M. S. Vitiello, G. Scalari, B. Williams, and P. D. Natale, "Quantum cascade lasers: 20 years of challenges," *Opt. Express*, vol. 23, no. 4, pp. 5167–5182, Feb. 2015.

[108] P. Dean, O. Mitrofanov, J. Keeley, I. Kundu, L. Li, E. H. Linfield, and A. Giles Davies, "Apertureless near-field terahertz imaging using the self-mixing effect in a quantum cascade laser," *Applied Physics Letters*, vol. 108, no. 9, p. 91 113, Feb. 2016.

[109] A. J. Huber, F. Keilmann, J. Wittborn, J. Aizpurua, and R. Hillenbrand, "Terahertz near-field nanoscopy of mobile carriers in single semiconductor nanodevices," *Nano Letters*, vol. 8, no. 11, pp. 3766–3770, 2008, PMID: 18837565.

[110] F. Buersgens, R. Kersting, and H.-T. Chen, "Terahertz microscopy of charge carriers in semiconductors," *Applied Physics Letters*, vol. 88, no. 11, p. 112 115, 2006.

[111] G. Acuna, S. F. Heucke, F. Kuchler, H.-T. Chen, A. J. Taylor, and R. Kersting, "Surface plasmons in terahertz metamaterials," *Opt. Express*, vol. 16, no. 23, pp. 18 745–18 751, Nov. 2008.

[112] R. Degl'Innocenti, R. Wallis, B. Wei, L. Xiao, S. J. Kindness, O. Mitrofanov, P. Braeuninger-Weimer, S. Hofmann, H. E. Beere, and D. A. Ritchie, "Terahertz Nanoscopy of Plasmonic Resonances with a Quantum Cascade Laser," *ACS Photonics*, vol. 4, no. 9, pp. 2150–2157, 2017.

[113] M. C. Giordano, S. Mastel, C. Liewald, L. L. Columbo, M. Brambilla, L. Viti, A. Politano, K. Zhang, L. Li, A. G. Davies, E. H. Linfield, R. Hillenbrand, F. Keilmann, G. Scamarcio, and M. S. Vitiello, "Phase-resolved terahertz self-detection near-field microscopy," *Opt. Express*, vol. 26, no. 14, pp. 18 423–18 435, Jul. 2018.

[114] W. L. Barnes, A. Dereux, and T. W. Ebbesen, "Surface plasmon subwavelength optics," *Nature*, vol. 424, p. 824, 2003.

[115] E. Ozbay, "Plasmonics: Merging photonics and electronics at nanoscale dimensions," *Science*, vol. 311, no. 5758, pp. 189–193, 2006.

[116] D. K. Gramotnev and S. I. Bozhevolnyi, "Plasmonics beyond the diffraction limit," *Nature Photonics*, vol. 4, no. 2, pp. 83–91, 2010.

[117] V. Z. Anatoly and I. S. Igor, "Near-field photonics: surface plasmon polaritons and localized surface plasmons," *Journal of Optics A: Pure and Applied Optics*, vol. 5, no. 4, S16, 2003.

[118] P. A. Huidobro, A. I. Fernández-Domínguez, J. B. Pendry, L. Martín-Moreno, and F. J. Garcia-Vidal, *Spoof Surface Plasmon Metamaterials*, Cambridge, 2018.

[119] Raether and Heinz, *Surface Plasmons on Smooth and Rough Surfaces and on Gratings*. Springer, 1988.

[120] X. Zhang, Q. Xu, L. Xia, Y. Li, J. Gu, Z. Tian, C. Ouyang, J. Han, and W. Zhang, "Terahertz surface plasmonic waves: a review," *Advanced Photonics*, vol. 2, no. 1, pp. 1–19, 2020.

[121] G. Goubau, "Surface waves and their application to transmission lines," *Journal of Applied Physics*, vol. 21, no. 11, pp. 1119–1128, 1950.

[122] D. L. Mills and A. A. Maradudin, "Surface corrugation and surface-polariton binding in the infrared frequency range," *Phys. Rev. B*, vol. 39, pp. 1569–1574, 3 Jan. 1989.

[123] J. B. Pendry, L. Martín-Moreno, and F. J. Garcia-Vidal, "Mimicking Surface Plasmons with Structured Surfaces," *Science*, vol. 305, no. 5685, pp. 847–848, 2004.

[124] D. R. Smith and N. Kroll, "Negative Refractive Index in Left-Handed Materials," *Physical Review Letters*, vol. 85, no. 14, pp. 2933–2936, 2000.

[125] D. R. Smith, W. J. Padilla, D. C. Vier, S. C. Nemat-Nasser, and S. Schultz, "Composite Medium with Simultaneously Negative Permeability and Permittivity," *Physical Review Letters*, vol. 84, no. 18, pp. 4184–4187, 2000.

[126] J. B. Pendry, "Negative Refraction Makes a Perfect Lens," *Physical Review Letters*, vol. 85, no. 18, pp. 3966–3969, 2000.

[127] J. B. Pendry and S. A. Ramakrishna, "Focusing light using negative refraction," *Journal of Physics: Condensed Matter*, vol. 15, no. 37, p. 6345, 2003.

[128] D. R. Smith, J. B. Pendry, and M. C. K. Wiltshire, "Metamaterials and Negative Refractive Index," *Science*, vol. 305, no. 5685, pp. 788–792, 2004.

[129] A. P. Hibbins, B. R. Evans, and J. R. Sambles, "Experimental verification of designer surface plasmons," *Science*, vol. 308, no. 5722, pp. 670–672, 2005.

[130] A. P. Hibbins, M. J. Lockyear, I. R. Hooper, and J. R. Sambles, "Waveguide arrays as plasmonic metamaterials: Transmission below cutoff," *Phys. Rev. Lett.*, vol. 96, p. 073 904, 7 Feb. 2006.

[131] C. R. Williams, S. R. Andrews, S. A. Maier, A. I. Fernández-Domínguez, L. Martín-Moreno, and F. J. García-Vidal, "Highly confined guiding of terahertz surface plasmon polaritons on structured metal surfaces," *Nature Photonics*, vol. 2, no. 3, pp. 175–179, 2008.

[132] N. Yu, Q. J. Wang, M. A. Kats, J. A. Fan, S. P. Khanna, L. Li, A. G. Davies, E. H. Linfield, and F. Capasso, "Designer spoof surface plasmon structures collimate terahertz laser beams," *Nature Materials*, vol. 9, no. 9, pp. 730–735, 2010.

[133] J. Dorfmüller, R. Vogelgesang, W. Khunsin, C. Rockstuhl, C. Etrich, and K. Kern, "Plasmonic Nanowire Antennas: Experiment, Simulation, and Theory," *Nano Letters*, vol. 10, no. 9, pp. 3596–3603, 2010.

[134] J. Pendry, A. Holden, D. Robbins, and W. Stewart, "Magnetism from conductors and enhanced nonlinear phenomena," *IEEE Transactions on Microwave Theory and Techniques*, vol. 47, no. 11, pp. 2075–2084, 1999.

[135] D. Schurig, J. J. Mock, and D. R. Smith, "Electric-field-coupled resonators for negative permittivity metamaterials," *Applied Physics Letters*, vol. 88, no. 4, p. 41 109, 2006.

[136] X. Shen, T. J. Cui, D. Martin-Cano, and F. J. Garcia-Vidal, "Conformal surface plasmons propagating on ultrathin and flexible films," *Proceedings of the National Academy of Sciences*, vol. 110, no. 1, pp. 40–45, 2013.

[137] D. Martin-Cano, M. L. Nesterov, A. I. Fernandez-Dominguez, F. J. Garcia-Vidal, L. Martin-Moreno, and E. Moreno, "Domino plasmons for subwavelength terahertz circuitry," *Opt. Express*, vol. 18, no. 2, pp. 754–764, Jan. 2010.

[138] A. E. Siegman, *Lasers*, A. Kelly, Ed. Sausalito, CA: University Science Books, 1986.

[139] S. O. Kasap, *Optoelectronics & Photonics: Principles & Practices*, 2nd. University of Saskatchewan: Pearson, 2013.

[140] P. Harrison and A. Valavanis, *Quantum Wells, Wires and Dots: Theoretical and Computational Physics of Semiconductor Nanostructures*, 4th. John Wiley & Sons, Ltd, 2016.

[141] P. S. Zory, *Quantum Well Lasers*. Academic Press, 1993.

[142] J. P. van der Ziel, R. Dingle, R. C. Miller, W. Wiegmann, and W. A. Nordland, "Laser oscillation from quantum states in very thin gaasal0.2ga0.8as multilayer structures," *Applied Physics Letters*, vol. 26, no. 8, pp. 463–465, 1975.

[143] R. Paiella, *Intersubband Transitions In Quantum Structures*. McGraw-Hill Education, 2010.

[144] J. Faist, F. Capasso, C. Sirtori, D. L. Sivco, A. L. Hutchinson, and A. Y. Cho, "Vertical transition quantum cascade laser with bragg confined excited state," *Applied Physics Letters*, vol. 66, no. 5, pp. 538–540, 1995.

[145] J. Faist, F. Capasso, C. Sirtori, D. L. Sivco, J. N. Baillargeon, A. L. Hutchinson, S.-N. G. Chu, and A. Y. Cho, "High power mid-infrared ($\lambda \sim 5$ µm) quantum cascade lasers operating above room temperature," *Applied Physics Letters*, vol. 68, no. 26, pp. 3680–3682, 1996.

[146] J. Faist, F. Capasso, C. Sirtori, D. Sivco, and A. Cho, *Intersubband Transitions in Quantum Wells: Physics and Device Applications II*, G. Mueller, Ed. San Diego, CA: Academic Press, 1999.

[147] B. S. Williams, "Terahertz quantum-cascade lasers," *Nature Photonics*, vol. 1, p. 517, 2007.

[148] J. Alton, S. Barbieri, C. Worral, M. Houghton, H. E. Beere, E. L. Linfield, and D. A. Ritchie, "Optimum resonant tunnelling injection and influence of doping density on the performance of THz bound-to-continuum cascade lasers," in *Terahertz and Gigahertz Electronics and Photonics IV*, R. J. Hwu and K. J. Linden, Eds., International Society for Optics and Photonics, vol. 5727, SPIE, 2005, pp. 65–73.

[149] B. S. Williams, H. Callebaut, S. Kumar, Q. Hu, and J. L. Reno, "3.4-thz quantum cascade laser based on longitudinal-optical-phonon scattering for depopulation," *Applied Physics Letters*, vol. 82, no. 7, pp. 1015–1017, 2003.

[150] M. I. Amanti, G. Scalari, R. Terazzi, M. Fischer, M. Beck, J. Faist, A. Rudra, P. Gallo, and E. Kapon, "Bound-to-continuum terahertz quantum cascade laser with a single-quantum-well phonon extraction/injection stage," *New Journal of Physics*, vol. 11, no. 12, p. 125 022, Dec. 2009.

[151] H. Grahn, "Low-voltage terahertz quantum-cascade lasers based on lo-phonon-assisted interminiband transitions," English, *Electronics Letters*, vol. 45, 1030–1031(1), 20 Sep. 2009.

[152] M. Rochat, L. Ajili, H. Willenberg, J. Faist, H. Beere, G. Davies, E. Linfield, and D. Ritchie, "Low-threshold terahertz quantum-cascade lasers," *Applied Physics Letters*, vol. 81, no. 8, pp. 1381–1383, 2002.

[153] J. Ulrich, R. Zobl, N. Finger, K. Unterrainer, G. Strasser, and E. Gornik, "Terahertz-electroluminescence in a quantum cascade structure," *Physica B: Condensed Matter*, vol. 272, no. 1, pp. 216–218, 1999.

[154] B. S. Williams, S. Kumar, H. Callebaut, Q. Hu, and J. L. Reno, "Terahertz quantum-cascade laser at $\lambda \approx 100$ µm using metal waveguide for mode confinement," *Applied Physics Letters*, vol. 83, no. 11, pp. 2124–2126, 2003.

[155] B. S. Williams, S. Kumar, Q. Hu, and J. L. Reno, "Operation of terahertz quantum-cascade lasers at 164 k in pulsed mode and at 117 k in continuous-wave mode," *Opt. Express*, vol. 13, no. 9, pp. 3331–3339, May 2005.

[156] G. Scalari, N. Hoyler, M. Giovannini, and J. Faist, "Terahertz bound-to-continuum quantum-cascade lasers based on optical-phonon scattering extraction," *Applied Physics Letters*, vol. 86, no. 18, p. 181 101, 2005.

[157] A. J. L. Adam, I. Kašalynas, J. N. Hovenier, T. O. Klaassen, J. R. Gao, E. E. Orlova, B. S. Williams, S. Kumar, Q. Hu, and J. L. Reno, "Beam patterns of terahertz quantum cascade lasers with subwavelength cavity dimensions," *Applied Physics Letters*, vol. 88, no. 15, p. 151 105, 2006.

[158] E. E. Orlova, J. N. Hovenier, T. O. Klaassen, I. Ka šalynas, A. J. L. Adam, J. R. Gao, T. M. Klapwijk, B. S. Williams, S. Kumar, Q. Hu, and J. L. Reno, "Antenna model for wire lasers," *Phys. Rev. Lett.*, vol. 96, p. 173 904, 17 May 2006.

[159] A. W. M. Lee, Q. Qin, S. Kumar, B. S. Williams, Q. Hu, and J. L. Reno, "High-power and high-temperature thz quantum-cascade lasers based on lens-coupled metal-metal waveguides," *Opt. Lett.*, vol. 32, no. 19, pp. 2840–2842, Oct. 2007.

[160] I. Kundu, "Frequency tunable terahertz quantum cascade lasers," Ph.D. dissertation, The University of Leeds, 2014.

[161] Y.-C. Shih, M. Murakami, E. L. Wilkie, and A. C. Callegari, "Effects of interfacial microstructure on uniformity and thermal stability of aunige ohmic contact to n-type gaas," *Journal of Applied Physics*, vol. 62, no. 2, pp. 582–590, 1987.

[162] D. Jucknischke, H. Buhlmann, M. Ilegems, B. Jeckelmann, and W. Schwitz, "Properties of alloyed augeni-contacts on gaas/gaalas-heterostructures," in *Conference on Precision Electromagnetic Measurements*, 1990, pp. 336–337.

[163] M. Hatzakis, B. J. Canavello, and J. M. Shaw, "Single-step optical lift-off process," *IBM Journal of Research and Development*, vol. 24, no. 4, pp. 452–460, 1980.

[164] T. Sands, "Compound semiconductor contact metallurgy," *Materials Science and Engineering: B*, vol. 1, no. 3, pp. 289–312, 1988.

[165] R. Köhler, A. Tredicucci, F. Beltram, H. E. Beere, E. H. Linfield, A. G. Davies, D. A. Ritchie, S. S. Dhillon, and C. Sirtori, "High-performance continuous-wave operation of superlattice terahertz quantum-cascade lasers," *Applied Physics Letters*, vol. 82, no. 10, pp. 1518–1520, 2003.

[166] N. M. Hinchliffe, "Fabrication and measurement of double metal terahertz quantum cascade lasers," PhD Thesis, University of Leeds, 2009.

[167] P. Rubino, J. Keeley, N. Sulollari, A. D. Burnett, A. Valavanis, I. Kundu, M. C. Rosamond, L. Li, E. H. Linfield, A. G. Davies, J. E. Cunningham, and P. Dean, "All-electronic phase-resolved thz microscopy using the self-mixing effect in a semiconductor laser," *ACS Photonics*, vol. 8, no. 4, pp. 1001–1006, 2021.

[168] I. Kundu, P. Dean, A. Valavanis, L. Li, Y. Han, E. H. Linfield, and A. G. Davies, "Frequency Tunability and Spectral Control in Terahertz Quantum Cascade Lasers With Phase-Adjusted Finite-Defect-Site Photonic Lattices," *IEEE Transactions on Terahertz Science and Technology*, vol. 7, no. 4, pp. 360–367, 2017.

[169] C. Belacel, Y. Todorov, S. Barbieri, D. Gacemi, I. Favero, and C. Sirtori, "Optomechanical terahertz detection with single meta-atom resonator," *Nature Communications*, vol. 8, no. 1, pp. 2–9, 2017.

[170] R. Degl'Innocenti, L. Xiao, D. S. Jessop, S. J. Kindness, Y. Ren, H. Lin, J. A. Zeitler, J. A. Alexander-Webber, H. J. Joyce, P. Braeuninger-Weimer, S. Hofmann, H. E. Beere, and D. A. Ritchie, "Fast Room-Temperature Detection of Terahertz Quantum Cascade Lasers with Graphene-Loaded Bow-Tie Plasmonic Antenna Arrays," *ACS Photonics*, vol. 3, no. 10, pp. 1747–1753, 2016.

[171] A. Toma, S. Tuccio, M. Prato, F. De Donato, A. Perucchi, P. Di Pietro, S. Marras, C. Liberale, R. Proietti Zaccaria, F. De Angelis, L. Manna, S. Lupi, E. Di Fabrizio, and L. Razzari, "Squeezing Terahertz Light into Nanovolumes: Nanoantenna Enhanced Terahertz Spectroscopy (NETS) of Semiconductor Quantum Dots," *Nano Letters*, vol. 15, no. 1, pp. 386–391, Jan. 2015.

[172] R. Degl'Innocenti, D. S. Jessop, Y. D. Shah, J. Sibik, J. A. Zeitler, P. R. Kidambi, S. Hofmann, H. E. Beere, and D. A. Ritchie, "Low-Bias Terahertz Amplitude Modulator Based on Split-Ring Resonators and Graphene," *ACS Nano*, vol. 8, no. 3, pp. 2548–2554, Mar. 2014.

[173] R. Degl'Innocenti, D. S. Jessop, C. W. O. Sol, L. Xiao, S. J. Kindness, H. Lin, J. A. Zeitler, P. Braeuninger-Weimer, S. Hofmann, Y. Ren, V. S. Kamboj, J. P. Griffiths, H. E. Beere, and D. A. Ritchie, "Fast Modulation of Terahertz Quantum Cascade Lasers Using Graphene Loaded Plasmonic Antennas," *ACS Photonics*, vol. 3, no. 3, pp. 464–470, Mar. 2016.

[174] B. Wei, S. J. Kindness, N. W. Almond, R. Wallis, Y. Wu, Y. Ren, S. C. Shi, P. Braeuninger-Weimer, S. Hofmann, H. E. Beere, D. A. Ritchie, and R. Degl'lnnocenti, "Amplitude stabilization and active control of a terahertz quantum cascade laser with a graphene loaded split-ring-resonator array," *Applied Physics Letters*, vol. 112, no. 20, p. 201 102, 2018.

[175] N. Meinzer, W. L. Barnes, and I. R. Hooper, "Plasmonic meta-atoms and metasurfaces," *Nature Photonics*, vol. 8, no. 12, pp. 889–898, 2014.

[176] J. Shi, Z. Li, D. K. Sang, Y. Xiang, J. Li, S. Zhang, and H. Zhang, "Thz photonics in two dimensional materials and metamaterials: Properties, devices and prospects," *J. Mater. Chem. C*, vol. 6, pp. 1291–1306, 6 2018.

[177] S. Keren-Zur, M. Tal, S. Fleischer, D. M. Mittleman, and T. Ellenbogen, "Generation of spatiotemporally tailored terahertz wavepackets by nonlinear metasurfaces," *Nature Communications*, vol. 10, no. 1, 2019.

[178] L. Luo, I. Chatzakis, J. Wang, F. B. Niesler, M. Wegener, T. Koschny, and C. M. Soukoulis, "Broadband terahertz generation from metamaterials," *Nature Communications*, vol. 5, pp. 1–6, 2014.

[179] T. Siday, P. P. Vabishchevich, L. Hale, C. T. Harris, T. S. Luk, J. L. Reno, I. Brener, and O. Mitrofanov, "Terahertz Detection with Perfectly-Absorbing Photoconductive Metasurface," *Nano Letters*, vol. 19, no. 5, pp. 2888–2896, May 2019.

[180] S. H. Lee, M. Choi, T. T. Kim, S. Lee, M. Liu, X. Yin, H. K. Choi, S. S. Lee, C. G. Choi, S. Y. Choi, X. Zhang, and B. Min, "Switching terahertz waves with gate-controlled active graphene metamaterials," *Nature Materials*, vol. 11, no. 11, pp. 936–941, 2012.

[181] F. Valmorra, G. Scalari, C. Maissen, W. Fu, C. Schönenberger, J. W. Choi, H. G. Park, M. Beck, and J. Faist, "Low-Bias Active Control of Terahertz Waves by Coupling Large-Area CVD Graphene to a Terahertz Metamaterial," *Nano Letters*, vol. 13, no. 7, pp. 3193–3198, Jul. 2013.

[182] H. T. Chen, J. F. O'Hara, A. K. Azad, A. J. Taylor, R. D. Averitt, D. B. Shrekenhamer, and W. J. Padilla, "Experimental demonstration of frequency-agile terahertz metamaterials," *Nature Photonics*, vol. 2, no. 5, pp. 295–298, 2008.

[183] Z. Ma, S. M. Hanham, P. Albella, B. Ng, H. T. Lu, Y. Gong, S. A. Maier, and M. Hong, "Terahertz All-Dielectric Magnetic Mirror Metasurfaces," *ACS Photonics*, vol. 3, no. 6, pp. 1010–1018, Jun. 2016.

[184] L. Liu, Y. Zarate, H. T. Hattori, D. N. Neshev, I. V. Shadrivov, and D. A. Powell, "Terahertz focusing of multiple wavelengths by graphene metasurfaces," *Applied Physics Letters*, vol. 108, no. 3, p. 31 106, Jan. 2016.

[185] S. H. Lee, J. Choi, H. D. Kim, H. Choi, and B. Min, "Ultrafast refractive index control of a terahertz graphene metamaterial," *Scientific Reports*, vol. 3, pp. 3–8, 2013.

[186] H.-R. Park, K. J. Ahn, S. Han, Y.-M. Bahk, N. Park, and D.-S. Kim, "Colossal Absorption of Molecules Inside Single Terahertz Nanoantennas," *Nano Letters*, vol. 13, no. 4, pp. 1782–1786, Apr. 2013.

[187] S. J. Park, J. T. Hong, S. J. Choi, H. S. Kim, W. K. Park, S. T. Han, J. Y. Park, S. Lee, D. S. Kim, and Y. H. Ahn, "Detection of microorganisms using terahertz metamaterials," *Scientific Reports*, vol. 4, pp. 1–7, 2014.

[188] Y. Todorov, A. M. Andrews, I. Sagnes, R. Colombelli, P. Klang, G. Strasser, and C. Sirtori, "Strong Light-Matter Coupling in Subwavelength Metal-Dielectric Microcavities at Terahertz Frequencies," *Phys. Rev. Lett.*, vol. 102, no. 18, p. 186 402, May 2009.

[189] G. Scalari, C. Maissen, D. Turčinková, D. Hagenmüller, S. De Liberato, C. Ciuti, C. Reichl, D. Schuh, W. Wegscheider, M. Beck, and J. Faist, "Ultrastrong Coupling of the Cyclotron Transition of a 2D Electron Gas to a THz Metamaterial," *Science*, vol. 335, no. 6074, pp. 1323–1326, 2012.

[190] R. Singh, C. Rockstuhl, and W. Zhang, "Strong influence of packing density in terahertz metamaterials," *Applied Physics Letters*, vol. 97, no. 24, p. 241 108, Dec. 2010.

[191] J. Wallauer, A. Bitzer, S. Waselikowski, and M. Walther, "Near-field signature of electromagnetic coupling in metamaterial arrays: a terahertz microscopy study," *Opt. Express*, vol. 19, no. 18, pp. 17 283–17 292, Aug. 2011.

[192] J. Keller, C. Maissen, J. Haase, G. L. Paravicini-Bagliani, F. Valmorra, J. Palomo, J. Mangeney, J. Tignon, S. S. Dhillon, G. Scalari, and J. Faist, "Coupling Surface Plasmon Polariton Modes to Complementary THz Metasurfaces Tuned by Inter Meta-Atom Distance," *Advanced Optical Materials*, vol. 5, no. 6, p. 1 600 884, 2017.

[193] P.-C. Li and E. T. Yu, "Flexible, low-loss, large-area, wide-angle, wavelength-selective plasmonic multilayer metasurface," *Journal of Applied Physics*, vol. 114, no. 13, p. 133 104, Oct. 2013.

[194] P. Alonso-González, P. Albella, F. Neubrech, C. Huck, J. Chen, F. Golmar, F. Casanova, L. E. Hueso, A. Pucci, J. Aizpurua, and R. Hillenbrand, "Experimental Verification of the Spectral Shift between Near- and Far-Field Peak Intensities of Plasmonic Infrared Nanoantennas," *Phys. Rev. Lett.*, vol. 110, no. 20, p. 203 902, May 2013.

[195] A. Bhattacharya, G. Georgiou, S. Sawallich, C. Matheisen, M. Nagel, and J. Gómez Rivas, "Large near-to-far field spectral shifts for terahertz resonances," *Phys. Rev. B*, vol. 93, no. 3, p. 35 438, Jan. 2016.

[196] A. Bhattacharya and J. Gómez Rivas, "Full vectorial mapping of the complex electric near-fields of THz resonators," *APL Photonics*, vol. 1, no. 8, pp. 0–8, 2016.

[197] F. Blanchard, K. Ooi, T. Tanaka, A. Doi, and K. Tanaka, "Terahertz spectroscopy of the reactive and radiative near-field zones of split ring resonator," *Opt. Express*, vol. 20, no. 17, pp. 19 395–19 403, Aug. 2012.

[198] A. Bitzer, A. Ortner, H. Merbold, T. Feurer, and M. Walther, "Terahertz near-field microscopy of complementary planar metamaterials: Babinet's principle," *Opt. Express*, vol. 19, no. 3, pp. 2537–2545, Jan. 2011.

[199] O. Mitrofanov, I. Khromova, T. Siday, R. J. Thompson, A. N. Ponomarev, I. Brener, and J. L. Reno, "Near-Field Spectroscopy and Imaging of Subwavelength Plasmonic Terahertz Resonators," *IEEE Transactions on Terahertz Science and Technology*, vol. 6, no. 3, pp. 382–388, May 2016.

[200] O. Mitrofanov, Z. Han, F. Ding, S. I. Bozhevolnyi, I. Brener, and J. L. Reno, "Detection of internal fields in double-metal terahertz resonators," *Applied Physics Letters*, vol. 110, no. 6, p. 61 109, Feb. 2017.

[201] A. J. Huber, F. Keilmann, J. Wittborn, J. Aizpurua, and R. Hillenbrand, "Terahertz Near-Field Nanoscopy of Mobile Carriers in Single Semiconductor Nanodevices," *Nano Letters*, vol. 8, no. 11, pp. 3766–3770, 2008.

[202] Z. Fei, A. S. Rodin, G. O. Andreev, W. Bao, A. S. McLeod, M. Wagner, L. M. Zhang, Z. Zhao, M. Thiemens, G. Dominguez, M. M. Fogler, A. H. C. Neto, C. N. Lau, F. Keilmann, and D. N. Basov, "Gate-tuning of graphene plasmons revealed by infrared nano-imaging," *Nature*, vol. 487, p. 82, 2012.

[203] J. Keeley, K. Bertling, P. L. Rubino, Y. L. Lim, T. Taimre, X. Qi, I. Kundu, L. H. Li, D. Indjin, A. D. Rakić, E. H. Linfield, A. G. Davies, J. Cunningham, and P. Dean, "Detection sensitivity of laser feedback interferometry using a terahertz quantum cascade laser," *Optics Letters*, vol. 44, no. 13, pp. 3314–3317, 2019.

[204] M. C. Giordano, S. Mastel, C. Liewald, L. L. Columbo, M. Brambilla, L. Viti, A. Politano, K. Zhang, L. Li, A. G. Davies, E. H. Linfield, R. Hillenbrand, F. Keilmann, G. Scamarcio, and M. S. Vitiello, "Phase-resolved terahertz self-detection near-field microscopy," *Optics Express*, vol. 26, no. 14, pp. 18 423–18 435, 2018.

[205] P. Di Pietro, M. Ortolani, O. Limaj, A. Di Gaspare, V. Giliberti, F. Giorgianni, M. Brahlek, N. Bansal, N. Koirala, S. Oh, P. Calvani, and S. Lupi, "Observation of Dirac plasmons in a topological insulator," *Nature Nanotechnology*, vol. 8, no. 8, pp. 556–560, 2013.

[206] B. Knoll and F. Keilmann, "Near-field probing of vibrational absorption for chemical microscopy," *Nature*, vol. 399, no. 6732, pp. 134–137, 1999.

[207] B. Deutsch, R. Hillenbrand, and L. Novotny, "Near-field amplitude and phase recovery using phase-shifting interferometry," *Optics Express*, vol. 16, no. 2, p. 494, 2008.

[208] A. S. McLeod, P. Kelly, M. D. Goldflam, Z. Gainsforth, A. J. Westphal, G. Dominguez, M. H. Thiemens, M. M. Fogler, and D. N. Basov, "Model for quantitative tip-enhanced spectroscopy and the extraction of nanoscale-resolved optical constants," *Phys. Rev. B*, vol. 90, no. 8, p. 85 136, Aug. 2014.

[209] B. Hecht, H. Bielefeldt, Y. Inouye, D. W. Pohl, and L. Novotny, "Facts and artifacts in near-field optical microscopy," *Journal of Applied Physics*, vol. 81, no. 6, pp. 2492–2498, 1997.

[210] V. E. Babicheva, S. Gamage, M. I. Stockman, and Y. Abate, "Near-field edge fringes at sharp material boundaries," *Opt. Express*, vol. 25, no. 20, pp. 23 935–23 944, Oct. 2017.

[211] S. Mastel, A. A. Govyadinov, C. Maissen, A. Chuvilin, A. Berger, and R. Hillenbrand, "Understanding the image contrast of material boundaries in ir nanoscopy reaching 5 nm spatial resolution," *ACS Photonics*, vol. 5, no. 8, pp. 3372–3378, 2018.

[212] D. R. Bacon, A. D. Burnett, M. Swithenbank, C. Russell, L. Li, C. D. Wood, J. Cunningham, E. H. Linfield, A. G. Davies, P. Dean, and J. R. Freeman, "Free-space terahertz radiation from a LT-GaAs-on-quartz large-area photoconductive emitter," *Optics Express*, vol. 24, no. 23, pp. 26 986–26 997, 2016.

[213] N. Ocelic, A. Huber, and R. Hillenbrand, "Pseudoheterodyne detection for background-free near-field spectroscopy," *Applied Physics Letters*, vol. 89, no. 10, pp. 2004–2007, 2006.

[214] A. D. Rakic, T. Taimre, K. Bertling, Y. L. Lim, P. Dean, A. Valavanis, and D. Indjin, "Sensing and imaging using laser feedback interferometry with quantum cascade lasers," *Applied Physics Reviews*, vol. 6, no. 2, pp. 0-19, 2019.

[215] P. Dean, A. Valavanis, J. Keeley, K. Bertling, Y. Leng Lim, R. Alhathlool, S. Chowdhury, T. Taimre, L. H. Li, D. Indjin, S. J. Wilson, A. D. Rakić, E. H. Linfield, and A. Giles Davies, "Coherent three-dimensional terahertz imaging through self-mixing in a quantum cascade laser," *Applied Physics Letters*, vol. 103, no. 18, p. 181 112, 2013.

[216] E. Yoxall, M. Navarro-Cía, M. Rahmani, S. A. Maier, and C. C. Phillips, "Widely tuneable scattering-type scanning near-field optical microscopy using pulsed quantum cascade lasers," *Applied Physics Letters*, vol. 103, no. 21, p. 213 110, 2013.

[217] E. Hecht, *Optics*, 2nd. Addison-Wesley, 1987.

[218] B. Schaefer, E. Collett, R. Smyth, D. Barrett, and B. Fraher, "Measuring the Stokes polarization parameters," *American Journal of Physics*, vol. 75, no. 2, pp. 163–168, 2007.

[219] P. Janassek, S. Hartmann, A. Molitor, F. Michel, and W. Elsäßer, "Investigations of the polarization behavior of quantum cascade lasers by Stokes parameters," *Optics Letters*, vol. 41, no. 2, p. 305, 2016.

[220] D. Dhirhe, T. J. Slight, B. M. Holmes, and C. N. Ironside, "Active polarisation control of a quantum cascade laser using tuneable birefringence in waveguides," *Optics Express*, vol. 21, no. 20, p. 24 267, 2013.

[221] S. A. Maier, S. R. Andrews, L. Martın-Moreno, and F. J. Garcıa-Vidal, "Terahertz surface plasmon-polariton propagation and focusing on periodically corrugated metal wires," *Phys. Rev. Lett.*, vol. 97, p. 176 805, 17 Oct. 2006.

[222] A. I. Fernández-Domínguez, E. Moreno, L. Martín-Moreno, and F. J. García-Vidal, "Terahertz wedge plasmon polaritons," *Opt. Lett.*, vol. 34, no. 13, pp. 2063–2065, Jul. 2009.

[223] A. I. Fernández-Domınguez, E. Moreno, L. Martın-Moreno, and F. J. Garcıa-Vidal, "Guiding terahertz waves along subwavelength channels," *Phys. Rev. B*, vol. 79, p. 233 104, 23 Jun. 2009.

[224] M. A. Kats, D. Woolf, R. Blanchard, N. Yu, and F. Capasso, "Spoof plasmon analogue of metal-insulator-metal waveguides," *Opt. Express*, vol. 19, no. 16, pp. 14 860–14 870, Aug. 2011.

[225] A. I. Fernández-Domínguez, C. R. Williams, F. J. García-Vidal, L. Martín-Moreno, S. R. Andrews, and S. A. Maier, "Terahertz surface plasmon polaritons on a helically grooved wire," *Applied Physics Letters*, vol. 93, no. 14, p. 141 109, 2008.

[226] E. M. G. Brock, E. Hendry, and A. P. Hibbins, "Subwavelength lateral confinement of microwave surface waves," *Applied Physics Letters*, vol. 99, no. 5, p. 051 108, 2011.

[227] Y. Zhang, Y. Xu, C. Tian, Q. Xu, X. Zhang, Y. Li, X. Zhang, J. Han, and W. Zhang, "Terahertz spoof surface-plasmon-polariton subwavelength waveguide," *Photonics Research*, vol. 6, no. 1, pp. 18–23, 2018.

[228] F. J. Garcia-Vidal, L. Martın-Moreno, and J. B. Pendry, "Surfaces with holes in them: New plasmonic metamaterials," *Journal of Optics A: Pure and Applied Optics*, vol. 7, no. 2, S97–S101, Jan. 2005.

[229] R. Quesada, D. Martín-Cano, F. J. García-Vidal, and J. Bravo-Abad, "Deep-subwavelength negative-index waveguiding enabled by coupled conformal surface plasmons," *Opt. Lett.*, vol. 39, no. 10, pp. 2990–2993, May 2014.

[230] L. Liu, Z. Li, B. Xu, P. Ning, C. Chen, J. Xu, X. Chen, and C. Gu, "Dual-band trapping of spoof surface plasmon polaritons and negative group velocity realization through microstrip line with gradient holes," *Applied Physics Letters*, vol. 107, no. 20, p. 201 602, 2015.

[231] X. Liu, Y. Feng, K. Chen, B. Zhu, J. Zhao, and T. Jiang, "Planar surface plasmonic waveguide devices based on symmetric corrugated thin film structures," *Opt. Express*, vol. 22, no. 17, pp. 20 107–20 116, Aug. 2014.

[232] X. Gao, J. Hui Shi, X. Shen, H. Feng Ma, W. Xiang Jiang, L. Li, and T. Jun Cui, "Ultrathin dual-band surface plasmonic polariton waveguide and frequency splitter in microwave frequencies," *Applied Physics Letters*, vol. 102, no. 15, p. 151 912, 2013.

[233] X. Liu, Y. Feng, B. Zhu, J. Zhao, and T. Jiang, "High-order modes of spoof surface plasmonic wave transmission on thin metal film structure," *Opt. Express*, vol. 21, no. 25, pp. 31 155–31 165, Dec. 2013.

[234] H. F. Ma, X. Shen, Q. Cheng, W. X. Jiang, and T. J. Cui, "Broadband and high-efficiency conversion from guided waves to spoof surface plasmon polaritons," *Laser & Photonics Reviews*, vol. 8, no. 1, pp. 146–151, 2014.

[235] X. Gao, L. Zhou, X. Y. Yu, W. P. Cao, H. O. Li, H. F. Ma, and T. J. Cui, "Ultra-wideband surface plasmonic y-splitter," *Opt. Express*, vol. 23, no. 18, pp. 23 270–23 277, Sep. 2015.

[236] Z. Han, Y. Zhang, and S. I. Bozhevolnyi, "Spoof surface plasmon-based stripe antennas with extreme field enhancement in the terahertz regime," *Opt. Lett.*, vol. 40, no. 11, pp. 2533–2536, Jun. 2015.

[237] J. Y. Yin, J. Ren, H. C. Zhang, B. C. Pan, and T. J. Cui, "Broadband Frequency-Selective Spoof Surface Plasmon Polaritons on Ultrathin Metallic Structure," *Scientific Reports*, vol. 5, no. 1, p. 8165, 2015.

[238] X. Gao, L. Zhou, Z. Liao, H. F. Ma, and T. J. Cui, "An ultra-wideband surface plasmonic filter in microwave frequency," *Applied Physics Letters*, vol. 104, no. 19, p. 191 603, 2014.

[239] H. C. Zhang, T. J. Cui, Q. Zhang, Y. Fan, and X. Fu, "Breaking the Challenge of Signal Integrity Using Time-Domain Spoof Surface Plasmon Polaritons," *ACS Photonics*, vol. 2, no. 9, pp. 1333–1340, Sep. 2015.

[240] Q. Zhang, H. C. Zhang, J. Y. Yin, B. C. Pan, and T. J. Cui, "A series of compact rejection filters based on the interaction between spoof SPPs and CSRRs," *Scientific Reports*, vol. 6, no. 1, p. 28 256, 2016.

[241] J. Xu, Z. Li, L. Liu, C. Chen, B. Xu, P. Ning, and C. Gu, "Low-pass plasmonic filter and its miniaturization based on spoof surface plasmon polaritons," *Optics Communications*, vol. 372, pp. 155–159, 2016.

[242] Y. Yang, H. Chen, S. Xiao, N. A. Mortensen, and J. Zhang, "Ultrathin 90-degree sharp bends for spoof surface plasmon polaritons," *Opt. Express*, vol. 23, no. 15, pp. 19 074–19 081, Jul. 2015.

[243] Y. Liang, H. Yu, H. C. Zhang, C. Yang, and T. J. Cui, "On-chip sub-terahertz surface plasmon polariton transmission lines in CMOS," *Scientific Reports*, vol. 5, no. 1, p. 14 853, 2015.

[244] H. C. Zhang, S. Liu, X. Shen, L. H. Chen, L. Li, and T. J. Cui, "Broadband amplification of spoof surface plasmon polaritons at microwave frequencies," *Laser & Photonics Reviews*, vol. 9, no. 1, pp. 83–90, 2015.

[245] Y. Yang, X. Shen, P. Zhao, H. C. Zhang, and T. J. Cui, "Trapping surface plasmon polaritons on ultrathin corrugated metallic strips in microwave frequencies," *Opt. Express*, vol. 23, no. 6, pp. 7031–7037, Mar. 2015.

[246] W. Zhang, G. Zhu, L. Sun, and F. Lin, "Trapping of surface plasmon wave through gradient corrugated strip with underlayer ground and manipulating its propagation," *Applied Physics Letters*, vol. 106, no. 2, p. 021 104, 2015.

[247] J. Y. Yin, J. Ren, H. C. Zhang, Q. Zhang, and T. J. Cui, "Capacitive-coupled Series Spoof Surface Plasmon Polaritons," *Scientific Reports*, vol. 6, no. 1, p. 24 605, 2016.

[248] B. C. Pan, J. Zhao, Z. Liao, H. C. Zhang, and T. J. Cui, "Multi-layer topological transmissions of spoof surface plasmon polaritons," *Scientific Reports*, vol. 6, no. 1, p. 22 702, 2016.

[249] Y. Li, J. Zhang, S. Qu, J. Wang, M. Feng, J. Wang, and Z. Xu, "K-dispersion engineering of spoof surface plasmon polaritons for beam steering," *Opt. Express*, vol. 24, no. 2, pp. 842–852, Jan. 2016.

[250] H. C. Zhang, Y. Fan, J. Guo, X. Fu, and T. J. Cui, "Second-harmonic generation of spoof surface plasmon polaritons using nonlinear plasmonic metamaterials," *ACS Photonics*, vol. 3, no. 1, pp. 139–146, 2016.

[251] H. Xiang, Y. Meng, Q. Zhang, F. F. Qin, J. J. Xiao, D. Han, and W. Wen, "Spoof surface plasmon polaritons on ultrathin metal strips with tapered grooves," *Optics Communications*, vol. 356, pp. 59–63, 2015.

[252] B. J. Yang and Y. J. Zhou, "Compact broadband slow wave system based on spoof plasmonic thz waveguide with meander grooves," *Optics Communications*, vol. 356, pp. 336–342, 2015.

[253] S. Becker, T. Fip, and M. Rahm, "Routing of strongly confined terahertz spoof surface plasmon polaritons on metasurfaces along straight and curved pathways with subwavelength width," *Opt. Express*, vol. 28, no. 5, pp. 6766–6780, Mar. 2020.

[254] P. Cheben, R. Halir, J. H. Schmid, H. A. Atwater, and D. R. Smith, "Sub-wavelength integrated photonics," *Nature*, vol. 560, no. 7720, pp. 565–572, 2018.

[255] X. Shen and T. Jun Cui, "Planar plasmonic metamaterial on a thin film with nearly zero thickness," *Applied Physics Letters*, vol. 102, no. 21, 2013.

[256] T. J. Cui and X. Shen, "Thz and microwave surface plasmon polaritons on ultrathin corrugated metallic strips," *Terahertz Science and Technology*, vol. 6, no. 2, pp. 147–164, 2013.

[257] X. Zhang, Q. Xu, L. Xia, Y. Li, J. Gu, Z. Tian, C. Ouyang, J. Han, and W. Zhang, "Terahertz surface plasmonic waves: a review," *Advanced Photonics*, vol. 2, no. 01, p. 1, 2020.

[258] P. Achmari, A. M. Siddiquee, G. Si, J. Lin, B. Abbey, and S. Kou, "Investigating the probe-tip influence on imaging using scanning near-field optical microscopy," *OSA Continuum*, vol. 4, no. 4, pp. 1143–1154, Apr. 2021.

[259] A. Garcıa-Etxarri, I. Romero, F. J. Garcıa de Abajo, R. Hillenbrand, and J. Aizpurua, "Influence of the tip in near-field imaging of nanoparticle plasmonic modes: Weak and strong coupling regimes," *Phys. Rev. B*, vol. 79, p. 125 439, 12 Mar. 2009.

[260] X. Liu, Y. Feng, K. Chen, B. Zhu, J. Zhao, and T. Jiang, "Planar surface plasmonic waveguide devices based on symmetric corrugated thin film structures," *Optics Express*, vol. 22, no. 17, p. 20 107, 2014.

[261] T. Holmgaard, Z. Chen, S. I. Bozhevolnyi, L. Markey, and A. Dereux, "Design and characterization of dielectric-loaded plasmonic directional couplers," *J. Lightwave Technol.*, vol. 27, no. 24, pp. 5521–5528, Dec. 2009.

[262] T. Nikolajsen, K. Leosson, and S. I. Bozhevolnyi, "Surface plasmon polariton based modulators and switches operating at telecom wavelengths," *Applied Physics Letters*, vol. 85, no. 24, pp. 5833–5835, 2004.

[263] L. Liu, Z. Han, and S. He, "Novel surface plasmon waveguide for high integration," *Opt. Express*, vol. 13, no. 17, pp. 6645–6650, Aug. 2005.

[264] A. Boltasseva, T. Nikolajsen, K. Leosson, K. Kjaer, M. S. Larsen, and S. I. Bozhevolnyi, "Integrated optical components utilizing long-range surface plasmon polaritons," *J. Lightwave Technol.*, vol. 23, no. 1, p. 413, Jan. 2005.

[265] H. S. Won, K. C. Kim, S. H. Song, C.-H. Oh, P. S. Kim, S. Park, and S. I. Kim, "Vertical coupling of long-range surface plasmon polaritons," *Applied Physics Letters*, vol. 88, no. 1, p. 011 110, 2006.

[266] R. Charbonneau, C. Scales, I. Breukelaar, S. Fafard, N. Lahoud, G. Mattiussi, and P. Berini, "Passive integrated optics elements based on long-range surface plasmon polaritons," *Journal of Lightwave Technology*, vol. 24, no. 1, pp. 477–494, 2006.

[267] F. Liu, Y. Rao, Y. Huang, W. Zhang, and J. Peng, "Coupling between long range surface plasmon polariton mode and dielectric waveguide mode," *Applied Physics Letters*, vol. 90, no. 14, p. 141 101, 2007.

[268] G. Veronis and S. Fan, "Crosstalk between three-dimensional plasmonic slot waveguides," *Opt. Express*, vol. 16, no. 3, pp. 2129–2140, Feb. 2008.

[269] D. K. Gramotnev, K. C. Vernon, and D. F. P. Pile, "Directional coupler using gap plasmon waveguides," *Applied Physics B*, vol. 93, no. 1, pp. 99–106, 2008.

[270] A. Degiron, S.-Y. Cho, T. Tyler, N. M. Jokerst, and D. R. Smith, "Directional coupling between dielectric and long-range plasmon waveguides," *New Journal of Physics*, vol. 11, no. 1, p. 015 002, Jan. 2009.

[271] A. Grier, P. Dean, A. Valavanis, J. Keeley, I. Kundu, J. D. Cooper, G. Agnew, T. Taimre, Y. L. Lim, K. Bertling, A. D. Rakić, L. H. Li, P. Harrison, E. H. Linfield, Z. Ikonić, A. G. Davies, and D. Indjin, "Origin of terminal voltage variations due to self-mixing in terahertz frequency quantum cascade lasers," *Optics Express*, vol. 24, no. 19, pp. 21 948–21 956, 2016.

[272] S. J. Kindness, N. W. Almond, W. Michailow, B. Wei, K. Delfanazari, P. Braeuninger-Weimer, S. Hofmann, H. E. Beere, D. A. Ritchie, and R. Degl'Innocenti, "A terahertz chiral metamaterial modulator," *Advanced Optical Materials*, vol. 8, no. 21, p. 2 000 581, 2020.

[273] K. Song and P. Mazumder, "Active terahertz spoof surface plasmon polariton switch comprising the perfect conductor metamaterial," *IEEE Transactions on Electron Devices*, vol. 56, no. 11, pp. 2792–2799, 2009.

[274] X. Wan, J. Y. Yin, H. C. Zhang, and T. J. Cui, "Dynamic excitation of spoof surface plasmon polaritons," *Applied Physics Letters*, vol. 105, no. 8, p. 083 502, 2014.

[275] K. Song and P. Mazumder, "Nonlinear spoof surface plasmon polariton phenomena based on conductor metamaterials," *Photonics and Nanostructures - Fundamentals and Applications*, vol. 10, no. 4, pp. 674–679, 2012.